2008

Investigation of superconductivity and physical properties of intermetallic compounds: MoN, Mo_3Sb_7, $MgCNi_3$ and transition metal diborides

Amar Bahadur Karki
Louisiana State University and Agricultural and Mechanical College, amarbdrkarki@hotmail.com

INVESTIGATION OF SUPERCONDUCTIVITY AND PHYSICAL PROPERTIES OF INTERMETALLIC COMPOUNDS: MON, MO_3SB_7, $MGCNI_3$ AND TRANSITION METAL DIBORIDES

A Dissertation

Submitted to the Graduate faculty of the
Louisiana State University and
Agricultural and Mechanical College
in partial fulfillment of the
requirement for the degree of
Doctor of Philosophy

in

The Department of Physics and Astronomy

by

Amar Karki
B.Sc., Tribhuvan University, 1991
M.Sc., Tribhuvan University, 1995
M.S., Southern University and A & M College, 2003
August 2008

ACKNOWLEDGEMENTS

I wish to offer my sincere thanks to Dr. David P. Young, thesis advisor, for his relentless guidance, great support, continuous encouragement, and true devotion to the completion of this exciting research project in a very timely manner.

I would like to extend my sincere thanks to Dr. Phillip W. Adams for his great contribution in the development of this thesis, mainly in helping me to synthesize thin films and microfibers and characterize them, and providing me valuable suggestions in writing the thesis. I also acknowledge Dr. Monica Moldovan for teaching me synthesis and characterization techniques.

I appreciate Dr. Michel Cherry, Chair of Department of Physics, for providing me with a very good working atmosphere in the department.

I would like to thank Dr. Dana Browne for his great work in theoretical calculations and justifications, for serving on my thesis committee, and for his advice and encouragement.

Especially, I wish to thank Dr. John F. DiTusa and Dr. Ilya Vekhter for their lucid and inspiring teaching during the Seminar class and Solid State Physics class. I also acknowledge Dr. Roy G. Goodrich for his contribution in my research work.

I would like to thank Dr. Julia Chan and her group for determining the crystal structure and lattice constants by X-ray diffraction measurements. I also thank Dr. Chan for serving on my thesis committee, and for her valuable suggestions.

I am grateful to the department of Physics and Astronomy, for providing a graduate teaching assistantship and to Dr. Young for a research assistantship and extending all possible

help during my Ph.D. I would also like to thank all the professors and staff in the department for their valuable help by different means.

Finally, I wish to thank my parents, Mr. Shambhu B. Karki and Mrs. Budda Kumari Karki and my brother, Dr. Bijaya Karki and sister in law, Shanti Karki for their encouragement and support to pursue higher study. My greatest thanks go to my wife, Mrs. Sushila Karki for her contribution to make my Ph.D. study successful in every way. Thanks to my two little stars Monika Karki and Marina Karki for their understanding and support and tolerating my odd work hours. I also want to thank my other brothers, sister in laws and my nephews for their love and inspiration.

TABLE OF CONTENTS

LIST OF TABLES

LIST OF FIGURES

ABSTRACT

In this dissertation work, I report on the interesting results of our detailed investigations of the synthesis, structural, electrical and magnetic characterization of three different classes of intermetallic systems.

Mo_3Sb_7 wires, thin films and microfibers exhibit the highest T_c ~ 8 K, which is substantially higher than the 2.2 K reported for the single crystal and powder of Mo_3Sb_7. The suppression of the spin fluctuations in Mo_3Sb_7 is evident by the absence of a parabolic dependence of magnetic susceptibility at 1 T. MoN wires, thin films and coated microfibers have T_c ~13 K which is consistent with the values reported in the literature. To my knowledge, for the first time we report on the magnetotransport and critical current measurements in MoN and Mo_3Sb_7 in these forms. We show $(1 - (T/Tc)^2)^{3/2}$ dependence of the critical current density of MoN- and Mo_3Sb_7-coated microfibers near the transition temperature, T_c. The extrapolated values of the critical current density to zero temperature for the MoN- and Mo_3Sb_7-coated fibers are $J_c(0) = 1.66 \times 10^8$ A/cm^2 and $J_c(0) = 7.7 \times 10^5$ A/cm^2 , respectively.

The results of magnetic susceptibility and transport properties measurements of $Mg_{1-x}Be_xCNi_3$ and $Mg_{1-x}Li_xCNi_3$ for x = 0 to 0.2 showed a very small change in T_c and H_{c2} due to Be and Li doping in $MgCNi_3$. The heat treatment of the carbon deficient samples MgC_xNi_3 for 2 h in N gas improved the superconductivity of the compounds. In $MgC_{0.7}Ni_3$, the superconductivity re-appeared after the treatment.

Single crystals and polycrystalline samples of VB_2 and other transition metal diborides were synthesized. $Cr_{1-x}V_xB_2$ are paramagnetic for x > 0.23, and no superconductivity is observed above 1.8 K. We also present the results of magnetotransport and de Haas–van Alphen (dHvA)

measurements on high quality single crystals of VB_2 grown from a molten aluminum flux. At low temperature the magnetoresistance of VB_2 is very large (~1100%) and is found to be extremely sensitive to sample quality (*RRR* value).

CHAPTER 1

INTRODUCTION

Superconductivity is a phenomenon occurring in certain materials at extremely low temperatures, characterized by exactly zero electrical resistance and the exclusion of the interior magnetic field (the Meissner effect). The onset of superconductivity is accompanied by abrupt changes in various physical properties, which is the hallmark of a phase transition. For example, the electronic heat capacity suffers a discontinuous jump at the superconducting transition temperature, and thereafter ceases to be linear. Superconducting magnets are some of the most powerful electromagnets known. They are used in maglev trains, MRI and NMR machines and the beam-steering magnets used in particle accelerators. Superconductors have also been used to build Josephson junctions which are the building blocks of SQUIDs (superconducting quantum interference devices), the most sensitive magnetometers known.

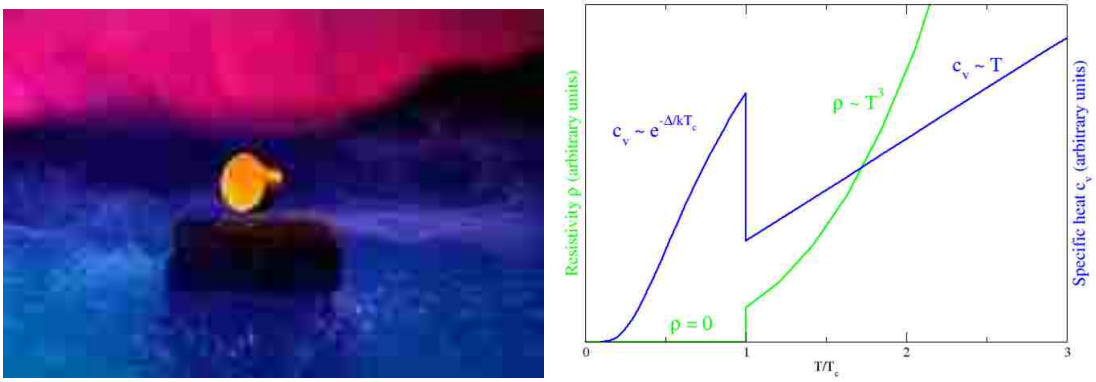

Fig: 1.1 Right: A magnet levitating above a high-temperature superconductor, cooled with liquid nitrogen. Left: Behavior of heat capacity (c_v) and resistivity (ρ) at the superconducting phase transition.

Since the discovery of the superconductivity in mercury in 1911 [1], a broad and significant research effort has been aimed at identifying and characterizing superconducting materials. In 1957 the first widely-accepted theoretical understanding of superconductivity (BCS

theory) was published. Since then, many theoretical and experimental results in this exciting research field have been discovered. Since 1986, copper oxide compounds have dominated the superconductivity fast-track, but copper oxides are not the only superconductors worthy of study. In 1953, researchers first saw the zero-resistance phenomenon in a multimetal compound based on niobium, designated A15 [2]. In 1974, a group of chemists achieved superconductivity at a temperature of 23.2 K in a niobium-based thin film-a breakthrough that has gone unchallenged for nearly 20 years [3]. Now, superconductivity researchers are refocusing attention on such "intermetallic" compounds [4]. My research work include following three major branches of intermetallic systems: i) AlB_2 type structure compounds, ii) Mg compounds containing refractory elements such as B and C and iii) A15 phase Mo based compounds.

In the framework of the BCS theory [5] lower-mass elements result in higher frequency phonon modes which may lead to enhanced transition temperatures. The highest superconducting temperature is predicted for the lightest element, hydrogen [6,7,8], under high pressure. At ordinary pressures, the light metallic element Li does not show any evidence of superconductivity down to 4 mK [9], but recent calculations for Li predict that T_c can reach 70 K at high pressures [10,11]. Be has a T_c of 0.25 mK, but in thin films this increases to 10.5 K [12,13]. For example molynitride compounds exhibit higher T_c in intermetallic. Finally, the recent discovery of superconductivity in MgB_2 and $MgCNi_3$ confirms the predictions of higher T_c in compounds containing light elements.

At the beginning of the 21st century, the discovery of 39 K superconductivity in MgB_2, with its unique multiple superconducting gap structure has reignited interest in the intermetallic superconductors [14]. MgB_2 have layered crystal structures - alternating hexagonal layers of Mg and B in the MgB_2 compound. MgB_2 has subsequently been intensively studied because of its exotic properties [14].

The AlB_2 structure type seems to favor a superconducting state in many materials [15-17]. The announcement of superconductivity in MgB_2 has proved to be catalyst for the discovery of several superconductors, some related to magnesium diboride. This discovery revived the interest in a search of superconductivity, especially in related boron compounds, with the very hope that this material will be the tip of a much 'hotter' iceberg, being the first in a series of diborides with a much higher T_c. The transition-metal borides are interesting because of their highly refractory properties and corrosion-resistant characteristics, and due to the discovery of superconductivity in MgB_2, the AlB_2-type transition-metal diborides have attracted a lot of interest, with many experimental and theoretical studies going on in these compounds [18]. However, a clear proof of superconductivity could not be shown for any of these isostructural compounds [15]. Most of the results suggest MgB_2 to be a conventional superconductor with the layers of the boron atoms playing a very important role for superconductivity of MgB_2 [20]. Hence, most work has concentrated on the research on the influence of the boron atoms on superconductivity of MgB_2. However, there is no doubt the metal atoms have played an important role in the superconductivity as well. Some research [21] has shown that the difference of the metal atom in these compounds can influence the electronic properties, phonon behavior and electron–phonon coupling effect. The fact that some borides have been found superconducting by some authors while others did not find traces of superconductivity in the same materials, suggests that non-stoichiometry may be an important factor in the superconductivity of this family [15]. This has been the case with TaB_2, ZrB_2 and BeB_2 [15, 19, 22]. Therefore, further work is necessary to settle the controversy in these systems. Growth of single crystals can provide the best measure of intrinsic properties. With the motivation from these developments I have synthesized and characterized some transitions metal diborides using

various techniques. I grew high quality single crystal of VB_2 which exhibit unusually large magnetoresistance [27].

Shortly after the discovery of MgB_2, a report on superconductivity in $MgCNi_3$ came as another surprise [23]. This was the first example of a perovskite superconductor that did not contain oxygen. Furthermore, the discovery of superconductivity in this compound has drawn attention owing to its high nickel content, which may complicate the origin of superconductivity. Additionally, $MgCNi_3$ may provide a possible link between the traditional intermetallic superconductors and the high T_c oxides. Energy band calculations show that the density of states (DOS) at the Fermi level, $N(E_F)$, is dominated by Ni d-states, and there is a von Hove singularity in the DOS just below E_F [24, 25, 26]. It is surprising that the conduction electrons are derived from partially filled Ni d-states, which typically lead to ferromagnetism in metallic Ni and many Ni-based alloys. Notwithstanding the widespread interest in $MgCNi_3$, its status as a non-BCS superconductor remains controversial. It has been theoretically suggested to be an unconventional superconductor and near instability to ferromagnetism [34]. Experimentally, the pairing mechanism of $MgCNi_3$ is quite controversial. Electron tunneling studies of the density of states in polycrystalline powders have yielded conflicting results as to whether or not $MgCNi_3$ exhibits a BCS density of states spectrum. London penetration depth and the earlier tunneling spectra suggested an unconventional pairing state, while the NMR relaxation rate, specific heat data, and the latter tunneling spectra support a conventional s-wave BCS type behavior [28-32, 44]. Though no long-range magnetic order has been observed, FM spin fluctuations have been confirmed to be vigorous in both pristine [30, 31] and doped [33] $MgCNi_3$. Tunneling into sintered powders is technically difficult, and indeed, a detailed quantitative characterization of $MgCNi_3$ has, in part, been hampered by the fact that only polycrystalline powder samples have been available.

Review of the literature indicates that the investigations of chemical doping in polycrystalline $MgCNi_3$ can result in more interesting properties. Chemical doping experiments are motivated by the unusual band structure of this compound. Most groups have doped in the Ni sites. Rosner et al have suggested if 12 % Mg is replaced by Na or Li, long range magnetic order can be observed [34]. It contains highly volatile Mg and refractory elements C and B. My goal is to investigate the effect of doping in Mg and C site to understand the role of Mg and C in SC and optimize the SC properties of $MgCNi_3$. A lattice compression is expected if the larger ion Mg is substituted by the smaller Be. In order to study the effects of valence change and lattice expansion on the superconducting properties of these intermetallic compounds, pseudo-quaternary $Mg_{1-x}M_xCNi_3$ polycrystalline samples with $0 \leq x \leq .2$, where M is Li or Be, have been synthesized. The effect of N on the superconducting properties of MgC_xNi_3 samples for x = 1.2, 1, 0.9, and 0.7 has also been investigated.

Over the past 20 years, both theoretical and experimental efforts were made on materials which not only undergo a superconducting transition but also exhibit rather unconventional properties in their normal and superconducting states. Among them, it is worth mentioning Chevrel phases containing rare-earth ions, such as the heavy-fermion $CeCu_2Si_2$ compound, which displays an intimate interplay of superconductivity and magnetism, [35-37] and the intermetallic actinides such as UPt_3 or UCo_2, with spin fluctuation behavior [38, 39]. Only a few materials without an actinide element exhibit both superconductivity and spin fluctuation behavior [40]. More precisely, spin fluctuation effects usually manifest themselves at low temperature as a T^2 term in the electrical resistivity, parabolic temperature dependence of the magnetic susceptibility and for some compounds, an upturn in the specific-heat temperature dependence [39].

Recently, a new type II superconductor, namely Mo_3Sb_7, which crystallizes in the Ir_3Ge_7-type structure (space group Im3m), was identified as being a Pauli paramagnet with a superconducting transition temperature, T_c, of 2.1 K and an upper critical field of 17 kOe [41]. In another study [42], the maximum energy gap value (0.32 meV) as well as the critical temperature, (2.2 K) have been derived from the Andreev reflection method. 0.32 meV is close to the expected BCS value of 0.35 meV and is in good agreement with that found by Bukowski *et al.* [41]. Candolfi *et al*. report on electrical resistivity, magnetic susceptibility, and, for the first time, heat capacity measurements on a Mo_3Sb_7 polycrystalline sample [43]. The results suggest that Mo_3Sb_7 could be classified as a coexistent superconductor-spin fluctuation system [43]. It is known for long time that spin fluctuations could suppress superconductivity. Many materials in low dimensional phases such as thin films and microfibers offer a lot of opportunity for the condensed matter researcher to investigate very interesting physical properties such as critical current density, magnetoresistance etc. Furthermore, some materials only show superconductivity in reduced dimensions. For example, Be can have T_c as high as 10 K in thin films [45]. This motivated us to study of Mo_3Sb_7 in the form of wires, thin films and microfibers. Substantially higher superconducting transition temperatures, T_c, and upper critical field, H_{c2}, were observed in Mo_3Sb_7 wires, thin films and coated C-microfibers. This has been explained as a result of the suppression of spin fluctuations in the system in these low dimensional forms.

Transition metal nitrides are known to have a set of interesting physical properties such as low compressibility, high melting point, magnetism, and superconductivity [46-50]. A large number of experimental and theoretical works exist which focus on their synthesis and on the microscopic understanding of these properties. Of particular interest is the molybdenum nitride phase which, at ambient conditions of pressure and temperature, is nitrogen deficient [51].

γ-Mo_2N is a known superconductor with T_c ~ 5 K [52]. It is reported that δ-Mo_2N is also a superconductor with T_c ~ 5 K [53]. The hexagonal δ-MoN was crystallized in a slightly distorted NiAs type structure under 6 GPa [54, 55], and the resulting phase showed superconductivity with T_c ~ 12 K [54]. A theoretical study predicted that N-ordered stoichiometric MoN with the cubic NaCl type structure (so called B1-MoN) would have a T_c as high as 29 K [56-59]. Since B1-MoN is believed to be a metastable phase, many studies adopted thin film deposition techniques, such as magnetron sputter, ion-beam assisted deposition, and ion implanting for the synthesis of this phase [60-63, 51, 64, 65]. The B1-MoN films reported in the literature, however, have not exhibited such "high T_c."

It could be argued that the above prediction of the *29 K-T_c* is not realistic for a high-T_c transition metal nitride because this class of compounds tends to form with vacancies on the nitrogen sub lattice [57]. Although δ-MoN with its hexagonal structure has been known for some time, [55] the quality of the crystals was not sufficiently good to determine the positions of the N atoms. Recently, stoichiometric δ-MoN has been produced with high pressure and high temperature annealing [56, 54]. Combined room temperature x-ray and low temperature neutron diffraction experiments [54] revealed the positions of the perfectly ordered N atoms. The superconducting transition temperature was 12.1 K.

MoN can be used to form high-hardness, refractory films making it potentially useful for micro-electromechanical components, tribological applications, and/or protective coatings [56, 57]. These in combination with its relatively high transition temperature T_c ~ 13 K provide ample motive for further development [52]. The bulk modulus of hexagonal δ-MoN phase is the highest of any known compound material [56, 66]. For the first time, we present the transport and critical current measurements on MoN- and Mo_3Sb_7-coated C-microfibers.

Young *et al* have created a new type of superconducting wire, made from an unusual magnesium-carbon-nickel compounds layered around a carbon fiber, that not only carries a high electric current without resistance but also is remarkably strong, thin and long [67]. This is the research work that motivated me to synthesize Mo_3Sb_7 and MoN on commercially available 40-nm thick Mo-coated C- microfibers.

The discovery of exciting physical properties in the above-mentioned novel intermetallic systems persuaded me to explore the superconductivity and magnetic properties of other magnesium compounds. Among the reported over 60,000 [68] intermetallic compounds, approximately 450 are binary, ternary, and quaternary magnesium compounds. There are only three known magnesium carbon compounds, and among them, $MgCNi_3$ is superconducting. Many of the magnesium compounds were found to still be uncharacterized. On the course of investigation of these known phases of magnesium, I synthesized and characterized several of them. The very recent discovery of a new 5-K non-centrosymmetric (without a center of inversion symmetry) intermetallic superconductor $Mg_{10}Ir_{19}B_{16}$ [69] has given me further encouragement in this research.

With the motivation from the review of the literature and the preliminary results of my work, I set up the general goal of my thesis to explore and apply efficient techniques in identification and characterization of superconducting compounds with elements N, Sb, C, Mg, B, Li and Be which are difficult to deal but favor to superconductivity and other interesting physical properties.

This thesis entitled “Investigation of superconductivity and physical properties of intermetallic compounds: MoN, Mo_3Sb_7, $MgCNi_3$ and Transition metal diborides” is organized into seven chapters. In this chapter a general introduction of superconductivity, literature review and my overall motivation and goals have been given. The detailed justification and procedural

steps of the synthesis of single and polycrystalline samples of transition metal diborides, powder pressed pellets of $MgCNi_3$ and doped systems and wires, thin films and thin coatings on C-microfibers of MoN and Mo_3Sb_7 are presented in Chapter 2. Chapter 3 and 4 provide the interesting results of our detailed investigations of the synthesis, structural, electrical and magnetic characterization of Mo_3Sb_7, MoN and $MgCNi_3$ are presented, respectively. The study of transition metal diborides is discussed in chapter 5. Then, with the brief presentation of future work in chapter 6 the thesis is concluded in chapter 7.

1.1 References

[1] Onnes, H K, 1911 *Commun. Phys. Lab* **12** 120

[2] Matthias B T, Geballe T H, Geller S, Corenzwit E 1954 *Phys. Rev.* **95**

[3] Muller J 1980 *Rep. Prog. Phys*. **43** 41

[4] Lipkin R 1994 *Science News*

[5] Barden J, Cooper L.N, Schrieffer J R 1957 *Phys. Rev.* **106** 162

[6] Ashcroft N W 1968 *Phys. Rev. Lett.* **21** 1748

[7] Richardson C F, Ashcroft N W 1997 *Phys. Rev. Lett.* **78** 118

[8] Papaconstantopoulos D A *et al.* 1977 *Phys. Rev. B* **15** 4221

[9] Lang K M *et al*. 1999 *J. Low Temp. Phys.* **114** 445

[10] Christensen N E, Novikov D L 2001 *Phys. Rev. Lett.* **86** 1861

[11] Neaton J B, N. W. Ashcroft N W 1999 *Nature* **400** 141

[12] Takei K, Nakamura K, Maeda Y 1985 *J. Appl. Phys.* **57** 5093

[13] Tutov V I *et al.* 1990 *J. Low Temp. Phys.* **16** 22

[14] Nagamatsu J, Nakagawa N, Muranaka T, Zenaitani Y and Akimitsu J 2001 *Nature* **410** 63

[15] Buzea C, Yamashita T 2001 *Supercond. Sci. Technol.* **14** R115

[16] Kuroiwa S *et al*. 2006 *Physical Review B* **74** 014517

[17] Sampathkumaran E V, Majumdar S, Schneider W, Molodtsov S L, Laubschat C 2002 *Phyica B-Condensed Matter* **312** 152-154

[18] Burdett J K, Canadell E, Miller G J, 1986 *J. Am. Chem. Soc.* **108** 6561–6568

[19] Gasparov V A, Sidorov N S, Zver'kova II, Kulakov M P 2001 *JETP Letters* **73** 532-535

[20] Burdett J K , Canadell E, Miller G J 1986 *J. Am. Chem. Soc.* **108** 6561–6568

[21] Vajeeston P, Ravindran P, Ravi C, Asokamani R 2001 *Phys. Rev. B* **63** 045115

[22] Young D P, Goodrich R G, Adams P W, Chan J Y, Fronczek F R, Drymiotis F, Henry L L 2002 *Physical Review B* **65** Art. No. 180518

[23] He T *et al* 2001 *Nature* **411** 54

[24] Kim J H, Ahn J S, Kim J, Park M-S, Lee S I, Choi E J and Oh S-J 2002 *Phys. Rev. B* **66** 172507

[25] Shim J H, Kwon S K and Min B I 2001 *Phys. Rev. B* **64** 180510

[26] Joseph P J, Singh P P 2005 *Phys. Rev. B* **72** 064519

[27] Karki A B, Gautreaux D P, Chan J Y, Harrison N, Browne D A, Goodrich R G, Young D P 2008 *Journal of Physics : Condensed Matter* **20** 000000 (5pp)

[28] Prozorov R, Snezhko A, He T, Cava R J 2003 *Phys. Rev. B* **68** 180502(R)

[29] Mao Z Q, Rosario M M, Nelson K D,Wu K, Deac I G, Schiffer P, Liu Y, He T, Regan K A

and Cava R J 2003 *Phys. Rev. B* **67** 094502

[30] Singer P M, Imai T, He T, Hayward M A, Cava R J 2001 *Phys. Rev. Lett.* **87** 257601

[31] Shan L, Liu Z Y, Ren Z A, Che G C, Wen H H 2005 *Phys. Rev. B* **71** 144516

[32] Shan L, Tao H J, Gao H, Li Z Z, Ren Z A, Che G C, and H. H. Wen H H, 2003 Phys. Rev. B **68** 144510

[33] Kumary T G, Janaki J,Mani A, Jaya S M, SastryV S,Hariharan Y, Radhakrishnan T S and ValsakumarMC 2002 *Phys. Rev. B* 66 064510

[34] Rosner H, Weht R, Johannes M D, Pickett W E, Tosatti E 2001 *Phys. Rev. Lett.* **88**, 027001

[35] Lynn J W, Shirane G, Thomlinson W, Shelton R N 1981 *Phys. Rev. Lett.* **46** 368

[36] Jarlborg T, Freeman A J 1980 Phys. Rev. Lett. **44** 178

[37] Steglich F, Aarts J, Bredl C D, Lieke W, Meschede D, Franz W, Scha¨fer H, 1979 *Phys. Rev. Lett.* **43** 1892

[38] Stewart G R, Fisk Z, Willis J O, Smith J L 1984 *Phys. Rev. Lett.* **52**, 679

[39] Frings P H, Franse J J M 1985 *Phys. Rev. B* **31** 4355

[40] Junod A, Jarlborg T, Muller J 1983 *Phys. Rev. B* **27** 1568

[41] Bukowski Z, Badurski D, Stepien-Damm J, Troc R 2002 *Solid State Commun.* **123** 283

[42] Dmitriev V M, Rybaltchenko L F, Ishchenko L A, Khristenko E V, Bukowski Z, Rroc R 2006 *Superconductor Science and Technology* **19** 573-576

[43] Candolfi C, Lenoir B, Dauscher A, Bellouard C, Hejtmanek J, Santava E, Tobola *J Phys. Rev. Lett.* **99** 037006

[44] Lin J-Y, Lin P H, Ho P L, Huang H L, Zhang Y-L, Yu R-C, Jin C-Q and Yang H D 2002 *J. Supercond.* **15** 485

[45] Assinese A, Iavarone M, Vaglio R et al. 2000 *Physical Review B* **62** (21): 13915-13918

[46] Levy F, Hones P, Schmid P E, Sanjines R, Diserens M, Wiemer C 1999 *Surf. Coat. Technol.* **120-121** 284

[47] Holleck H 1986 *J. Vac. Sci. Technol. A* **4**, 2661

[48] Suzuki K, Yamaguchi Y, Kaneko T, Yoshida H, Obi Y, Fujimori H, Morita H 2001 *J. Phys. Soc. Jpn.* **70** 1084

[49] Vandenberg J M, Matthias B T 1974 *Mater. Res. Bull.* **9** 1085

[50] Sahu B R, Kleinman L 2004 Physical Review B **70** 073103

[51] Ihara H, Kimura Y, Senzaki K, Kezuka H, and Hirabayashi M 1985 *Phys. Rev. B* **31** 3177

[52] Matthias B T, Hulm J K 1952 *Phys. Rev.* **87** 799

[53] Inumaru K, Baba K, Yamanaka S 2005 *Chem. Mater.* **17** 5935-5940

[54] Bull C L, McMillan P F, Soignard E , and Leinenweber K 2004 *J. Solid State Chem.* **177**, 1488

[55] Bezinge A, Yvon K, Muller J 1987 *Solid State Commun.* **63** 141

[56] Papaconstantopoulos D A, Pickett W E, Klein B M, Boyer L L 1985 *Phys. Rev. B* **31** 752

[57] Papaconstantopoulos D A, Pickett W E 1985 *Phys. Rev. B* **31** 7093

[58] Pickett W E, Klein B M, Papaconstantopoulos D A 1981 *Physica B* **107** 667

[59] Papaconstantopoulos D A, Pickett W E, Klein B M, Boyer L L 1984 *Nature* (London) **308** 494

[60] Linker G, Smithey R, Meyer O 1984 *Journal of Physics F* **14** L115

[61] Yamamoto H, Miki T, Tanaka M 1986 *Adv. Cryog. Eng.* **32** 671

[62] Terada N, Nose M, Hoshi Y 1986 *Adv. Cryog. Eng.* **32**, 663

[63] Saito K, Asada Y 1987 *J. Phys. F: Met. Phys.* **17** 2273

[64] Ihara H, Hirabayashi M, Senzaki K, Kimura Y, Kezuka H 1985 *Phys. Rev. B* **32** 1816

[65] Savvides N 1987 *J. Appl. Phys.* **62** 600

[66] McMillan P F 2002 *Nature Material* **1** 19

[67] Young D P, Moldovan M, Adams P W 2004 *Phys. Rev. B* **70** 064508

[68] Pearson's hand book of crystallographic data for intermetallic phases/P.Villars & L.D. Calvart – 2nd edition

[69] Klimczuk T, Xu3 Q, Morosan E, Zandbergen H W, Cava R J, Cond-mat/papers/ 0608/ 0608576

CHAPTER 2

EXPERIMENTAL DETAILS

2.1 Introduction

In this chapter, we discuss in brief the methodology (synthesis and characterization procedures), and technical details of the instruments used in this work. The synthesis and characterization are essential parts of an investigation dealing with intermetallic systems. Several new synthesis and characterization techniques have been developed recently for the investigation of the physical properties of these materials which depend upon the nature of the sample of study. The material synthesis, structural characterization, and the measurement of physical properties were performed in material science laboratories in the Department of Physics, Chemistry and Geology at Louisiana State University. The details of the equipment set up, sample preparation and characterization procedure are discussed in the following sections.

2.2 Synthesis

The equipment set up in our laboratories makes a variety of synthesis techniques available which are necessary for preparing the materials discussed in this thesis. These techniques include: 1) preparation of polycrystalline samples by solid state reaction in high-temperature tube and box furnaces and by induction and arc melting, 2) synthesis of volatile materials in sealed Ta tubes, 3) single crystal growth by chemical vapor transport and metallic fluxes, and 4) thin film growth by e-beam vaporization.

2.2.1 Polycrystalline Samples

2.2.1.1 Solid State Reaction

The bulk polycrystalline samples with the starting materials like Mg powder which are volatile above 647 °C, are prepared in the form of a pressed pellet [1]. Stoichiometric amounts of the powders of starting materials are mixed and ground well in an alumina mortar. The mixture

is then pressed into pellets of 10 mm diameter under 635 MPa pressure using a stainless steel Graseby Specac die and hydraulic press (Figure 2.1).

Fig: 2.1 Tools used for preparation of pellets of materials in powder form.

Fig: 2.2 High temperature tube furnaces used to anneal the samples.

The pellets are then wrapped with Ta foil and put in an alumina (Al_2O_3) crucible. The crucibles are sealed in a quartz tube in vacuum or under Ar atmosphere. The sealed tube is then put in a horizontal tube furnace for sintering. For some samples the crucibles with pellets are placed in a long quartz tube and heated in a horizontal tube furnace in a stream of gases like Ar, N or NH_3. We can set the different sequence of heating treatments as required. In this kind of furnace available to our lab we can heat up to 1200 $^{\circ}$C.

2.2.1.2 Arc and RF Induction Melting

Polycrystalline samples of nonvolatile materials, especially intermetallics, can be prepared by arc and RF induction melting [2]. To arc melt the samples, desired compositions are weighed and reacted under flowing ultra high purity argon gas in an arc melter using a tungsten electrode and a water-cooled copper hearth. A Zr button was used as an oxygen getter. The sample was flipped over and re-melted 3-5 times to ensure homogeneous mixing of the constituent elements. The sample chamber is pumped, purged and sealed at least three times before melting.

Fig: 2.3 Arc melting chamber and copper hearth.

Fig: 2.4 RF induction melting system.

If the starting materials are in powder form, the powders are mixed and pressed into pellets as explained in previous section. This resulted in the formation of small buttons. The sample button is wrapped in Ta foil, sealed in a quartz tube under vacuum, and annealed at suitable temperature and time period. RF Induction heating provides reliable, repeatable, non-contact and energy-efficient heat in a minimal amount of time. The power supply sends alternating current through a coil, generating a magnetic field. When the workpiece (sample) is placed in the coil, the magnetic field induces eddy currents in the workpiece, generating precise amounts of clean, localized heat without any physical contact between the coil and the workpiece. Induction heating provides fast, controllable temperature ramp, allowing for consistent quality results. Both ferrous and non-ferrous alloys can be melted in induction furnaces. The sample is placed in a crucible wrapped with a tantalum foil as a susceptor inside the induction coil and RF power is supplied. The charge can be melted and then maintained in

the liquid state, depending on the application requirements. The operating frequency of our RF supply is 0-100 KHz.

2.2.2 Single Crystals

A polycrystalline sample of a material that belongs to one of the non cubic crystal systems can have significant built-in strain. Single crystals do not exhibit artificial effects due to strain or impurities. This is the first reason why access to single crystals is important. Secondly, it is necessary to study the anisotropic, or directionally dependent, properties of a material in a single crystal. The properties of many crystalline materials depend on the axis along which they are measured. For example, some materials are thought to be metallic (conducting) along one axis and insulating along another. Crystals can belong to one of several crystal systems, each of which is characterized by certain symmetries. There are various ways of single crystals growth. The two techniques we have adopted are explained below.

2.2.2.1 Metallic Flux Growth

Flux growth is a comparatively simple technique: the crystals are grown out of a solvent that reduces the melting point of the desired compound. If we heat the mixture of starting materials up to melting point, it turns out that the small amount of the material is dissolved into molten metallic flux, which has a relatively low melting point. The melt is then slowly cooled, and beautiful single crystals can grow out of the flux, sometimes several mm in length. Single crystals of many intermetallic compounds can be grown in a metallic flux [3]. It is a versatile technique that allows for the growth of congruently and incongruently melting materials with equal ease. The primary requirement for growth is that there be an exposed primary solidification surface in the appropriate equilibrium phase diagram.

For the materials with low melting point, below 1200 °C, starting materials in a stoichiometric ratio are placed in a small alumina crucible and filled with metal used as flux, for

example antimony or tin. The approximate material-to-flux mass ratio is taken as 1:10 initially. The open side of the crucible is closed by quartz wool and then sealed in an evacuated quartz ampule. Then the sample undergoes a suitable sequence of heat treatment in a box furnace. The quartz tube should be vertical. The temperature sequence is determined by studying the phase diagram of the material. The sample is cooled very slowly to just above the melting point of the metallic flux. Then very quickly the quartz tube is taken out of furnace, inverted, and spun in a centrifuge for 30 seconds keeping it upside down. The flux drains out of crucible and leaves the crystals of the material at the bottom [4].

Fig: 2.5 High temperature vertical furnaces used for single crystal growth.

This method is not always feasible to grow single crystals of the materials with very high melting points, for example boron and carbon [5]. In that case we melt the material inside a bigger vertical tube furnace using molten Al as a flux. A 10 - 50 ml alumina crucible is filled with stoichoimetric amounts of starting raw materials and the metal used as flux, with material to

flux mass ratio 1:70. The crucible is put inside vertical mullite tube which passes through the middle of the vertical furnace. For volatile materials like Mg, the alumina crucible is sealed in a Ta crucible of a larger size in an Ar atmosphere in a glove box [3]. Then the sample is heated under flowing Ar atmosphere with a suitable heating program. After the sample is cooled to room temperature the single crystals are extracted from the solid Al by etching it away with a hot solution of NaOH. By this method we can heat different samples using four different crucibles at the same time. The surface of the grown crystals is cleaned by etching them in very dilute nitric acid. Then the crystals are washed, rinsed with ethanol, and dried.

2.2.2.2 Chemical Vapor Transport

Nonvolatile solid substances can be transported through a vapor phase by chemical vapor transport (CVT) when the suitable reactive gases are provided in the presence of a temperature gradient, such as to transform the solid substances into gaseous compounds via heterogeneous chemical reactions and vice versa. The vapor-grown crystals are often perfect enough and good enough quality crystals to be used in solid state physics experiments [6]. In our lab single crystals are grown by the CVT method using iodine as the transporting agent. A mixture of elements is placed in a quartz ampule of length 18 cm and a diameter of 1 cm along with an iodine concentration of 10 mg/cm^3. The ampule is evacuated to around $2x10^{-6}$ torr, and sealed off. The ampule is placed in a horizontal furnace with small openings on each side. The determination of suitable growth duration and the temperature gradient along the source zone and growth zone is a key to this method.

2.2.3 Thin Films and Micro Fibers

Thin film science and technology play an important role in the high-tech industries. Thin film technology has been developed primarily for the integrated circuit industry. The demand for development of smaller and smaller devices with higher speed, especially in the next generation

of integrated circuits, requires advanced materials and new processing techniques suitable for future giga scale integration (GSI) technology. In this regard, the physics and technology of thin films can play an important role to achieve this goal. Thus, knowledge and determination of the nature, functions and new properties of thin films can be used for the development of new technologies for future applications [7, 8].

Fig: 2.6 Experimental set up for thin film growth.

There are various types of chemical and physical deposition processes of thin films. In our lab we do an electron-beam deposition [9]. The material to be deposited is placed on a boat (crucible) made of a material with high melting point. Depending on the type of the materials to be deposited, a carbon or tantalum boat is used. An electron beam evaporator fires a high-energy beam from an electron gun to boil a small spot of material; since the heating is not uniform, lower vapor pressure materials can be deposited. The beam is usually bent through an angle of 270° in order to ensure that the gun filament is not directly exposed to the evaporant flux.

Typical deposition rates for electron beam evaporation range from 0.1 to 10 nanometer persecond in a 2 micro Torr vacuum.

Fig: 2.7 Mo- coated C fibers produced by JW Composities LC.

A carbon fiber is a long, thin strand of material about 0.0002-0.0004 in (0.005-0.010 mm) in diameter and composed of carbon atoms. Carbon fiber-reinforced composite materials are used to make aircraft and spacecraft parts, racing car bodies, golf club shafts, bicycle frames, fishing rods, automobile springs, sailboat masts, and many other components where light weight and high strength are needed. There are various ways of synthesizing the carbon fibers [10]. JW Composites has developed a unique technology for incorporating graphite fibers into a copper matrix [11]. Graphite fibers are not wetted by many metals including copper. By providing a thin layer of molybdenum metal on the surface of each graphite filament, the coated fibers are spontaneously wetted by molten copper. The molybdenum coating provides a strong bond

between the fibers and copper; a bond that is stable even above the melting point of copper! Once coated with molybdenum, the graphite fibers have a typical metallic appearance.

Fibers coated with various metals (nickel, copper, gold, etc.) for use in aerospace, defense, electronics, communications and biomedical applications. David Young et.al have found a way to synthesize a layer of $MgCNi_3$ an 8 K superconductor directly onto tiny carbon fibers that are five times smaller than a human hair, and the results could lead to advances in space travel and transport [12]. MoN and Mo_3Sb_7 were synthesized in our lab reacting the Mo coated carbon fibers with N and Sb, respectively.

2.3 Characterization

Sample structure and phase purity analysis will be performed by powder and single crystal X-ray diffraction using Cu Kα diffractometer equipped with an incident beam monochromator in the Chemistry Department. SEM images and elemental analysis were done using JEOL 840A. The physical properties measurements were carried out in Quantum Design Physical Property Measurement System (PPMS).

2.3.1 Structure and Elemental Analysis

2.3.1.1 X-ray Diffraction

The X-Ray diffraction method is most useful for qualitative rather than quantitative analysis (although it can be used for both) of powders, single crystals and thin films. We can use it to identify phases, to measure crystal lattice parameters, residual stress, texture, and crystalline size of nanomaterials.

The X-ray radiation most commonly used is that emitted by copper, whose characteristic wavelength for the radiation is λ = 1.54056 Å. For powder X-ray diffraction, well grounded powder of the samples was placed onto a sample holder of the diffractometer equipped with Cu K_α radiation (λ = 1.54056 Å).

Fig: 2.8 A Bruker D8 Advance Powder Diffractometer housed at Chemistry department.

Data were collected from 2 θ = 20^{o} to 80^{o} with a constant scan speed of 2^{o} min^{-1} at room temperature. When the incident beam strikes a powder sample, diffraction occurs in every possible orientation of 2θ. The diffracted beam may be detected by using a moveable detector such as a Geiger counter, which is connected to a chart recorder. In normal use, the counter is set to scan over a range of 2θ values at a constant angular velocity. Routinely, a 2θ range of 10 to 80° is sufficient to cover the most useful part of the powder pattern. The scanning speed of the counter is usually 2° min^{-1} and therefore, about 30 minutes are needed to obtain a trace. In this work, XRD measurements were carried out using the Bruker D8 Advance Powder Diffractometer housed in the Department of Chemistry at Louisiana State University. To perform

the single crystal X-ray diffraction, a small crystal fragment is glued to a glass fiber and mounted on the goniometer of a Nonius Kappa CCD diffractometer equipped with Mo K_α radiation (λ = 0.71073 Å). Data were collected at 298 K.

2.3.1.2 EDX Spectroscopy and SEM Microscopy

Energy dispersive X-ray spectroscopy (EDS or EDX) is an analytical technique used predominantly for the elemental analysis or chemical characterization of a specimen [13]. Being a type of spectroscopy, it relies on the investigation of a sample through interactions between electromagnetic radiation and matter, analyzing X-rays emitted by the matter in this particular case. Its characterization capabilities are due in large part to the fundamental principle that each element of the periodic table has a unique atomic structure allowing x-rays that are characteristic of an element's atomic structure to be uniquely distinguished from each other. Spectroscopy data is often portrayed as a graph plotting x-ray energy vs. count rate. The peaks correspond to characteristic elemental emissions.

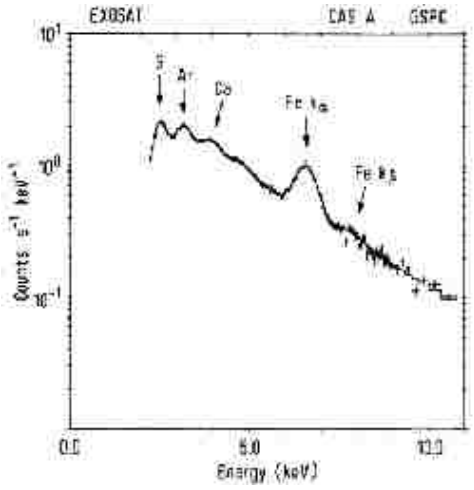

Fig: 2.9 Spectroscopy data for an elemental analysis.

There are four primary components of the EDS setup: the beam source; the X-ray detector; the pulse processor; and the analyzer. A number of free-standing EDS systems exist. However, EDS systems are most commonly found on scanning electron microscopes (SEM).

Electron microscopes are equipped with a cathode and magnetic lenses to create and focus a beam of electrons, and since the 1960s they have been equipped with elemental analysis capabilities. A detector is used to convert X-ray energy into voltage signals; this information is sent to a pulse processor, which measures the signals and passes them onto an analyzer for data display and analysis. The scanning electron microscope (SEM) is a type of electron microscope that creates various images by focusing a high energy beam of electrons onto the surface of a sample and detecting signals from the interaction of the incident electrons with the sample's surface. The SEM also produces images of high resolution, which means that closely spaced features can be examined at a high magnification. Preparation of the samples is relatively easy since most SEMs only require the sample to be conductive.

Fig: 2.10 JEOL 840A Scanning electron microscope in the geology department at LSU.

The types of signals gathered in an SEM vary and can include secondary electrons, characteristic x-rays, and back-scattered electrons. In an SEM these signals come not only from the primary beam impinging upon the sample, but from other interactions within the sample near the surface.

The SEM is capable of producing high-resolution images of a sample surface in its primary use mode, secondary electron imaging.

SEM images of our samples were taken using a JEOL 840A SEM in the SEM and Microprobe lab at the Department of Geology and Geophysics. This machine is equipped with four detectors (SE, BE, CL, and X-ray). Analog photography of secondary and backscatter images is supported by a dedicated CRT and Polaroid camera. A Mac G4 computer with dual monitors is used to work with a 4Pi ADC (Spectral Engine II) and multichannel analysis system to acquire digital SEM images and EDS spectrum. NIH Image or Evolution of 4pi is used to acquire and analyze image data. The sample stage supports 12 mm stub, 32 mm stub, and thin section. Sample exchange is rapid and sample throughput potentially quite fast. This instrument is very simple and quite robust.

2.3.2 Physical Properties

2.3.2.1 Overview of PPMS

The Physical Property Measurement System (PPMS) provides a flexible, automated workstation that can perform a variety of experiments requiring precise thermal control. The unique open architecture of our Model 6000 PPMS allows us to use different measurement options, such as the AC Measurement System option, AC transport option, and heat capacity option. We can also use a breakout box to connect with external instruments to measure transport critical current density and the thermoelectric effect. The sample environment controls include fields up to ± 9 Tesla and temperature range of 1.8 - 400 K. Temperature is reported with a typical accuracy of ±0.5%. The slew rate is $0.01 \leq dt \leq 12$ K/min. with full sweep capability. The PPMS unit operates with a nitrogen- jacketed dewar. The dewar contains the liquid helium bath in which the probe is immersed. The probe's intricate design incorporates the basic temperature control hardware, the superconducting magnet, the helium-level meter, the gas lines, the sample

puck connectors and a variety of electrical connections. The pins from the sample puck connector are wired to the pins on the gray-ringed Lemo connector that is on the probe head. The state-of-the art technology of the AC Measurement System offers extensive susceptibility and magnetization capabilities while retaining a user-friendly environment. The ACMS houses the drive and detection coils, thermometer, and electrical connections for the ACMS system. The AC drive coil set provides an alternating excitation field, and the detection coil set inductively responds to the combined sample moment and excitation field. The insert fits directly in the PPMS sample chamber and contains a sample space that lies within the uniform magnetic field region of the host PPMS, so DC field and temperature control can be performed with conventional PPMS methods. The ACMS coils are connected to the PPMS electronics through the 12- pin connector located in the base of PPMS sample chamber. The ACMS is both a DC magnetometer and an AC susceptometer.

Fig: 2.11 Physical Property Measurement System.

2.3.2.2 Resistivity and Hall Coefficient

The measurement of transport properties such as electrical resistivity, magnetoresistivity, and Hall coefficient are performed in the AC transport option of the PPMS MultiVu software.

Fig: 2.12 Liquid He tank and other tools for sample installment inside the PPMS.

We adopt a standard four-probe technique. Hall coefficient measurements, however, measure the sample's Hall voltage and therefore require a different configuration. The sample is cut or polished into a bar with dimensions of approximately 2 × 1 × 1 mm. The sample is glued on a special kind of plastic holder (G10) using VGE varnish. Four pieces of 0.002 inch size platinum wire are used to make electric contact to the smooth surface of the sample using a conductive epoxy (Epotek H20E). It is placed on a hot plate for several minutes to cure the epoxy. Then the wires are connected to the current and voltage points on a PPMS sample puck. The contact resistance is checked with a voltmeter. The puck is placed inside the PPMS for the measurement.

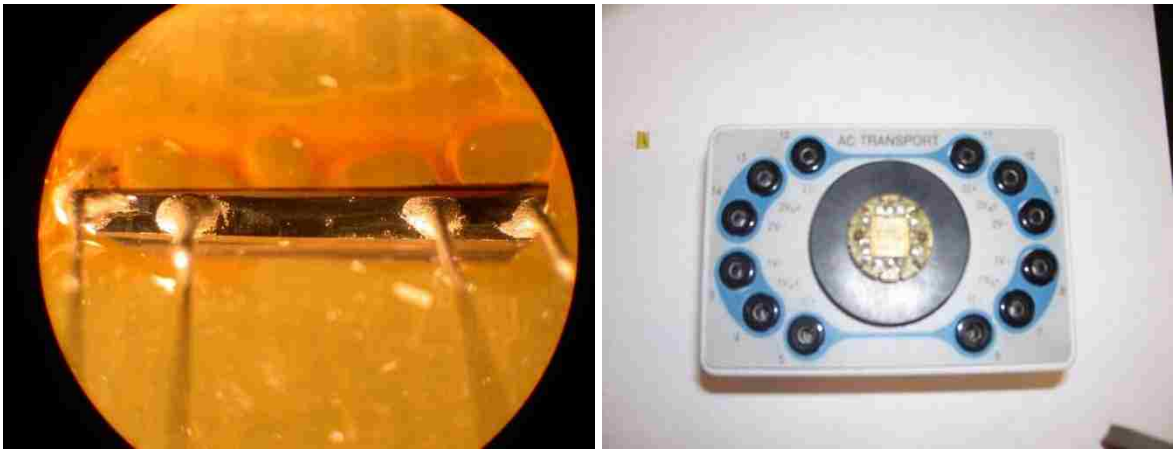

Fig: 2.13 Single crystal with four current and voltage leads and Samples puck and base for Ac transport.

In the active AC transport option, the resistivity control center makes basic system operations such as installing samples, selecting or creating data files, measurement sequences, and setting up and running immediate mode resistance measurements. With the help of the PPMS MultiVu software, the magnitude of excitation current and the sequence of temperature and magnetic field variation for the measurement are provided. The resistivity measurements are typically made by passing a known current through the sample and measuring the voltage drop across the sample in one direction. We can turn on the magnetic field for magnetoresistivity and Hall coefficient measurements.

The resistivity in different directions of applied magnetic field can be measured using a rotator. The sample is mounted on a special sample puck which fits on a rotating holder.

2.3.2.3 Magnetization and Susceptibility

For magnetization and susceptibility measurements in the PPMS, samples may be mounted directly on the ACMS sample holder, a teflon cup or on clear plastic drinking straw. The teflon and clear plastic straw adds a negligible magnetic moment. We can also use a nonmagnetic material like quartz wool or piece of tape to ensure that the sample will not shift within the holder. The sample holder is held within the insert's coil set on the end of a thin, rigid

sample rod. The purging, evacuating, sealing, centering the sample and measurement can be performed in the ACMS option using PPMS MultiVu software. DC magnetization measurements measure a sample's magnetic moment in an applied magnetic field H at a specific temperature T (M= M(H,T)). The sample is moved quickly through both sets of coils, inducing a signal in them according to Faraday's law and it is analyzed with a digital signal processor (DSP) to determine the sample's magnetic moment. Magnetic susceptibilty is given by magnetic moment per mole per unit field.

2.3.2.4 Thermoelectric Power

The Seebeck coefficient (also called the thermopower) is the ratio between the elecric field and the temperature gradient (or equivalently, the ratio between the voltage difference and temperature difference between the ends of the sample). The sign of the Seeback coefficient depends on the sign of the majority charge carriers (whether positive or negative charge builds up on the cold end). So measuring the Seebeck coefficient is a way to determine whether the charge carriers in a particular material are holes or electrons. Seeback coefficients measurements are performed by using a comparative technique with a constantan standard (S_c = 40μV/K). We have designed a special board on a PPMS puck where a 1000 ohm resistance heater is thermally attached to the plate. The sample and the constantan are approximately of the same dimensions and attached to the plate parallel to each other so that the temperature gradient across each is equal. When the heater is on, one end of both the constantan and the sample are heated. From the temperature gradient (ΔT) and potential difference (ΔV) between the ends, the Seeback coefficient can be obtained by $S_s = \Delta V_s/\Delta T_s$ for the sample and for the constantan ($S_c = \Delta V_c/\Delta T_c$). Since $\Delta T_s = \Delta T_c$, $S_s = (\Delta V_s/\Delta V_c)\, S_c$. Temperature dependence of the Seeback coefficient can be performed with the help of LabView software by placing the sample puck inside the PPMS. The software takes the data for ΔV_s and ΔT_s until the temperature ΔT saturates

with time. The Seeback coefficient S, given by the slope of the graph of ΔV_s vs. ΔT_s , at different temperatures is recorded.

2.3.2.5 Critical Current Density

The critical currents of the samples in the form of microfibers with very large normal state resistivity are measured in a four probe geometry using a standard pulsed technique [12]. The sample is mounted on a PPMS transport puck as explained in section 2.3.3.2. The current and voltage leads were directly bonded to the surface of the fiber with a distance of 3-6 mm between them. The puck is then installed into the PPMS sample chamber so that the temperature and the magnetic field can be varied as required. The electrical connection is carried out to the critical current measurement system from the probe head of PPMS through the breakout box.

Fig: 2.14 Equipments for the measurement of critical current density.

Below the superconducting transition temperature of the material, currents are driven using a pulse duration of 1-2 μs with a duty cycle of 1/1000, and resulting voltages are measured

via a boxcar integrator. We need to insure that the pulse width and duty cycle are low enough to avoid significant heating at the contacts. Superconductors can support only a finite amount of supercurrent. As the current increases, the voltage drop across the sample is monitored. As long as the sample remains superconducting, the measured voltage should be zero. When the sample becomes resistive, the current through it generates a potential difference across the sample. The current at which this occurs in a given superconductor is the critical current. The data for input and output voltages are recorded and plotted using LabView software. We can calculate the current density using the resistance of the resistor used and the cross sectional area of the sample.

2.4 References

[1] Ren Z A, Che G C, Jia S L, Chen H, Ni Y M, Liu G D, Zhao Z X 2002 *Physica C* **371** 1

[2] Jackson D D, McCall S K, Weir S T, Karki A B, Young D P, Qiu W, Vohra Y K 2007 *Physical Review B* **75** (22): Art. No. 224422

[3] Canfield P C, Fisher I R 2001 *Journal of crystal growth* **225** 155-161

[4] Cho J Y, Moldovan M, Young D P et.al. 2007 *Journal of Physics : Condensed Matter* **19** (26): Art. No. 266224

[5] Karki A B, Gautreaux D P, Chan J Y, Harrison N, Browne D A, Goodrich R G, Young D P 2008 *Journal of Physics : Condensed Matter* **20** 000000 (5pp)

[6] Wang J F, Saitou S, Ji S Y et al. 2006 *Journal of Crystal Growth* **295** (2): 129-132

[7] Assinese A, Iavarone M, Vaglio R et al. 2000 *Physical Review B* **62** (21): 13915-13918

[8] Physics and Technology of thin Films IWTF 2003 Proceedings of the International Workshop Tehran, Iran 22 February - 6 March 2003 edited by A Z Moshfegh (Sharif University of Technology, Iran), H v Känel (Politecnico di Milano, Italy), S C Kashyap (Indian Institute of Technology-New Delhi, India) & M Wuttig (I Physikalisches Institut der RWTH Aachen, Germany)

[9] Young D P *et al.* 2003 *Physical Review B* **68** (2) Art. No. 020501

[10] Li Y J, Lau S P, Tay B K, Chen G Y, Sun Z, Chen J S, You G F, Sheeja D 2001 *Diamond and Related Materials* **10** 878-882

[11] J.W. Composites, LC, 420 South 500 West, Salt Lake City, UT 84101

[12] Young D P, Moldovan M, Adams P W 2004 *Phys. Rev. B* **70** 064508

[13] http://en.wikipedia.org/wiki/Energy-dispersive_X-ray_spectroscopy

CHAPTER 3

MOLYBDENUM NITRIDES AND ANTIMONIDES IN THE FORM OF WIRES, THIN FILMS AND COATINGS ON C-MICROFIBERS

3.1 Introduction

Transition metal-based superconductors have been a historically important class of materials, primarily due the fact that the A15 intermetallics such as Nb_3Sn became widely used in high magnetic field applications, such as in the windings of superconducting solenoids [1]. Though the most extensive research has been carried out on niobium intermetallics, there has been a recent renewal in interest in two particular molybdenum-based superconductors. The first compound is Mo_3Sb_7 which has recently been classified as a strong spin fluctuation superconductor [8,9]. The second is molybdenum nitride which has attracted much attention as superconducting material due to its relatively high T_c (13 K) for an intermetallic. [2].

Mo_3Sb_7 is the only intermediate line compound in the Mo-Sb system. It decomposes peritectically at 780 ^oC into pure components i.e. liquid antimony and solid molybdenum [14]. It has the cubic Ir_3Ge_7-type crystal structure [15, 16]. Bukowski et al. have shown Mo_3Sb_7 to be a type-II superconductor with T_c = 2.08 K [8]. It is believed to be similar to the non-conventional superconductor $MgCNi_3$, which also exhibits strong spin fluctuations due to its proximity to a ferromagnetic ground state. In both these latter systems, strong spin fluctuations alter the superconducting ground state properties in non-trivial ways [10, 11]. Spin fluctuations may compete with superconductivity or even lead to an exotic pairing mechanism other than conventional s-wave. Up to now, more than 20 of the T_3X_7-type compounds (T is a transition metal, X is p-electron metalloid, mainly In, Ge, Ga, Sn), have been recognized to crystallize in this type of structure [17]. However, very little is known on the physical properties of these phases. Most of them are metallic, known exceptions are semiconducting Tc_3As_7 [17] and

$Nb_3Sb_2Te_5$ [18]. Metallic properties [19] and diamagnetism [17, 20, 21] were reported for Re_3As_7. The superconductivity with T_{sc} = 0.87 K was discovered in Ir_3Ge_7 by Raub et al. [22]. In turn, Chakoumakos et al. studied a single crystal of Ru_3Sn_7 and reported it as a diamagnetic metal, being nonsuperconducting down to 2 K [23].

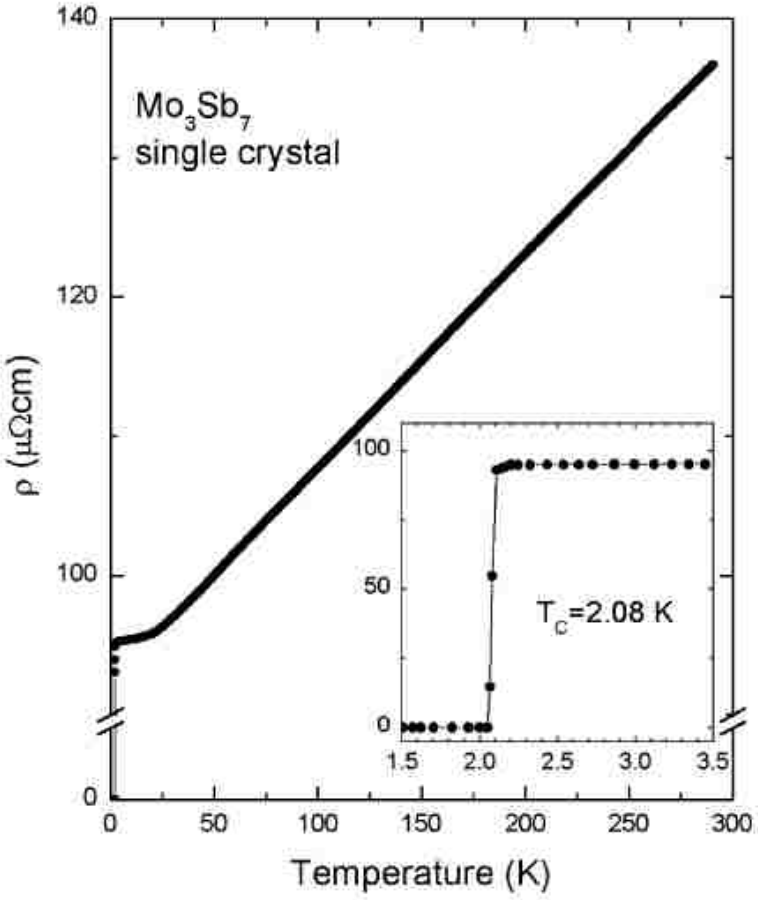

Fig: 3.1 Temperature dependence of the electrical resistivity for a Mo_3Sb_7 single crystal. The inset shows an enlargement of the data at low temperature, in the vicinity of the superconducting transition [8].

There are a few studies on Mo_3Sb_7. The detailed crystal structure of Mo_3Sb_7 has been determined by Jensen et al. [24] on single crystals prepared by chemical vapor transport. Hulliger reported metallic properties and practically temperature- independent paramagnetism (570 and 580 x 10^{-6} emu/mol at 80 and 300 K, respectively) for polycrystalline Mo_3Sb_7 [17]. The decomposition pressures of the Mo_3Sb_7 compound were measured by Mart *et al.* [25].

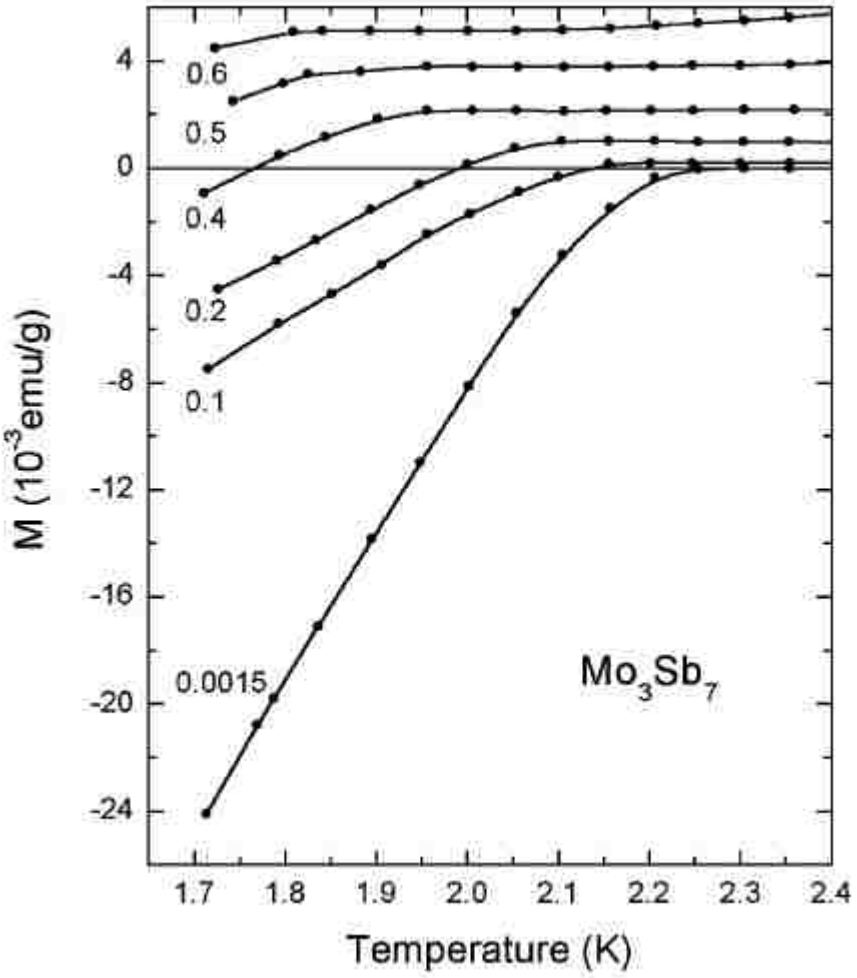

Fig: 3.2 Magnetization of Mo_3Sb_7 as a function of temperature at various magnetic fields. Numbers denote applied magnetic fields in T [8].

Molybdenum nitride forms several crystalline nitrides including γ-Mo_2N (cubic), β-Mo_2N (tetragonal), and hexagonal δ-MoN [6,42]. γ-Mo_2N and β-Mo_2N are known as superconductors with T_c ~ 5 K [30,43]. According to the Mo-N phase diagram only the hexagonal δ-MoN exists at the stoichiometric composition [6]. MoN with B1-type structure has been predicted to have a higher superconducting transition temperature (T_c) than NbN [44,41]. B1-MoN does not appear in the equilibrium phase diagram of the Mo-N system [47]. This and the high density of antibonding states make it difficult to synthesize a perfect crystal of B1-MoN. Recently some workers have succeeded in preparing B1-MoN films by sputter-deposition techniques [36,45,48].

The observed onset T_c, 12.5 K, however, is not as high as the theoretical prediction [36,44]. This has been explained by the occurrence of nitrogen vacancies and nitrogen defects at the interstitial sites [45].

Bukowski *et al.* have reported on electrical resistivity and magnetization measurements of single crystals of Mo_3Sb_7, grown via a peritectical reaction between Mo metal and liquid Sb [8]. The summary of the experimental procedure is as follows. Approximately 10 g of Sb (purity 99.99%) was placed in a thick-wall molybdenum crucible and sealed under an Ar atmosphere. The crucible was heated in a vacuum furnace to 1000 ^oC and slowly cooled (3 $^oC/h$) to 700 ^oC which was followed by furnace cooling to room temperature. Then the crucible was opened and transferred to a silica glass tube and an excess of Sb was removed by means of sublimation in vacuum at 620 ^oC. The single crystal has the cubic Ir_3Ge_7 structure (space group Im–3m) with lattice parameter a = 9.582 Å, which is slightly higher than a = 9:5713 Å, reported in *Ref.* [24].

Recently, Candolfi *et al*. have reported on electrical resistivity, magnetization and heat capacity measurements on a Mo_3Sb_7 polycrystalline sample [9]. The compound was prepared via a metallurgical route. Stoichiometric amounts of Sb shot and Mo powders were loaded into a quartz ampoule which was heated up to 750 ^oC and left at this temperature for 10 days. The product was then powdered and finally densified by hot pressing at 600 ^oC for 2 h under 51 MPa pressure using graphite dies.

The onset superconducting transition temperature T_c = 2.2 K, the residual resistivity ρ_0 = 95 μΩ-cm and the debye temperature θ_D = 162 K were obtained by Bukowski *et al*. [8]. The T_c is comparable to the value, 2.3 K, obtained from the sharp specific-heat discontinuity ΔC, as shown in Figure 3.3(b) [9]. It must be noted that, surprisingly, the temperature dependence of the resitivity reported by Bukowski *et al* on a Mo_3Sb_7 single crystal [8] (Figure 3.1) is different from that reported by Candolfi *et al* on the Mo_3Sb_7 polycrystalline sample (Figure 3.3(a)) [9]. It is

interesting to note that the normal state resistivity is relatively high (ρ_0 = 95 μΩ-cm, ρ_{300}/ρ_0 = 1.4) for the single crystal. The high ρ_0 reflects the presence in this compound a rather strong electron-phonon coupling [8]. The onset superconducting transition temperature T_c = 2.2 K from the magnetization measurement in an applied magnetic field of 15 Oe agrees well with that determined from the resistivity data in 0 T [8] [Figure 3.2].

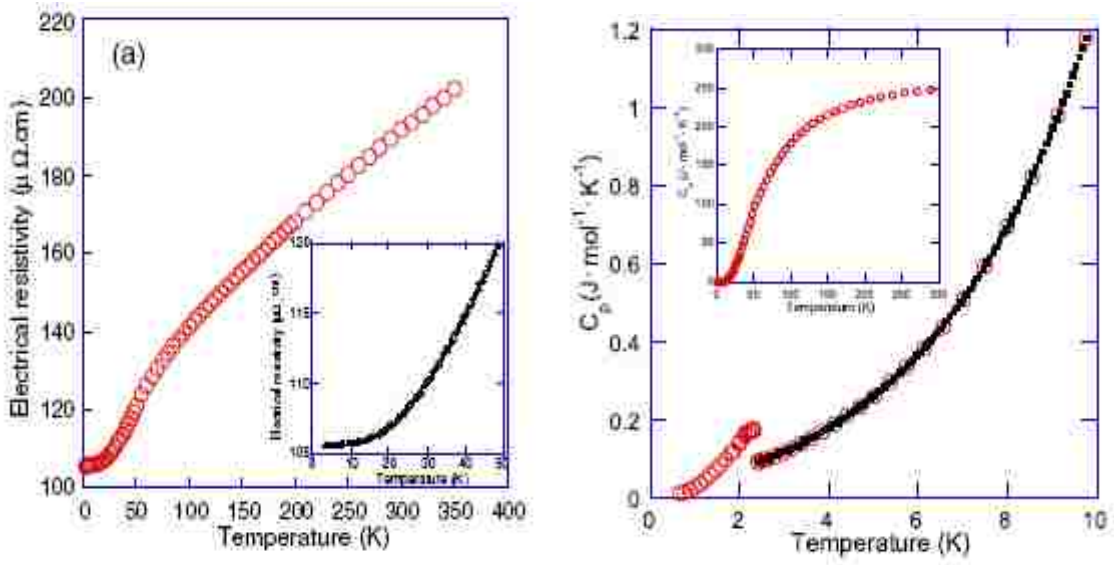

Fig: 3.3 (a) Electrical resistivity as a function of the temperature. Inset: parabolic dependence of the electrical resistivity at low temperature. (b). Temperature dependence of the specific heat Cp of Mo_3Sb_7 at low temperature highlighting the specific heat jump at the transition temperature. Inset: temperature dependence of the specific heat up to 300 K [9].

At room temperature Mo_3Sb_7 is paramagnetic with χ_M = 240 x 10^{-6} emu/mol [8]. Surprisingly this value is about two times lower than that reported by Hulliger [17] and Candolfi *et al.* [9] for the polycrystalline sample. The magnetic susceptibility measurement performed in a relatively high magnetic field (B = 1 T) shows a constant behavior above 50 K suggesting that this compound is a Pauli paramagnet [8]. The upper (B_{c2}) and lower (B_{c1}) critical fields were roughly estimated to be 0.6 T and 1 mT, respectively [8].

The value of $B_{c2}(0)$ was estimated by Bukowski *et al.* [8] using a simple empirical formula:

$B_{c2}(T) = B_{c2}(0)\,(1-(T/T_c)^2)$ ……(1)

Their value of $H_{c2}(0)$ is 1.7 T, which is in close agreement with the result from the Andreev reflection measurement by Dmitriev *et al*. [26]. The maximum energy gap $\Delta(0) \cong 0.32$ meV, which is slightly smaller than that expected from BCS theory, $\Delta^{BCS}(0) \cong 0.35$ meV was reported by Dmitriev *et al*. [26]. The smaller experimental gap value may be attributed to the magnetic character of this material, where a destructive role of the spin-flip processes still cannot be disregarded entirely.

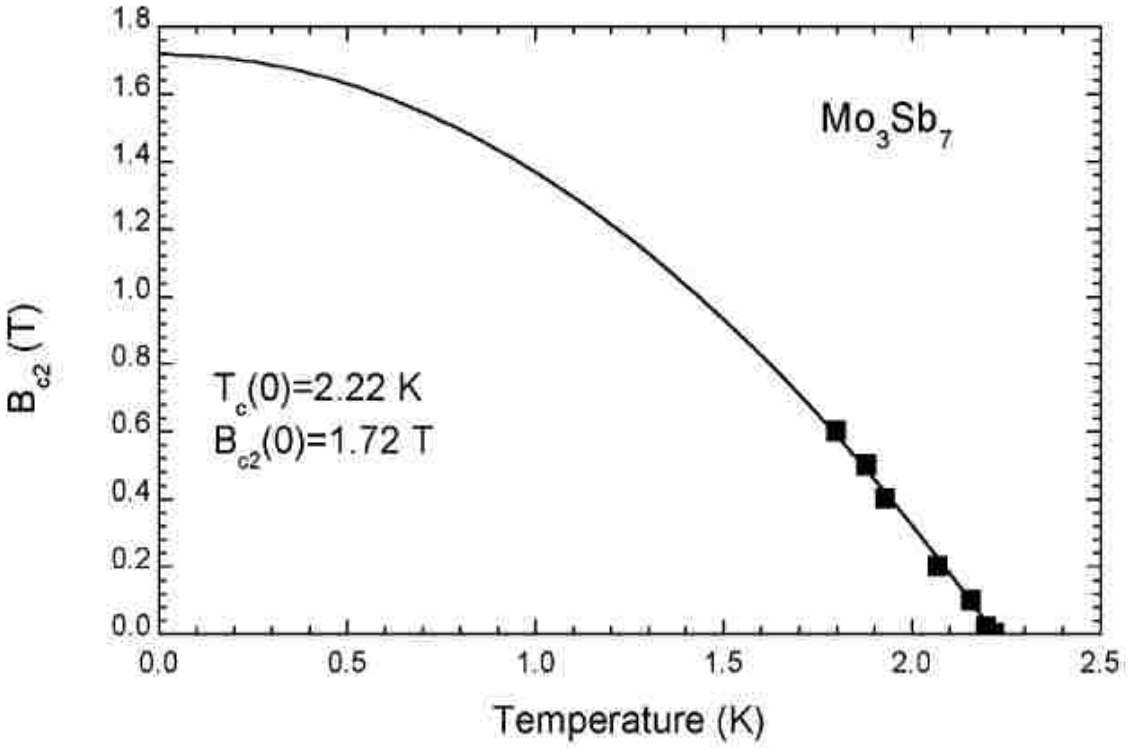

Fig: 3.4 The upper critical field B_{c2} of Mo_3Sb_7 vs. temperature. The solid line is the best fit to Eq. (1) [8].

Candolfi *et al.* have reported Mo_3Sb_7 is also a spin fluctuation system on the basis of the results of the electrical resistivity, specific heat capacity and susceptibility measurements [9]. According to the literature, the first strong evidence is the typical quadratic temperature dependence of the electrical resistivity, ρ, at low temperature ($T < 50$ K), associated with both a large value and saturation in going up to room temperature (Figure 3.3a).

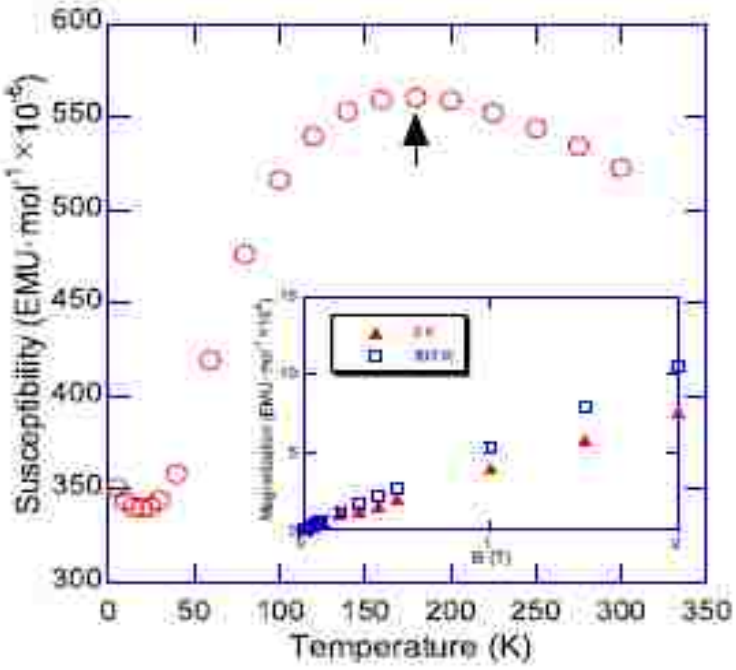

Fig: 3.5 Magnetic susceptibility as a function of the temperature in Mo_3Sb_7. The arrow indicates the position of the maximum. Inset: low field magnetization curves for the two extreme temperatures investigated (5 and 300 K)[9].

Second is the temperature dependence of the magnetic susceptibility (Figure 3.5). The susceptibility displays a parabolic dependence at low temperature, then increases with temperature, and at higher temperature becomes maximum around 180 K. Above this temperature it obeys Curie-Weiss law. The parabolic dependence, which was also noticed in the UAl_2 compound [27], is consistent with the theoretical prediction made by Beal-Monod *et al.* [28] on a spin fluctuation contribution to the temperature dependence of the magnetic susceptibility. The third evidence for Mo_3Sb_7 to be considered as a spin fluctuator is the fair agreement of the ratio A/γ^2_n ~0.55 x 10^{-5} μΩ-cm(K-mol/mJ)^2 of this system with the Kadowaski-Woods relation A/γ^2_n ~1.55 x 10^{-5} μΩ-cm(K-mol/mJ)^2 , which can be explained in terms of the spin fluctuation theory [29]. The most encouraging part of this literature [9] is that the transition temperature obtained by the McMillan relation without spin fluctuation rescaling is substantially higher, i.e., T_c ~ 8.7 K -11 K. The density of states at the Fermi level is reported to be high due to

the contribution of the Mo d-states, leading this material to the border of magnetic ordering [9, 38].

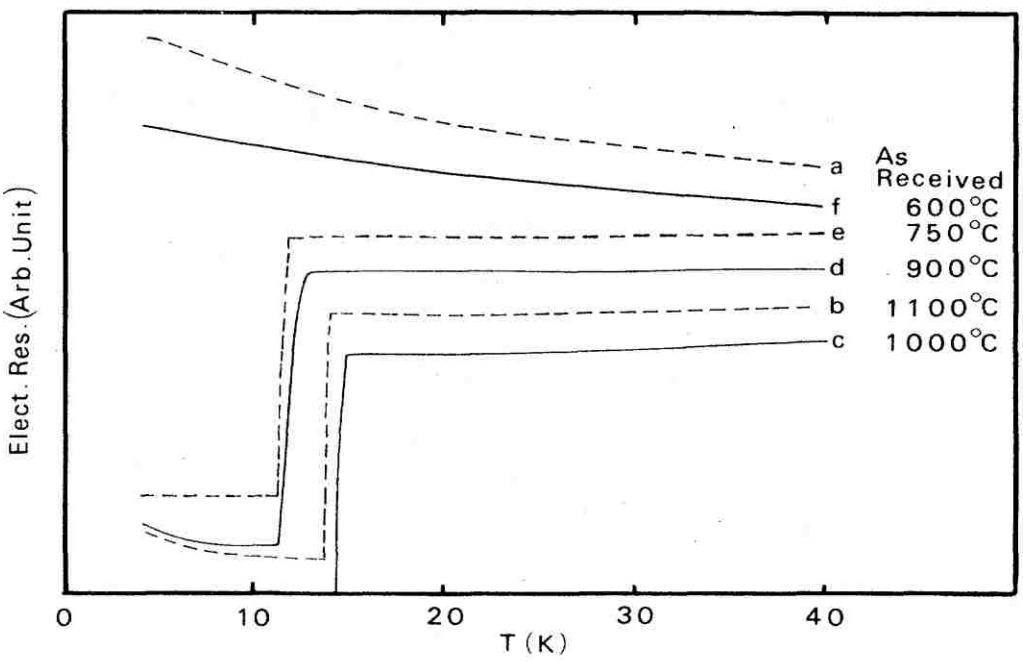

Fig: 3.6 Electrical resistance vs. temperature for the starting material, and pressure-annealed MoN films at various temperatures [7].

δ-MoN crystallizes in a hexagonal structure [3] (space group number 186) and the lattice parameters reported are a = 5.73 and c = 5.60 Å. The unit cell contains 8 formula units of MoN. Sahu *et al*. have performed LDA and GGA electronic structure calculations on the N ordered phase of δ-MoN [33-35]. Linker *et al*. have shown that a highly disordered phase (MoN_x with x = 0.20) with a T_c of 9.2 K was produced by ion implanatation of nitrogen into molybdenum [39]. For x > 0.20 a phase transformation to a FCC phase was observed. Later, Linker showed that the lattice parameter of the FCC phase revealed a linear increase as a function of N concentration up to a value of x = 0.5 [40]. Moreover, Linker *et al*., in view of the above predictions for T_c, have fabricated nominally stoichiometric but not highly ordered MoN in the NaCl structure (B1 structure) to see if more nitrogen could be incorporated into the FCC phase by non-equilibrium

techniques, so that the stoichiometric B1 phase could finally be obtained. The reactive sputtering of the 150-400-nm thick films was carried out in a RF system, and then implantation of nitrogen was performed into Mo films using multiple ion energies. The superconducting transition temperature is only about 3 K, in contrast to expectations raised by theoretical and empirical predictions [36, 44]. The resistivity values of MoN are considerably larger than those of other refractory superconductors also prepared by sputtering.

Ihara *et al*. attempted to stabilize the nonequilibrium B1-phase MoN and fill the N vacancies by interstitial N atoms by high-pressure annealing, because the density of the B1-MoN is larger than that of the equilibrium hexagonal MoN [7, 41]. They prepared B1-MoN films by sputtering, and annealed under a pressure of 6 GPa at a temperature between 600 and 1100 ^{o}C for 8 h. The B1 phase MoN is converted mainly to the hexagonal-phase and partly to tetragonal-phase Mo_2N when annealed at temperature above 750 ^{o}C. A residual phase was observed only at an annealing temperature of 600 ^{o}C. The onset T_c of the 1000 ^{o}C-annealed films was 14.9 K. This is the maximum value found in the literature for the Mo-N system [7]. Though they could reveal the existence of the pure hexagonal-phase MoN with high T_c, high pressure larger than 6 GPa was needed to obtain the nonequilibrium B1 phase MoN. Saur *et al*. prepared MoN in the form of wires by heating the Mo wires of 0.5 mm at temperatures between 750 and 950 ^{o}C in a stream of ammonia gas under atmospheric pressure [37]. The highest transition temperature of about 12.95 K was obtained by a heat treatment at 800 ^{o}C for 232 hr.

To the best of my knowledge, there are no reports on the study of Mo_3Sb_7 synthesized in the form of wires, films and microfibers, and there are no reports on magnetotransport properties of MoN. This chapter reports on the synthesis and characterization of Mo_3Sb_7 and MoN wires, films and coatings on carbon microfibers. This is first report on the transport critical current measurements of annular MoN and Mo_3Sb_7 fibers as a function of temperature.

3.2 Synthesis

1 gram of bulk polycrystalline Mo_3Sb_7 was synthesized by RF melting with nominal formula $Mo_3Sb_{7.5}$. The powders of Molybdenum (99.95 % Alfa Aesar) and Antimony shot (99.9999 % Alfa Aesar) were thoroughly mixed and ground well for 10-15 minutes. Then the powder was pressed into a pellet of 10 mm in diameter. The pellet was put into an Al_2O_3 crucible wrapped by a thick foil of tantalum from the outside. The crucible with the sample was then placed inside an induction coil and RF power was supplied. The operating frequency was increased slowly until sufficient heat was produced to melt the pellet. The process was carried out in a stream of high purity Ar.

Hard and 99.8% pure metallic Molybdenum wires of 0.013 mm and 0.07 mm in diameter were obtained through Alfa Aesar from the Johnson Matthey Company. During the production of these wires, a very small percent of W, Cr and Si can become impurities. Similarly the commercial fibers consisting of a 6-micron diameter carbon core, which are coated a 40 nm thick film of molybdenum metal, were obtained from JW Composites, LC [13]. To synthesize Mo_3Sb_7 samples a few centimeter long pieces of the wires and the fibers were placed in a small alumina (Al_2O_3) crucible. The crucible with a small amount of Sb shot (99.999% Alfa Aesar) was sealed in an evacuated quartz tube and heated at temperatures between 800 °C and 1030 °C for different time periods. The entire tube was quenched-cooled to room temperature. To optimize the superconducting properties, the synthesis of samples was carried out many times with different amounts of Sb at different temperatures, and for different time periods.

MoN wires and coatings were prepared by reacting the Mo wires and Mo-coated carbon fibers in a 1 ATM stream of ammonia gas (NH_3) at 800 °C – 1030 °C for different times. Exposures at 900 °C for 1h and 30 min resulted in the samples with the best superconducting properties. To compare the structure and properties before and after the reaction, the wires and

the fibers as obtained from the manufacture, were annealed at 900 °C for 1 hour and 30 minutes without Sb.

In addition, we formed planar films of each compound first by evaporating 60-nm films of Mo onto sapphire substrates via e-beam vacuum deposition of arc-melted molybdenum buttons (99.999 % Alfa Aesar). Typical deposition rates were ~ 0.1 nm/s in a 2 μTorr vacuum. The resulting Mo films were then exposed to either ammonia gas or Sb vapor as per the recipes used to form the fiber coatings. Because the planar film synthesis did not involve carbon, it provided us with control samples from which we could determine the effects of possible carbon contamination from the fiber cores. The planar geometry, however, is not particularly suitable for critical current measurements.

3.3 Characterization

The reacted thin wires and coated carbon microfibers of MoN and Mo_3Sb_7 were examined with a scanning electron microscope (SEM) and their chemical composition were determined using EDX analysis by JEOL 840A Scanning electron microscope.

A bunch of approximately 4-cm long pieces of wire and the fibers were heated with Sb and in a stream of NH_3 at a suitable temperature and time period to get the sufficient amount of powder of Mo_3Sb_7 and MoN respectively for X-ray diffraction. Well grounded powder of each sample was placed onto a sample holder of a powder X-ray diffractometer equipped with Cu K_α radiation (λ = 1.54056 Å). Data were collected from 2 θ = 20^o to 80^o with a constant scan speed of 2^o min^{-1} at room temperature. The phase purity of Mo_3Sb_7 and MoN thin films were also verified by powder XRD.

To measure the transport properties of the samples the contacts were made with two mil platinum wires by applying Epotek conductive epoxy or silver paint directly on to the wires, fibers and thin films. The electric resistance and magnetoreisatance measurements were

performed by the standard four-probe ac technique at 27 HZ with an excitation current of 3 mA for the wire and 0.01 mA for fibers and thin films. Critical currents of 3 - 5 mm long fibers were measured in the 4-probe geometry using a standard pulsed technique. Superconductors can support only a finite amount of supercurrent. As the current increases, the voltage drop across the sample was monitored. The current at which the sudden potential drop occurs in a given superconductor is the critical current. Currents were driven using pulse durations of 1-2 μs with a duty cycle of 1/1000, and the resulting voltages were measured via a boxcar integrator. The data for input and output voltages were recorded and plotted using LabView software. Care was taken to ensure that the pulse width and duty cycle were low enough to avoid significant Joule heating at the contacts. The current density was calculated using the resistance of the resistor used and the cross sectional area of the sample. The samples were cooled by the vapor down to 1.8 K in magnetic fields up to 9 T via a Quantum Design PPMS.

The temperature dependence of the magnetic susceptibility of Mo_3Sb_7 wires of 70 μm in diameter were measured at magnetic fields of 20 Oe and 1T. A bunch of pieces of Mo_3Sb_7 wires was packed in a plastic capsule and attached to the ACMS sample holder of the PPMS.

3.4 Results and Discussions

3.4.1 Polycrystalline Mo_3Sb_7

The low temperature electrical resistivity of the RF melted polycrystalline sample of Mo_3Sb_7 is shown in Figure 3.7. The superconducting transition temperature, Tc, (midpoint) is 2.35 K, which is comparable to the value reported for the single crystal and polycrystalline sample of Mo_3Sb_7 [8, 9]. The T_c obtained from lower temperature dependence of magnetic susceptibility of the sample at a magnetic field of 20 Oe is consistent with the 2.35 K. The powder sample of Mo_3Sb_7, prepared by solid state reaction, also shows the superconducting transition around the same temperature.

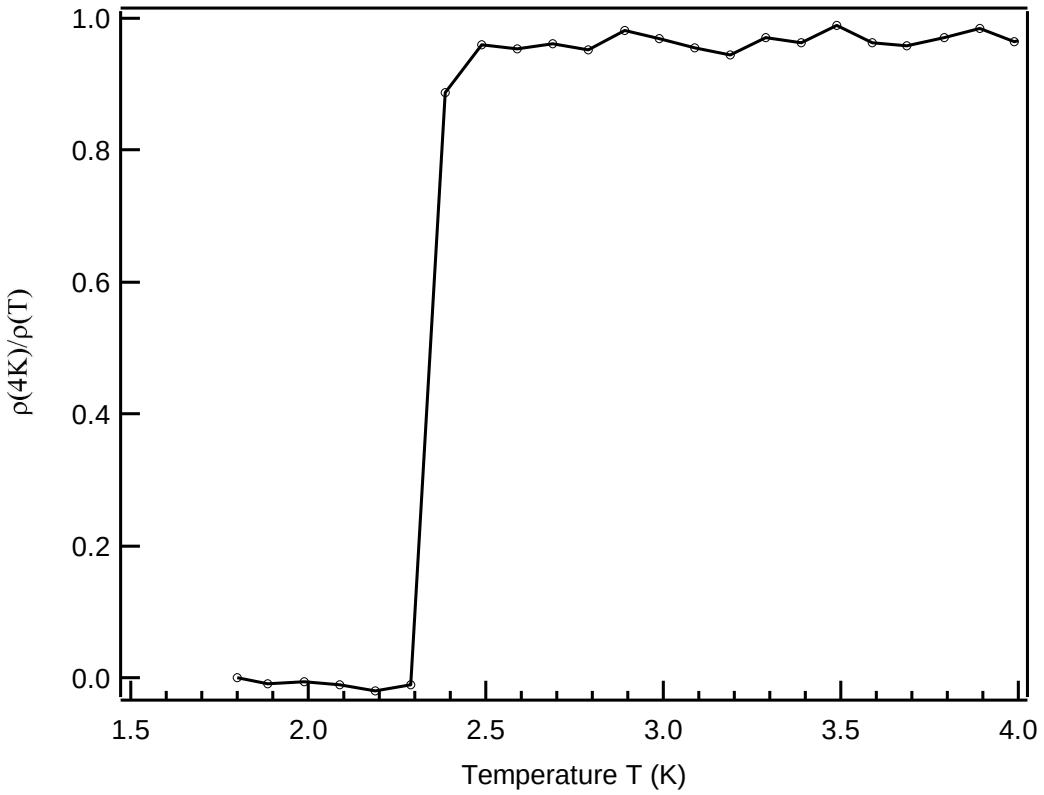

Fig : 3.7 Superconducting transition of a RF melted polycrystalline sample of Mo_3Sb_7. The solid line is a guide to the eye.

3.4.2 Mo_3Sb_7 and MoN Wires

Scanning electron microscopy of un-reacted and reacted wires showed an obvious change in the Mo wires due to the reaction with either Sb or N. The cross-sectional area of the Mo_3Sb_7 wire increased by approximately four times due to the reaction, while that of MoN did not change substantially. Figures 3.8 and 3.9 show the cross-sectional view of bare Mo and Mo_3Sb_7 wires of 70 μm in diameter respectively. As shown in Figure 3.9 for the Mo_3Sb_7 wire of 70 μm in diameter, the reaction is not throughout the wire. We can see clearly a portion of un-reacted Mo in the core of the wire obtained by the heat treatment at 900 ^oC for 1 h in Sb vapor.

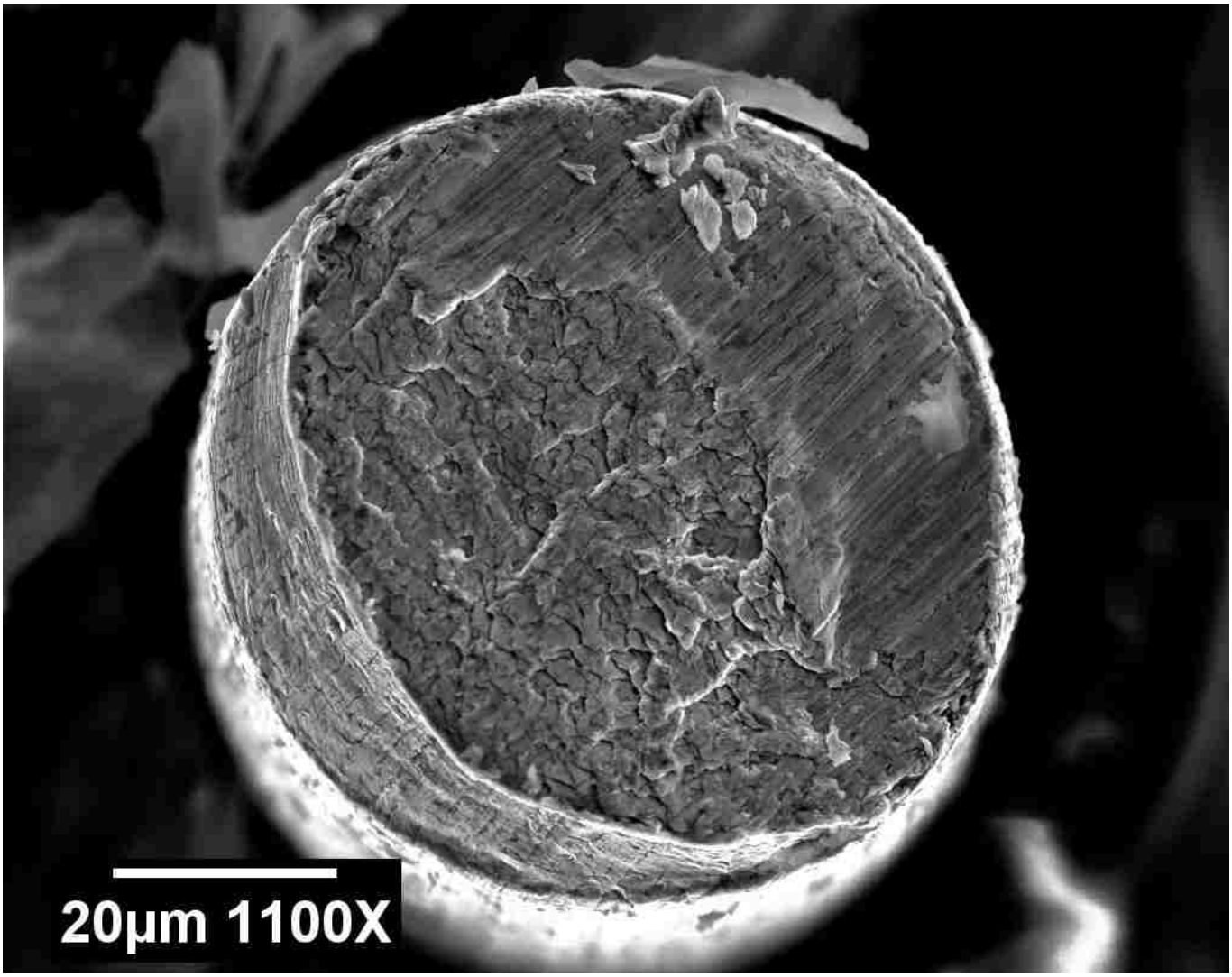

Fig: 3.8 Scanning electron micrograph of a Mo wire of 70 µm in diameter.

The EDX analysis of the wire revealed the chemical composition of Mo_3Sb_7 in the reacted portion of the wire, while in the middle portion there is only Mo. The powder X-ray diffraction obtained from the powder of Mo_3Sb_7 wires has revealed the presence of the cubic phase with the Ir_3Ge_7 structure type. A few impurity peaks, which correspond to the un-reacted Mo, were also observed. XRD of powdered MoN wires verified the crystallization in the hexagonal δ-MoN phase.

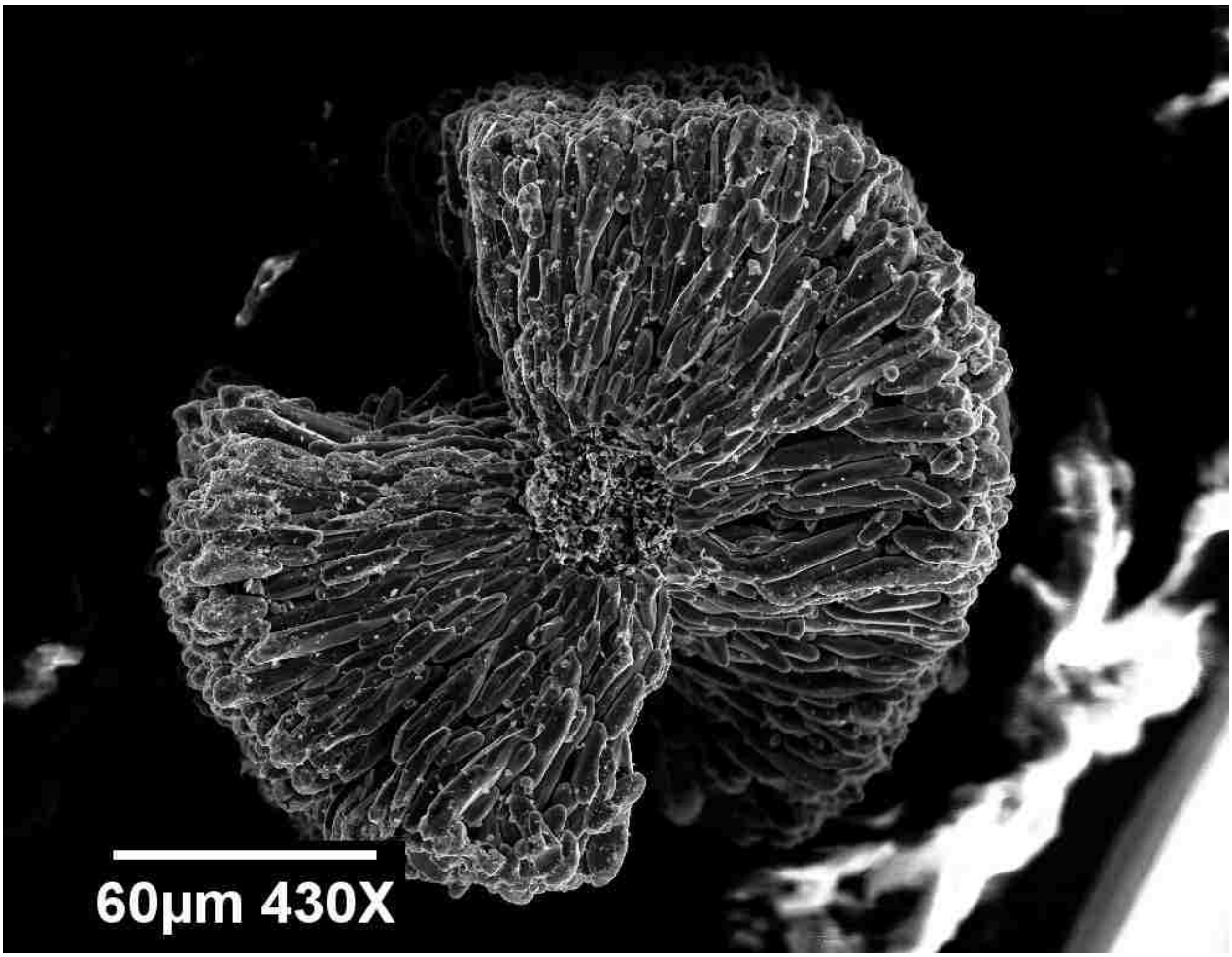

Fig: 3.9 Scanning electron micrograph of Mo_3Sb_7 of wire of 70 µm in diameter showing a cross-sectional view.

The temperature dependence of electrical resistivity of Mo and Mo_3Sb_7 wires of 70 µm in diameter is shown in Figure 3.10. The Mo_3Sb_7 sample was prepared by heating Mo wire with a lot of Sb at 900 ^oC for 1 hour, which was followed by slow cooling down to room temperature. As shown in the inset of Figure 3.10, the superconducting transition temperature, T_c, is 2.1 K which is in good agreement with the values reported for single crystal and polycrystalline bulk samples [8,9]. The shape and the magnitude of the normal state resistivity of Mo_3Sb_7 are very much different from that of Mo wire.

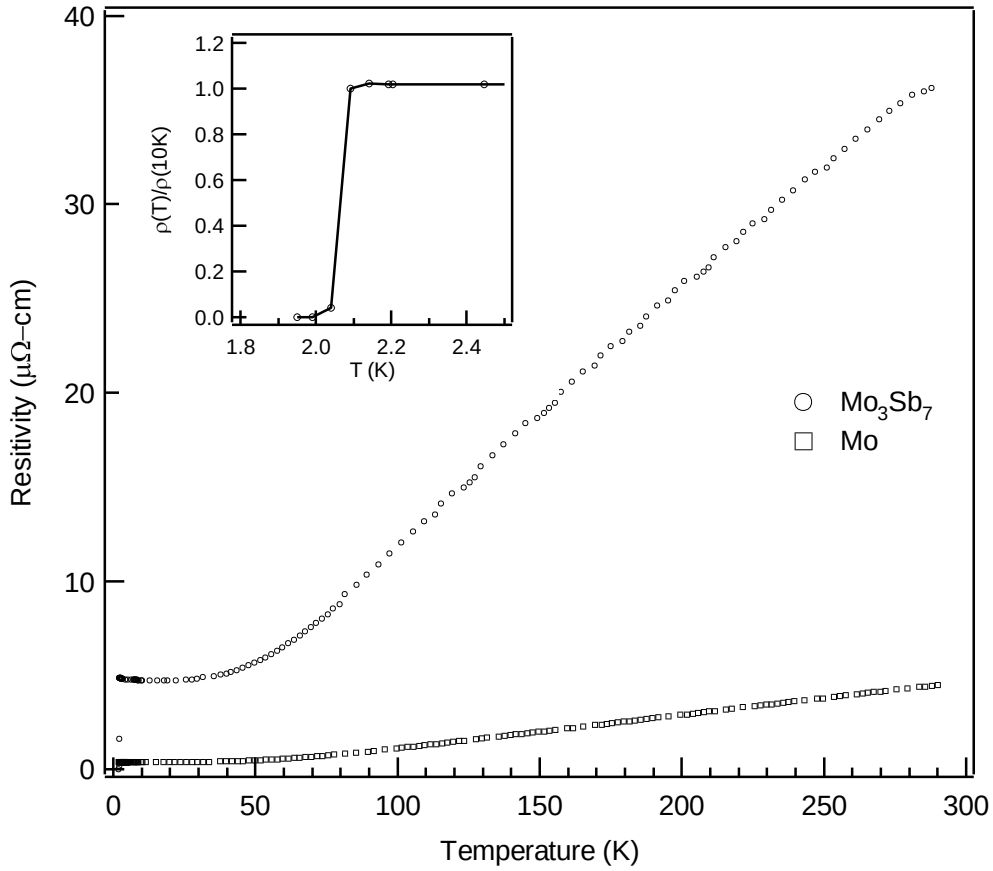

Fig: 3.10 Temperature dependence of the resistivity of Mo and Mo_3Sb_7 wires of 70 μm in diameter. Inset: Superconducting transition in the resistivity vs. temperature plot of Mo_3Sb_7.

Surprisingly, we found the transition temperature, T_c, of the Mo_3Sb_7 thin wire, which is 13 μm in diameter, is almost a factor of four higher than the T_c = 2.1 K for the Mo_3Sb_7 wire of 70 μm in diameter, presented earlier. The cross-sectional view of the SEM picture of the Mo_3Sb_7 thin wire is shown in Figure 3.11. Figure 3.12 shows the superconducting transition of the Mo_3Sb_7 thin wire. The transition temperature T_c is about 8.05 K with a transition width (ΔT_c) of ~ 0.1 K. The T_c is substantially higher than that reported for single crystal and polycrystalline samples of Mo_3Sb_7 synthesized in various forms [8, 9, 24]. To optimize the physical properties of the material the synthesis and characterization of these Mo_3Sb_7 wires were performed several times. The heat treatment at 900^{o}C for 1 hour and 20 minutes is found to be the best synthesis route.

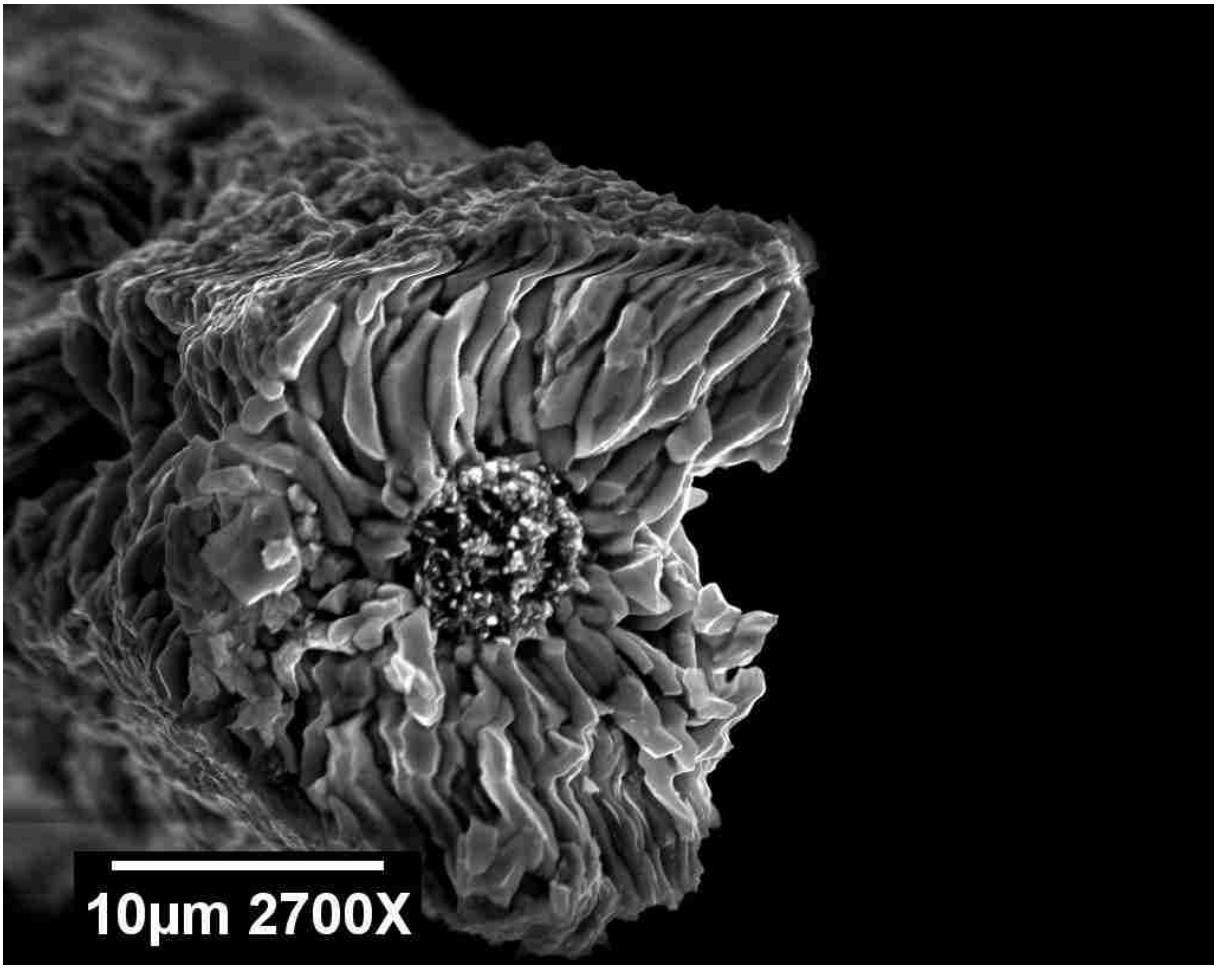

Fig: 3.11 Scanning electron micrograph of a Mo_3Sb_7 wire of 13 µm diameter showing a cross-sectional view. The reaction does not occur throughout the wire.

It can be seen that the shape of the $\rho(T)$ curve for the thin wire (onset in Figure 3.12) is similar to that for thick wire as depicted in Figure 3.10. One can observe an upward curvature of $\rho(T)$ at low temperature followed by a downward one for high temperature. It looks similar to that of conventional metals and different from the simply linear-T dependence observed in copper oxide superconductors. A similar shape has been observed in $MgCNi_3$ in which $\rho(T)$ fits well to the curve predicted by Bloch-Gruneisen theory consistent with the electron-phonon scattering [31].

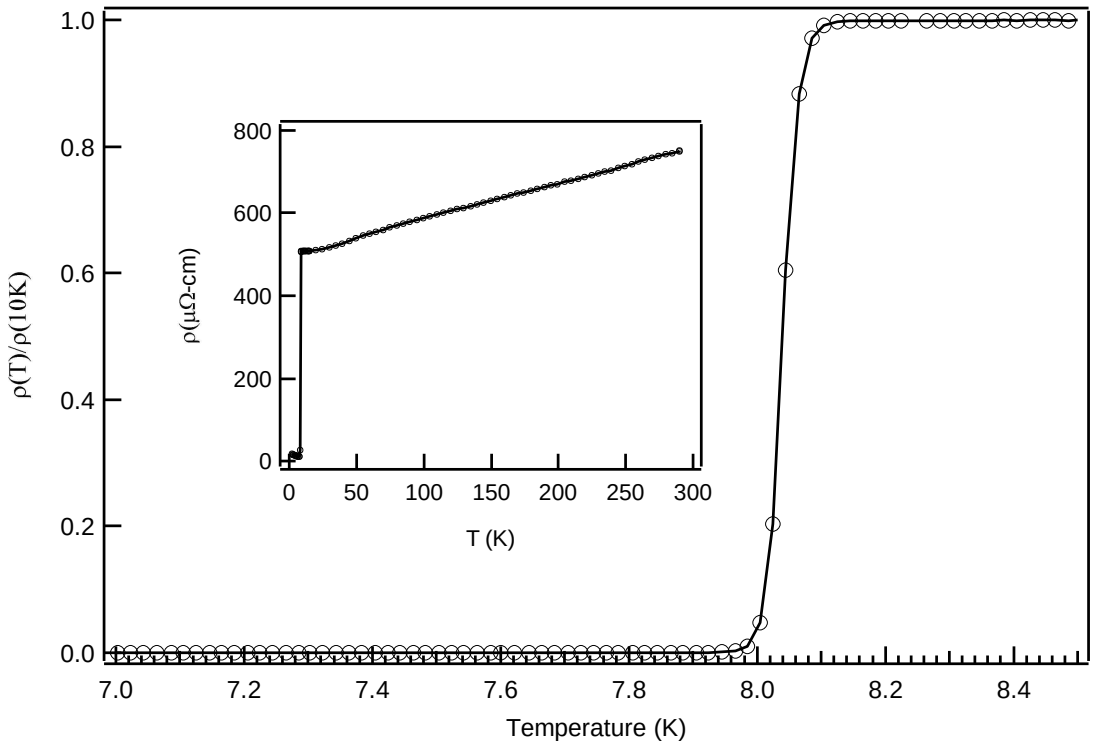

Fig: 3.12 Low temperature resistivity of Mo_3Sb_7 wire of 13 μm in diameter. Resistivity is normalized by its normal state value. Inset: Resistivity vs. temperature plot over the temperature range from 7 K to 290 K. Solid lines are a guide to the eye.

However, the magnitude of the resistivity ($\rho_{290\ K}$ = 751 μΩ-cm and $\rho_{10\ K}$ = 506 μΩ-cm) observed for Mo_3Sb_7 thin wire is much higher than that reported by Bukoswski *et al.* and Candolfi *et al.* [8, 9]. These values are approximately 100 times higher than that obtained for the Mo_3Sb_7 thick wire, which shows the lower transition. On the other hand, the residual resistivity ratio [$RRR = \rho_{(290\ K)} / \rho_{(10\ K)}$] of the thick wire is 7.4, which is substantially bigger than the one for thin wire (1.4). The cross-sectional view in a SEM micrograph of MoN wire of 70 μm in diameter in Figure 3.13 clearly shows the reaction of N with Mo. Unlike in Mo_3Sb_7 wire, the expansion in the MoN wire due to the reaction is not observed. Shown in Figure 3.14, is the temperature dependence of the electrical resistivity of MoN in the form of thin wire of 13 μm in diameter.

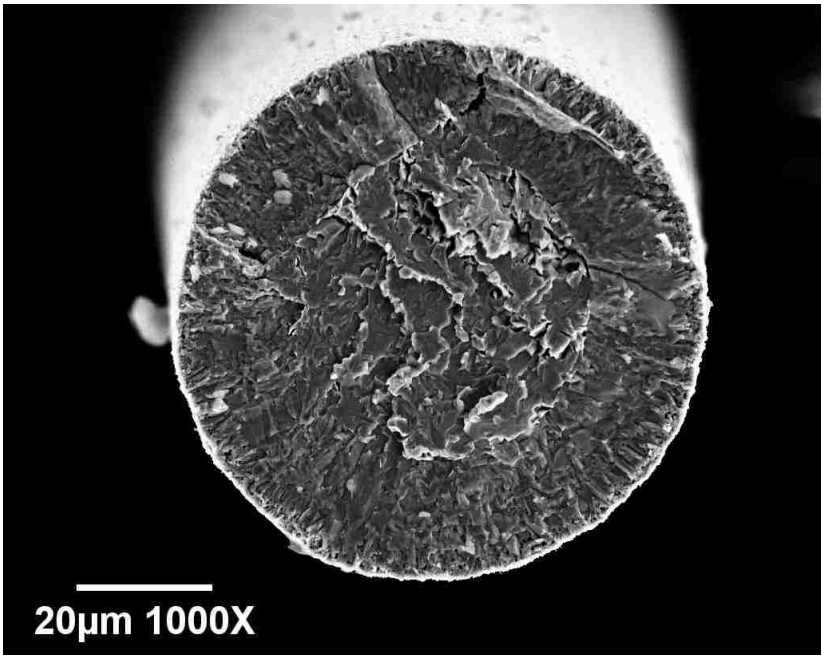

Fig: 3.13 Scanning electron micrograph of a MoN wire of 70 µm in diameter showing a cross-sectional view.

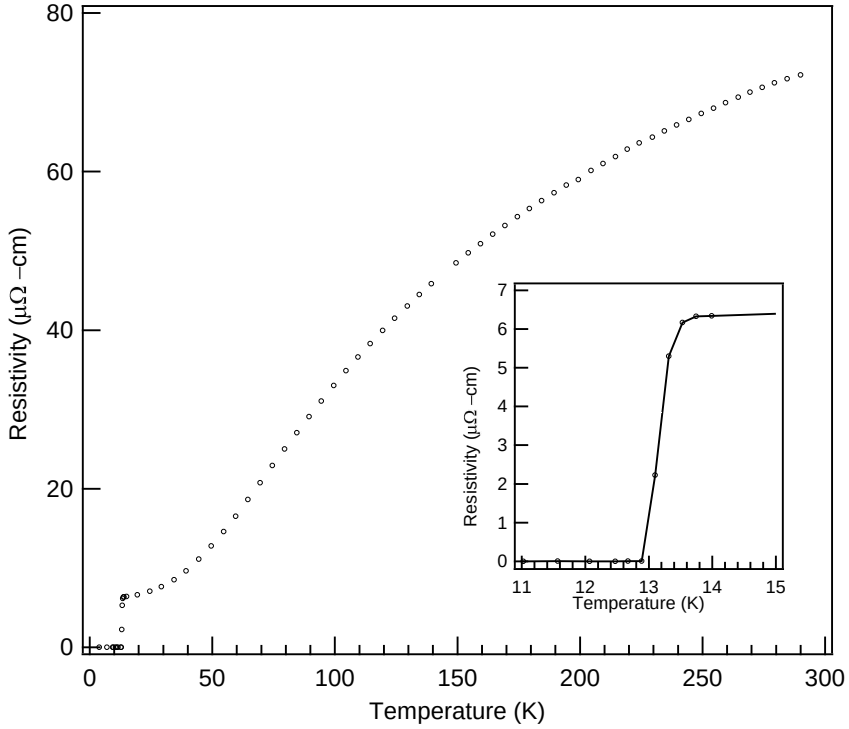

Fig: 3.14 Temperature dependence of resistivity of MoN wire (13 µm dia.). Inset: Resistive transition of the MoN wire.

The shape of the $\rho(T)$ curve of the MoN thin wire is different from that of the Mo_3Sb_7 thin wire. Its residual ratio (RRR) is 10, which indicates the complete reaction of N with Mo in the wire.

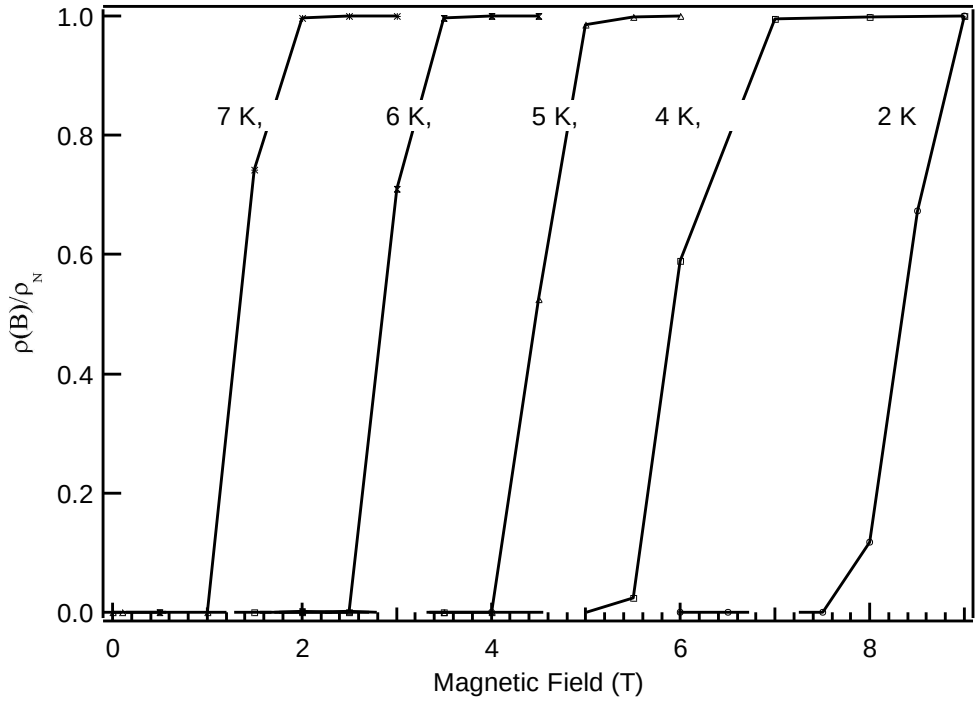

Fig: 3.15 Magnetic field dependence of resistivity of Mo_3Sb_7 wire (13 μm dia.) at 2 , 4, 5, 6 and 7 K (from right to left). The resistivities are normalized by their normal state values. The solid lines are a guide to the eye.

To the best of my knowledge, there is no report on the measurement of the resistivity of MoN in the form of a wire as a function of temperature in the range of 1.9 to 290 K. The lower temperature resistivity measured at zero magnetic field for the MoN thin wire is shown in the inset of Figure 3.14. The sharp superconducting transition at 13.2 K with a small transition width $\Delta T_c \sim 0.3$ K can be observed. This value is higher than the $T_c \sim 12.95$ K, reported for the MoN wire by Saur *et al*. [37]. They obtained the highest transition temperatures of about 12.95 K (midpoint) by the heat treatment at 800 ^oC for 232 hrs. In my experiment, the highest transition temperature of about 13.2 K (midpoint) was obtained by the heat treatment at 900 ^oC for 5 hrs.

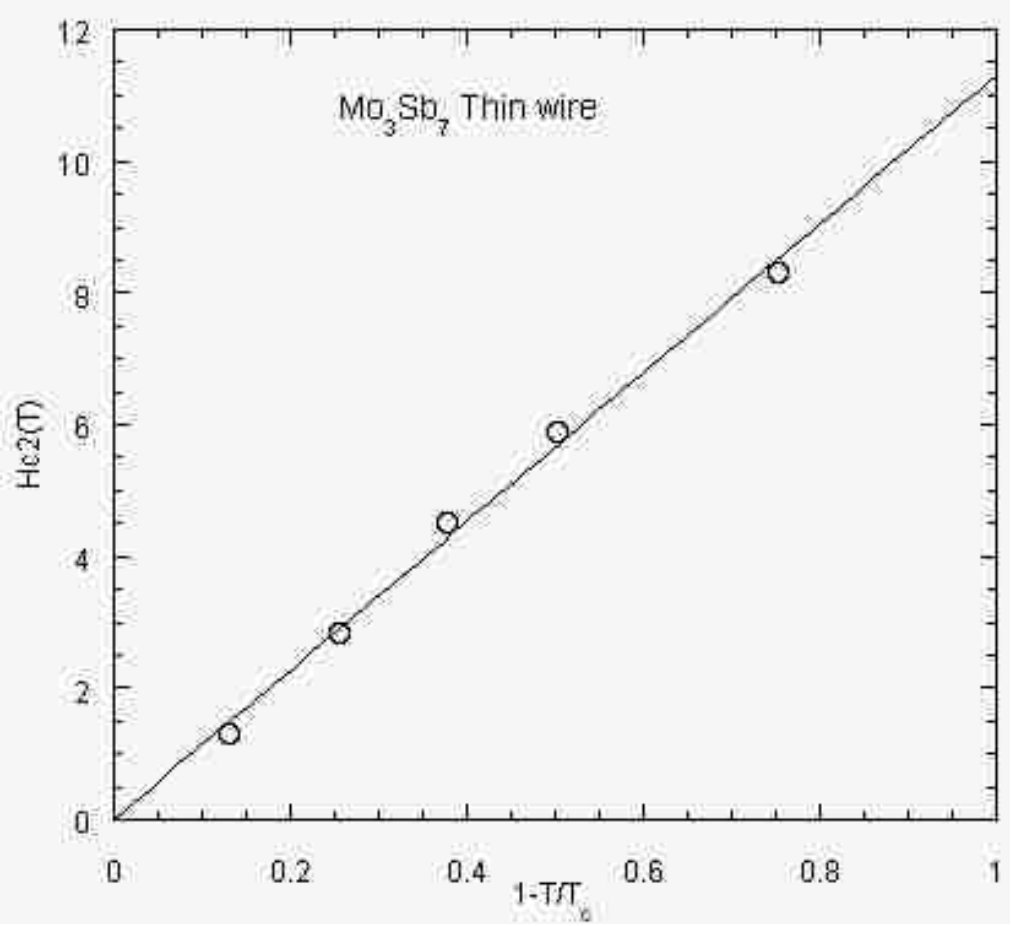

Fig: 3.16 Upper critical field H_{c2} as a function of temperature for Mo_3Sb_7 wire (13 μm dia.). The solid line is the fit to equation (2).

The upper critical field $H_{c2}(0)$ of Mo_3Sb_7 and MoN thin wires were determined from the resistivity (ρ) data at various temperatures. The magnetic field was applied along the wire axis. Figure 3.15 presents the magnetic field dependence of resistivity at 2, 4, 5, 6, and 7 K for Mo_3Sb_7. The transition width (ΔH) is fairly small, indicating a sharp transition. Critical field , H_{c2}, is defined as the midpoint of the transitions. The error bar is ± 0.2 T. In Figure 3.16 the upper critical field of Mo_3Sb_7 is plotted as a function of reduced temperature. The temperature dependence of the upper critical field $Hc_2(T)$ is defined by a simple empirical formula:

$H_{c2}(T) = H_{c2}(0)\ (1-T/T_c)$ ……..…(3.2)

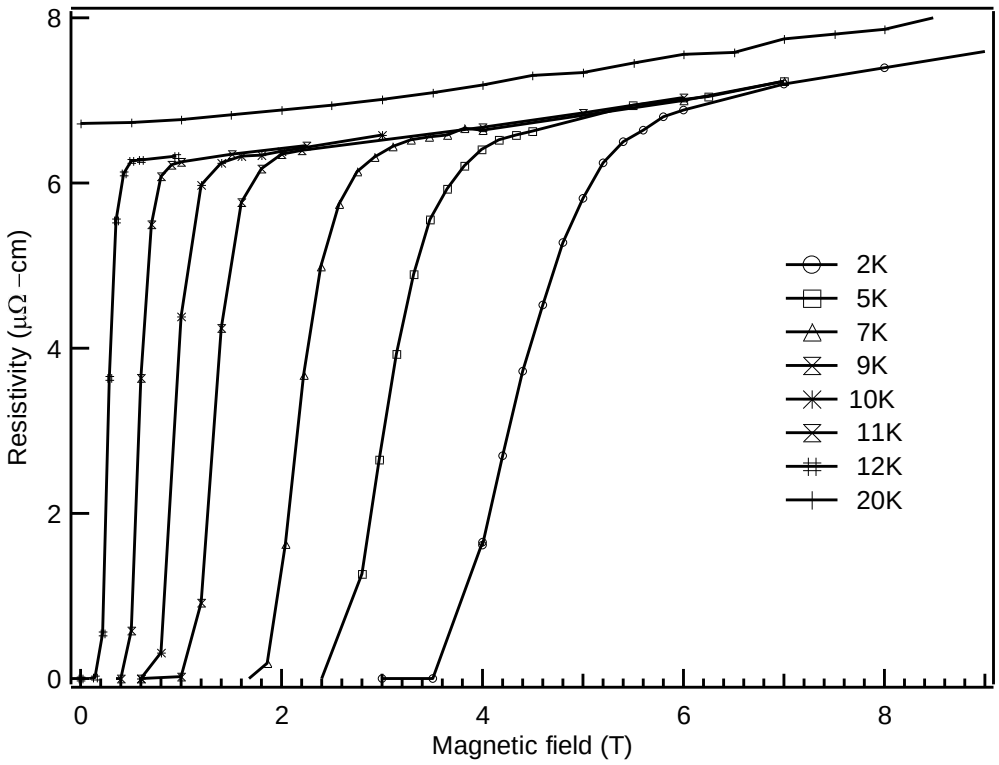

Fig: 3.17 Magnetic field dependence of resistivity of MoN wire (13 μm dia.) at 2, 5, 7, 9, 10, 11, 12, and 20 K. The solid lines are a guide to the eye.

$H_{c2}(0)$ is the upper critical field extrapolated to 0 K and T_c is the superconducting transition temperature in zero applied magnetic field. The solid line in Figure 3.16 represents the best fit of the experimental data to equation (3.2) for Mo_3Sb_7. The extrapolation yielded $H_{c2}(0)$ = 11.3 T. This corresponds to a superconducting coherence length $\xi(0)$ = 54 Å, estimated using the Ginzberg Landau formula for an isotropic three dimensional superconductor $H_{c2}(0) = \Phi_0/2\pi\xi(0)^2$, where Φ_0 = 2.0678 x 10^9 Oe Å^2 is a flux quantum. The upper critical field of the single crystal of Mo_3Sb_7 is 1.7 T [8, 26]. Not only is the critical field of the Mo_3Sb_7 wire significantly higher than that of the single crystal, but the reduced critical field H_{c2}/T_c ~ 1.4 T/K is also significantly higher than the 0.55 T/K of the single crystal. Indeed, the former is near the Clogston limit [12].

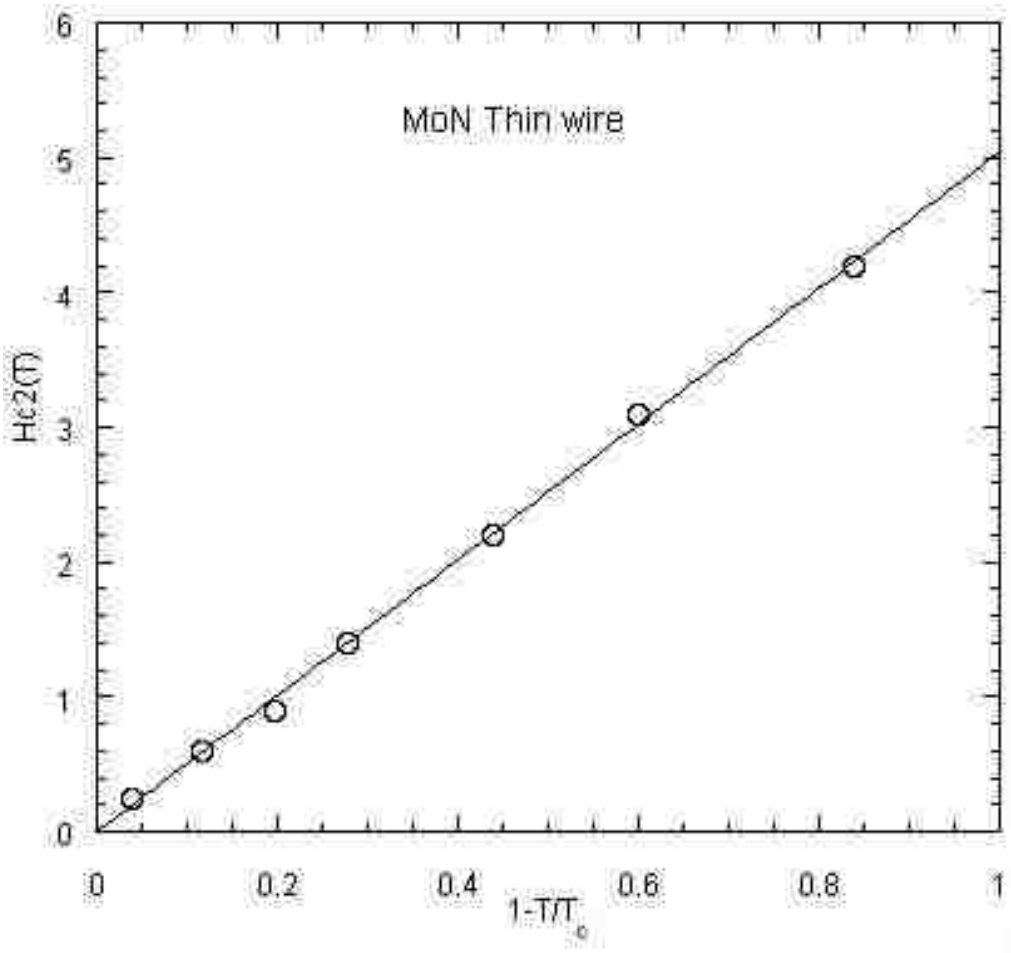

Fig: 3.18 Upper critical field H_{c2} as a function of temperature for MoN wire (13 μm dia.). The solid line is the fit to equation (3.2).

Resistivity of MoN thin wire was measured at the temperatures 2, 5, 7, 9, 10, 11, 12, and 20 K with varying magnetic field. It can be seen that this sample has a 15 % magnetoresistance [$(\rho_{9T}-\rho_0)/\rho_0$]. The midpoint values of the magnetoresistive transitions vs. magnetic field were plotted in Figure 20 as a function of reduced temperature. The data were fitted to equation 3.2, and extrapolated to zero temperature, which yielded an upper-critical field $H_{c2}(0)$ = 5 T. To the best of my knowledge, this is the first report on the magnetic field dependence of the resistivity for this system. It is to note that this value is pretty low in comparison to the value of $H_{c2}(0)$ for the Mo_3Sb_7 thin wire.

3.4.3 Mo_3Sb_7 and MoN Thin Films

Results of powder X-ray diffraction confirm the growth of Mo, Mo_3Sb_7, and MoN thin films with the absence of any impurities. The molybdenum films were grown on sapphire via e-beam deposition of Mo buttons held in tungsten boats, thus there was no carbon involved in the process.

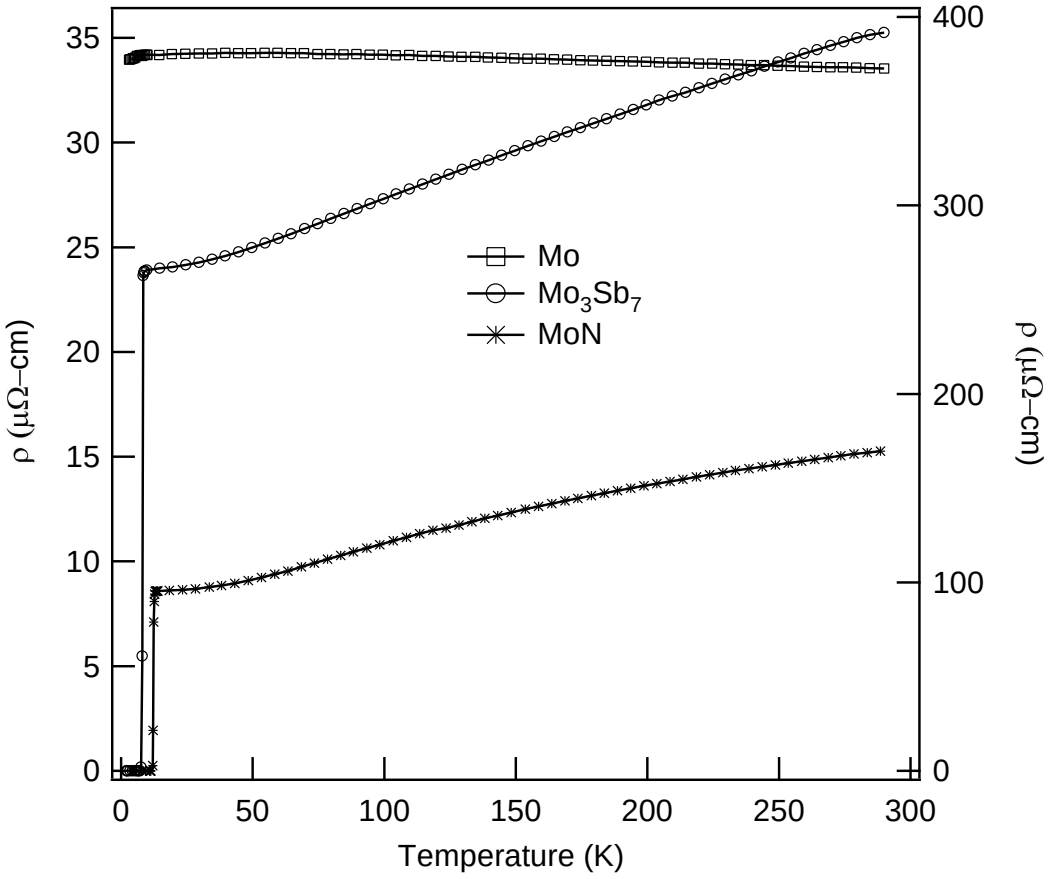

Fig: 3.19 Temperature dependence of resistivity of 60-nm thick film of Mo_3Sb_7 and MoN (left axis) and Mo (right axis). The solid lines are a guide to the eye.

The best samples in terms of the phase purity and the value of T_c were obtained by exposing 60-nm thick Mo films to (a) antimony vapor at 900 ^oC for 30 minutes for Mo_3Sb_7 and (b) a stream of NH_3 at 900 ^oC for 5 hrs. The MoN film was formed in hexagonal δ-MoN phase.

Shown in Figure 3.19 is the temperature dependence of the resistivity of the thin films of Mo, MoN and Mo_3Sb_7. The shape of $\rho(T)$ curve is similar to that of wires of respective materials. The normal state resistivity decreased by an order of magnitude when the Mo reacted to form Mo_3Sb_7 and MoN in thin films. MoN film is observed to be more ordered than Mo_3Sb_7. The residual resistivity ratios (RRR) are 1.5 and 1.7 for Mo_3Sb_7 and MoN, respectively. Sharp superconducting transitions are observed in thin films of MoN and Mo_3Sb_7.

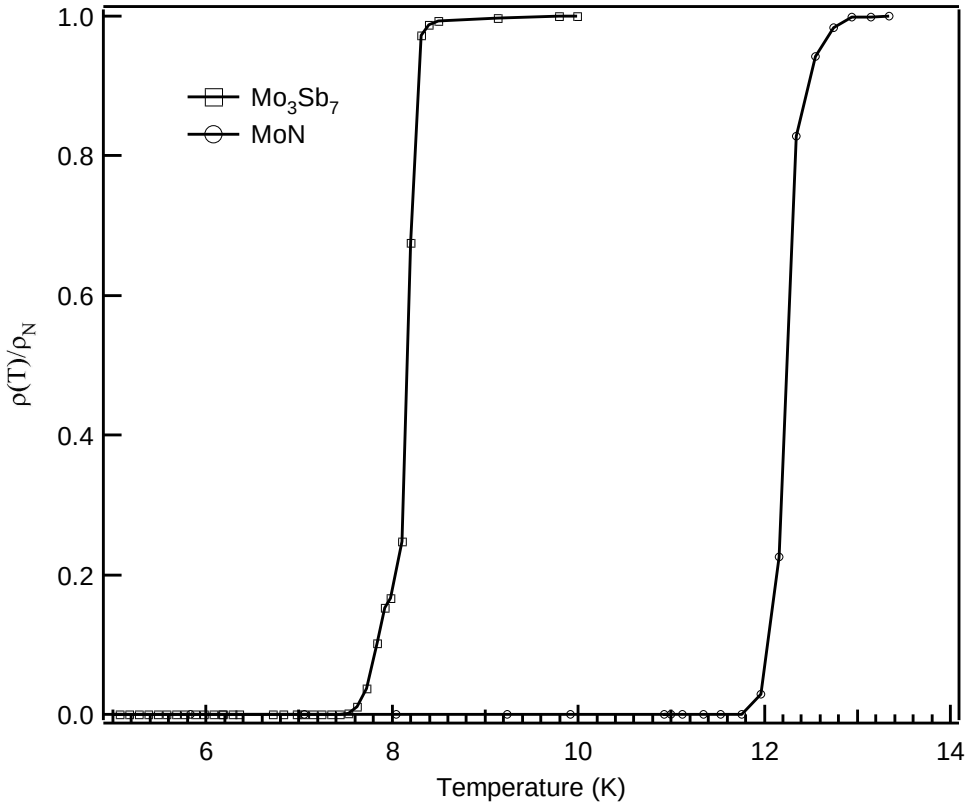

Fig: 3.20 Low temperature resistivity normalized by its normal state value of 60-nm thick films of Mo_3Sb_7 and MoN. The solid lines are a guide to the eye.

The low temperature resistivity data for MoN and Mo_3Sb_7 thin films are shown in Figure 3.20. The resistivity is normalized by its normal state value. The T_c from the midpoint of the transition for Mo_3Sb_7 is 8.2 K with the transition width $\Delta T_c \sim 0.4$ K. This value is close to the value obtained for the thin wire. The transition temperature T_c (midpoint) of the MoN thin film is 12.3

K with ΔT_c ~ 0.2 K , which is consistent with that of MoN thin wire and the values reported for δ-MoN in literature [5,7,36,2,46].

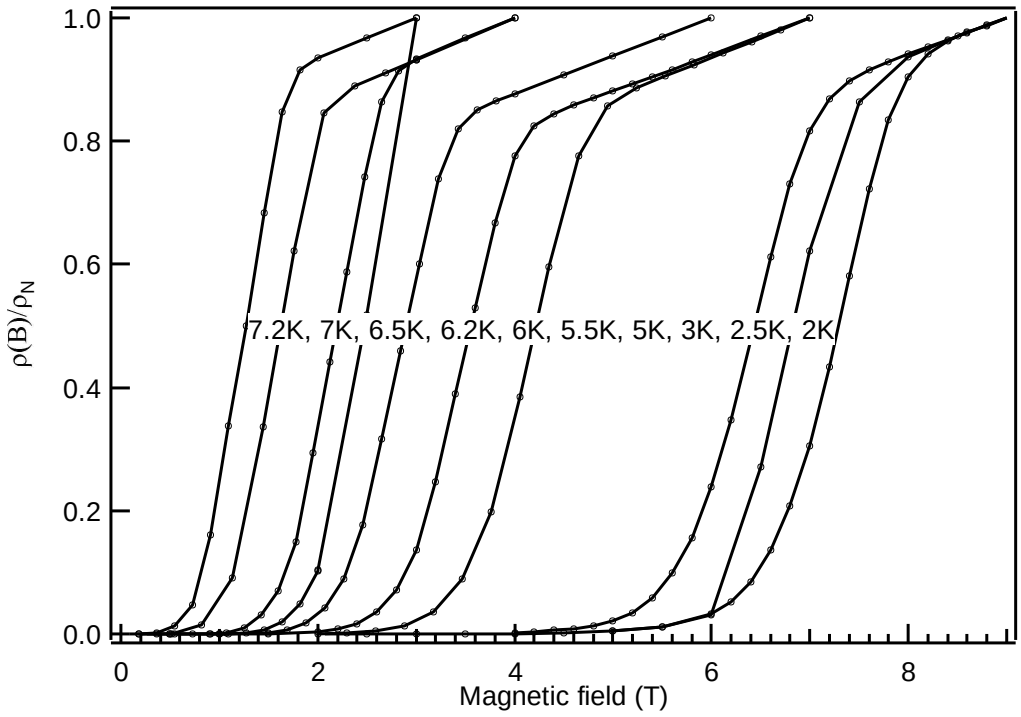

Fig: 3.21 Magnetic field dependence of resistivity of a 60-nm thick film of Mo_3Sb_7 at 2, 2.5, 3, 5, 5.5, 6, 6.2, 6.5, 7, and 7.2 K. The resistivity is normalized by its normal state value.

Figures 3.21 and 3.22 present the magnetic field dependence of the resistivity of the Mo_3Sb_7 and MoN thin films at various temperatures. The resistivity is normalized by its value at 9 T. It can be seen that for both samples the transition width *(ΔH)* decreases with increase in temperature. The *H-T* phase diagram of each compound was derived from the upper-critical field H_{c2} obtained from the midpoints of the transitions in the *R(H)* data at various temperatures in Figures 3.21 and 3.22 with error bar ± 0.4 T. The data thus obtained was fit to equation (2) as shown in Figure 3.23 and 3.24 (solid lines). The extrapolation of the fit lines produces the $H_{c2}(0)$ = 9.6 and 10 T for Mo_3Sb_7 and MoN thin films, respectively. These values of $H_{c2}(0)$ correspond to coherence lengths ξ (0) = 58.5 and 57 Å for Mo_3Sb_7 and MoN, respectively.

The upper critical field $H_{c2}(0)$ of the thin film is approximately 2 T less than the value obtained for the Mo_3Sb_7 thin wire. The decrease of H_{c2} can be explained in terms of the H_{c2} dependence on the effective coherence length (ξ): $H_{c2} \propto \Phi_0/\xi^2$, where Φ_0 is a flux quantum.

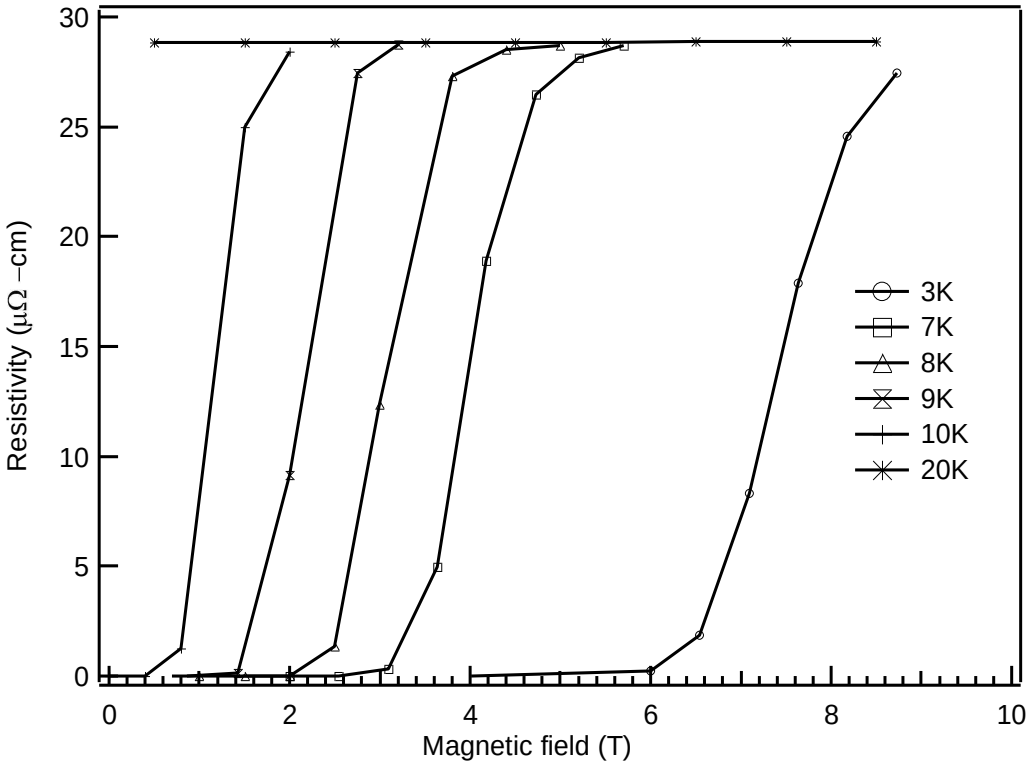

Fig: 3.22 Magnetic field dependence of resistivity of a 60-nm thick film of MoN at 3, 7, 8, 9, 10, and 20 K. The resistivity is normalized by its normal state value. Solid lines are a guide to the eye.

For dirty superconductors the effective coherence length is defined as $1/\xi = 1/\xi_0 + 1/l$, where ξ_0 is the Pippard coherence length and l is the mean free path [32]. We know l varies with residual resistivity ρ_0 through $l = 2mV_F/(ne^2\rho_0)$, for the sample used in [31], where n is the carrier density and V_F is the Fermi velocity. The thin film is more ordered with the normal state resistivity ρ_0 approximately 100 times lower than that of the thin wire, which leads to the elongation of the mean free path l. On the other hand, ξ_0 is related to the critical temperature: $\xi_0 = a(h/2\pi)v_0/kT_c$, where a is a constant and v_0 is the velocity at the Fermi level [32]. It did not

shorten ξ_0 simultaneously by increasing T_c in the same proportion. In this situation one can expect the lower value of H_{c2} in this sample.

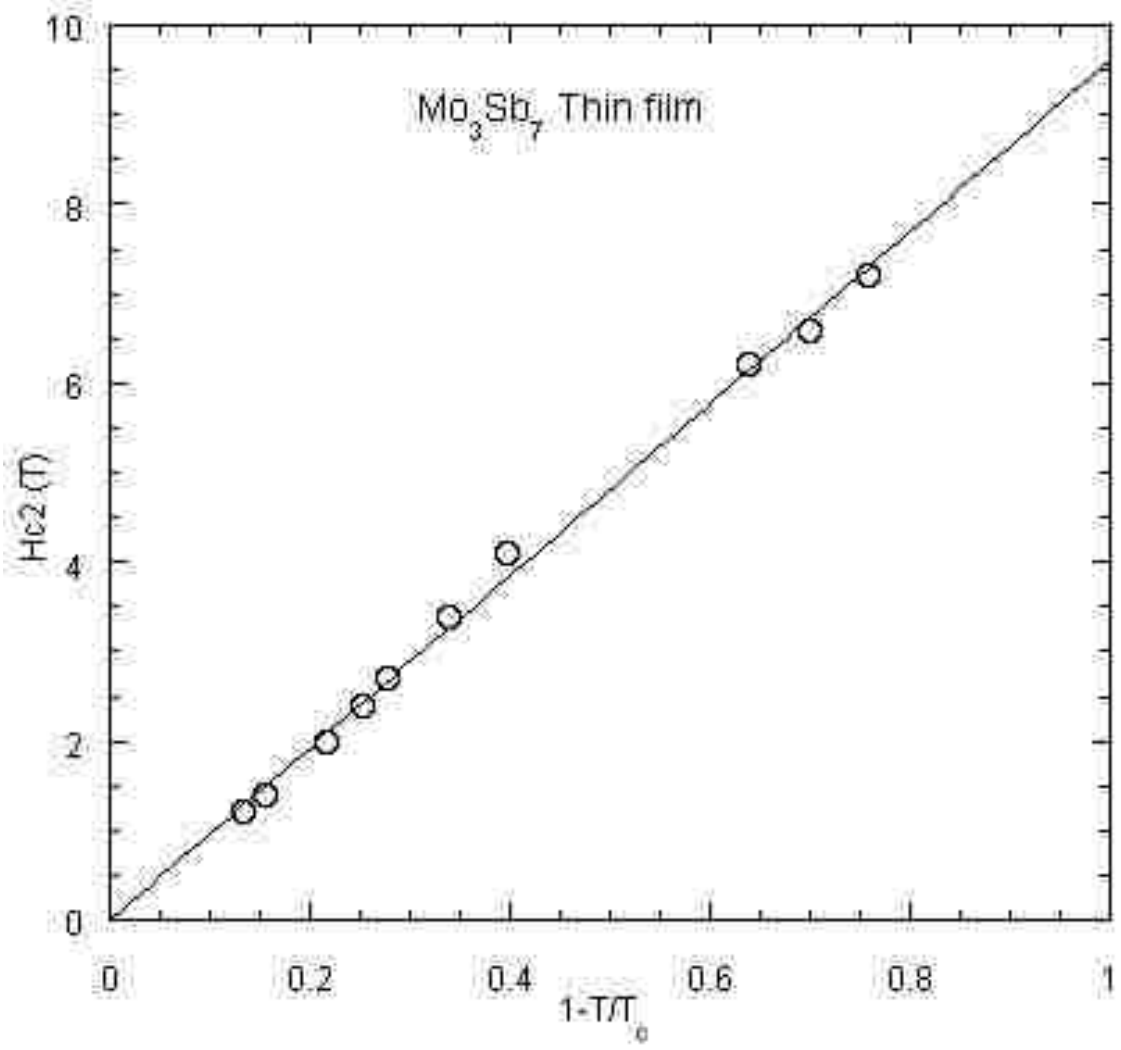

Fig: 3.23 Upper critical field H_{c2} as a function of temperature for a 60-nm thick film of Mo_3Sb_7. The solid line is a fit to equation (3.2).

Upper critical field $H_{c2}(0)$ of the MoN thin film is approximately double of that of the MoN thin wire reported earlier. To my knowledge, there are no any other reports on magneto-trnasport measurements of MoN in any phase.

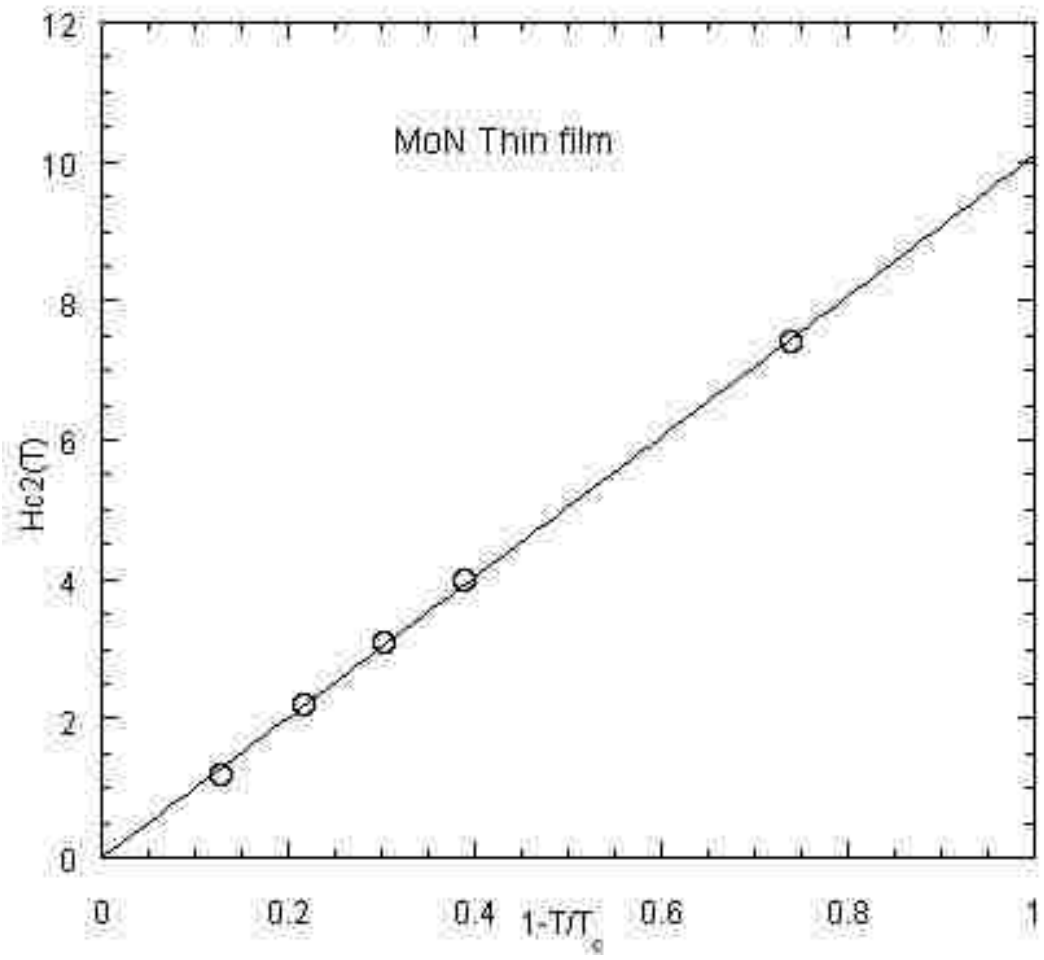

Fig: 3.24 Upper critical field H_{c2} as a function of temperature for 60-nm thick film of MoN. The solid line is a fit to equation (3.2).

The magnetoresistance (*MR*) which is defined by $[(\rho(H) - \rho(0))/\rho(0)]$, versus applied magnetic field at 20 K and 290 K for the thin film of Mo_3Sb_7 is shown in Figure 3.25a. At both temperatures, the magnetoresistance increases with the applied field. At 20 K the magnetoresistance at 9 T is large (~61%) and shows no tendency toward saturation. The study of dependence of MR with the variation of thickness of the films will be interesting. The MR of MoN thin films is found very small.

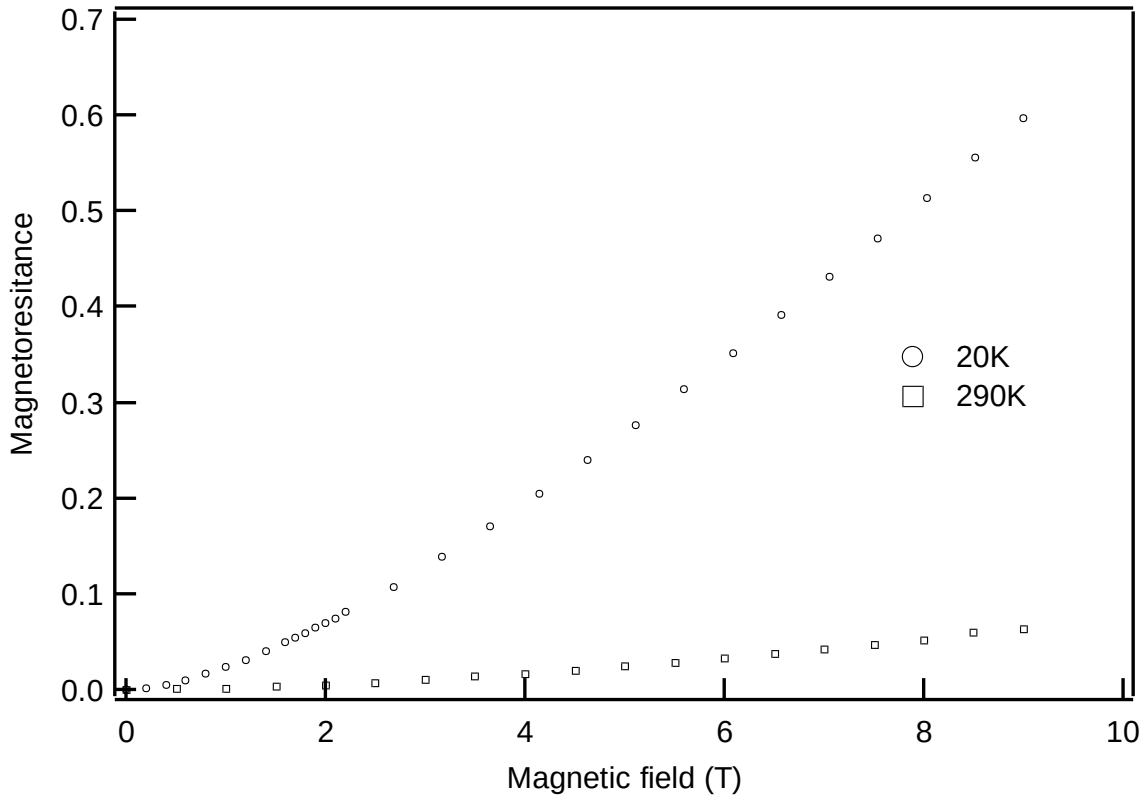

Fig: 3.25a Dependence of magnetoresistance (MR) of the Mo_3Sb_7 60-nm thick film on magnetic field at 20 and 290 K.

The Hall voltage data for the Mo_3Sb_7 thin film at 10 K is shown in Figure 3.25b. Note that the field dependence of the Hall voltage is not linear over the entire range of magnetic field. It has a different slope at different segments of the field range. The data and fit to the linear equation $\rho_H = R_H B$ for the lower field regime are shown in the lower right corner, and for the higher filed regime the at upper left corner in the inset of Figure 3.25. At low field, $R_H = 4.673 \times 10^{-10}$ m^3/C, and the calculated carrier density is $1.33 \times 10^{22}/cm^3$, while at higher field, $R_H = 9.617 \times 10^{-10}$ m^3/C and the carrier density is $6.4 \times 10^{21}/cm^3$. The main feature of the Hall effect is the positive R_H. It definitely indicates that the carrier is hole type, which is strongly supported by the positive thermoelectrical power S = 8 μV/K, observed at the room temperature in the wire. The behavior of ρ_H and the decrease in carrier density with field remains an open question.

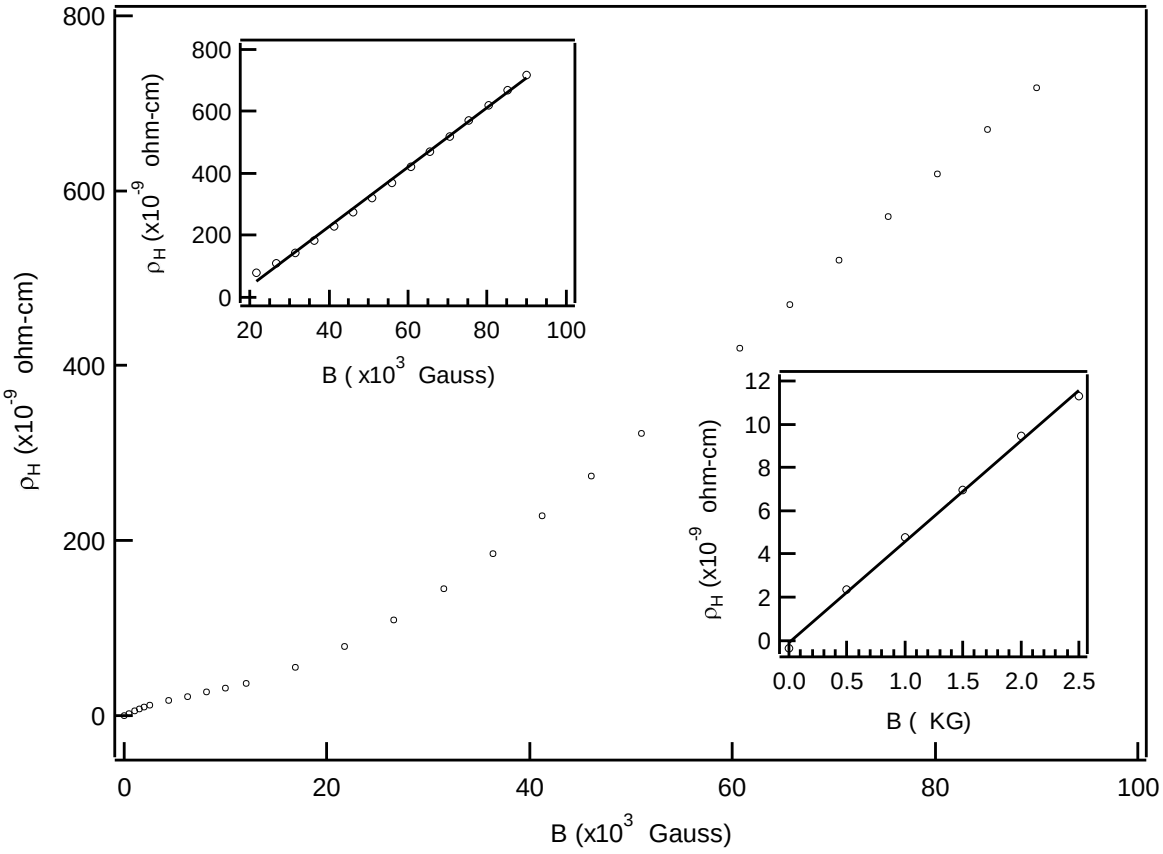

Fig: 3.25b Hall voltage vs. magnetic field data of a 60-nm thick film of Mo_3Sb_7 measured at 10K. Inset: upper left is $\rho_H(H)$ at high field and lower right is $\rho_H(H)$ at low field. The solid lines are fits to the linear equation $\rho_H = R_H B$.

On other hand, the negative slope of the $\rho_H(B)$ curve of the MoN thin film indicates the electron type carrier. This is supported by the negative value of the thermoelectric coefficient S = -5.1 μV/K measured at room temperature for the MoN wire. The data were more scattered, so that they are not presented here.

3.4.4 Mo_3Sb_7 and MoN Coatings on C Microfibers

The scanning electron micrograph of Mo_3Sb_7 and MoN coated C microfibers are shown in Figures 3.26 and 3.27. Since the coating is very thin (40- 160 nm), the SEM pictures of Mo_3Sb_7 coated fiber [Figure 3.27(a)] and that of MoN coated fiber [Figure 3.27(b)] look similar.

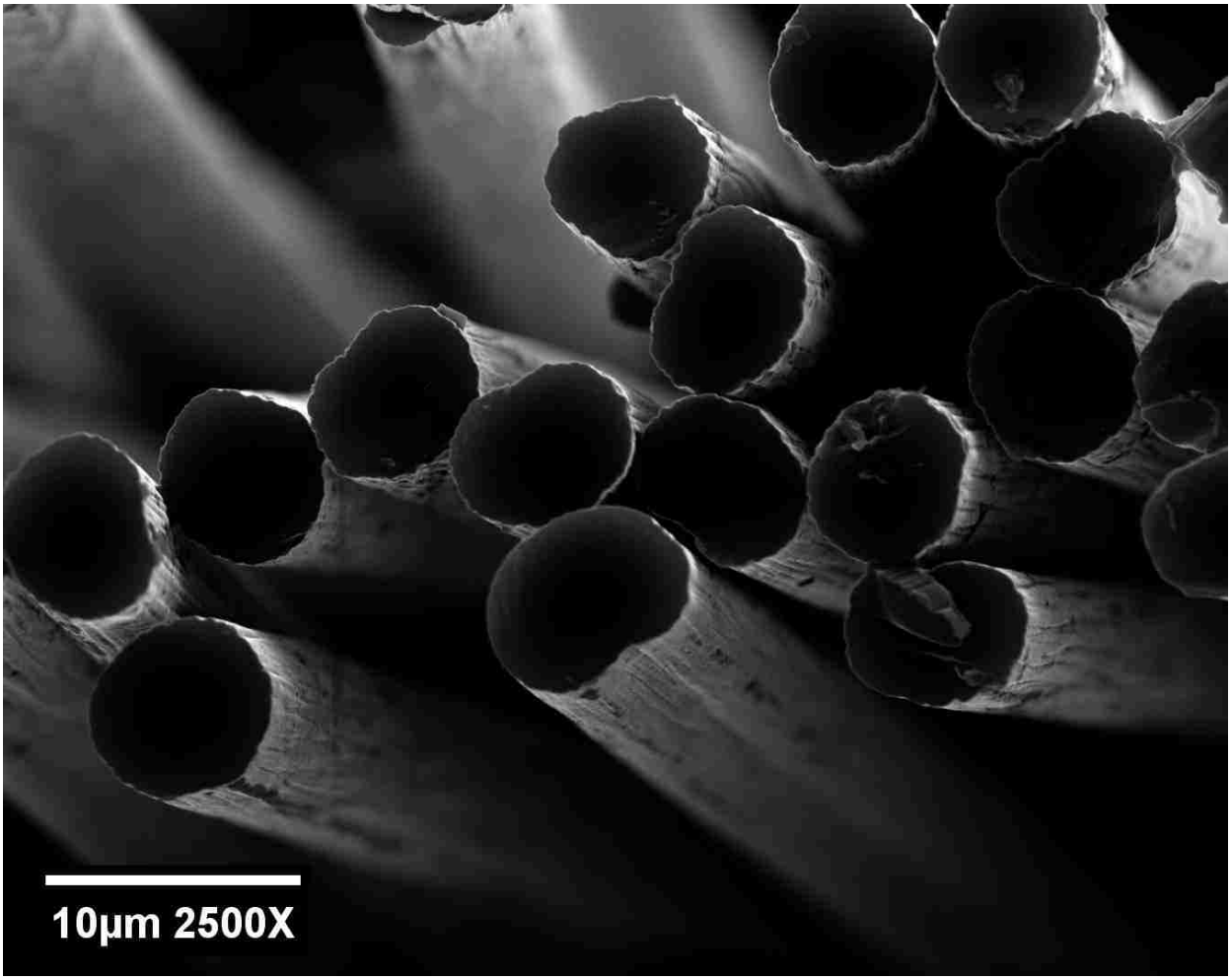

Fig: 3.26 Scanning electron micrograph of Mo_3Sb_7 coated carbon fibers.

The result of the XRD of ground fibers verified the formation of Mo_3Sb_7 with a lot of un reacted carbon as expectation. From the observation of the expansion in the Mo_3Sb_7 wire due to the reaction of Mo with Sb, one can consider the similar result in case of the Mo_3Sb_7 coating in the fiber. Shown in Figure 3.28 is the temperature dependence of the resistivity of a pristine Mo-coated fiber, Mo_3Sb_7-coated fiber and a MoN-coated fiber. The shape of the $\rho(T)$ curves of all three compounds is different, but they are similar to that of their respective films. The residual resistivity ratios ρ_{290K}/ρ_{10K} are 1.49 and 1.8 which are consistent with those of the thin films.

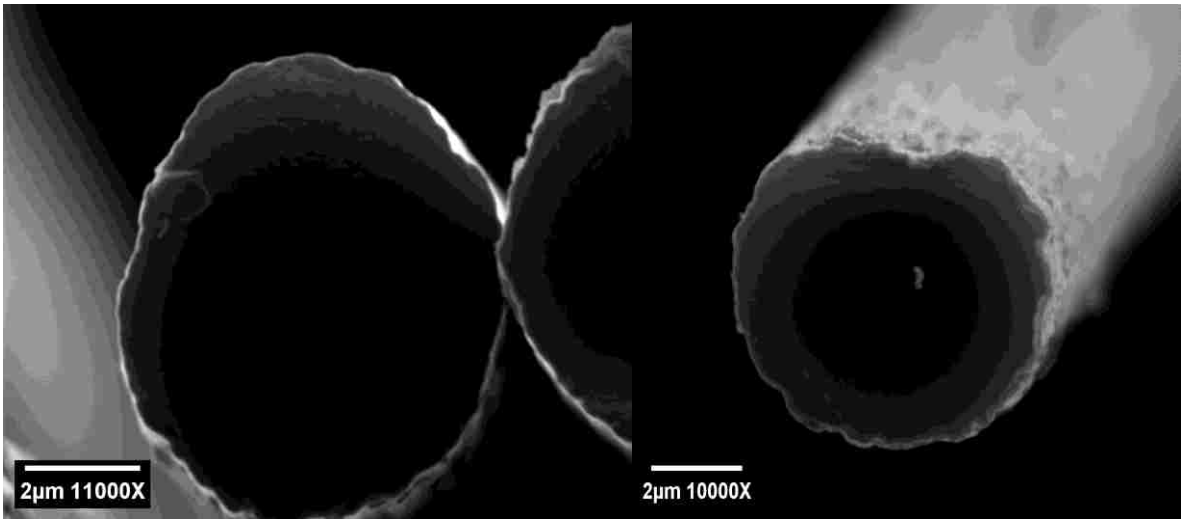

Fig: 3.27 Scanning electron micrograph of (a) Mo_3Sb_7 (left) and (b) MoN (right) coated carbon fibers showing the cross-sectional view.

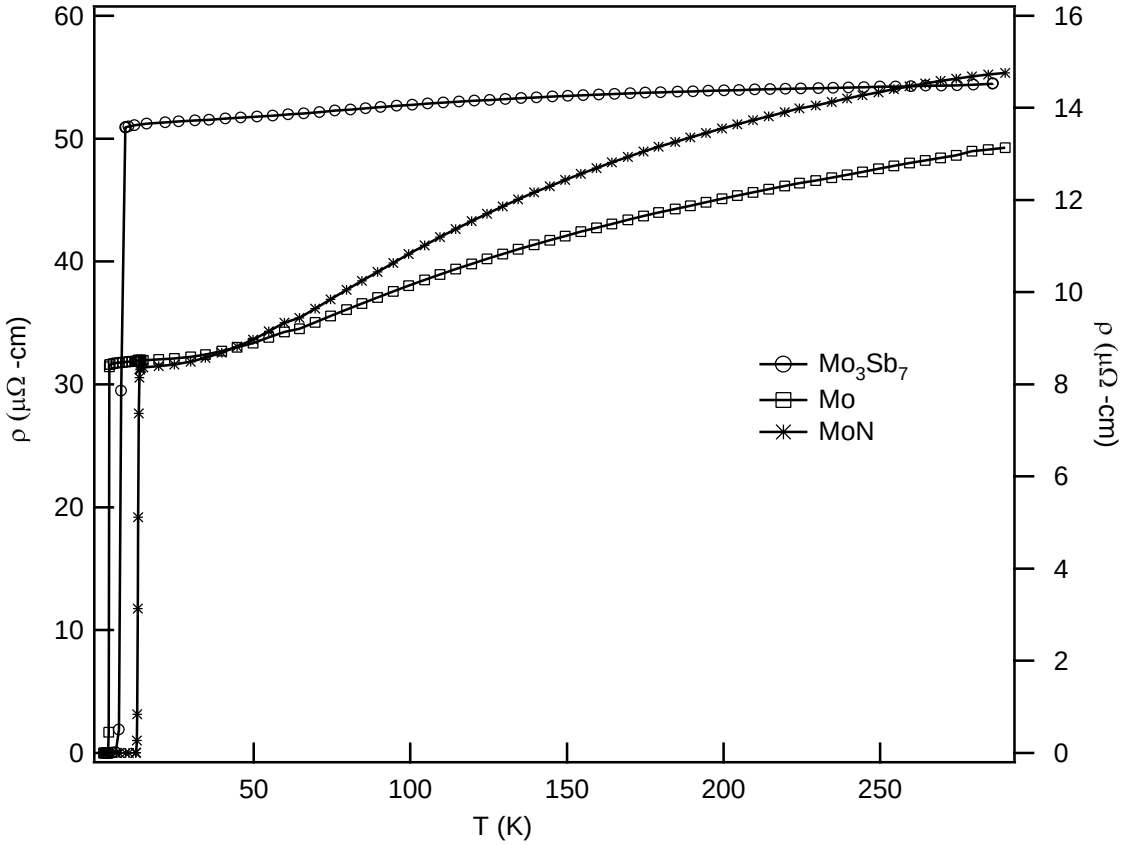

Fig: 3.28 Temperature dependence of resistivity of C fibers coated with Mo and MoN (right), and Mo_3Sb_7 (left). The solid lines are a guide to the eye.

Note that each of these fibers underwent a superconducting transition at a temperature well above 1 K. The transition temperatures are T_c = 3.7 K, 7.8 K and 12.9 K for the Mo, Mo_3Sb_7 and MoN coated fibers, respectively. The relatively high transition temperature of the pristine Mo-coated fiber is due to the fact that a portion of the molybdenum coating reacted with the carbon core to form Mo_2C, which itself has a T_c ~ 3 K [4]. The fibers have very sharp resistive superconducting transitions, with a width ΔT_c ~ 0.2 K. T_c of the fibers are slightly smaller than that of the respective wires and thin films. The heat treatment of a Mo-coated C fiber at 900 ^oC for 1 h and 20 minutes in Sb vapor resulted in Mo_3Sb_7 with the highest T_c. Similarly, the exposure of Mo-coated C fibers to the stream of NH_3 at 900 ^oC for 1 h and 20 minutes produced MoN with the highest T_c. We were successful to reproduce the samples with the above synthetic route.

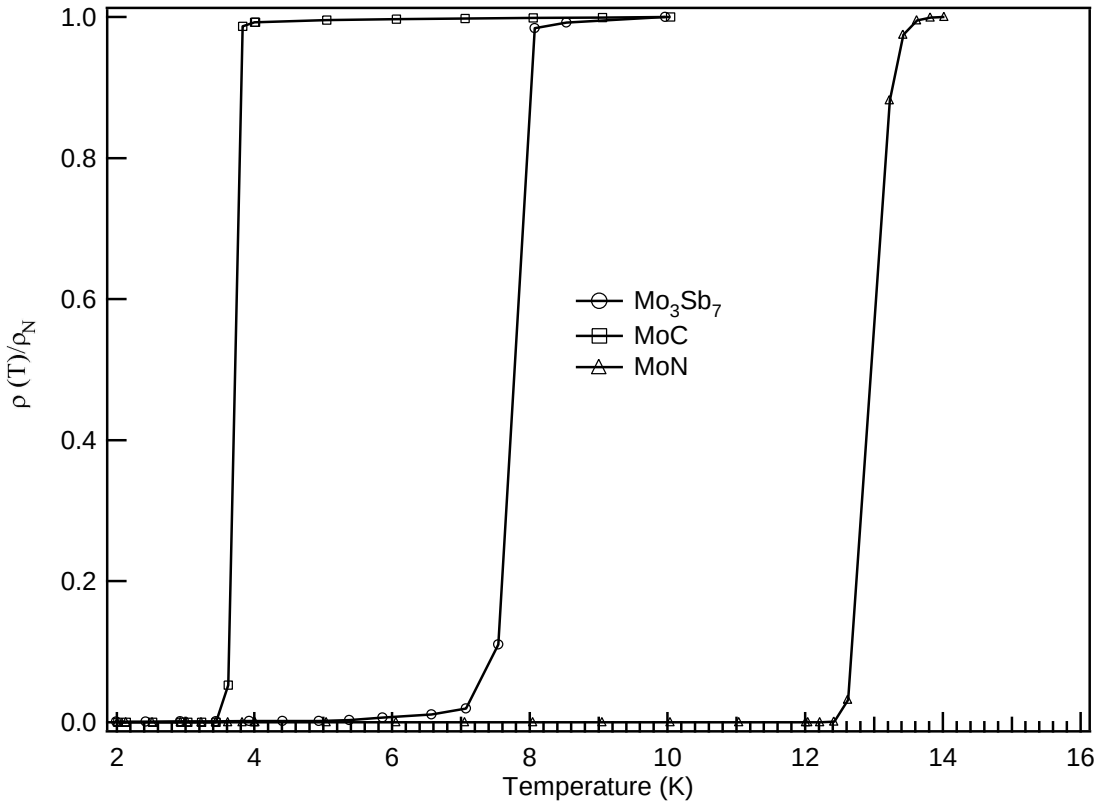

Fig: 3.29 Low temperature resistivity normalized by its normal state value of C fibers coated with Mo, Mo_3Sb_7, and MoN. The solid lines are a guide to the eye.

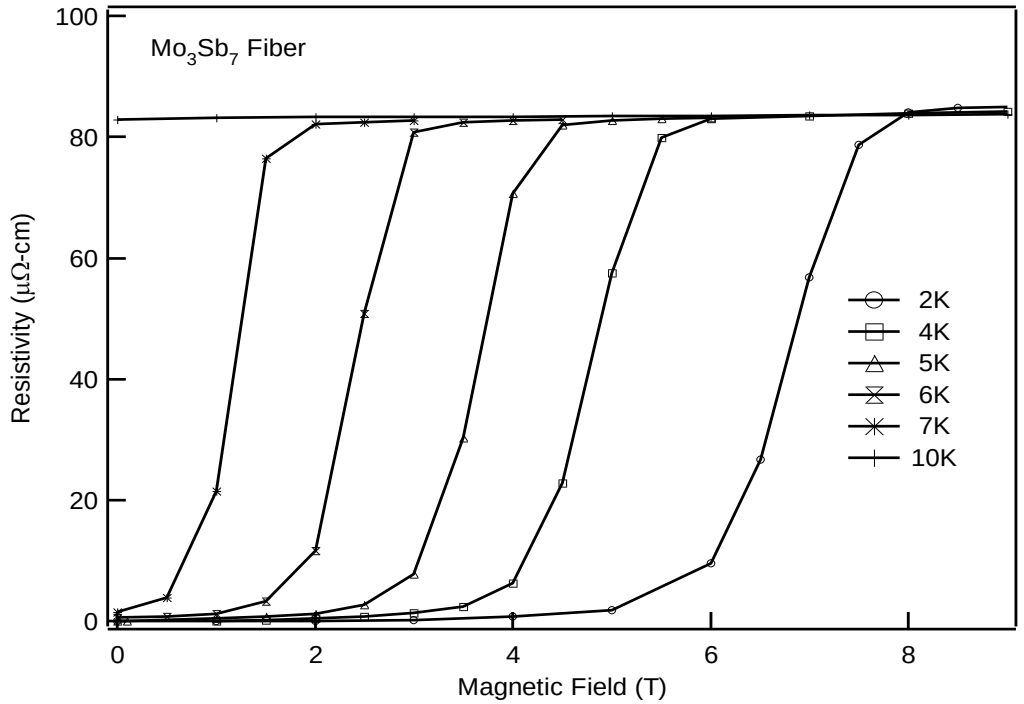

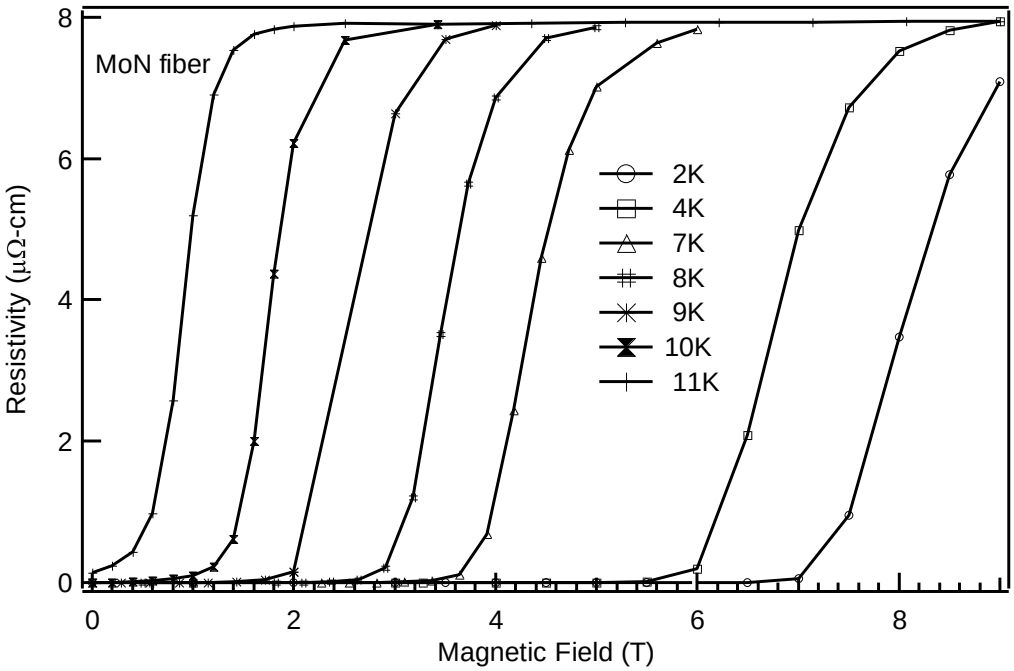

Fig: 3.31 Magnetic field dependence of the resistivity normalized by its normal state value of Mo_3Sb_7 and MoN coated C fibers at various temperatures. Solid lines are a guide to the eye.

The magnetic field dependence of the resistivity of Mo_3Sb_7 and MoN coated fibers at various temperatures are presented in Figures 3.30 and 3.31, respectively. The magnetic field was applied along the fiber axis.

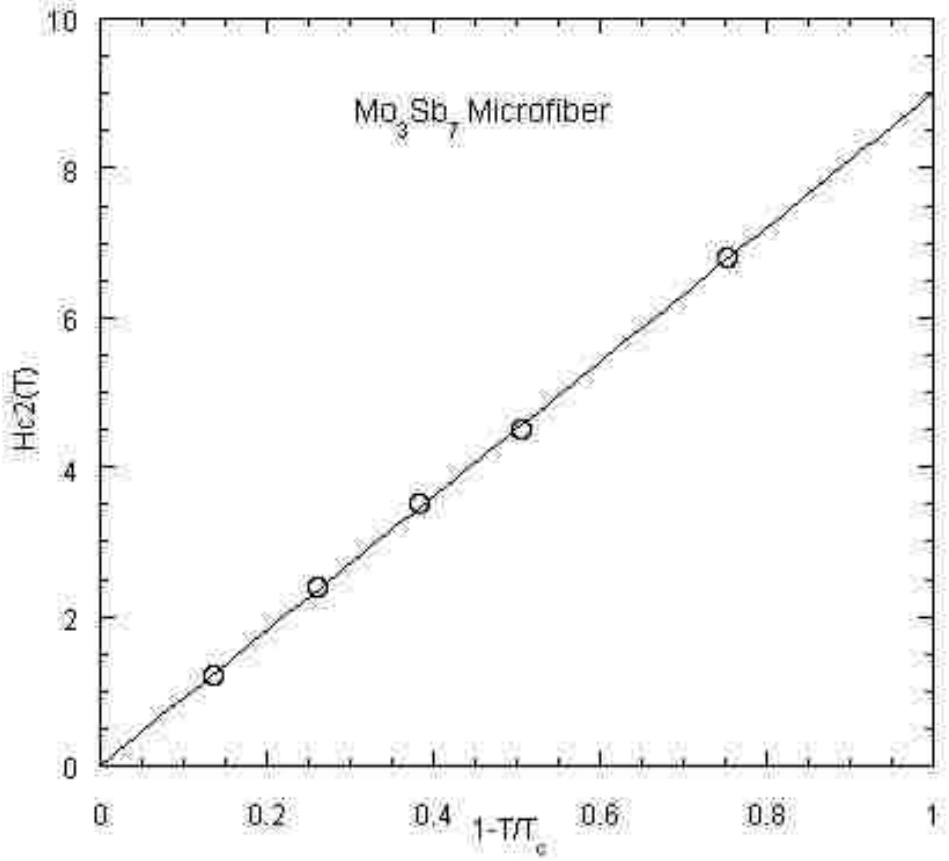

Fig: 3.32 Upper critical field H_{c2} as a function of temperature for a C fiber coated with Mo_3Sb_7. The solid line is a fit to equation (3.2).

The resistive superconducting transition shifts to the lower field with the increase in the temperature. The onset magnetic field decreases and the superconducting transition is absent at 10 K. Figures 3.32 and 3.33 show the H_{c2}-T phase diagram obtained from the ρ vs. H curves at various temperatures. Here, H_{c2} is defined as the midpoint of the transition with error bar ± 0.5 T. The upper critical field at zero temperature, $H_{c2}(0)$, was estimated by fitting the data to equation (2) for each compound. $H_{c2}(0)$ and the superconducting coherence lengths $\xi(0)$ are found to be 9

T and 60 Å for Mo_3Sb_7 and 9.5 T and 58 Å for MoN. Since ξ is much less than the Mo_3Sb_7 coating, the superconducting layers are essentially in the finite thickness limit.

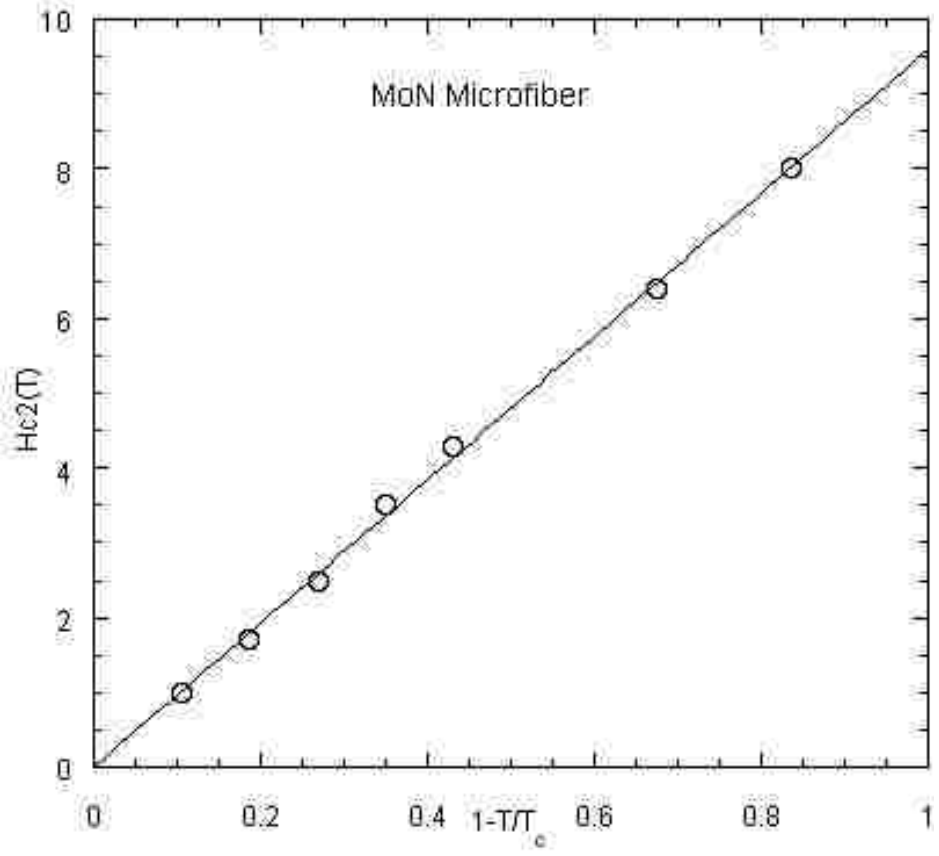

Fig: 3.33 Upper critical field H_{c2} as a function of temperature for a C fiber coated with MoN. The solid line is fit to equation (3.22).

$H_{c2}(0)$ for Mo_3Sb_7 coated fiber is slightly smaller than that for Mo_3Sb_7 thin film and 3 T less than that for the wire. On other hand $H_{c2}(0)$ for MoN coated fiber is slightly higher than that for MoN thin film, while it is more than 3 T higher than that for MoN wire.

A set of typical I-V curves of the Mo_3Sb_7 coated fiber in zero field, where the boxcar integrator output is plotted as a function of the current pulse magnitude at T = 5.8, 5.5, 5.2, 5, 4.8, 4.5, 4.3, 4, 3.5, 3, and 2.5 K, is shown in Figure 3.34. Similarly, Figure 3.35 shows the I-V plot of a MoN coated fiber in zero field at T = 12, 11.8, 11.6, 11.4, 11.2, 11, 10.8, 10.7, 10.6, and 10.5 K.

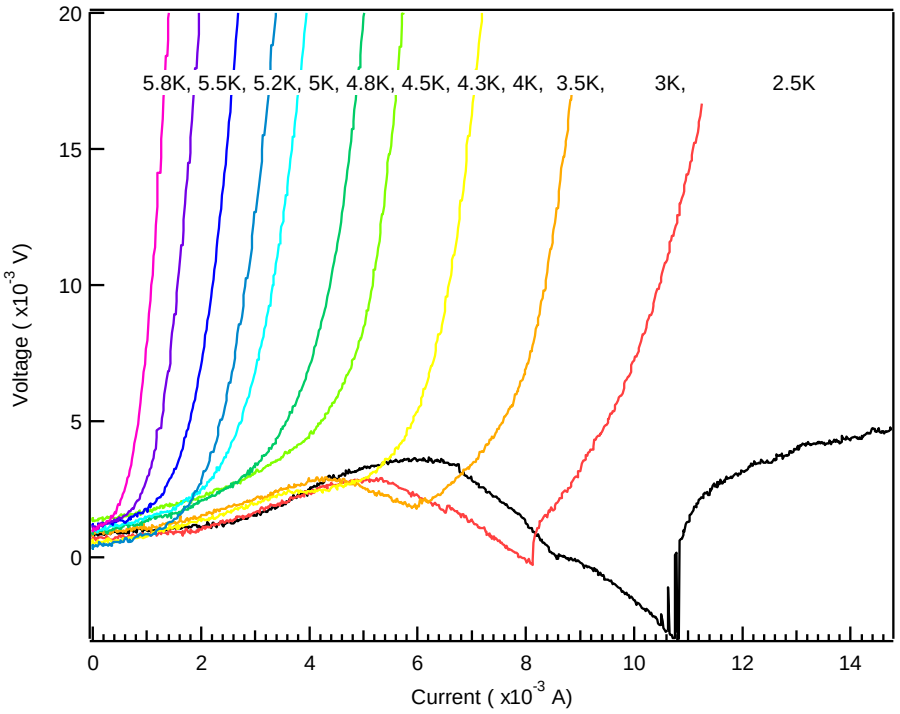

Fig: 3.34 Typical I-V characterstics of a Mo_3Sb_7 coated C fiber in zero field, where the boxcar integrator output is plotted as a function of the current pulse magnitude.

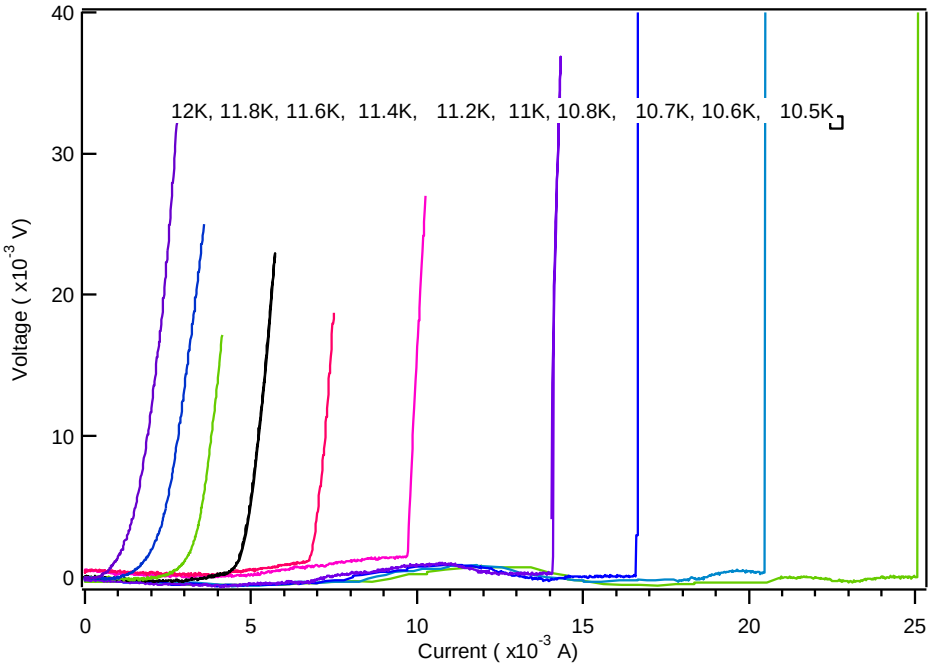

Fig: 3.35 Typical I-V characterstics of a MoN coated C fiber in zero field, where the boxcar integrator output is plotted as a function of the current pulse magnitude.

Critical current measurements were limited to the temperatures above 10.5 K in MoN fibers due to both the limitation of the electronics and the risk of damaging the samples. For the Mo_3Sb_7 fiber data were obtained down to 2.5 K without destroying the fiber. It can be seen from the *I(V)* data that the transitions from the superconducting state (i.e. zero voltage) to the normal state are very sharp at lower temperature, while near T_c the transitions are broad. Here, the critical current threshold I_c is defined as the intersection of the linear extrapolation of the most rapidly changing part of *V(I)* and that of the superconducting state.

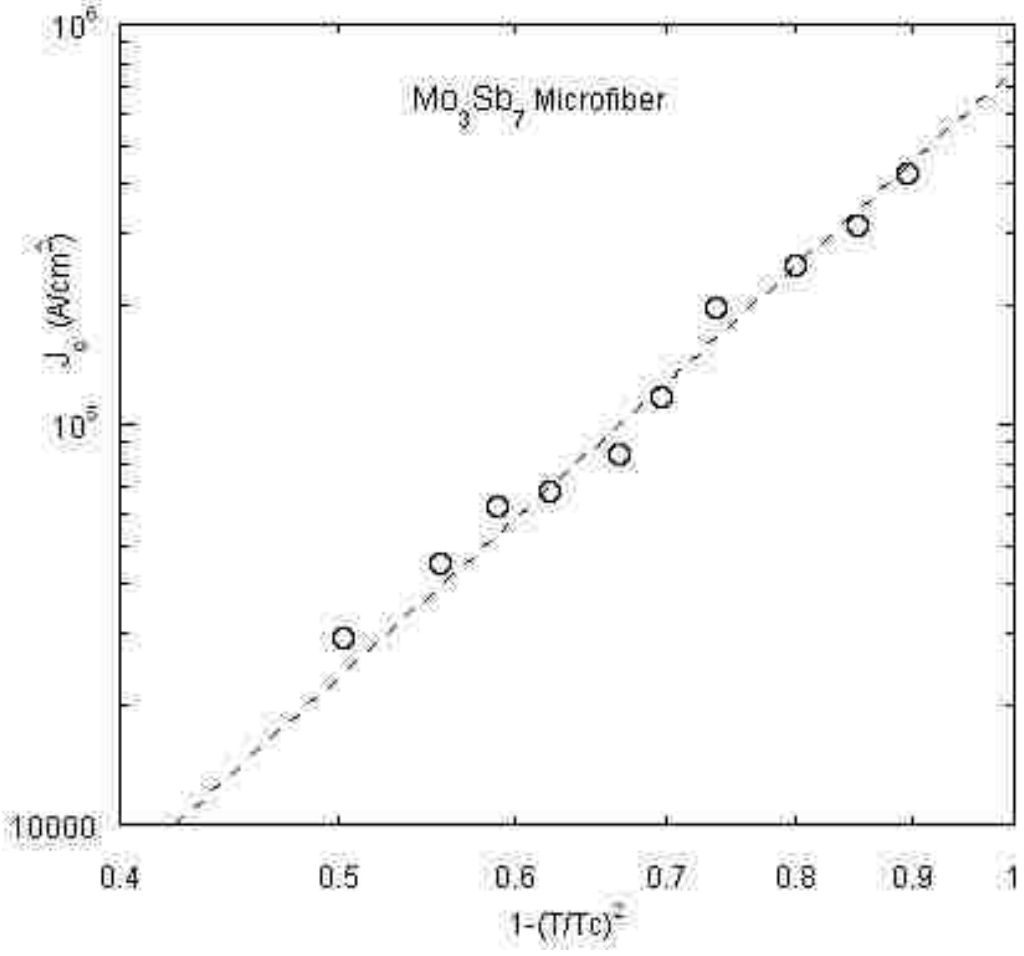

Fig: 3.36 Log-log plot of the critical current density in zero magnetic field for a Mo_3Sb_7 coated fiber. The dotted line is provided as a guide to the eye and extrapolates to a zero temperature density $J_c(0) = 7.7 \times 10^5$ A/cm^2.

The critical current density, J_c , was calculated from I_c by dividing it by the cross sectional area of the Mo_3Sb_7- or MoN-coating in the fibers. The cross-sectional area of the coating was calculated from the difference of the cross-sectional area the fiber after the reaction and that of the carbon core in the fiber provided by the company.

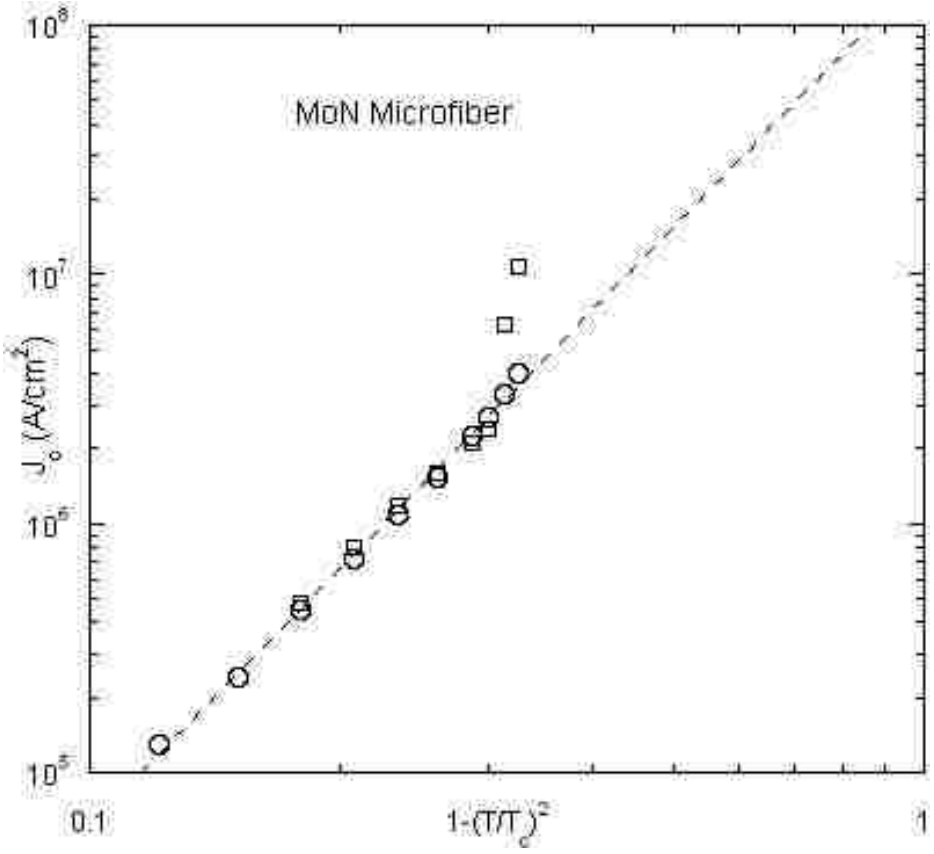

Fig: 3.37 Log-log plot of the critical current density in zero magnetic field for two different samples of MoN coated fiber. The dotted line is provided as a guide to the eye and extrapolates to a zero temperature density $J_c(0) = 1.66 \times 10^8$ A/cm^2.

Figures 3.36 and 3.37 present a log–log plot of the critical current density(J_c) in zero magnetic field as a function of reduced temperature for Mo3Sb_7- and MoN-coated fibers. Care was taken to reduce the pulse width and duty cycle to the point were no hysteresis was observed across the critical current threshold. The dashed lines in Figures 3.36 and 3.37 are provided as a guide to the eye which follows the Ginzburg-Landau (G-L) critical current behavior for a superconductor with a homogeneous order parameter [12].

The Ginzburg-Landau (G-L) equation is as follows:

$$J_c = \frac{H_c(T)}{3\sqrt{6}\pi\lambda(T)} \propto [1-(T/T_c)^2]^{3/2} \qquad \text{.....(3.3)}$$

where H_c is the thermodynamic critical field and λ is the London penetration depth. Though both systems exhibited the expected 3/2 scaling behavior, the critical current densities in the Mo_3Sb_7 microfibers were roughly an order of magnitude lower than that of the MoN fibers. The critical fields were lower too. The Mo_3sb_7 coatings may not be as homogeneous as the MoN coatings. Whether or not this is an intrinsic property of Mo_3Sb_7 remains unclear. Obviously, cracks and grain boundaries can undermine the maximum critical current density, but the fact that the data agree well with Equation 3.3 suggests that the low critical current density of the Mo_3Sb_7 is an intrinsic property.

Interestingly, upon lowering the temperature below 10 K, we observed a precipitous upturn in the critical current density of all the MoN microfibers, suggesting a possible phase transition.

3.4.5 Series of Mo_3Sb_7 Wires

Figure 3.38 shows the resistive superconducting transitions of a series of samples of Mo_3Sb_7 with Mo wires of 70 μm in diameter at the same temperature (900 ^oC) and period (30 minutes), but with different amounts of Sb. Synthesis of samples A, B, C, D, E, F, and G were done using 0.75, 0.36, 0.25, 0.16, 0.044, 0.029, and 0 g of Sb using Mo wire of equal mass in each experiment. The superconducting transition temperature, T_c, and the transition width ΔT_c changed with the amount of Sb used. The sharp transition at 2.1 K can be seen for sample A, which is from the experiment with the highest amount of Sb. This agrees with T_c observed in bulk Mo_3Sb_7. Then the transition broadens for the samples from the experiment with lower

amount of Sb. A sharp transition at highest temperature ~ 7.8 K is observed for sample F, reacted with the lowest amount of Sb.

The calculated required mass of stoichiometric Mo_3Sb_7 is smaller than 0.029 g which was used to synthesis sample F. We tried to explain the variation in the result of experiment with the amount of Sb used during the synthesis in terms of the vapor pressure and the number of molecules per unit volume of Sb, but the analysis remained inconclusive [49].

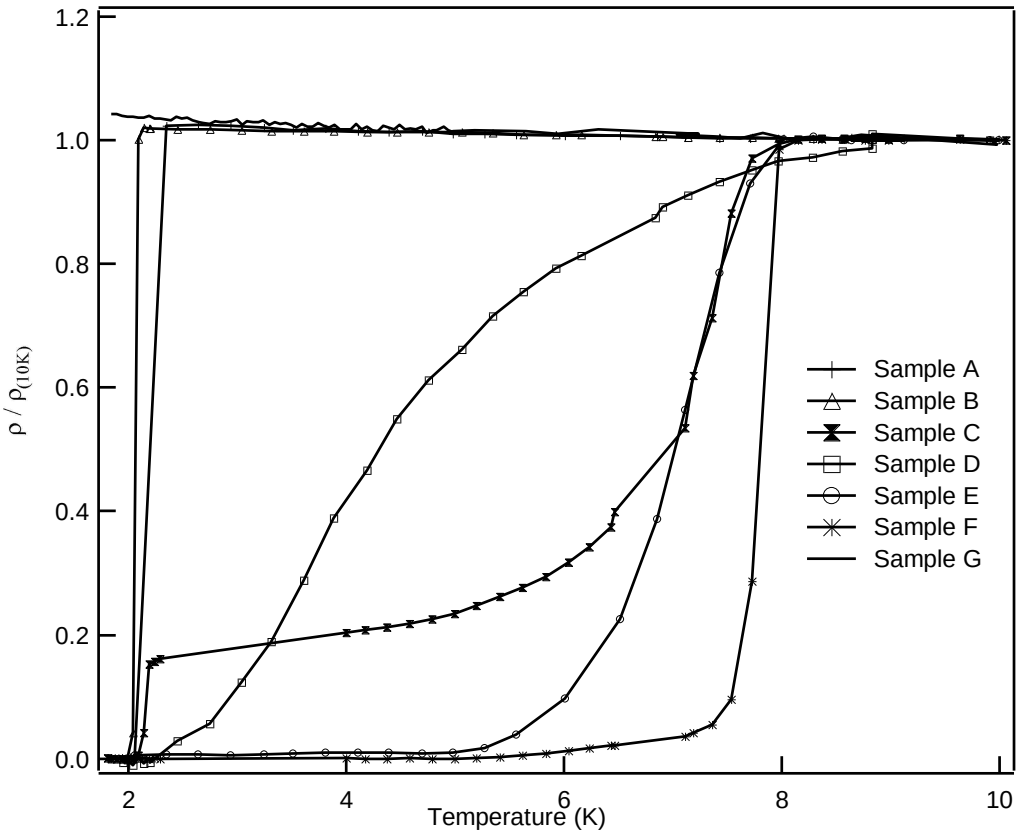

Fig: 3.38 The superconducting transition temperature of the Mo_3Sb_7 wire changes with the amount of Sb used during the synthesis of Mo wires of 70μm in diameter.

3.4.6 Magnetic Susceptibility of Mo_3Sb_7 Wires

Figure 3.39 shows the temperature dependence of the magnetic susceptibility measured in an applied magnetic field of 1 T for the Mo_3Sb_7 wires. A plastic capsule packed with a bunch of

pieces of reacted wires of 70 μm in diameter was attached to the ACMS holder with the help of a plastic straw. Both the capsule and the straw have negligible magnetic background. Low temperature resistivity data shows that sample A, which was synthesized using a lot of Sb, has T_c ~ 2.3 K and sample B, which was synthesized using little Sb, has T_c ~ 7 K. The lower Tc is consistent with the values observed in polycrystalline and single crystal Mo_3Sb_7 [8, 9].

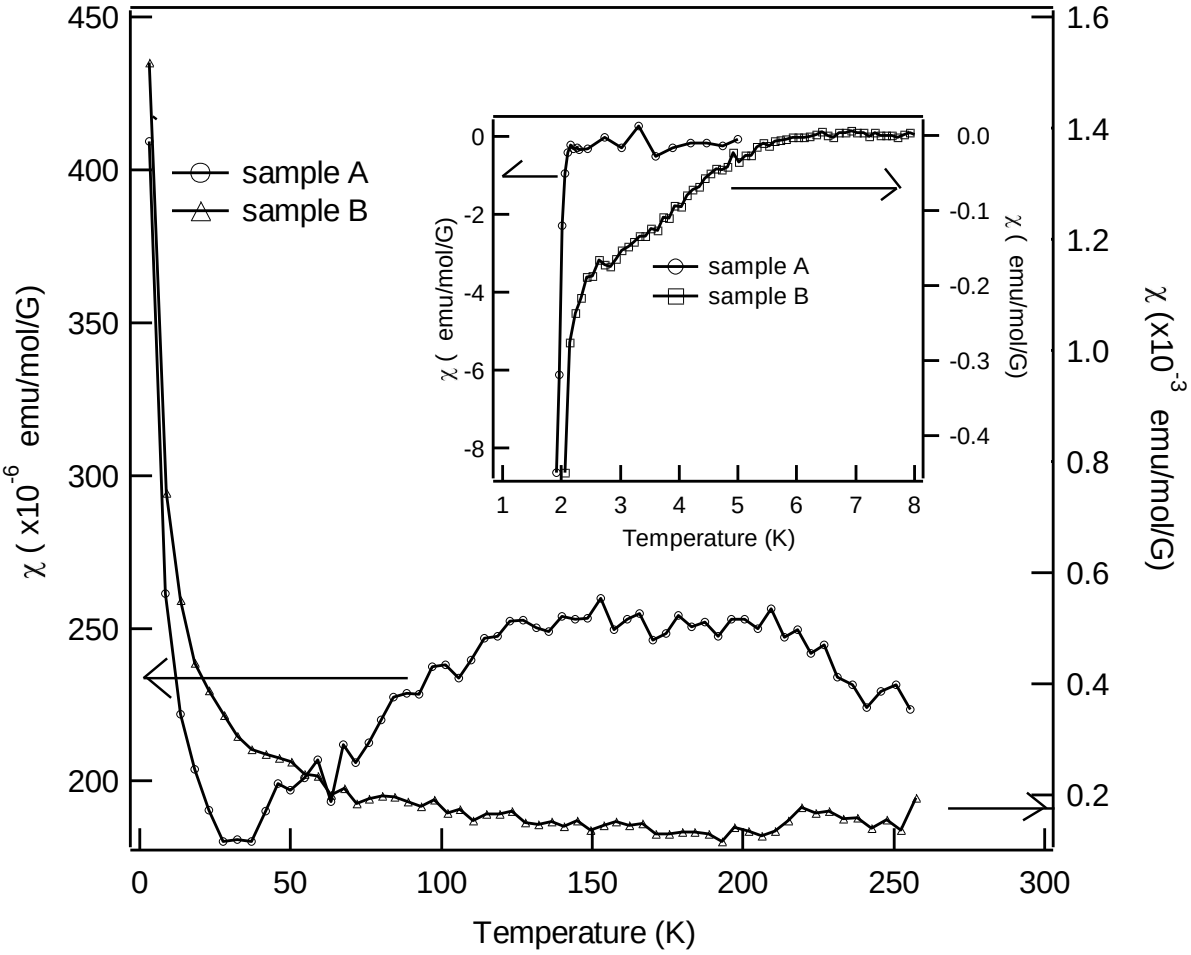

Fig: 3.39 Magnetic susceptibility as a function of temperature in an applied magnetic field of 1 T for the Mo_3Sb_7 wires (sample A (left) and sample B (right)). Inset: Superconducting transition in susceptibility vs. the temperature in an applied magnetic field of 20G in Mo_3Sb_7 wires, where sample A has Tc ~ 2.1 K (left) and sample B has Tc ~ 6 K (right).

In the inset of Figure 3.39, the superconducting transitions in the temperature dependence susceptibility (ZFC) data at an applied field of 20 Gauss for both samples, are shown. As the

wires are fragile, they cannot be packed tightly in the capsule which produced some noise in data. The temperature dependence of the susceptibility in the applied magnetic field of 1 T has an interesting feature. The susceptibility of sample A displays a parabolic dependence at low temperature, then increases with temperatures, becoming maximum around 180 K, and then obeying a Curie-Weiss law at higher temperature. The same feature was reported in the polycrystalline sample of Mo_3Sb_7 by Candolfi et al in [9], which has been considered as a strong evidence to consider Mo_3Sb_7 as a spin fluctuation system. The parabolic dependence of the magnetic susceptibility at low temperature was also noticed in the spin fluctuation system UAl_2 [27]. The value of the magnetic susceptibility at room temperature is 225 x 10^{-6} emu/mol. This is in good agreement with that measured by Bukowski *et al.* for the single crystal [8], but it is 2 times lower than the values reported by Candolfi *et al*. and Hulliger for polycrystalline samples [9, 17].

A more striking result is obtained in the measurement of the temperature dependence of the magnetic susceptibility in sample B at a magnetic field of 1 T. Here, the parabolic dependence at low temperature is absent in this sample. It is paramagnetic with a value of susceptibility slightly lower than the values observed for sample A. Both samples have sharp tails at low temperature which could be a Curie tail due to impurities. From the result of SEM and EDX, it can be seen that the wires are not reacted throughout the sample. There is a small amount of Mo in the core of wires. This clearly indicates the contribution of Mo impurities in the susceptibility of the samples.

I performed a lot of experiments on Mo_3Sb_7 wires with P, As, Se, Te, and S to investigate the effect of doping, but none of the results are better than pure Mo_3sb_7. The partial substitution for Mo by Cr and W also did not improve the superconducting properties.

3.5 Conclusions

I reported on the synthesis of Mo_3Sb_7 and MoN in the form of wires, thin films and coatings on microfibers and their characterization via electric transport, magneto-transport and magnetization properties measurements. The superconducting properties of both compounds were optimized by exposing the wires, thin films and carbon microfibers of Mo to either ammonia gas or antimony vapor at various temperatures for different time periods. Scanning electron micrographs and powder x-ray diffraction analysis verified the Ir_3Ge_7 type structure (space group Im3m) of Mo_3Sb_7 and the hexagonal δ-MoN phase.

The Mo_3Sb_7 wire, obtained by the heat treatment of Mo wire of 70 μm in diameter at 900 ^oC for 30 minutes with a lot of Sb, shows the superconducting transition around 2.2 K . This is consistent with the superconducting transitions observed in single crystal and polycrystalline samples of Mo_3Sb_7 reported by different groups [8, 9, 26]. Surprisingly, for Mo_3Sb_7 wire of same diameter treated at same temperature and period, but with a little amount of Sb has a superconducting transition temperature T_c ~ 8 K, which is almost a factor of four higher than the value of the former sample and that reported for the single crystal and powder of Mo_3Sb_7 [8,9,26]. This result is consistent with the T_c ~ 8.05 K of Mo_3Sb_7 thin wire of 13 μm in diameter, obtained by the heat treatment at 900 ^oC for 1h and 20 minutes. This sample has the upper critical field $H_{c2}(0)$ ~ 11.3 T, which is substantially higher than the 1.72 T of single crystal and powder samples [8,9,26]. The Mo_3Sb_7 thin films and coating on C fibers also exhibit superconducting transitions around ~ 8.2 and 7.8 K, respectively. The upper critical fields $H_{c2}(0)$ are also close to the 11.3 T of the Mo_3Sb_7 thin wire. This suggests that contamination (for example C, W, Si etc.) was not a significant factor in determining the high T_c's of the samples. To the best of my knowledge this is the first report on a study of Mo_3Sb_7 in the form of wires,

thin films and coating on microfibers. The anomalously high T_c and $H_{c2}(0)$ of Mo_3Sb_7 is also a new discovery in this system.

I believe that the enhanced T_c's observed in the wires, microfibers and films is due to the suppression of spin fluctuations. There is a speculation that the relatively low 2.1 K transition temperature of the bulk Mo_3Sb_7 is a result of the attenuating effects of strong spin fluctuations and that the "bare" transition temperature is near 10 K [9]. This speculation is strongly supported by the absence of the parabolic dependence of the magnetic susceptibility at lower temperature in the sample with higher T_c. The parabolic dependence was clearly observed in the $\chi(T)$ curve of my sample with lower T_c and also in the report on the powder of Mo_3Sb_7 by Candolfi et al [9]. The suppression of spin fluctuations in the Mo_3Sb_7 wires, thin film and fibers could be a stress effect. There is, in fact, a factor of four expansion associated with the antimony reaction, which can, in principle, produce large internal stresses, especially in a thin film geometry. In this scenario, stress may act to suppress the spin fluctuation amplitude thus resulting in a higher T_c. If this is, indeed, the case, then one would expect the superconducting phase of Mo_3Sb_7 to be pressure sensitive. Clearly, the pressure dependence of T_c in Mo_3Sb_7 should be measured and correlated with its normal state magnetic susceptibility.

A novel synthesis route for δ-MoN in the form of wires, thin films and coating in microfibers were developed. The sample of MoN wire, exhibiting the $T_c \sim 13.2$ K slightly higher than the highest T_c reported by Saur *et al*, was obtained by heat treatment for a very short period. To our knowledge the H_{c2} has never been reported in MoN in any form.

For the first time the magnetotransport and critical current measurements of MoN- and Mo_3Sb_7-coated carbon microfibers are reported. The transition temperatures of the micro-fibers are comparable to that of wires and thin films of respective compounds.

The Mo_3Sb_7 microfibers, however, exhibited transition temperatures that were almost a factor of four higher than reported in powder samples. The critical current density of the MoN fibers was well described by Equation 3 down to 10 K but increased much faster than $(1 - (T/Tc)^2)^{3/2}$ at lower temperatures. The extrapolated value of Critical current density for MoN-coated fiber is $J_c(0) = 1.66 \times 10^8$ A/cm^2. In contrast, the critical current density of the Mo_3Sb_7 fibers is $J_c(0) = 7.7 \times 10^5$ A/cm^2 , which is anomalously low .

Of course, further study is needed to settle the issue of anomalously high T_c observed in Mo_3Sb_7.

3.6 References

[1] Muller J 1980 *Rep. Prog. Phys*. **43** 41

[2] Inumaru K, Baba K, Yamanaka S 2006 *Physical Review B* **73** 052504

[3] Bull C L, McMillan P F, Soignard E , and Leinenweber K 2004 *J. Solid State Chem.* **177**, 1488

[4] Matthias B T, Hulm J K 1952 *Phys. Rev.* **87** 799

[5] Papaconstantopoulos D A, Pickett W E, Klein B M, Boyer L L 1985 *Phys. Rev. B* **31** 752

[6] Jehn H, Ettmayer P 1978 *J. Less-Common Met.* **58** 85

[7] Ihara H, Hirabayashi M, Senzaki K, Kimura Y, Kezuka H 1985 *Phys. Rev. B* 32 1816

[8] Bukowski Z, Badurski D, Stepien-Damm J, Troc R 2002 *Solid State Commun.* **123** 283

[9] Candolfi C, Lenoir B, Dauscher A, Bellouard C, Hejtmanek J, Santava E, Tobola *J Phys. Rev. Lett.* **99** 037006

[10] He T, Huang Q, Ramirez A P, Wang Y, Regan K A, Rogado N, Hayward M A, Haas M K, Slusky J S, Inumara K, Zandbergen H W, Ong N P, Cava R J 2001 *Nature* **411** 54

[11] Young D P, Moldovan M, Adams P W 2004 *Phys. Rev. B* 70 064508

[12] Tinkam M Introduction to Superconductivity (McGraw-Hill, New York, 1996)

[13] J.W. Composites, LC, 420 South 500 West, Salt Lake City, UT 84101

[14] Massalski T B 1986 *Binary Alloy Phase Diagrams, first ed. American Society for Metals* 1628

[15] Brown A 1965 *Nature* **206** 502

[16] Jensen P, Kjekshus A, Scansen T 1966 *Acta Chem. Scand.* **20** 403

[17] Hulliger F 1966 *Nature* **209** 500

[18] Jensen P, Kjekshus A 1967 *J. Less-Common Metals* **13** 357

[19] Jensen P, Kjekshus A, Scansen T 1969 *J. Less-Common Metals* **17** 455

[20] Furuseth S, Kjekshus A 1966 *Acta Chem. Scand.* **20** 246

[21] Klein M, von Schnering H G 1966 *J. Less-Common Metals* **11** 298

[22] Raub Ch J, Zachariasen W H, Geballe T H, Matthias B T 1963 *J. Phys. Chem. Solids* **24** 1093

[23] Chakoumakos B C, Mandrus D 1998 *J. Alloys Compd* **281** 157

[24] Jensen P, Kjekshus A 1966 *Acta Chem. Scand.* **20** 417

[25] Mart P L, Murray J J, Taylor J B 1979 *J. Less-Common Metals* **65** 71

[26] Dmitriev V M, Rybaltchenko L F, Ishchenko L A, Khristenko E V, Bukowski Z, Rroc R 2006 *Superconductor Science and Technology* **19** 573-576

[27] Trainor R J, Brodsky M B, Culbert H V 1975 *Physical Review Letter* **34** 1019

[28] Beal-Monod M T, Ma S K, Fredkin D R 1968 *Physical Review Letter* **20** 929

[29] Wada H, Shimamura N, Shiga M 1993 *Physical review B* **48** 10221

[30] Inumaru K, Baba K, Yamanaka S 2005 *Chem. Mater.* **17** 5935-5940

[31] Li S Y *et al* 2001 *Phys. Rev. B* **64** 132505

[32] Andrzejewski B, Klimczuk T, Cava R J 2007 *Physica C* **460-462** 706-707

[33] Sahu B R, Kleinman L 2004 *Physical Review B* **70** 073103

[34] Perdew J P, Wang Y 1992 *Phys. Rev. B* **45**, 13 244

[35] Perdew J P, Burke K, Ernzerhof M 1996 *Phys. Rev. Lett.* **77** 3865

[36] Linker G, Smithey R, Meyer O 1984 *Journal of Physics F* **14** L115

[37] Saur E J, Schechinger H D, Rinderer 1981 *IEEE Transactions on Magnetics* **MAG-17** 1

[38] Candolfi C *et al*. (to be published)

[39] Linker G, Meyer O 1976 *Solid state communication* **20** 695

[40] Linker G 1982 *Ion Implantation into Metals ed.* V Ashworth *et al* (Oxford: Pergamon) 284

[41] You-xiang Z, Shou-an H 1983 *Solid State Comminication* **45** 281

[42] Ettmayer P 1970 *Monatsch. Chem.* **101** 127

[43] Matthias B T, Hulm J K 1952 *Phys. Rev.* **87** 799

[44] Pickett W E, Klein B M, Papaconstantopoulos D A 1981 *Physica B* **107** 667

[45] Ihara H, Kimura Y, Senzaki K, Kezuka H, and Hirabayashi M 1985 *Phys. Rev. B* **31** 3177

[46] Isaev E I, Ahuja R, Simak S I, Lichtenstein A I, Vekilov Y K, Johansson B. Abrikosov 2005 *Physical Review B* **72** 064515

[47] Hansen M 1958 *Constitution of Binary Alloys*, 2nd ed. (MacGraw-Hill, NewYork) 966

[48] Webb A W, Skelton E F, Quadri S B, Franscavilla T L, Onodera A, Suito K 1984 *Bull Am. Phys. Soc.* **29** 484

[49] Roseublatt G M, Birchenall C E 1961 *The Journal of Chemical Physics* **35** 788

CHAPTER 4

$MgCNi_3$ AND DOPED SYSTEMS

4.1 Introduction

The intermetallic $MgCNi_3$ was discovered as an 8 K superconductor by He *et al.* [1] in 2001. The discovery is rather surprising, considering its high Ni content. It has a perovskite structure [1] like that of $CaTiO_3$ with equivalence of Ca to Mg, Ti to C and O to Ni. Its structure is also like that of the 30-K non-cuprate oxide cubic superconductor [1] $Ba_{1-x}K_xBiO_3$. It is found to possess the classical cubic perovskite structure with the space group $Pm3m$ and the lattice constant $a \sim 3.81221$ Å at 295 K [1, 2, 3, 4, 5].

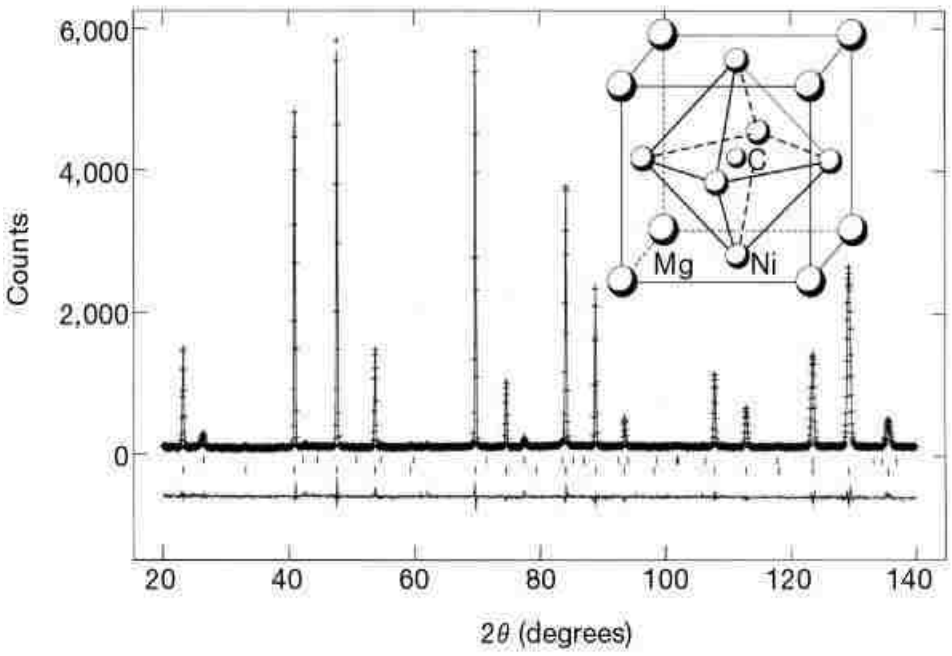

Fig: 4.1 The powder neutron diffraction pattern at ambient temperature for the sample of nominal composition $MgC_{1.25}Ni_3$ and the perovskite crystal structure for the superconducting compound $MgCNi_3$ (inset)[1].

The high proportion of Ni in this compound suggests that magnetic interactions may play a dominant role in the origin of its superconductivity. In fact, the density of states (DOS) in the

vicinity of the Fermi level are dominated by the Ni *d* states [6–11], and though it may not be large enough to induce a magnetic instability [8], it is associated with the superconducting properties [10]. Experimental investigation and theoretical computation reveal that there is a von Hove singularity (vHs) in the DOS just below E_F [12, 11]. The vHs peak gives rise to a large DOS at E_F which can be directly related with the superconducting coupling constant. The single-phase perovskite structure in MgC_xNi_3 is found [13] only in a narrow range of carbon content ($0.88 < x < 1.0$). The band structure calculations [41] indicate that as x decreases in MgC_xNi_3, the proximity to ferromagnetism increases, and increasing spin fluctuations may be responsible for the reduction of *Tc*. The DOS of the components of $MgCNi_3$ along with the total DOS [6] are displayed in Figure 4.2.

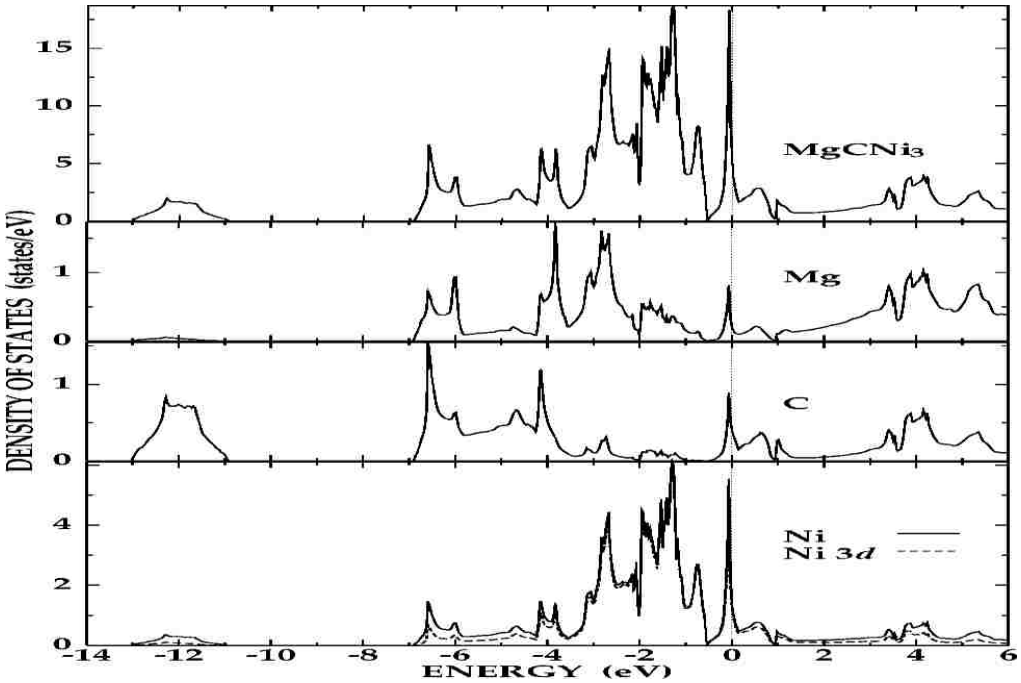

Fig: 4.2 The total and atomic site projected local DOS of $MgCNi_3$ [6].

MgC_xNi_3 samples with x = 0.9–1.5 were prepared by He *et al.* [1] using as raw materials Mg flakes, fine Ni powder and glassy spherical carbon powder. The starting materials were properly mixed and pressed into pellets. The pellets were placed into Ta foil, put in an alumina

boat and fired in a quartz tube furnace in a mixed gas (95% Ar and 5% H_2) environment. The samples were heat treated at 600 ˚C for 1⁄2 h, followed by treatment for 1 h at 900 ˚C. The samples were cooled, ground, pressed and heated at 900 ˚C for one more hour. Owing to the volatility of Mg, 20% in excess of its stoichiometric ratio was added to the initial mixture. The preparation procedures of other groups are almost the same as that of He *et al.* [1].

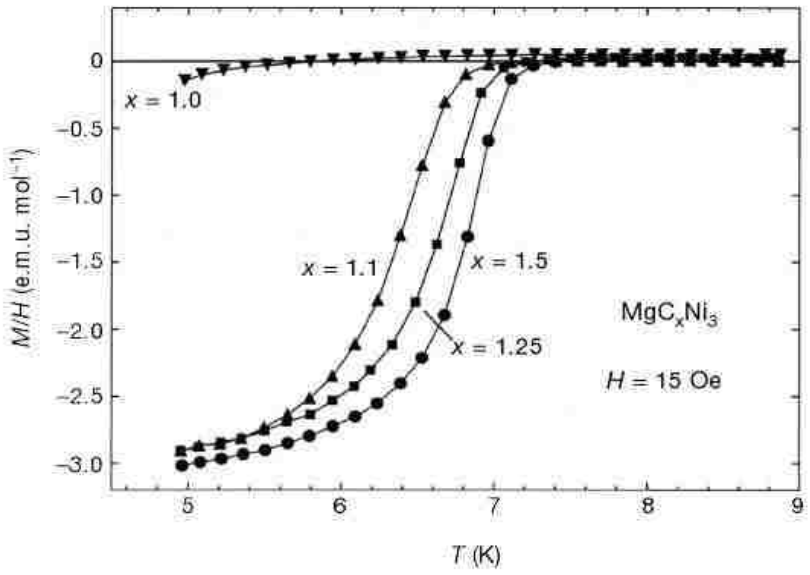

Fig: 4.3 Magnetic characterization of the superconducting transitions for the intermetallic perovskite superconductor of nominal composition MgC_xNi_3. [1]

From neutron diffraction studies, it is found [1, 2] that the formula for the superconducting phase is $MgC_{0.96}Ni_3$ for the nominal composition $MgC_{1.25}Ni_3$. This is due to the small amount of un-reacted graphite found in the sample [1, 2]. The chemically doped samples reported by different groups were also prepared by more or less the same procedure used by He *et al.* [14, 15, 16, 4, 17–22]. So far, there has been only one report on the preparation of $MgCNi_3$ as a thin film [23]. He *et al.* [1] observe the onset of T_c for a sample with nominal composition $MgC_{1.5}Ni_3$ at 8.4 K from resistivity measurements and 7.4 K from magnetization measurements. Differences among the values of T_c derived from resistivity, magnetization and specific heat

measurements are also found by several other groups [24-27]. Different values of T_c being obtained by different techniques is also a well known fact for other intermetallic and oxide superconductors; they mainly depend on the sample homogeneity and transition width.

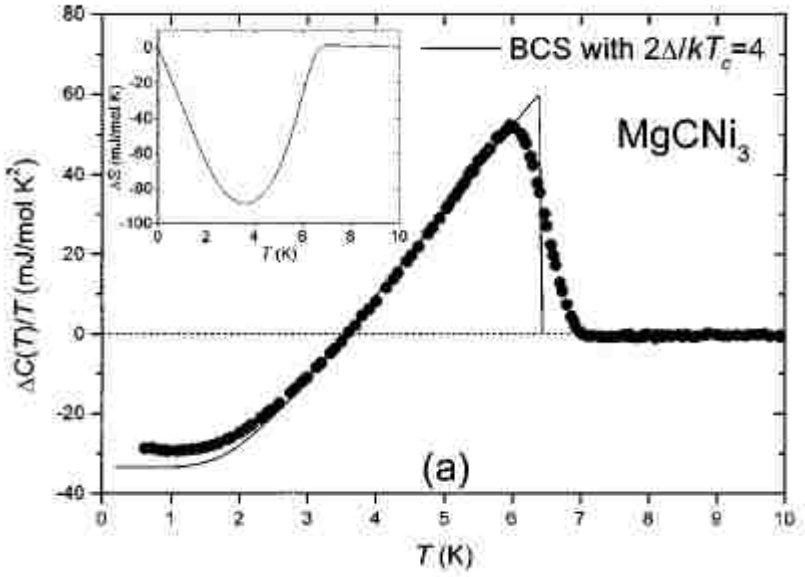

Fig: 4.4 ΔC(T)/T vs T. The data are presented as the solid circles. The solid line is the BCS ΔC(T)/T with 2Δ/kTc=4. The deviation at low temperatures from the solid line is due to the magnetic contribution of a small amount of the paramagnetic centers in the sample. Inset: entropy difference ΔS by integration of ΔC(T)/T according to the data above 3 K and the solid line below 3 K [26].

Young *et al.* [23] report on the T_c of $MgCNi_3$ thin films thicker than ~40 nm have $T_c \sim 8$ K, which is comparable to that of polycrystalline bulk samples. The T_c is found to decrease systematically with decreasing carbon concentration [13] from the stoichiometric value. It is concluded from theoretical calculations that the absence of superconductivity for non-stoichiometric compositions $MgC_{1-x}Ni_3$ is due to the transition of the system to the magnetic state [38]. Excess of Mg and C in the initial material mixture is favorable for improving T_c and for obtaining single-phase samples [1, 15]. The upper critical field $H_{c2}(0)$ of $MgCNi_3$ is determined both from the specific heat (C) and from the resistivity (ρ) data [1, 24, 25, 28, 29, 13, 26, 3, 23, 30, 31, 32 , and 33]. Within the weak-coupling BCS theory, $Hc_2(0)$ can be estimated

using the Werthamer-Halfand-Hohenberg formula, $\mu oHc_2(0) = -0.69\ T_c\ (dHc_2/dT)_{Tc}$ which leads to a $\mu oHc_2(0)$ value of 15.0 T [24]. Taking into accounts the effect of strong coupling, Mao *et al* estimated $Hc_2(0)$ to be around 14.4 T from a reasonable extrapolation [28].

The specific heat (C), a thermodynamic bulk property, of $MgCNi_3$ has been intensely studied by several groups [1, 26, 34, 21, and 32]. The normal state specific heat, $C_n(T) = \gamma_n T + C_{lattice}(T)$, was extracted from H = 8 T data by Lin *et al.* [26] between 4 and 10 K. $C_{lattice}(T) = \beta T^3 + \delta T^5$ represents the phonon contribution, and $\gamma_n T$ the electronic contribution, with γ_n as the coefficient of the electronic specific heat in the normal state. It was found by several groups that γ_n = 9.8–11.2 mJ K^{-2} (mol Ni)$^{-1}$. Both the specific heat jump $C/\gamma_n T_c$ = 1.7–2 at T_c [26] and the quantity $2\Delta/k_B T_c \sim 4.0$, where Δ is the superconducting energy gap, are higher than the BCS weak coupling value ~1.43 and ~3.52, respectively indicating strong electron – phonon coupling. The nuclear spin-lattice relaxation rate $1/^{13}T_1$ exhibits typical behavior for isotropic *s*-wave superconductivity with a coherence peak below T_c = 7.0 K [35]. However, the field dependent specific heat and resistivity results imply that it is a moderate coupling, type II, s-wave BCS superconductor [1, 29, 26, 21, 31, 32]; this is supported by tunneling and other experiments as well as theoretical calculations [36, 4, 6, 8, 37]. Again, the penetration depth distinctly exhibits a non-s-wave BCS low temperature behavior [38], instead of showing quadratic temperature dependence, suggestive of a nodal order parameter. Band calculation by Rosner *et al.* also suggests $MgCNi_3$ is a non s-wave superconductor [11]. Thus the nature of the superconductivity in $MgCNi_3$ is still controversial and needs more effort to clarify it.

The chemical doping experiments are motivated by the unusual band structure of this material. Shein *et al* [10] have shown theoretically the deterioration of the superconducting characteristics of $MgCNi_3$ that occurs upon hole-doping. The decline of the superconductivity upon electron doping ($MgCNi_{3-x}Cu_x$) is due to the filling of anti bonding states and a sharp drop

in the DOS at the Fermi level, $N(E_F)$ [38]. Most groups have doped at the Ni site. However, the effect of doping at the Mg site is also studied [21, 22]. Complete and partial replacement of Mg by Zn was carried out from the nominal compositions $Zn_{1.2}C_{1.3}Ni_3$ and $(MgZn)_{1.2}C_{1.3}Ni_3$, respectively, [21, 22]. Rosner *et al.* [11] have suggested that $MgCNi_3$ is near a ferromagnetic instability that can be reached by hole doping on the Mg site (if 12% Mg is replaced by Na or Li, i.e., 0.04 hole/Ni) and the effective carriers are Ni-derived holes of very high band mass. The Hall coefficient and thermoelectric power data show that the carriers in this superconductor are electrons [24]. The doping at the Ni site with Cu and Co decreases T_c significantly [14, 15]. Doping at the Ni site with Co, Fe, Mn, Cu, etc. also causes a decrease of T_c except for the initial increase with Fe doping [16]. Calculation of the expected electronic DOS suggests that electron (Cu) and hole (Co) doping should have different effects on T_c [14]. However, the T_c of $MgCNi_{3-z}Cu_z$ decreases systematically from 7 to 6 K for $z = 0.1$ [14]. No magnetic ordering was found for $MgCNi_2Co$ and $MgCNiCo_2$ [40]. This indicates that the hole doping does not produce the magnetic instability which could be responsible for pair breaking [39]. Again, no long range magnetic ordering is observed in the magnetic susceptibility of $MgCNi_{3-z}Co_z$ [14]. The detected variation of T_c is explained in terms of the competition between an increase in T_c due to increase in the DOS and a decrease in spin fluctuations [16]. Thus, the review of literature shows that the physics of the origin of superconductivity in this system is complicate and more theoretical and experimental investigations on doping effects may help to settle the controversies.

This chapter focuses on the effect of Li, Be, Ga and La substitution for Mg, and B and N substitution for C on superconducting and normal state properties of $MgCNi_3$. As reported in [40], the magnetic susceptibility measurements show that superconductivity is suppressed slowly with increasing x in $MgC_{1-x}B_xNi_3$. The mixing of carbon and boron on the B site in MgB_2 has a substantial effect on $H_{c2}(T)$. Analogies between the role of B in that compound and C in $MgCNi_3$

persuaded me to have the study of $Hc_2(T)$ in B substituted $MgCNi_3$, but no enhancement in Hc_2 was observed. Data are not shown here due to the null result. Similarly results on Ga and La doping were also not discussed here, as they do not have any influential effect.

The synthesis of $MgCNi_3$ requires an excess of both Mg and C to compensate for Mg evaporation and to ensure carbon incorporation. Therefore, controlled doping of both the Mg site and the C site is difficult, and crystal structure analysis is required to determine the true composition. The reports on synthesis and characterization of $MgCNi_3$, $Mg_{1-x}Be_xCNi_3$, $Mg_{1-x}Li_xCNi_3$ and $MgC_xN_yNi_3$ are presented in the following subsections.

4.2 Synthesis and Characterization

1g of bulk polycrystalline $MgCNi_3$ was prepared with nominal formula $Mg_{1.2}C_{1.5}Ni_3$. The starting materials were powder of Mg (99.8% Alfa Aesar), Ni (999.996% Alfa Aesar), and glassy carbon spherical (Alfa Aesar) or acetylene black carbon. Glassy carbon spherical powder is found to be better in forming hard pellets. The powders were thoroughly mixed and ground well for 10-15 minutes and then pressed into a pellet of 12 mm in diameter. The pellet was placed in an alumina (Al_2O_3) crucible and covered by Ta foil. The sample was heated in a stream of Argon by placing the crucible inside a quartz tube in a horizontal tube furnace. The heat treatment follows the following sequences. First, it was heated at 600 $^{\circ}$C for 30 minutes, which was followed by a treatment for 1 h at 900 $^{\circ}$C. After cooling, the sample was reground, pressed into the pellet and heated at 900 $^{\circ}$C for 90 minutes. Owing to the volatility of Mg, 20% in excess of its stoichiometric ratio was added to the initial mixture.

A series of 1-g samples with compositions $Mg_{1-x}Be_x\ C_{1.5}Ni_3$ (x = 0.01, 0.05, 0.1, 0.15, 0.2, and 1) were prepared with the same procedure explained above. The starting materials were powders of Mg, Be (99+% Alfa Aesar), Ni and glassy carbon. The initial stoichiometry was $(Mg_{1-x}Be_x)_{1.2}C_{1.5}Ni_3$.

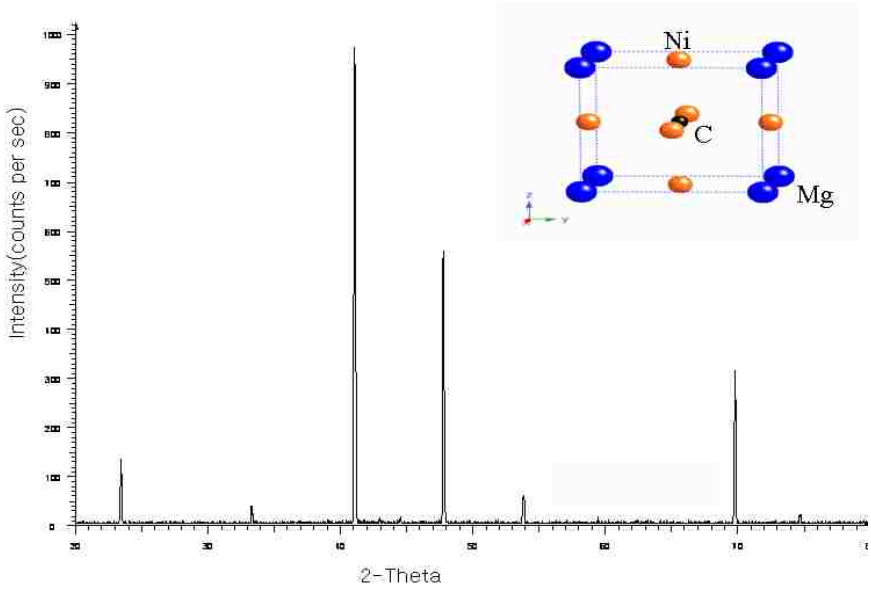

Fig: 4.5 The X-ray diffraction pattern at ambient temperature for the sample of nominal composition $MgC_{1.5}Ni_3$ and the perovskite crystal structure for the superconducting compound $MgCNi_3$ (inset).

Since Li is not available in powder form and oxidized very quickly in air, it was found to be rather difficult to synthesize $Mg_{1-x}Li_xCNi_3$ samples. Various methods and sources of Li have been used to dope Li in this system. We used borothermal reduction as a method using lithium carbonate as a source of Li. The reaction is as follows:

$$1.08\ Mg + 1.56\ C + 3Ni + 0.12\ LiC0_3 \rightarrow (Mg_{0.9}Li_{0.1})_{1.2}C_{1.5}Ni_3 + 0.18\ Co_2$$

So far the following method seems to be better but not the best, I think, to incorporate the Li into the Mg compounds. The powders of all the elements but Li were mixed and ground well. A sandwich of Li metal granules (99.3% Alfa Aesar) with mixed powder of the rest of the starting materials is pressed into a pellet. It should be done very fast before the Li metal gets oxidized. After first stage heating (i.e. at 600 ˚C for 30 min and at 900˚C for 1 h), the pellets were reground and mixed well again. The rest of the synthesis procedure is same as the described above. The resulting samples $Mg_{1-x}Li_x\,C_{1.5}Ni_3$ (x = 0.03, 0.05, 0.1, and 0.2) are hard pellets.

Following the procedure explained earlier, C deficient compounds $Mg_{1.2}C_xNi_3$ (x = 1.5, 1.2, 1, 0.9, and 0.7) were prepared. After having XRD and magnetization measurements, these samples were reground, pressed into the pellets and heated at 900˚C for 2 hours under a flowing atmosphere of N_2.

The structure, phase purity, and peak shift of the prepared samples were analyzed by powder X-ray diffraction using a diffractometer equipped with Cu K_α radiation (λ = 1.54056 Å). Data were collected from 2 θ = 20^o to 80^o with a constant scan speed of 2^o min^{-1} at room temperature.

$MgCNi_3$ and doped samples were characterized by magnetization and transport properties measurement. Samples were mounted directly on the ACMS sample holder, a teflon cup, to measure zero field cooling dc magnetizations in the range of 1.9 - 10 K in the PPMS. Some of the pellets were hard enough to cut into bars (1.5 x 2 x 3 mm^3). The electrical resistivity, magnetorsistance and upper critical field were measured in the range of 2 – 290 K and 0 – 9 T using the standard four probe technique in the PPMS.

4.3 Results and Discussions

4.3.1 $MgCNi_3$

Figure 4.5 shows the x-ray diffraction pattern at ambient temperature for the sample of nominal composition $Mg_{1.2}C_{1.5}Ni_3$ and the perovskite crystal structure for the superconducting compound $MgCNi_3$. The sample is of good quality, with sharp x-ray diffraction peaks. No impurities such as elemental Ni and Mg were observed. From the calculation based on hkl(111) peak the lattice constant was found to be $a \sim 3.80596$ Å which is slightly smaller than the values reported in the literature [1, 2, 3, 4, 5].

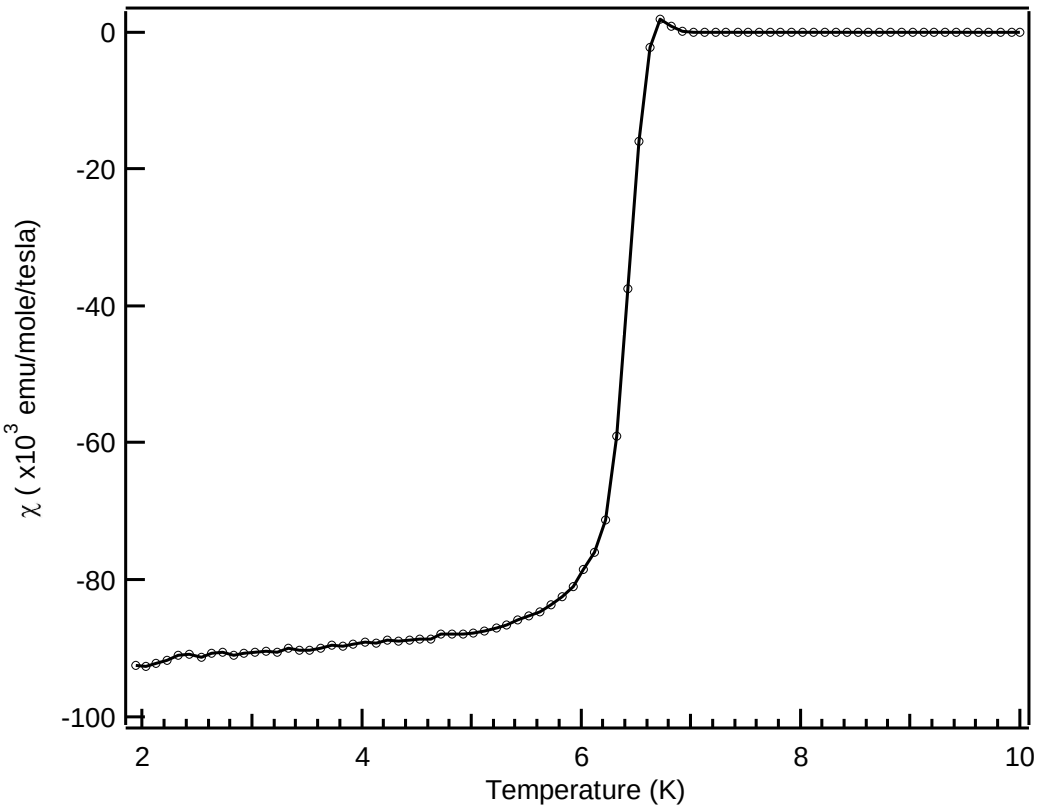

Fig: 4.6 Susceptibility versus temperature for $MgCNi_3$ in an applied magnetic field of 20 Gauss.

Shown in Figure 4.6 is the temperature dependence of zero-field cooling dc magnetization of pristine $MgCNi_3$ measured at a magnetic field of 20 Oe. The superconducting transition is sharp, and the onset transition temperature is 6.7 K.

The resistivity of $MgCNi_3$, measured in between 2 K and 290 K as a function of temperature in zero magnetic field is shown in Figure 4.7. It can be seen that the shape of the R(T) curve presented here is very similar to those reported by He *et al* and Li *et al* [1,24]. The residual resistivity ratio ($RRR = \rho_{(290\ K)} / \rho_{(10\ K)} = 2.4$) is similar to that obtained by He *et al* [1, 24]. However, the magnitude of the resistivity ($\rho_{290\ K} = 1200$ μΩ-cm and $\rho_{10\ K} = 500$ μΩ-cm) obtained in this study is higher than that of [1]. A natural explanation for the high resistivity of the investigated sample, which was not subjected to high-pressure sintering, is a relatively large

resistance of grain boundaries [32]. The conclusion is supported by *Hc2(0)* and T_c values of low-resistivity thin film data (ρ_0 down to 20 μΩ-cm) by Young *et al* [23].

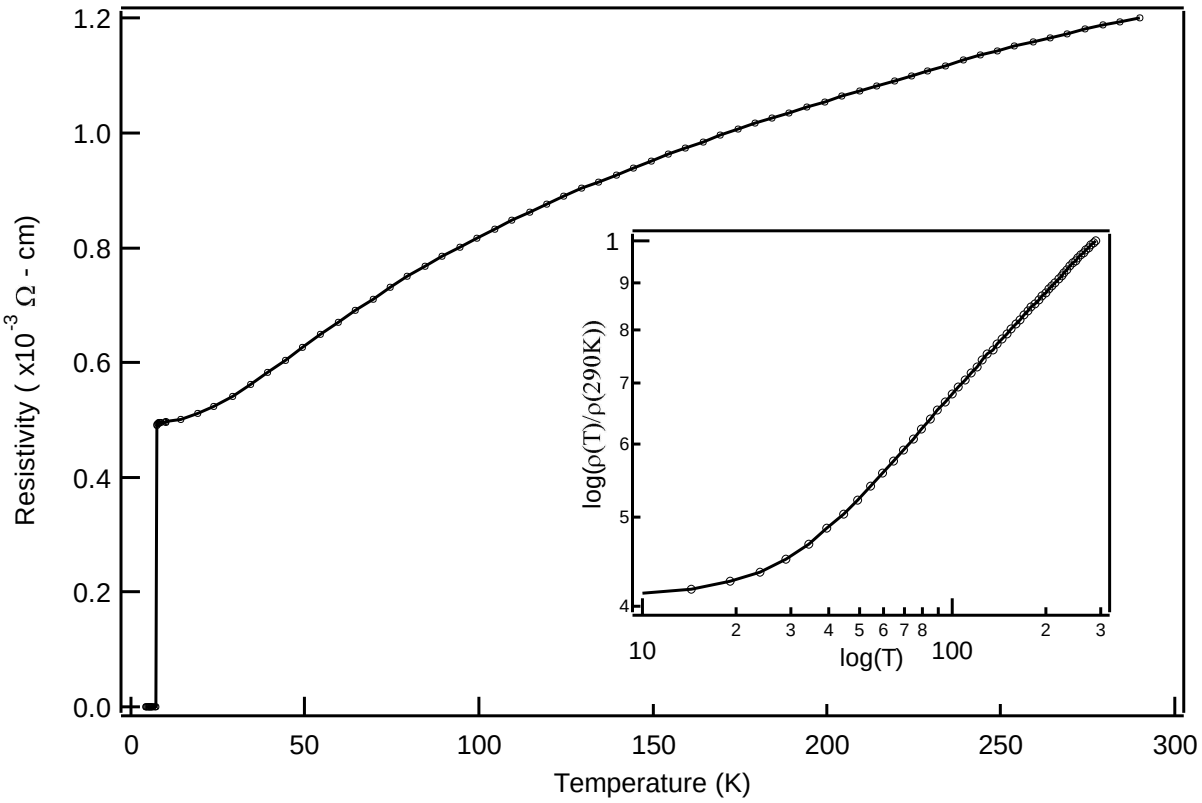

Fig: 4.7 Resistivity of $MgCNi_3$ as a function of temperature. Log-log plot of normal state resistivity as a function of temperature (inset). The solid line is a guide to the eye.

A superconducting transition with an onset (mid) T_c of 7.35 K (7.25) is observed (90-10 % of the transition width ΔT_c = 0.1 K). This is slightly higher than the value obtained from magnetization which we normally find in polycrystalline samples. The upper critical field $H_{c2}(0)$ of $MgCNi_3$ is determined from the resistivity *(ρ)* data at different temperatures. Figure 4.9 presents the magnetic field dependence of resistivity at 4 K, 4.5 K, 5.3 K, 5.8 K, 6.3 K, and 6.7 K. The transition width (ΔH) is fairly small to be considered as sharp transition. Critical field , H_{c2}, is defined as the midpoint of the transitions with error bar ± 0.3 T.

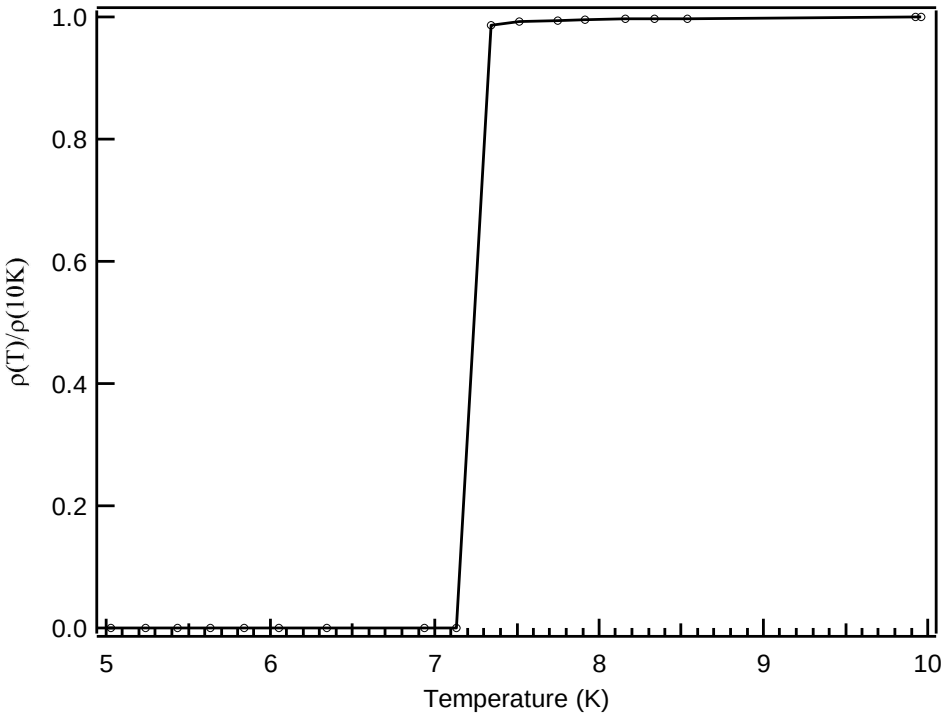

Fig: 4.8 The low temperature resistivity normalized by its normal state value of $MgCNi_3$. The solid line is a guide to the eye.

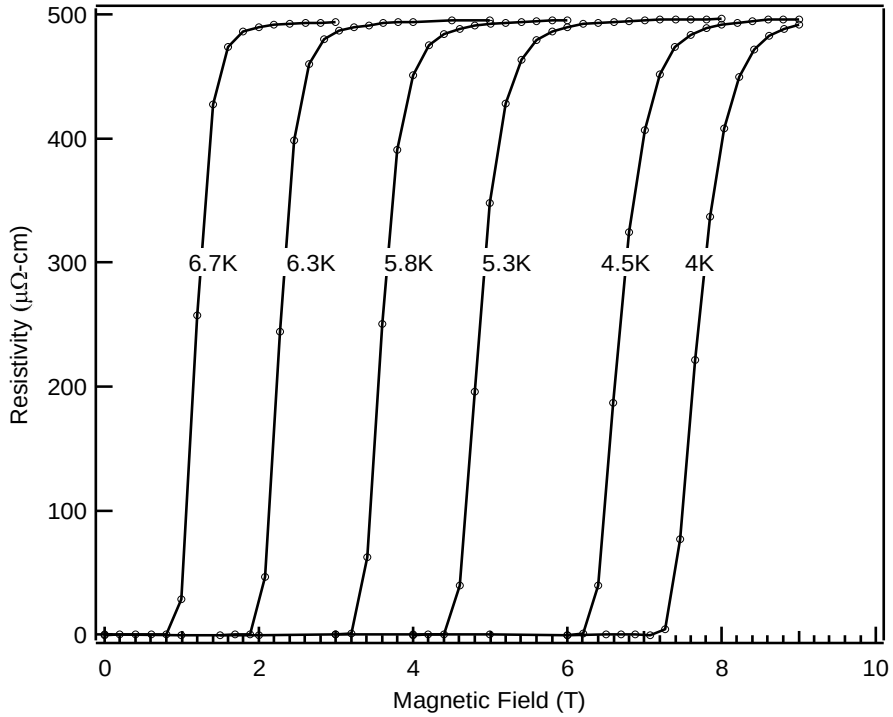

Fig: 4.9 Magnetic field dependence of resistivity of $MgCNi_3$ measured at 4 K, 4.5 K, 5.3 K, 5.8 K, 6.3 K and 6.7 K. The solid lines are guide to the eye.

The temperature dependence of the upper critical field $Hc_2(T)$ with the prediction of BCS theory can be expressed as follows :

$H_{c2}(T) = H_{c2}(0)\,(1-(T/T_c)^2)$ (at low T) ……..…(1)

where $H_{c2}(0)$ is the upper critical field extrapolated to 0 K, and T_c is the superconducting transition temperature in zero applied magnetic field. The solid line in Figure 4.10 represents the best fit of the experimental data to equation 1. The $H_{c2}(T)$ curve, exhibits negative curvature over a wide range of temperature, characteristic of conventional superconductivity [42]. The best fitting resulted in $H_{c2}(0)$ = 11.26 T. This value is below the paramagnetic limit $H_p = 1.84T_c$ = 13 T, suggesting that the Zeeman pair breaking mechanism is ineffective in this case.

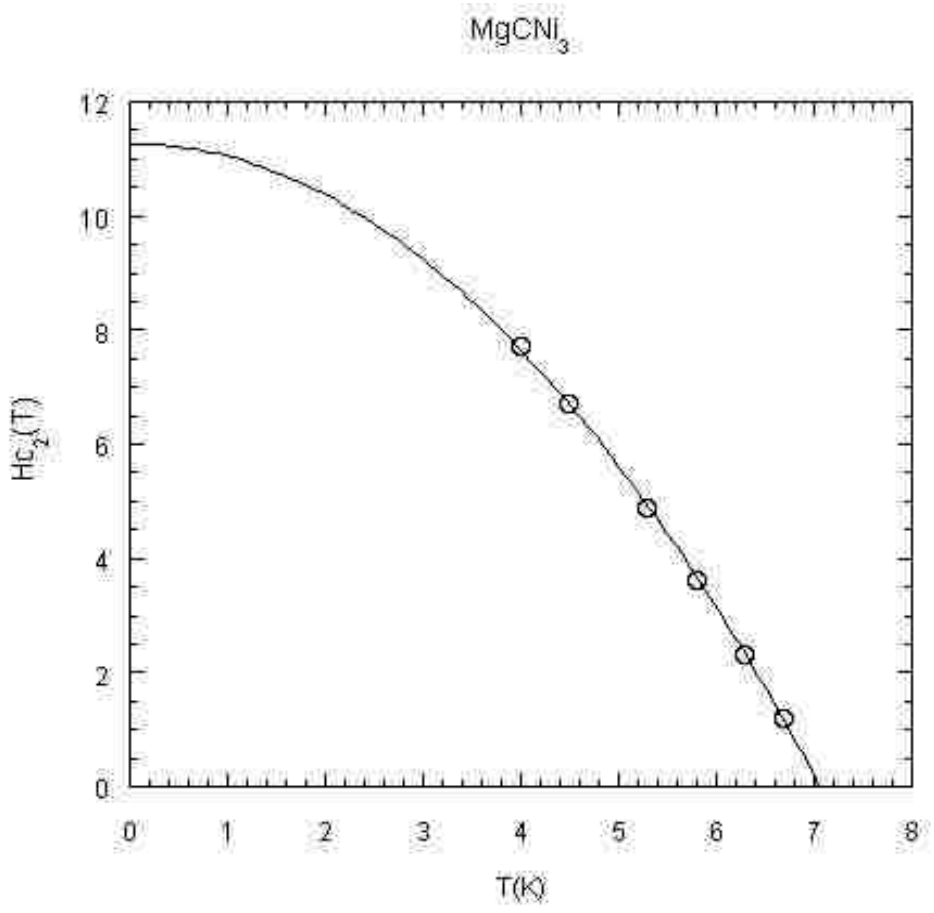

Fig: 4.10 Upper critical field H_{c2} as a function of temperature for $MgCNi_3$. The solid line is fit to the equation (1) and extrapolated to the $H_{c2}(0)$.

4.3.2 $Mg_{1-x}Be_xCNi_3$

Powder x-ray diffraction patterns of $Mg_{1-x}Be_xCNi_3$ for x = 0, 0.01, 0.05, 0.15 and 0.2 are shown in Figure 4.11. All samples reacted to form single cubic phases (a~3.805 ± 0.005 Å). Be substitution on Mg up to 20 % does not change the X-ray diffraction pattern much, but only the positions of diffraction peaks are shifted slightly towards higher angle side on 2θ axis, indicating a decrease in lattice parameters. The lattice parameter shrinks slightly as x increases. This decrease of a with x is consistent with the fact that Be is a smaller ion than Mg. The systematic shift of the peaks in XRD pattern confirms the incorporation of Be into the samples.

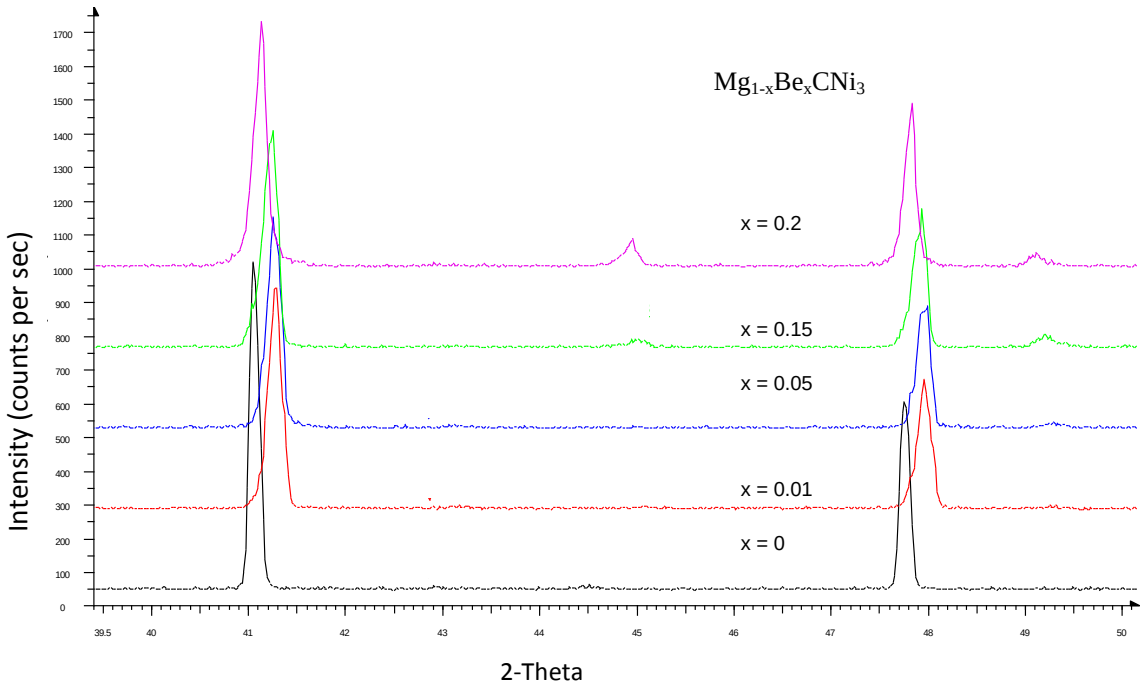

Fig: 4.11 Powder X-ray diffraction pattern of $Mg_{1-x}Be_xCNi_3$ (x = 0, 0.01, 0.03, 0.05, 0.1, 0.15 and 0.2) samples.

For samples with x ≥ 0.15 a few extra peaks which correspond to elemental Ni, are observed. Change in the direction of shifting the position of peaks in $Mg_{0.8}Be_{0.2}CNi_3$ indicates that x = 0.1 is the solubility limit of Be in Mg.

Figure 4.12 shows the temperature dependence of zero-field cooling dc magnetization for typical samples of $Mg_{1-x}Be_xCNi_3$ (x = 0, 0.01, 0.05, 0.1, 0.15 and 0.2) in an applied field of 20 Oe. The transitions for all samples are sharp and larger diamagnetism is observed. The suppression of superconductivity of the system up to 20 % doping concentration is not noticeable. The variation in T_c (ΔT_c) is less than 0.1 K. It is surprising that T_c is so robust, even at 10% Be.

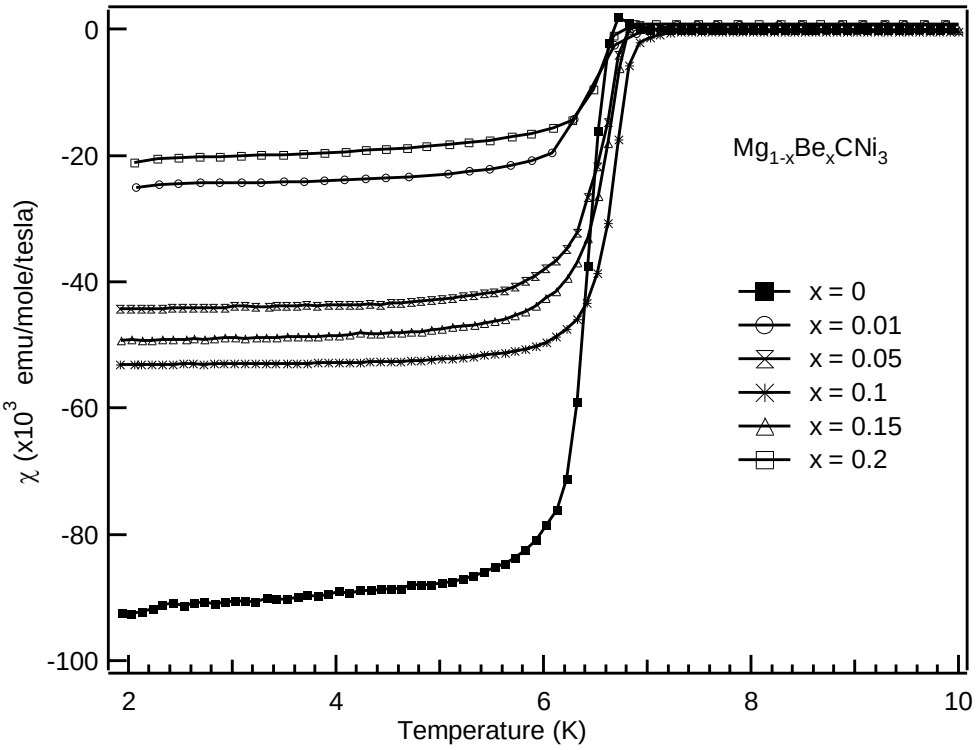

Fig: 4.12 Susceptibility versus temperature for $Mg_{1-x}Be_xCNi_3$ (x = 0, 0.01, 0.03, 0.05, 0.1, 0.15 and 0.2) in an applied magnetic field of 20 Gauss. The solid line is a guide to the eye.

In order to elucidate the magnetic consequences of the Be doping on MgCNi3, the normal state susceptibilities of these materials were measured between 10 K and 300 K. Un-reacted ferromagnetic Ni metal, always present in very small (fractional percentage) amounts in un-doped and doped $MgCNi_3$ powder preparation (no single crystals have yet been reported), complicates the measurement of the normal state magnetic susceptibility [43]. Therefore, to approximate the intrinsic susceptibility of $Mg_{1-x}Be_xCNi_3$ compounds, the difference in

magnetization (ΔM) between the applied fields of 4 T and 2 T was determined at each temperature to estimate the susceptibility ($\chi = \Delta M/\Delta H$) for all samples.

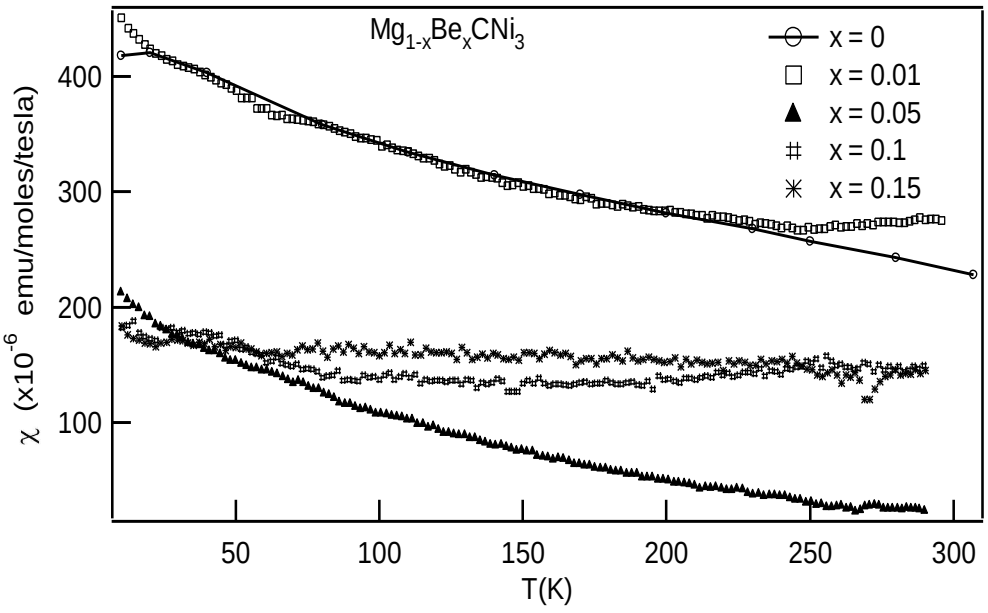

Fig: 4.13 Normal state magnetic susceptibilities of $Mg_{1-x}Be_xCNi_3$ (x = 0,0.01,0.05,0.10, and 0.15).

The susceptibilities derived in such a fashion for representative samples with x = 0, 0.01, 0.05, 0.1, and 0.15 are shown in Figure 4.13 for temperature between 5 K and 290 K. The susceptibilities for lower concentrations of Be, x, increase with decreasing temperature, as previously observed for $MgCNi_3$ [17, 44]. There is substantial decrease in the susceptibility at 10 K for $x \geq 0.05$. The susceptibilities for x = 0.1 and 0.15 are essentially temperature independent (Pauli paramagnetic). The variation of resistivity normalized by its value at room temperature $\rho(T)/\rho(290K)$ with temperature for $Mg_{1-x}Be_xCNi_3$ (x = 0, 0.05, 0.1, and 0.15) is shown in Figure 4.14. It can be seen that no substantial change in shape and magnitude of the $\rho(T)/\rho(290K)$ curves is observed for the entire range of doping. The residual resistivity ratio (*RRR* ~2.4) is almost constant. Though, the resistive superconductive transition temperature (T_c ~ 7.2 K) for

each sample is higher than the one obtained from the magnetization, the variation of T_c with x is less than 0.1 K.

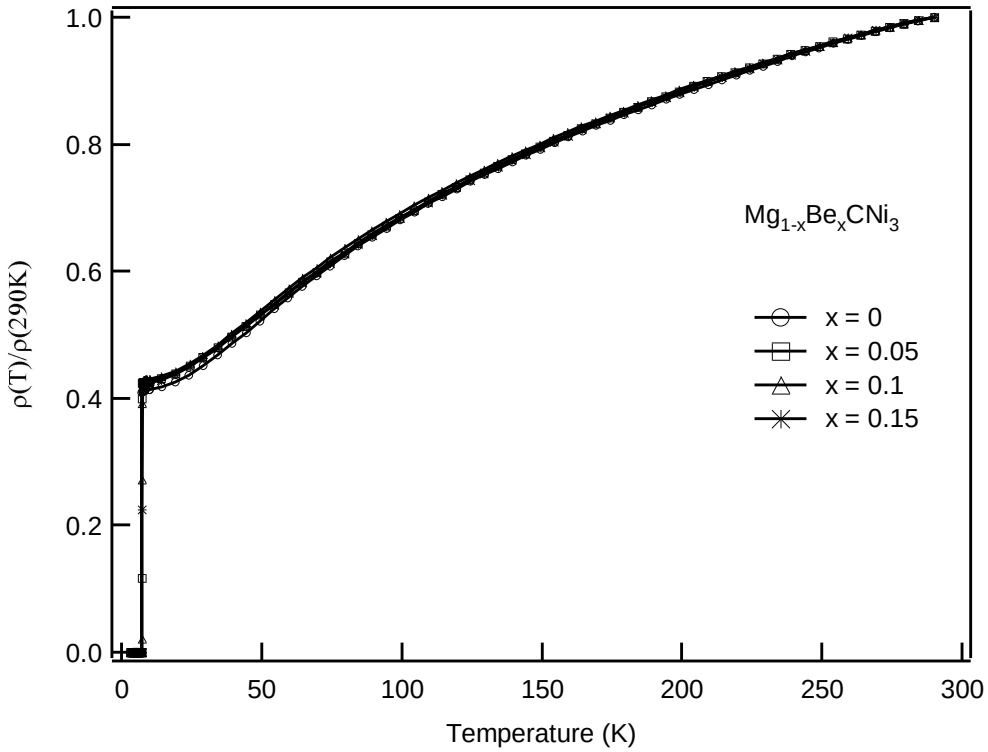

Fig: 4.14 Resistivity of $Mg_{1-x}Be_xCNi_3$ (x = 0, 0.05, 0.1, and 0.15) normalized by its room-temperature value as a function of temperature. The solid line is a guide to the eye.

The behavior of T_c was also tried to be understood by invoking the well known McMillan formula [45] (refined by Allen and Dynes [47])

$$T_c = \frac{\langle\omega\rangle}{1.2} exp\left[\frac{-1.04(1+\lambda)}{\lambda-\mu^*(1+0.62\lambda)}\right], \qquad (2)$$

where $\langle\omega\rangle$ is the average characteristic phonon frequency, μ^* is the effective Coulomb repulsion and $\lambda = N(0)\langle I^2\rangle/M\langle\omega^2\rangle$ denotes the electron-phonon coupling constant, in which N(0) is the density of states (DOS) at the Fermi level E_F, $\langle I^2\rangle$ is the square averaged electronic matrix element for the electron-phonon interaction, M is ionic mass. Since this is an isoelctronic

substitution, assuming $\langle I^2 \rangle$ does not change significantly, the robustness of the T_c can be realized by analyzing how N(0), $\langle \omega \rangle$ and M change under substitution [48].

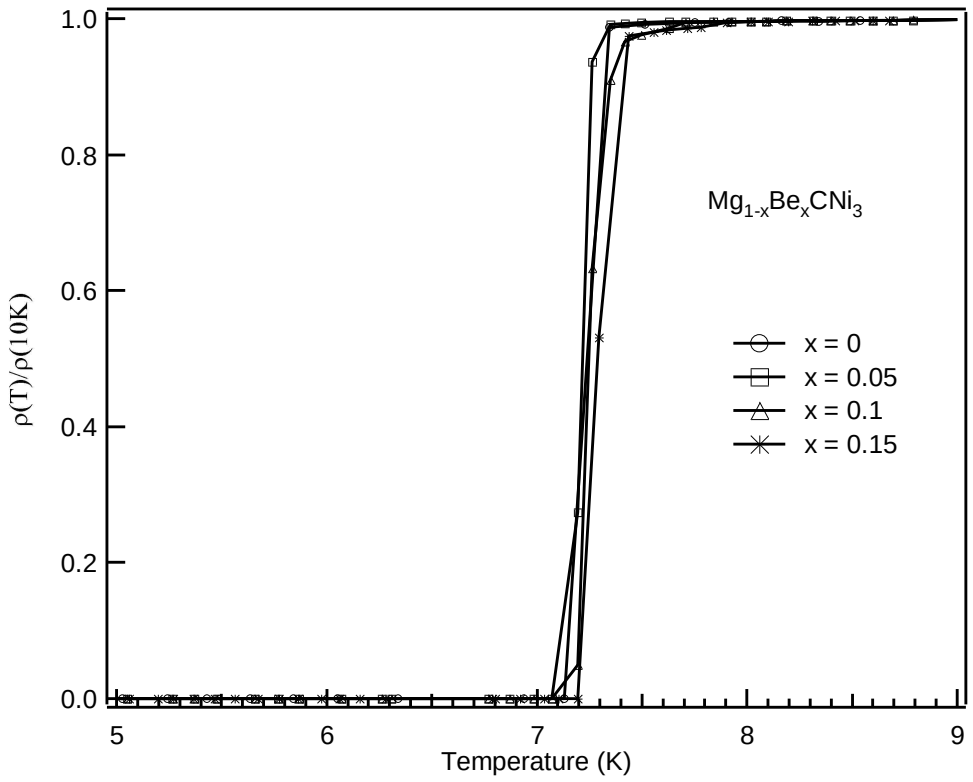

Fig: 4.15 Resistive transitions for $Mg_{1-x}Be_xCNi_3$ (x = 0, 0.05, 0.1, and 0.15).

There will not be a significant increase in $\langle \omega \rangle$ too, as the decrease in lattice volume is very small. On the other hand, M decreases by a factor of ~ 2.7 which causes a decrease in λ. Since behavior of N(0) under Be substitution is not known, we cannot explain if N(0) has the opposite effect on λ to keep T_c constant.

Figure 4.16 presents the magnetic field dependence of resistivity of $Mg_{1-x}Be_xCNi_3$ (x = 0, 0.05, 0.1, and 0.15) at 4 K. Keeping consistent with the result of the magnetic and resistive transitions, no substantial change in the upper critical field is observed due to the Be substitution for Mg. The resistivity measured at 4 K as a function of magnetic field shows Hc_2 for the sample

with x = 0.05 is minimum, (approximately 0.3 T less than Hc_2 for x = 0). For the sample x = 0.15 Hc_2 is even slightly higher that of the un-doped sample.

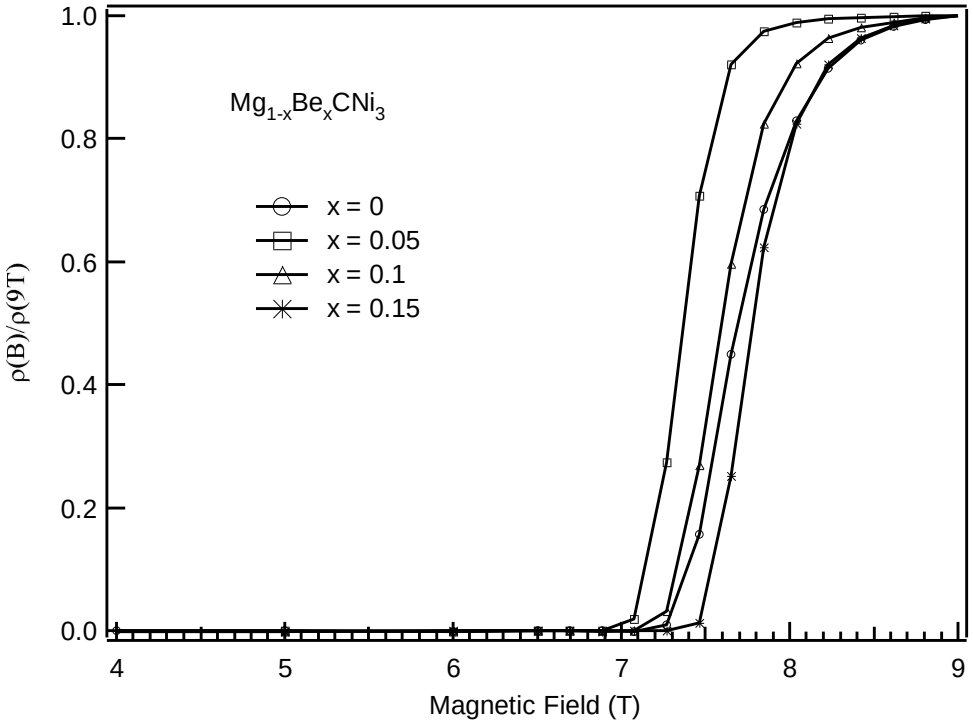

Fig: 4.16 Magnetic field dependence of resistivity at 4K, normalized by its normal state value, for $Mg_{1-x}Be_xCNi_3$ (x = 0, 0.05, 0.1, and 0.15). The solid lines are a guide to the eye.

The temperature dependence of the upper critical field $Hc_2(T)$ for $Mg_{1-x}Be_xCNi_3$ (x = 0, 0.05, 0.1, and 0.15) is shown in Figure 4.17. The solid and broken lines in Figure 4.17 represent the best fit of experimental data to equation (1). This small variation is followed by the upper critical field $H_{c2}(0)$ at zero temperature, yielded by extrapolation of the fit to T = 0 K. $H_{c2}(0)$ for x = 0, 0.05, 0.1 and 0.15 are 10.616 T, 11.125 T, 11.267 T, and 11.299 T respectively. Superconducting coherence lengths $\xi(0)$ can be estimated using the Ginzberg Landau formula for an isotropic three dimensional superconductor, $H_{c2}(0) = \Phi_0/2\pi\xi(0)^2$, where Φ_0 = 2.0678 x 10^9 Oe $Å^2$ is a flux quantum. The estimated values of $\xi(0)$ are 56 Å for $Mg_{0.95}Be_{0.05}CNi_3$ and 54 Å

for the rest of samples including un-doped $MgCNi_3$. These values are slightly higher than the value reported by Young *et al* for thin film of $MgCNi_3$ [23].

We know $H_{c2} \propto \Phi_0/\xi^2$, and for dirty superconductors the effective coherence length is defined as $1/\xi = 1/\xi_0 + 1/l$, where ξ_0 is the Pippard coherence length and l is the mean free path [42]. For Be doped $MgCNi_3$ samples the above results show that there is no effect of doping on expansion or contraction of ξ_0 and l.

The Be study seems to be in agreement with electronic structure calculations, where the majority of the DOS at EF are Ni 3-d states, and Mg p-states contribute very little [6-11].

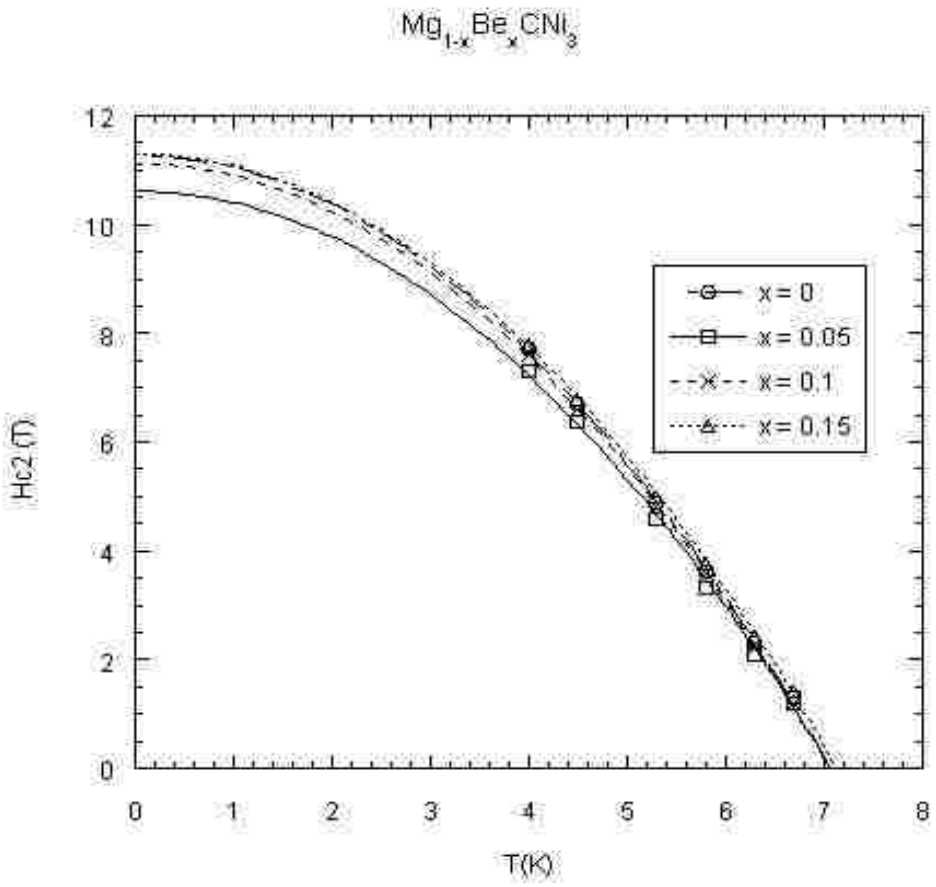

Fig: 4.17 The dependence of the upper critical field $H_{c2}(T)$ on temperature for $Mg_{1-x}Be_xCNi_3$ (x = 0, 0.05, 0.1, and 0.15). The lines are fit to equation (1) and extrapolated to $H_{c2}(0)$ for comparison.

4.3.3 $Mg_{1-x}Li_xCNi_3$

The powder X-ray diffraction pattern of $Mg_{1-x}Li_xCNi_3$ (x = 0, 0.03, 0.05, 0.1, and 0.2) are shown in Figure 4.18. As in the case of MgB_2 [45], due to the closeness in the atomic volume values of these elements, Li substitution on Mg in $MgCNi_3$ up to 20% does not change the x-ray diffraction pattern. As shown in Figure 4.19, the XRD peaks shift slightly but systematically toward higher angle on 2θ axis as Li concentration, x, is increased from x = 0 to 0.2. The value of lattice parameters (a~3.805 ± 0.003 Å) of the doped samples remained practically unchanged.

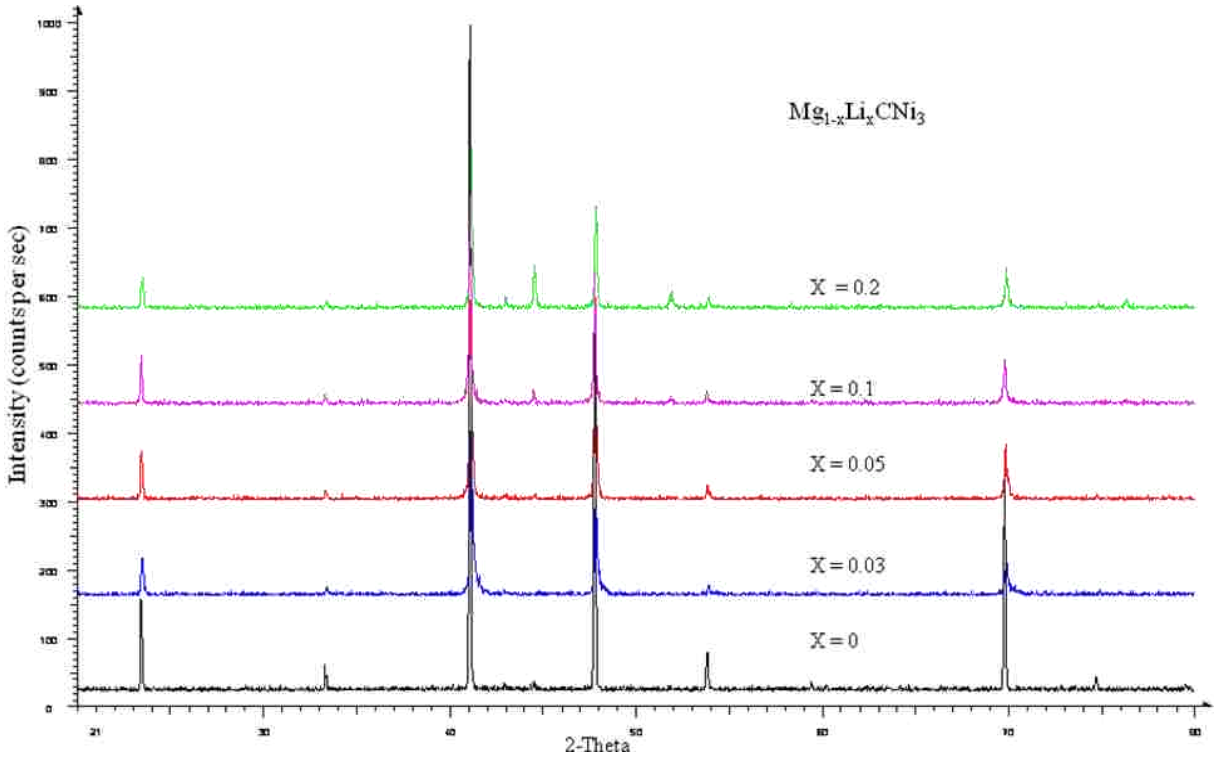

Fig: 4.18 Powder X-ray diffraction pattern of $Mg_{1-x}Li_xCNi_3$ (x = 0, 0.03, 0.05, 0.1, and 0.2) samples.

In the $Mg_{0.8}Li_{0.2}CNi_3$ sample a few extra peaks, which correspond to un-reacted Ni, were observed. On the other hand, because no reaction with the crucible wall was detected, and no un-

reacted Mg was observed, any variation in the physical behavior, should give the best indication of the incorporation of Li element into the $MgCNi_3$ structure.

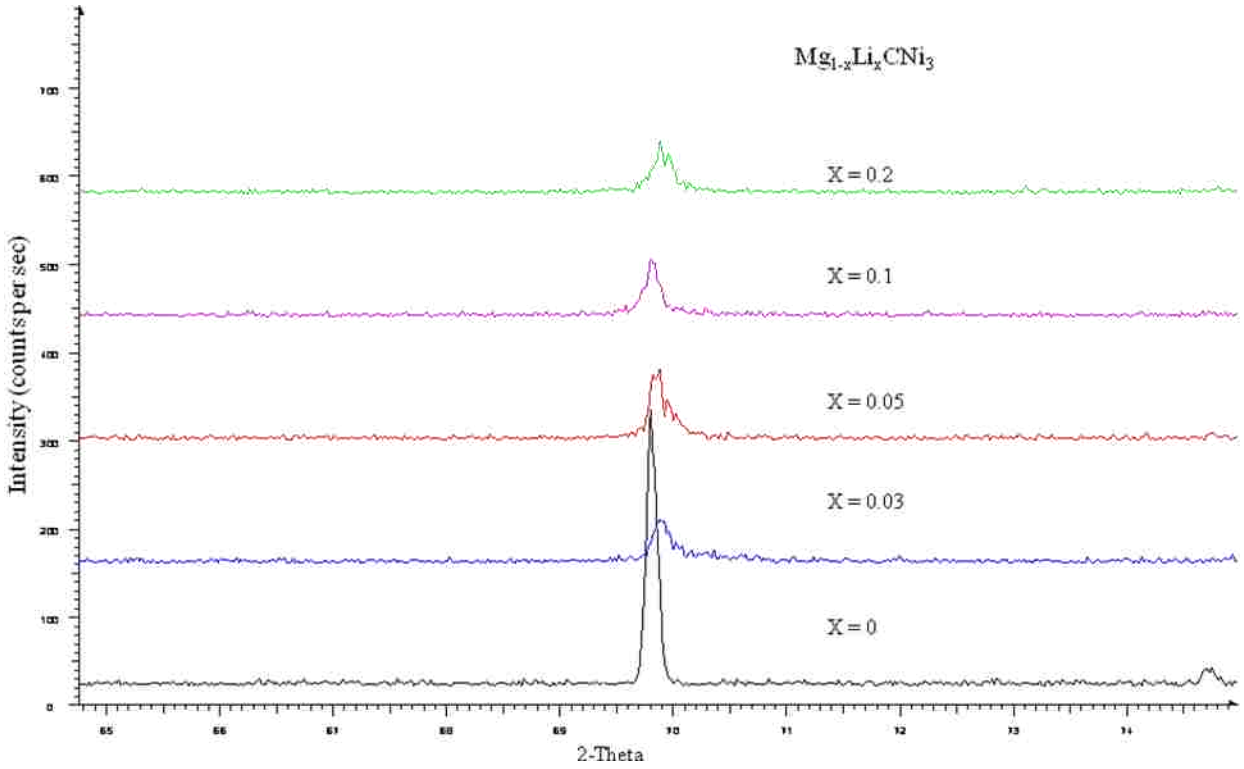

Fig: 4.19 Powder X-ray diffraction pattern of $Mg_{1-x}Li_xCNi_3$ (x = 0, 0.03, 0.05, 0.1, and 0.2) samples focused on one peak near 70^o.

Figure 4.19 shows the susceptibility measurements versus temperature for $Mg_{1-x}Li_xCNi_3$ (x = 0, 0.03, 0.05, 0.1 & 0.2) at a constant magnetic field of 20 Oe. It can be seen that all the samples up to x = 0.2 exhibit superconductivity. The variation of the onset T_c as a function of Ni concentration, x is shown in Figure. It is observed that T_c does not decrease monotonically with increasing x. Initially, T_c decreases by approximately 1 K with 3% of Mg substitution with Li. With further doping T_c comes back and, for 15 and 20 % Li substitution, it is almost the same as the un-doped sample.

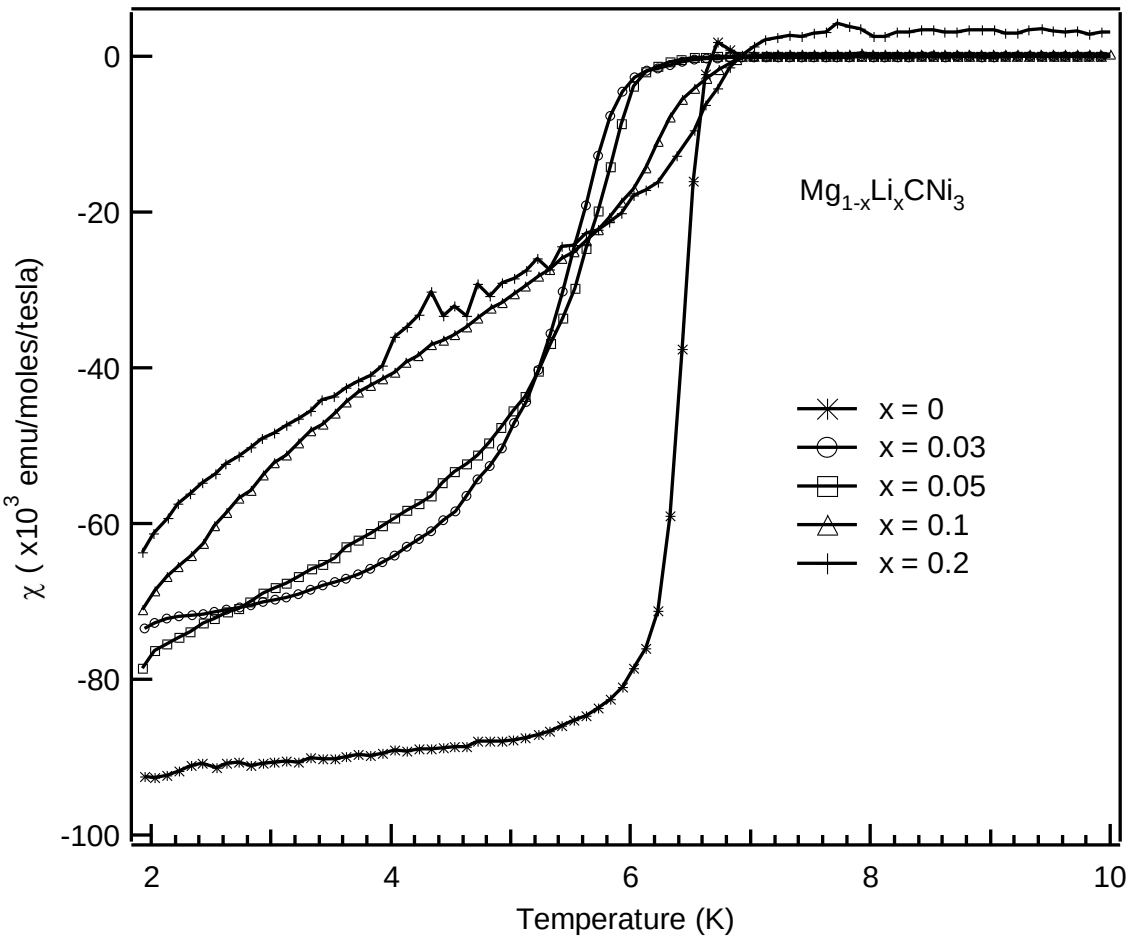

Fig: 4.20 Susceptibility versus temperature for $Mg_{1-x}Li_xCNi_3$ (x = 0, 0.03, 0.05, 0.1, and 0.2) in an applied magnetic field of 20 Gauss. The solid lines are a guide to the eye.

Though, it has been suggested that $MgCNi_3$ is near a ferromagnetic instability that can be reached by hole doping on the Mg site (if 12% Mg is replaced by Li), no long range magnetic ordering was observed in normal state susceptibility of $Mg_{1-x}Li_xCNi_3$ measured at 0.1 T in between 3 K and 290 K [11]. Figure 4.21 shows the variation of resistivity normalized by its value at room temperature $\rho(T)/\rho(290K)$ for $Mg_{1-x}Li_xCNi_3$ (x = 0, 0.03, 0.1, and 0.2). It can be seen that no substantial change in shape of the $\rho(T)/\rho(290K)$ curves is observed for the entire range of doping. The magnitude of the absolute resistivity increases monotonically with Li

concentration, x (inset of Figure 4.21). For the 20 % Li doped sample the resistivity at 10 K is approximately 20 times more than that of pure $MgCNi_3$.

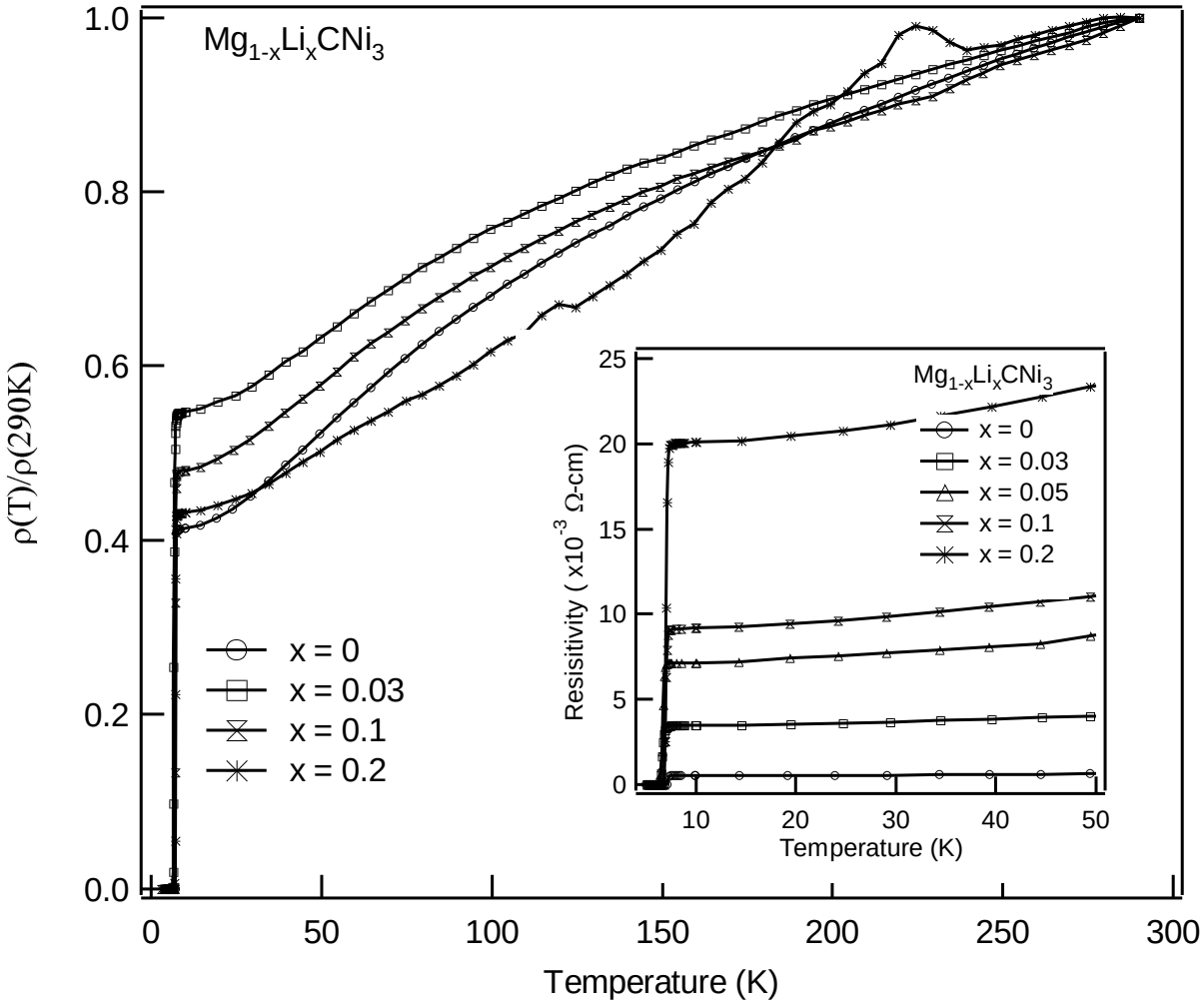

Fig: 4.21 Resistivity of $Mg_{1-x}Li_xCNi_3$ (x = 0, 0.03, 0.1, and 0.15) normalized by its room-temperature value as a function of temperature. Inset: Low temperature resistivity as a function of temperature. The solid lines are a guide to the eye.

The temperature dependence of resistance of $Mg_{1-x}Li_xCNi_3$ (x = 0, 0.03, 0.05, 0.1, and 0.2) in the vicinity of the superconducting transition is shown in Figure 4.22. Overall, the resistive transitions are sharper, and at higher temperature than observed in dc magnetization. The transitions are broadened and T_c is smaller for lower concentration of Li. As shown in Figure 4.23, the variation of the onset T_c as a function of Li concentration, x is consistent with that

observed from susceptibility. The error bar for T_c is ± 0.2 K. $Mg_{0.97}Li_{0.03}CNi_3$ has minimum T_c (mid point) ~ 6.62 K with ΔTc ~0.3 K. Then, for $Mg_{0.95}Li_{0.05}CNi_3$, Tc ~ 6.7 K with ΔTc ~ 0.4 K, for $Mg_{0.9}Li_{0.1}CNi_3$, Tc ~ 6.97 K with ΔTc ~ 0.2 K, and for $Mg_{0.8}Li_{0.2}CNi_3$, Tc ~ 7 K with ΔTc ~ 0.2 K, and for $MgCNi_3$, Tc ~ 7.25 K with ΔTc ~ 0.1 K.

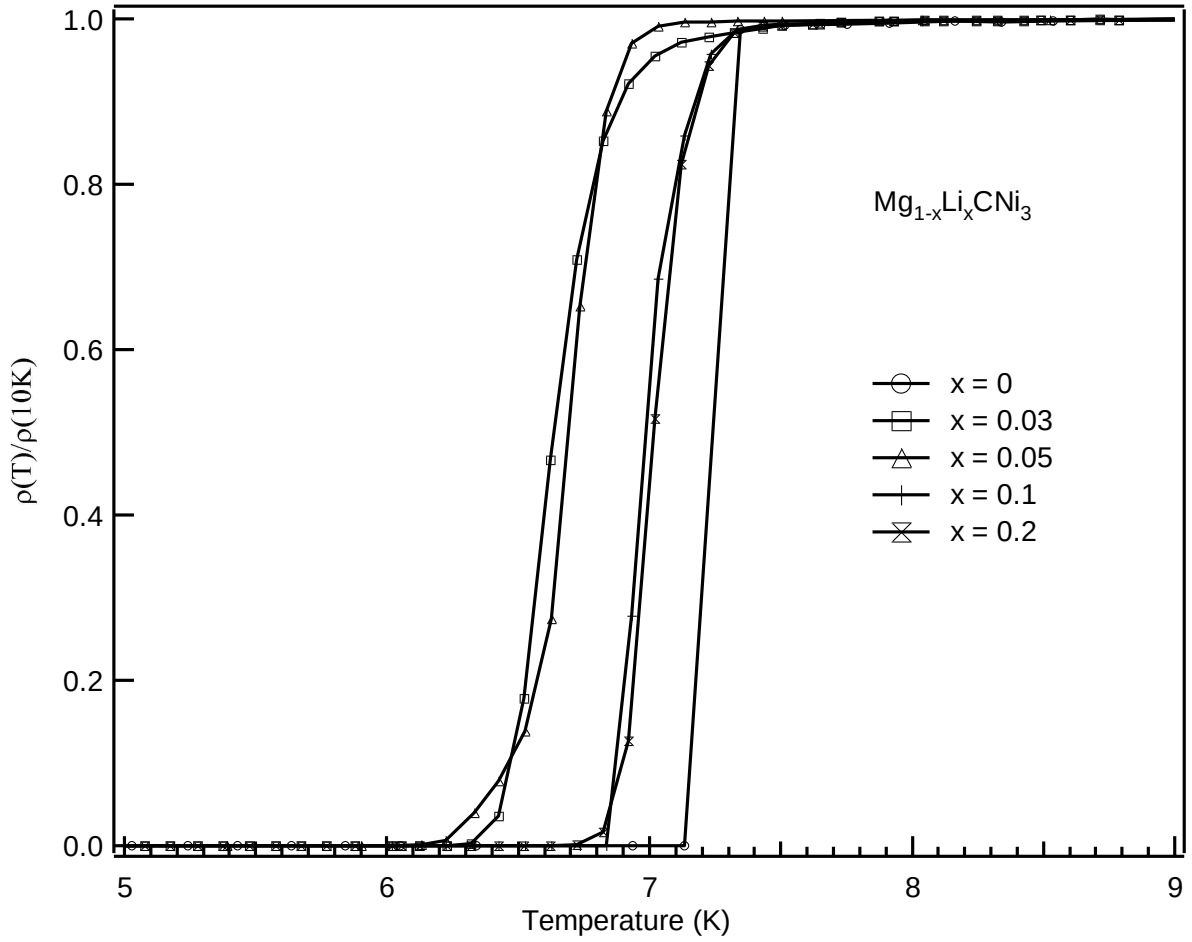

Fig: 4.22 Resistive transitions for $Mg_{1-x}Li_xCNi_3$ (x = 0,0.03, 0.05, 0.1, 0.2).The solid lines are a guide to the eye.

Shown in Figure 4.24 is the magnetic field dependence of electrical resistivity of $Mg_{1-x}Li_xCNi_3$ (x = 0, 0.03, 0.05, 0.1, and 0.2) at 4 K. Note that the transition is broadened for lower concentration of Li.

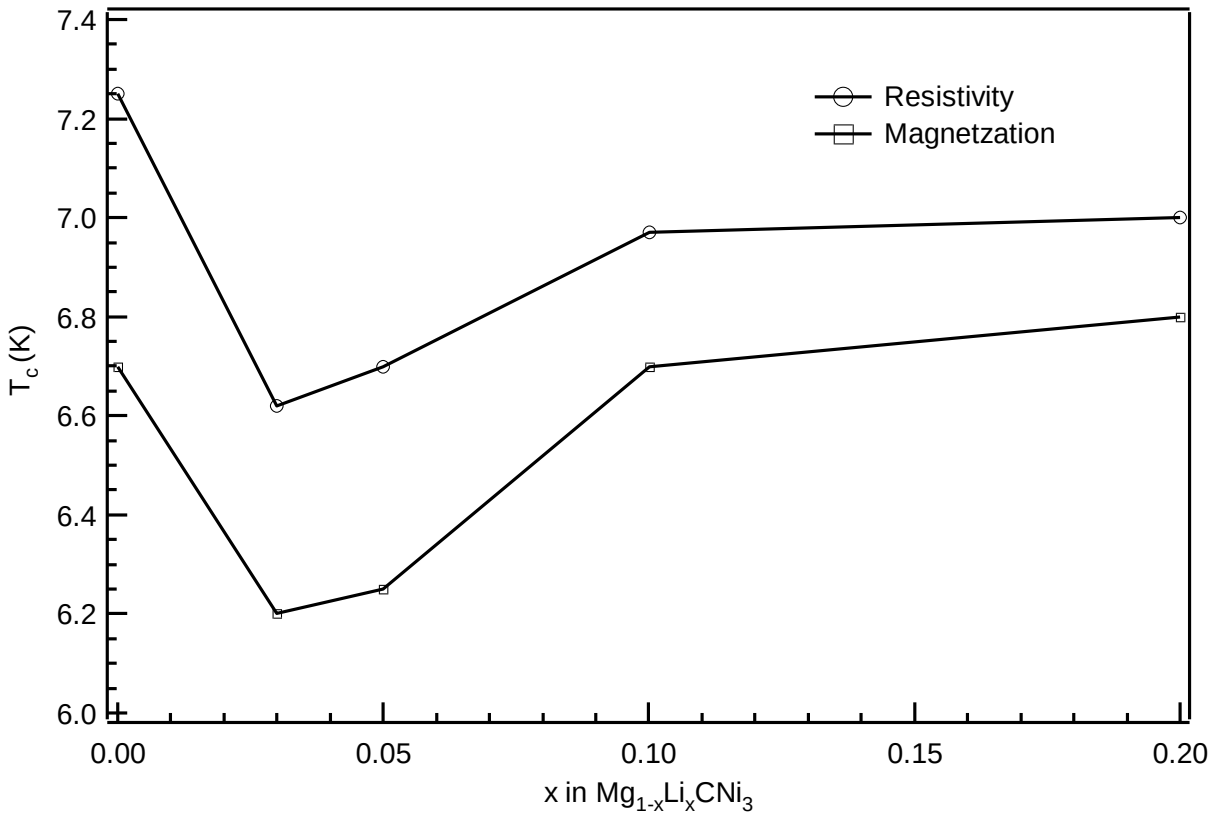

Fig: 4.23 Variation of the transition temperature as a function of Li concentration, x in $Mg_{1-x}Li_xCNi_3$. The solid lines are a guide to the eye.

The variation of the upper critical field H_{c2}(4 K) as a function of Li concentration, x in $Mg_{1-x}Li_xCNi_3$ is shown in Figure 4.24. The error bar for H_{c2} is ± 0.3 T. The magnitude of H_{c2} for the sample with x = 0.03 is minimum, (approximately 1.3 T less than the value for sample x = 0). Samples with x = 0.1 and 0.2 have upper critical field, 8.6 T and 8.8 T, respectively, which are higher than that of the un-doped $MgCNi_3$ sample. The temperature dependence of the upper critical field $H_{c2}(T)$ for $Mg_{0.97}Li_{0.03}CNi_3$ and $Mg_{0.8}Li_{0.2}CNi_3$ are shown in Figure 4.26 and Figure 4.27, respectively. The error bar is ± 0.3 T for each of them. The lines in the figures represent the best fit of experimental data to equation (1).

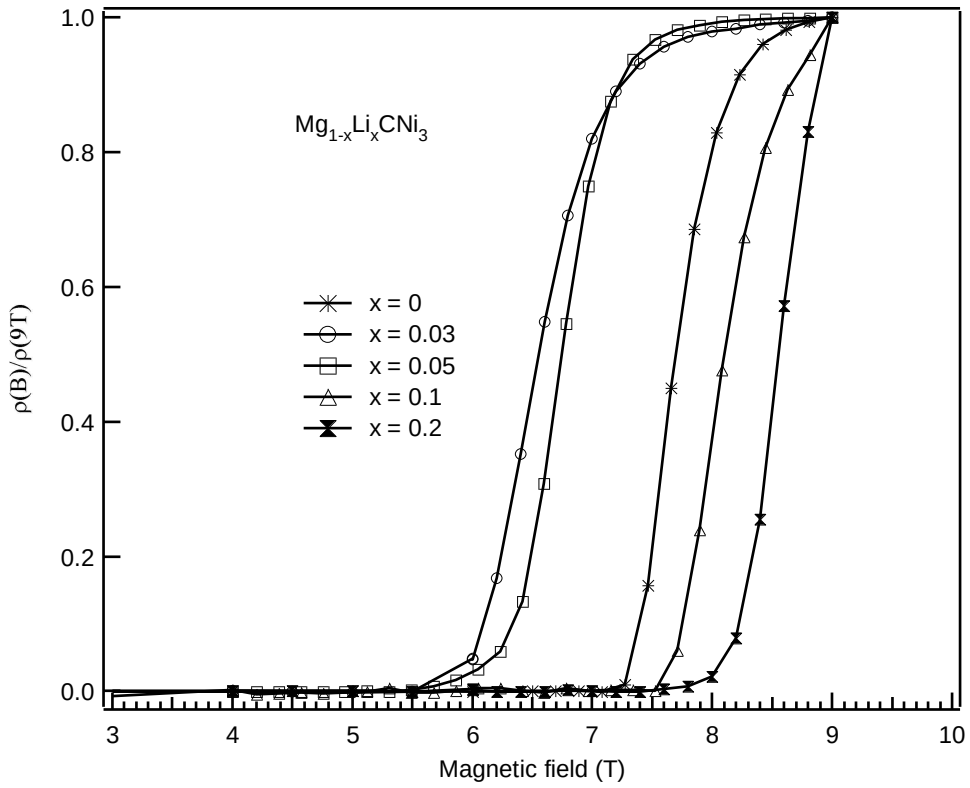

Fig: 4.24 Magnetic field dependence of normalized resistivity of $Mg_{1-x}Li_xCNi_3$ measured at 4 K. The solid lines are a guide to the eyes.

The upper critical field $H_{c2}(0)$ at zero temperature, yielded by extrapolation of the fit to T = 0 K are 10.616 T, 10.628 T, and 12.684 T for x = 0, 0.03 and 0.2, respectively. Superconducting coherence lengths $\xi(0)$ were estimated to be 55.6, 55.6 and 51.11 Å for x = 0, 0.03 and 0.2, respectively. Given that Li and Mg have different covalent radii, the lack of change in the cell parameters in $Mg_{1-x}Li_xCNi_3$ has made the conclusion on the incorporation and the effect of Li indecisive. Kumary et al. [16] also find no significant changes of lattice parameter upon partial replacement of Ni with Fe or Co. Li partially substitute Mg and each Li introduces only one hole to the system, where as Fe and Ru substitute for Ni and introduce two holes. The significant effect of Fe substitution in reduction of T_c can be explained by the Cooper pair breaking mechanism by the 3d electrons in Fe [49].

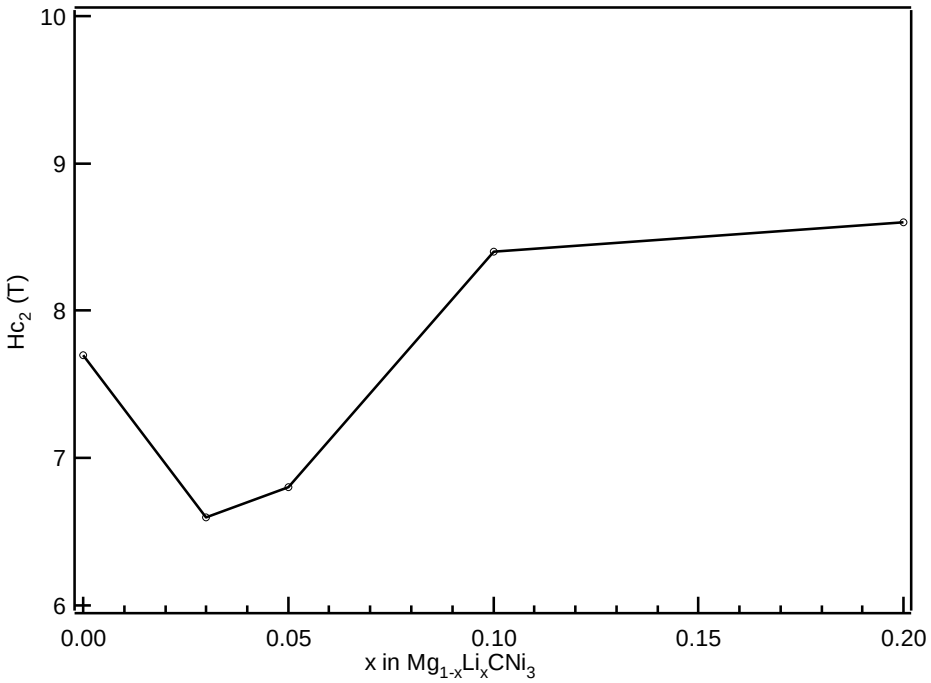

Fig: 4.25 Variation of upper critical field (Hc2) at 4 K as a function of Li concentration, x in $Mg_{1-x}Li_xCNi_3$. The solid lines are a guide to the eyes.

In $Mg_{1-x}Li_xCNi_3$ systems, in spite of theoretical prediction [11], the absence of magnetic ordering indicates that the hole-doping does not produce the magnetic instability which could be responsible for pair breaking [39]. The reason could be that the electronic structure of $MgCNi_3$ indicated that its electronic states at the Fermi energy (E_F) are dominated by the 3d-orbitals of Ni. The detected variation of T_c is tried to be understood by invoking equation (2), the well known McMillan formula [45, 47].Certainly, there will not be much change in $\langle\omega\rangle$ as the decrease in lattice constant is negligible. The decrease in λ due to the decrease in M by a factor of ~ 4 could lead to a decrease in T_c. Again, since there are no reports on theoretical calculations of the electronic structure of Li-doped $MgCNi_3$, further discussion is rather difficult with our experimental results. The enhancement of the upper-critical field is an interesting result of the Li doping in $MgCNi_3$. $H_{c2}(0)$ for the sample with 20 % Li concentration is approximately 2 T more than that of pure $MgCNi_3$.

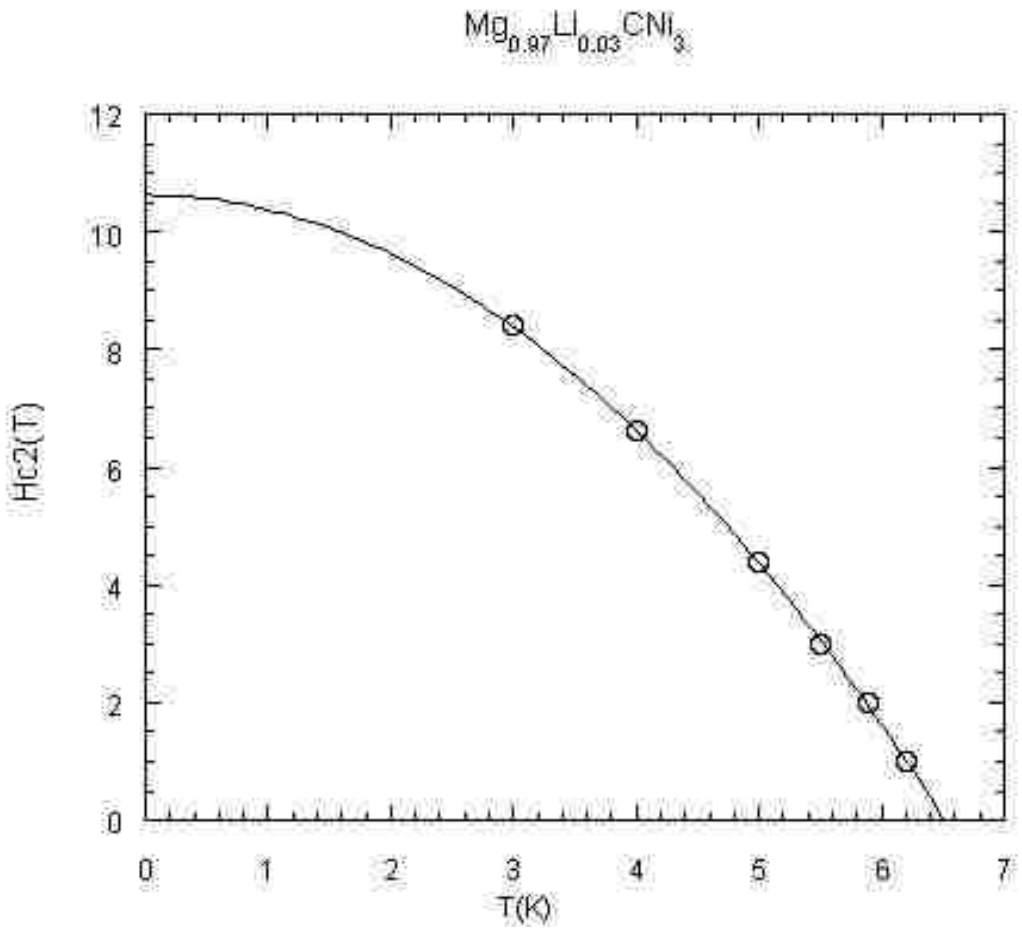

Fig: 4.26 The dependence of the upper critical field $H_{c2}(T)$ on temperature for $Mg_{0.97}Li_{0.03}CNi_3$. The dotted line is a fit to equation (1) and extrapolated to $H_{c2}(0)$=10.628 T.

The increase of H_{c2} can be explained in terms of the H_{c2} dependence on the effective coherence length (ξ): $H_{c2} \propto \Phi_0/\xi^2$, where Φ_0 is a flux quantum. For dirty superconductors the effective coherence length is defined as $1/\xi = 1/\xi_0 + 1/l$, where ξ_0 is Pippard coherence length and l is the mean free path [42]. We know l varies with the residual resistivity ρ_0 through $l = 2mV_F/(ne^2\rho_0)$, for the sample used in [24], where n is carrier density and V_F is Fermi velocity. On the other hand, ξ_0 is related to the critical temperature: $\xi_0 = a(h/2\pi)v_0/kT_c$, where a is a constant and v_0 is the velocity at the Fermi level [42]. Doping leads to shortening of the mean free path [50], and if it does not elongate ξ_0 simultaneously by suppressing Tc, one can expect the increase in the H_{c2} value. This is valid for $Mg_{1-x}Li_xCNi_3$ with x 0.1 and x = 0.2 because both

of these samples have ρ_0 (8-20 times) more than that of the un-doped $MgCNi_3$ and no decrease in T_c (Inset of Figure 4.21).

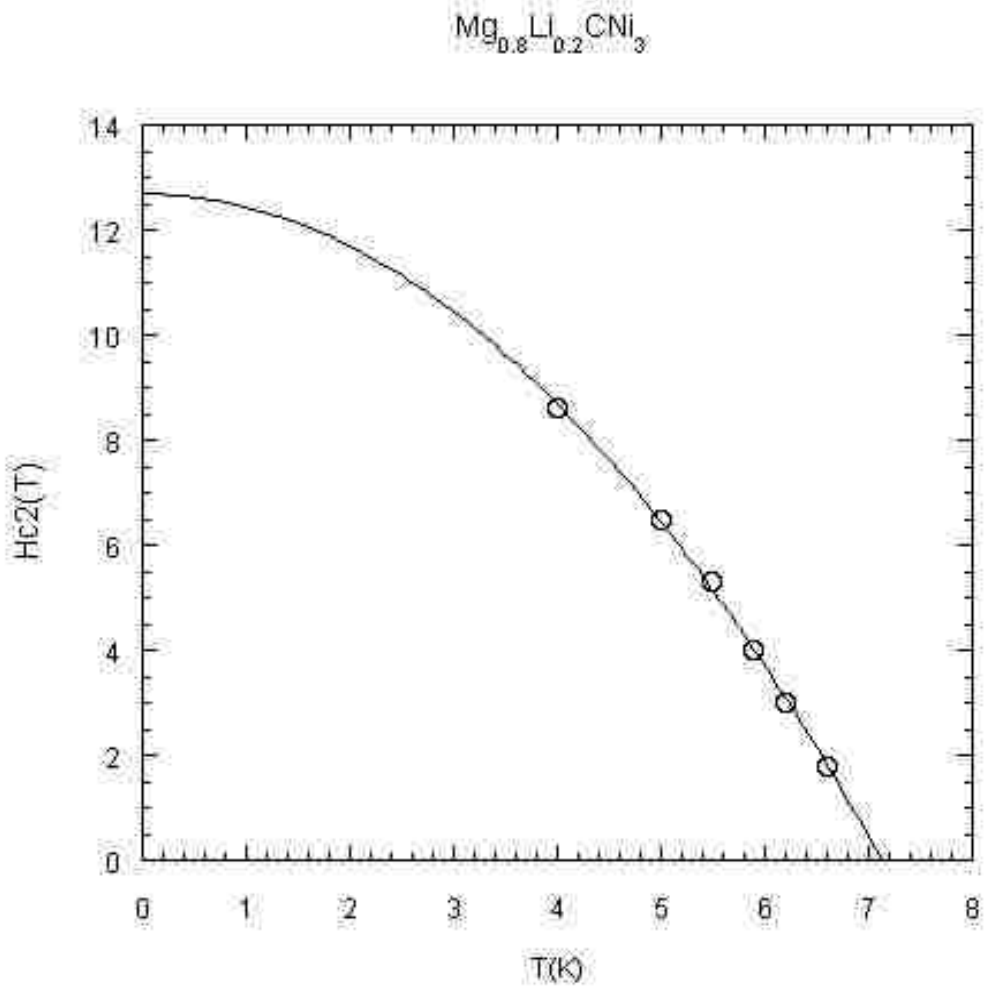

Fig: 4.27 The dependence of the upper critical field $H_{c2}(T)$ on temperature for $Mg_{0.8}Li_{0.2}CNi_3$. The dotted is fit to the equation (1) and extrapolated to $H_{c2}(0)$=12.684 T.

4.3.4 $MgC_xN_yNi_3$

The XRD patterns of C deficient samples with nominal compositions MgC_xNi_3 (x = 1.5, 1.2, 1, 0.9, and 0.7) are shown in Figure 4.28. It can be seen that the XRD patterns of all the C deficient samples are similar to that of the pristine $MgCNi_3$, indicating the formation of the requisite phase. There are a few impurity peaks in $MgC_{0.9}Ni_3$ and $MgC_{0.7}Ni_3$ samples identified

to be due to the presence of very small traces of un-reacted Ni. It is apparent from Figure 4.29 that the XRD peaks shift slightly towards higher angle on 2θ axis as C concentration, x, is decreased from x = 1.5 to 0.9. The shift is significant for x = 0.9. The change in lattice parameter, a, extracted from the analysis of the XRD peak *hkl* (111) is consistent with the peak shift. The lattice constants for x = 1.5, 1.2, 1, 0.9, and 0.7 are 3.80596, 3.80273, 3.80105, 3.80171, and 3.77194 Å respectively.

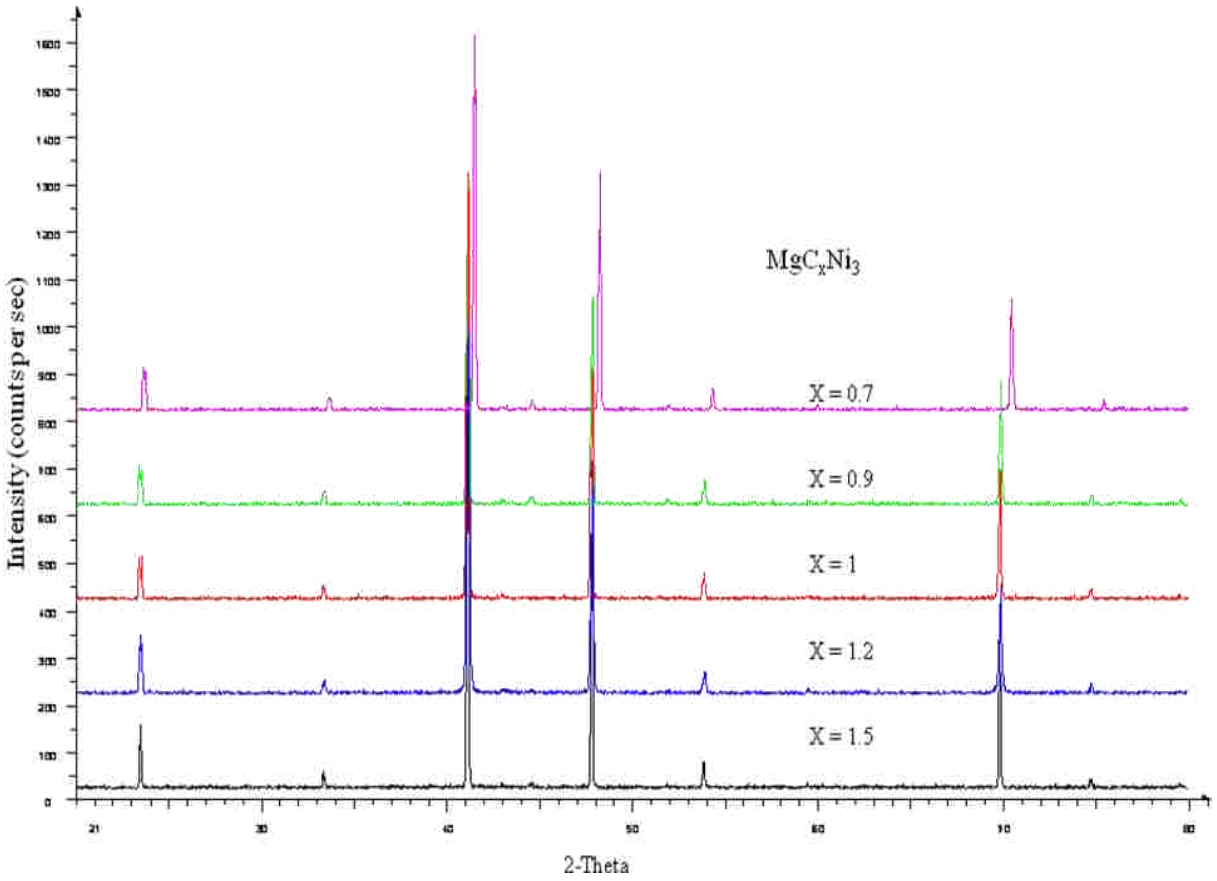

Fig: 4.28 Powder X-ray diffraction pattern of samples prepared with nominal composition MgC_xNi_3 (x =1.5, 1.2, 1, 0.9, and 0.7).

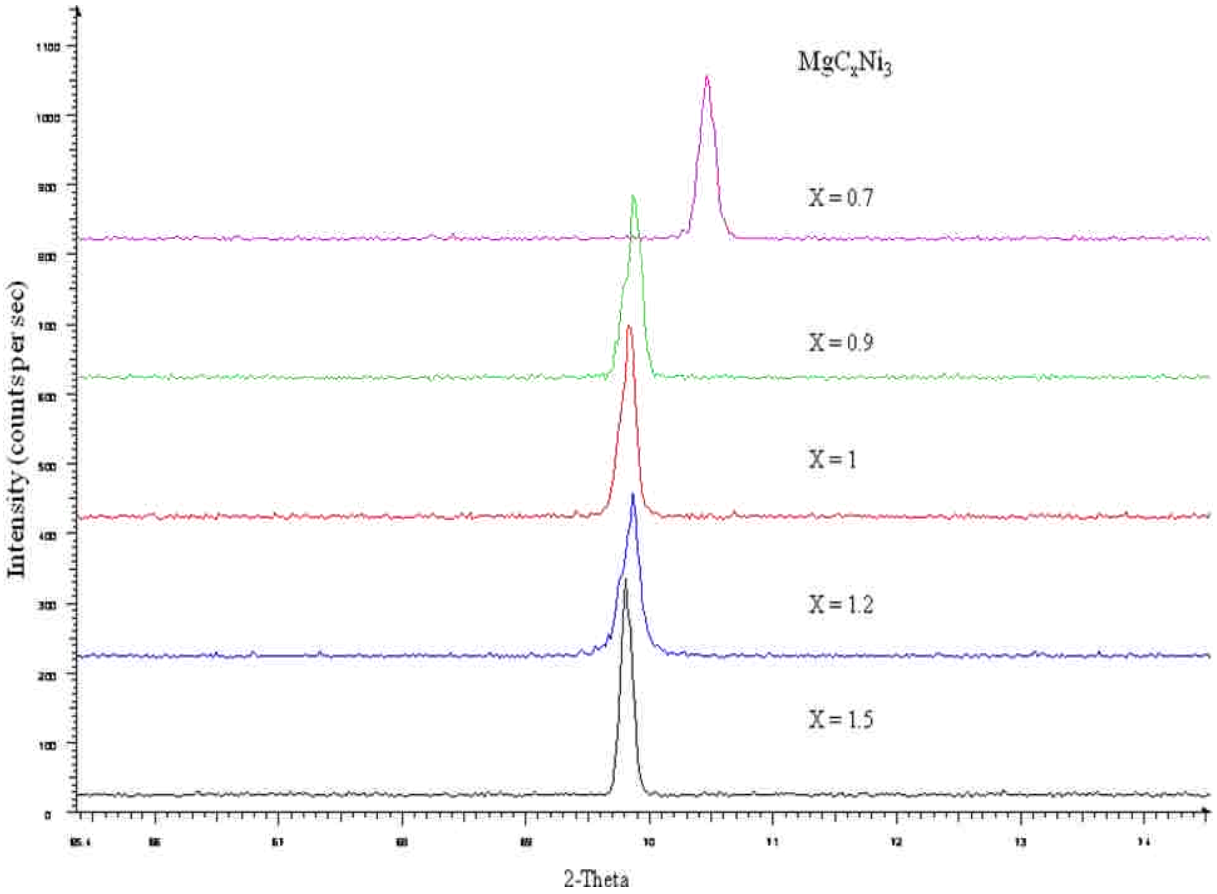

Fig: 4.29 Powder X-ray diffraction pattern of samples prepared with nominal composition MgC_xNi_3 (x =1.5, 1.2, 1, 0.9, and 0.7) shows the peak shift around 70^0.

The temperature dependence of susceptibility of all the samples is shown in Figure 4.30. It can be seen that all samples down to x = 0.9 exhibit superconductivity. T_c is found to decrease monotonically with decreasing x in MgC_xNi_3. Eventually, the compound with x = 0.7 does not show a superconducting transition down to 2 K. The XRD results and susceptibility measurements of C deficient samples of $MgCNi_3$ strongly support the report which says the carbon atom in $MgCNi_3$ plays a crucible role in its superconductivity [1], and a single-phase superconducting compound occurs only in a narrow range of carbon content [51].

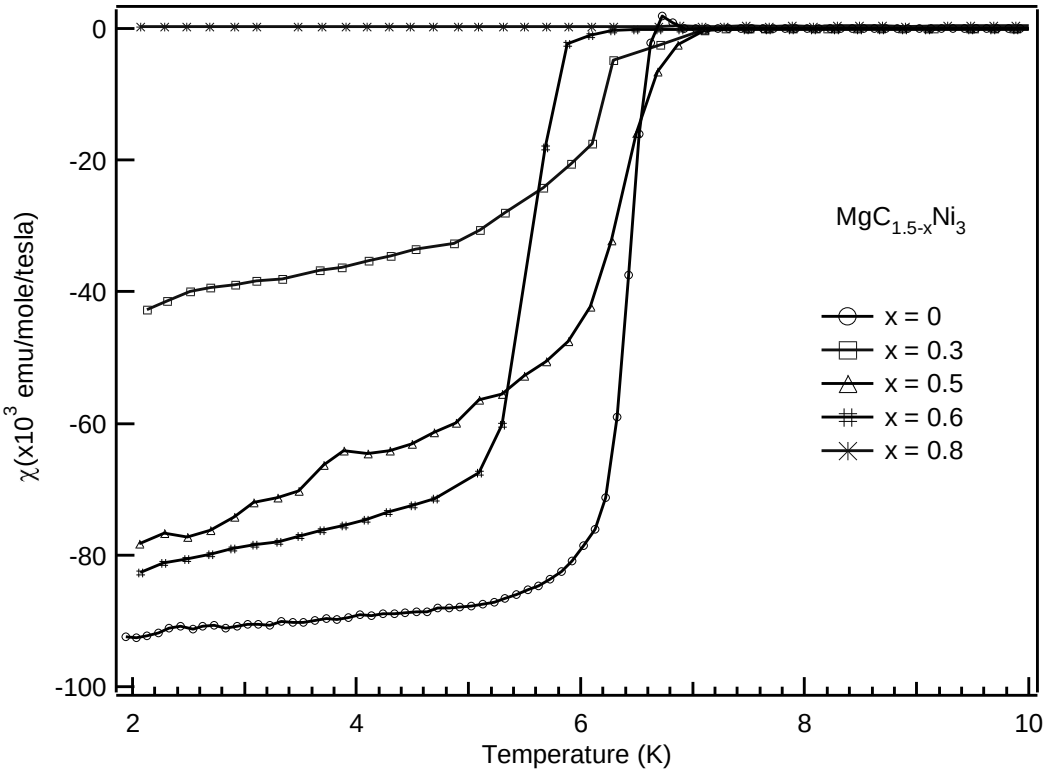

Fig: 4.30 Susceptibility versus temperature for samples prepared with nominal composition MgC_xNi_3 (x =1.5, 1.2, 1, 0.9, and 0.7) in an applied magnetic field of 20 Gauss.

Shan *et al* proposed that the disappearance of superconductivity in MgC_xNi_3 is due to a substantial depression of the electron-phonon coupling caused by decreasing x [31]. The powder x-ray diffraction pattern of MgC_xNi_3 samples after 2 hours long heat treatment in a stream of nitrogen gas is shown in Figure 4.31. All the samples are in single phase, but Figure 4.32 clearly shows the peak shift in each sample (with x = 1.2, 1, 0.9, and 0.7) towards lower angle on 2θ from its previous position. It can be seen that the peaks in all samples but in $MgC_{0.7}Ni_3$ shift slightly towards lower angle even from the position of the peak in $MgC_{1.5}Ni_3$. The increase in the lattice constants of these nitrogen doped samples (MgC_xN_yNi3) is consistent with the shifting of the peaks towards lower angle on the 2θ axis.

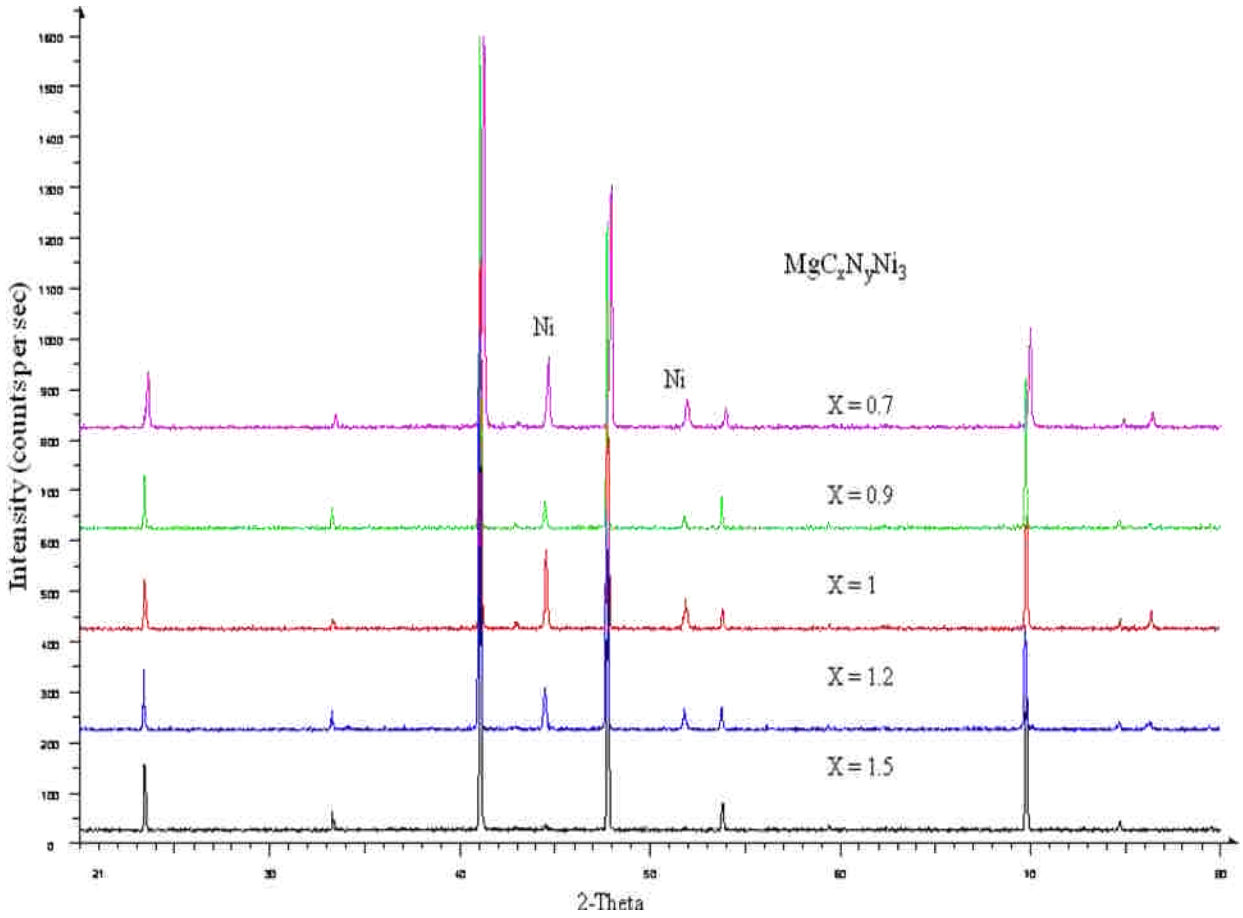

Fig: 4.31 Powder X-ray diffraction pattern of MgC_xNi_3 (x =1.5, 1.2, 1, 0.9, and 0.7) after the heating in flow of N_2.

The lattice constants for x = 1.5, 1.2, 1, 0.9, and 0.7 are 3.80596, 3.81145, 3.80578, 3.80819, and 3.78997 Å respectively. Though, the gain in mass after 2 hours heating in nitrogen gas flow was recorded, the precise value of the parameter y in the formula $MgC_xN_yNi_3$ is not known because we lost mass of Mg and C at the same time. In the extended XRD pattern (Figure 4.31) of $MgC_xN_yNi_3$ a few extra peaks which correspond to elemental Ni are observed.

Shown in Figure 4.33 is the temperature dependence of the magnetization of the samples $MgC_xN_yNi_3$ (x = 1.5, 1.2, 1, 0.9, and 0.7) at an applied dc magnetic field of 20 Oe. All compounds are found to superconduct. After heating in N_2 the sample with nominal formula

$Mg_{1.2}C_{0.7}Ni_3$ shows the superconducting transition with T_c (onset) ~ 5.9 K. T_c *'s* of other samples are also observed to be slightly increased.

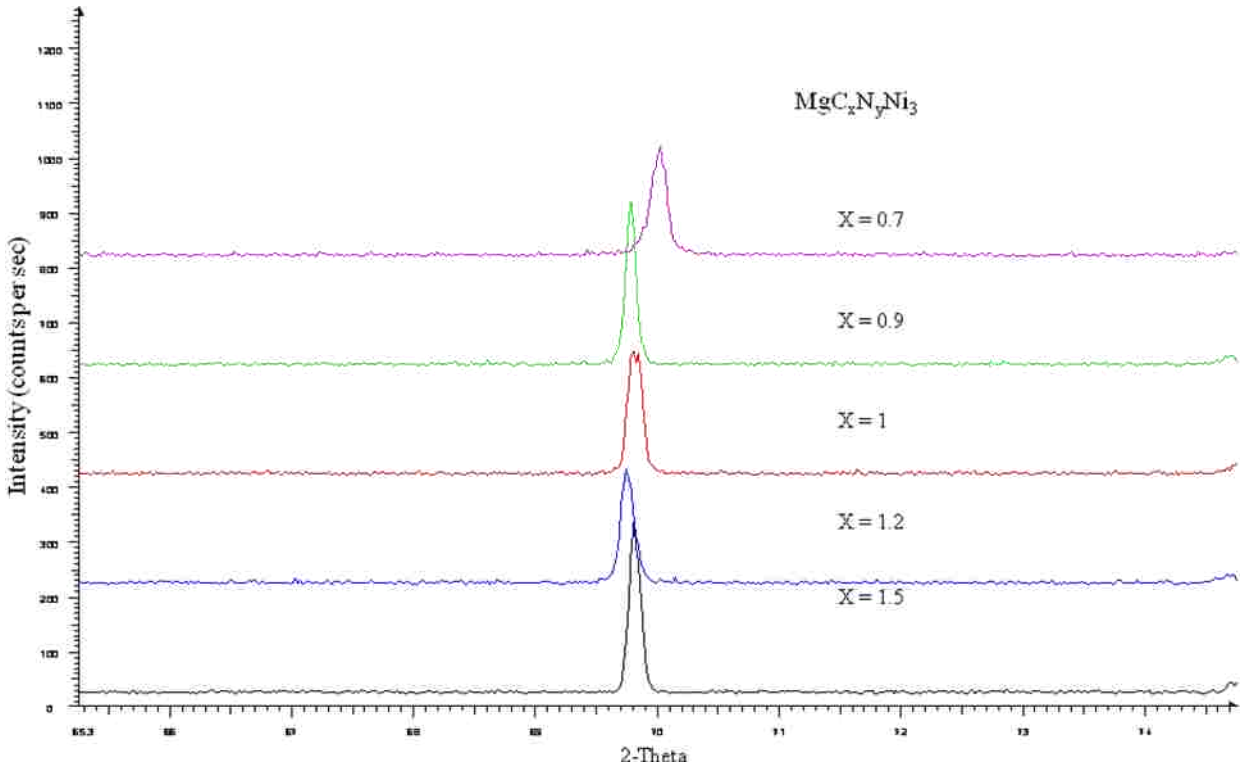

Fig: 4.32 Powder X-ray diffraction pattern of MgC_xNi_3 (x =1.5, 1.2, 1, 0.9, and 0.7) showing peak shift in opposite direction after the heat treatment in flow of N_2.

For carbon deficient samples, the change in the parameters $\langle\omega\rangle$ and N(0) contribute to the reduction in the transition temperature. The results of XRD and magnetization measurements indicates that the decrease in λ was compensated by the substitution of N to some extent. According to Wie *et al.* replacement of C by N or B greatly reduces the DOS peak near E_F [6]. Certainly, electron doping (N) doping reduces $N(E_F)$ in $MgCNi_3$. There will not be significant change in ionic mass M, but $\langle\omega\rangle$ decreases due to the increase in lattice volume. The net effect, therefore, can be expected to be an increase in λ in some extent leading to the observed

reappearance of superconductivity in the N-doped $MgC_{0.7}Ni_3$ sample and increase in T_c for the rest of samples.

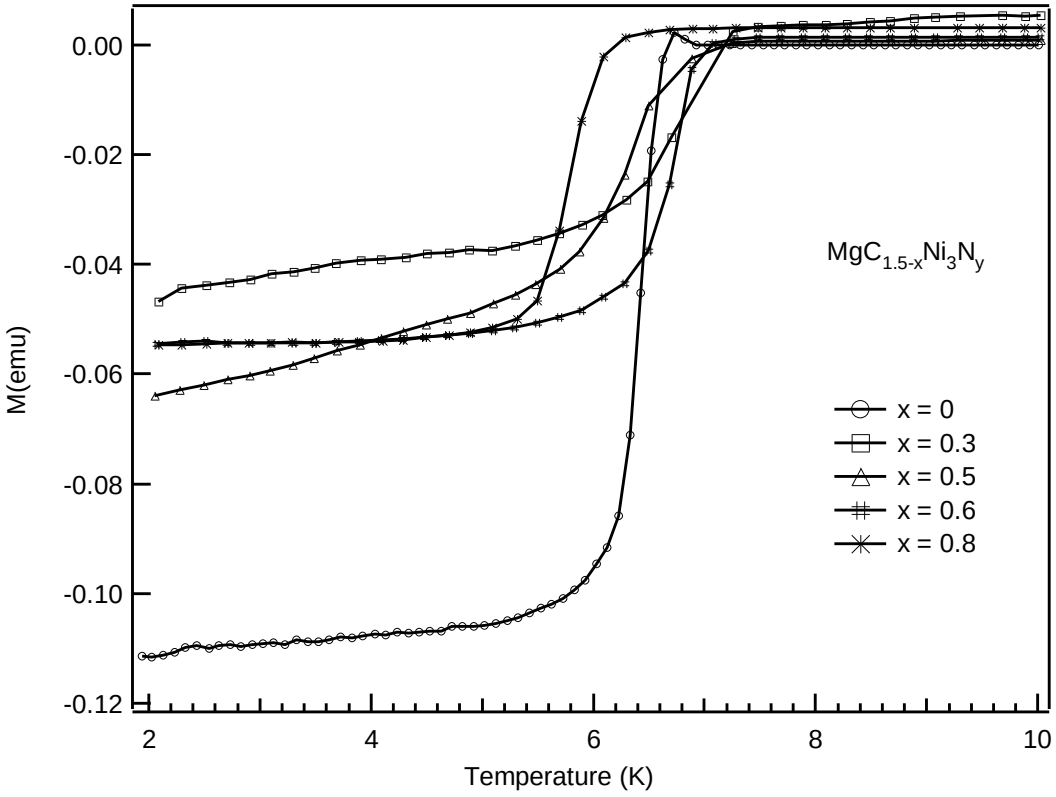

Fig: 4.33 Low temperature magnetization for samples prepared with nominal composition MgC_xNi_3 (x =1.5, 1.2, 1, 0.9, and 0.7) and heat treatment with N_2. The solid lines are a guide to the eyes.

4.4 Conclusions

Solid state reaction method under the stream of high purity Ar has been employed for the synthesis of $Mg_{1-x}Be_xCNi_3$ (x = 0, 0.01, 0.05, 0.1, 0.15 and 0.2) , $Mg_{1-x}Li_xCNi_3$ (x = 0, 0.03, 0.05, 0.1, and 0.2) and MgC_xNi_3 (x =1.5, 1.2, 1, 0.9, and 0.7) samples. All the samples were characterized by powder XRD to examine the phase purity and determination of lattice parameter. The basic superconductivity parameters in Be-and Li-doped samples were studied by magnetization and transport measurements, while only magnetization measurements were performed for N-doped samples as the pellets are not hard enough to cut into bars.

All the samples formed a single phase with sharp X-ray diffraction peaks. A few impurity peaks, which correspond to un-reacted elemental Ni, were observed in XRD pattern of samples with concentration higher than x = 0.1 of Be and Li. No significant change in lattice parameter was observed in Be and Li substitutions. For C deficient samples, the lattice parameter decreased with decreasing the C content, while it increased after the heat treatment in flowing N_2. The transition temperature T_c and upper critical field for $Mg_{1-x}Be_xCNi_3$ does not change with Be concentration, x. It is surprising that T_c is so robust up to 20 % Be substitution. No substantial change in T_c for $Mg_{1-x}Li_xCNi_3$ is observed. The upper critical field of $Mg_{1-x}Li_xCNi_3$ decreased initially and then increased with increasing in x. The enhancement of the upper critical field for Li-doped samples could be due to reduction of the mean free path. The negative curvature of the $H_{c2}(T)$ curve over a wide range of temperature is a characteristic of conventional superconductivity. The results of the study of Be-and Li-doped systems suggest Mg plays a small role in the superconductivity.

As expected, the superconductivity was suppressed by the reduction of C content in MgC_xNi_3 the deficient samples. No superconductivity was observed in $MgC_{0.7}Ni_3$. After the heat treatment of C deficient samples in the stream of N_2 for a couple of hours, T_c was found to be increased slightly for samples with x =1- 0.9. Furthermore, superconductivity appeared in $MgC_{0.7}Ni_3$. The results of the study of this system indicate the contribution of N in the superconductivity in $MgC_xN_yNi_3$.

4.5 References

[1] He T *et al* 2001 *Nature* **411** 54

[2] Huang Q, He T, Regan K A, Rogado N, Hayward M, Hass M K, Inumaru K and Cava R J 2001 *Physica C* **363** 215

[3] Lin J-Y, Lin P H, Ho P L, Huang H L, Zhang Y-L, Yu R-C, Jin C-Q and Yang H D 2002 *J. Supercond.* **15** 485

[4] Liu F M, Li J Q, Dong C, Wang T M, Zhou Y Q and Chen H 2002 *Supercond. Sci. Technol.* **15** 1316

[5] Wei Z F, Chen X L, Che G C, Wang F M, Li W C and He M 2002 *Chin. Phys. Lett.* **19** 249

[6] Shim J H, Kwon S K and Min B I 2001 *Phys. Rev. B* **64** 180510

[7] Singh D J and Mazin I I 2001 *Phys. Rev. B* **64** 140507

[8] Dugdale S B and Jarlborg T 2001 *Phys. Rev.* B 64 100508

[9] Szajek A 2001 *J. Phys.: Condens. Matter* **13** L595

[10] Shein I R, Ivanovskii A L and Medvedeva N I 2001 *JETP Lett.* **74** 122

[11] Rosner H, Weht R, Johannes M D, Pickett W E and Tosatti E 2002 *Phys. Rev. Lett.* **88** 027001

[12] Kim J H, Ahn J S, Kim J, Park M-S, Lee S I, Choi E J and Oh S-J 2002 *Phys. Rev. B* **66** 172507

[13] Amos T G, Huang Q, Lynn J W, He T and Cava R J 2002 *Solid State Commun.* **121** 73

[14] Hayward M A, Hass M K, Ramirez A P, He T, Regan K A, Rogado N, Inumaru K and Cava R J 2001 *Solid State Commun.* **119** 491

[15] Ren Z A, Che G C, Jia S L, Chen H, Ni Y M and Zhao Z X 2001 *Preprint cond-mat*/0105366
Ren Z A, Che G C, Jia S L, Chen H, Ni Y M and Zhao Z X 2001 *Sci. China A* **44** 1205

[16] Kumary TG, Janaki J,Mani A, Jaya S M, SastryV S,Hariharan Y, Radhakrishnan T S and ValsakumarMC 2002 *Phys. Rev. B* **66** 064510

[17] Das A and Kremer R K 2003 *Phys. Rev. B* **68** 064503

[18] Alzamora M, Sanchez D R, Cindra M and Baggio-Saitovitch E M 2002 *Braz. J. Phys.* **32** 755

[19] Chen L, Li H and Mei L M 2004 *J. Mater. Sci. Technol.* **20** 203

[20] Chen L and Li H 2004 *Acta Phys. Sin.* **53** 922

[21] Park M S, Giim J S, Park S H, Lee Y W, Lee S I and Choi E J 2004 *Supercond. Sci. Technol.* **17** 274

[22] Park S H, Lee Y W, Giim J, Jung S H, Ri H C and Choi E J 2004 *Physica C* **400** 160

[23] Young D P, Moldovan M, Craig D D, Adams P W and Chan J Y 2003 *Phys. Rev. B* **68** 020501

[24] Li S Y, Fan R, Chen X H, Wang C H, Mo W Q, Xiong Y M, Luo X G, Zhang H T, Li L, Sun Z, Cao L Z 2001 *Phys. Rev. B* **64** 132505

[25] Li S Y, Mo W Q, Yu M, Zheng W H, Wang C H, Xiong Y M, Fan R, Wu B M, Cao L Z Chen X H 2002 *Phys. Rev. B* **65** 064534

[26] Lin J-Y, Ho P L, Huang H L, Lin P H, Zhang Y-L, Yu R-C, Jin C-Q and Yang H D 2003 *Phys. Rev. B* **67** 052501

[27] Yang H D, Mollah S, Huang WL, Ho P L, Huang H L, Liu C-J, Lin J-Y, Zhang Y-L, Yu R-C and Jin C-Q 2003 *Phys. Rev. B* **68** 092507

[28] Mao Z Q, Rosario M M, Nelson K D,Wu K, Deac I G, Schiffer P, Liu Y, He T, Regan K A and Cava R J 2003 *Phys. Rev. B* **67** 094502

[29] Cooley L D, Song X, Jiang J, Larbalestier D C, He T, Regan K A and Cava R J 2002 *Phys. Rev. B* **65** 214518

[30] Jin C Q, Zhang Y L, Liu Z X, Li F Y, Yu W and Yu R C 2003 *Physica C* **561** 388-389

[31] Shan L, Xia K, Liu Z Y, Wen H H, Ren Z A, Che G C and Zhao Z X 2003 *Phys. Rev. B* **68** 024523

[32] Waelte A, Fuchs G, Mueller K-H, Handstein A, Nenkov K, Narozhnyi V N, Drechsler S-L, Shulga S, Schultz L and Rosner H 2004 *Physical review B* **70** 174503

[33] Lin J-Y and Yang H D 2004 *Superconductivity Research at the Leading Edge* ed P S Lewis (New York: Nova Science) pp 111–30

[34] Rosner H *et al* 2003 *Physica C* **563** 388/389

[35] Singer P M, Imai T, He T, Hayward M A, and Cava R J 2001 *Phys. Rev. Lett*. **87** 257601

[36] Kinoda G *et al* 2001 *Japan. J. Appl.Phys.***40** L1365

[37] Tan M Q, Tao X M, Xu X J, He J H and Ye G X 2003 *Physica B* 337 95

[38] Prozorov R, Snezhko A, He T, and Cava r J 2003 *Phys. Rev. B* **68** 180502(R)

[39] Shein I R, Ivanovskii A L, Kurmaev E Z,Moewes A, Chiuzbian S, Finkelstein L D, Neumann M, Ren Z A and Che G C 2002 *Phys. Rev. B* **66** 024520

[40] Yang H D, Lin J-Y, Li H H, Hsu F H, Liu C-J, Li S-C, Yu R-C and Jin C-Q 2001 *Phys. Rev. Lett.* **87** 167003

[41] Shan L, Tao H J, Gao H, Li Z Z, Ren Z A, Che G C, and Wen H 2003 *Phys. Rev. B* **68**, 144510

[42] Andrzejewski B, Klimczuk T, Cava R J 2007 *Physica C* **460-462** 706-707

[43] Klimczuk T, Gupta V, Lawes G, Ramirez A P, Cava R J 2004 *Physical Review B* **70** 094511

[44] Hayward M A, Haas M K, Ramirez A P, He T, Regan K A, Rogado N, Inumaru K, Cava R J 2001 *Solid State Communication* **119** 491

[45] Cimberle M R, Novak M, Manfrinetti P and Palenzona A 2002 *Superconductor Science and Technology* **15** 43-47

[46] MacMillan W L 1968 *Physical review* **167** 331

[47] Allen P B and Dynes R C 1975 *Physical Review B* **12** 905

[48] Mani A, Kumary T G, Bharathi A, Kalavathi S, Sankara Sastry V, Hariharan Y 2005 *Physica C* **433** 139-145

[49] Klimczuk T, Cava R J 2004 *Solid State Communications* **132** 379

[50] Masui T, Lee S, Yamamoto A, Uchiyama H, Tajima S 2004 *Physica C* **412-414** 303

[51] Amos T G, Huang Q, Lynn J W, He T, and Cava R J 2002 *Solid State Communication* **121** 73

CHAPTER 5

TRANSITION METAL DIBORIDES*

5.1 Introduction

Transition metal diborides with the simple AlB_2 structure type have been studied since the late 1940s. These early works focused primarily on the mechanical properties of these materials, because they have high microhardnesses and are very refractory, making them useful in high temperature applications [1, 2, 3]. The transition metal diborides are also of interest, since they form an isostructural series that runs from Sc through Fe in the first row of transition metals. Thus, these materials offer a rare opportunity to study the variation in electronic properties within this single structure type as one move along the series.

More recently, however, the diborides are being reinvestigated after the discovery of the MgB_2 phase as an intermetallic superconductor with an exceptionally high-transition temperature near 40 K [4]. MgB_2 and the transition metal diborides of Cr, Fe, Mn, Mo, Nb, Sc, Ta, Ti, V, W, Y, and Zr all form in the simple hexagonal AlB_2 structure type. With the exception of Nb, none of the other transition metal diborides have been confirmed as superconductors [5]. There have been further attempts to prepare new superconducting borides. The reports are still controversial, with some authors reporting superconductivity in one compound and others finding the material normal [5]. This has been the case with TaB_2, which was found to be a normal metal in earlier experiments (Leyarovska and Leyarovski 1979) and recently discovered to have a transition temperature of Tc = 9.5 K (Kaczorowski et al 2001b). A similar situation applies for ZrB_2, found to be non-superconducting by Kaczowski et al (2001b) and superconducting at 5.5 K by Gasporov et al. [6].

*portions reprinted by permission of IOP Publishing Limited.

BeB_2 did not superconduct in stoichiometric form (Fener 2001), but superconductivity at 0.7 K was found for the composition $BeB_{2.75}$ [7]. Nb_xB_2 and $Mo_{0.96}Zr_{0.04}B_2$ are found to superconduct with Tc = 8.5 K and Tc = 5.9 K, respectively [8]. The non-stoichimetry requirement for optimized superconducting properties is frequently observed in low-Tc as well as in high-Tc superconductors.

As explained earlier, the transport properties of the samples depend sensitively on their quality. Nice single crystals of some transition metal diborides were grown by metallic fluxes and their transport properties were measured. In the following sections there are reports on the synthesis and characterization of single crystals and polycrystalline samples of transition metal di-boride compounds CrB_2, VB_2, TiB_2, TaB_2, MoB_2, OsB_2, NbB_2 and ZrB_2 and doped systems.

5.2 $Cr_{1-x}V_xB_2$

5.2.1 Introduction

The theoretical predictions on the possibility of superconductivity in many compounds have been normally made on the basis of electronic structure, density of states and electron – phonon interaction. There are some materials in which superconductivity appears by the modification of the above mentioned electronic properties due to external pressure and /or chemical doping. It is believed that superconductivity in MgB_2 is due to the electron-phonon interaction. Hole doping in AlB_2-type transition metal diborides lowers the Fermi level to lower energies and hence the density of states increases at the Fermi level, which may result in the appearance of superconductivity due to the electron-phonon interaction [9]. In the case of some antiferromagnetic materials, the *Neel* temperature can be tuned by applying physical and/or chemical pressure. When the Neel temperature becomes zero at some critical value of pressure or doping concentration, a quantum mechanical phase transition occurs in the material and a superconducting phase can appear in the vicinity of a quantum critical point (QCP) [10].

Different studies confirmed that CrB_2 orders antiferromagnetically below 85 K, while VB_2 shows paramagnetic behavior over the entire temperature range [11]. There are no reports of superconcoductivity in either of these compounds. If VB_2 does superconduct, then it is predicted to do so at temperatures <1 K [10]. Casting *et al*. reported that the antiferromagnetic ordering in CrB_2 disappears at 23% V doping [14]. A series of doped samples $Cr_{1-x}V_xB_2$ in the range of x = 0 to x = 1 were synthesized and characterized to investigate the superconductivity and transport properties. The high quality of the samples has allowed us to experimentally determine the Fermi surface of VB_2 and compare it to theoretical calculations [13]. An unusually large magnetoresistance is observed at low temperature in the highest quality crystals.

5.2.2 Synthesis

The single crystals of $Cr_{1-x}V_xB_2$ (x = 0, 0.1, 0.2, 0.4, 0.5, 0.97, and 1) were synthesized by a metallic flux technique using molten aluminum at high temperature. This is a standard synthesis method for refractory borides. The starting materials consisted of V and Cr turnings (99.7% CERAC, INC.), amorphous B powder (99.99% Alfa AESAR), and Al shot (99.999% Alfa AESAR). Stoichiometric amounts of V, Cr and B were placed in an aluminum oxide crucible with excess Al shot. The molar ratio of the starting elements to Al was 1:70. The crucible was then placed at the center of a vertical tube furnace and heated in an inert atmosphere of flowing ultrahigh purity argon gas. The samples were heated from room temperature to 1400 ˚C in 6 h and maintained at that temperature for 10 h, followed by cooling to 1000 ˚C at a rate of 50 ˚C h^{-1}. The slow cooling rate aids in the growth of larger single crystals. The furnace was shut off and allowed to cool to room temperature. The single crystals were extracted from the solid aluminum by etching it away with a hot solution of NaOH. The crystals were collected and their surfaces were cleaned by etching in very dilute nitric acid. Finally, the crystals were washed,

rinsed with ethanol, and dried. Shown in Figure 5.1 are the single crystals of VB_2 grown both as rods and flat plates, with typical dimensions on the order of 1 mm × 1 mm× 4 mm.

5.2.3 Characterization

The structure and the phase purity of the samples were verified by single crystal and powder X-ray diffraction. A small crystal fragment is glued to a glass fiber and mounted on the goniometer of a Nonius Kappa CCD diffractometer equipped with Mo K_α radiation (λ = 0.71073 Å). Data were collected at 290 K and 90 K.

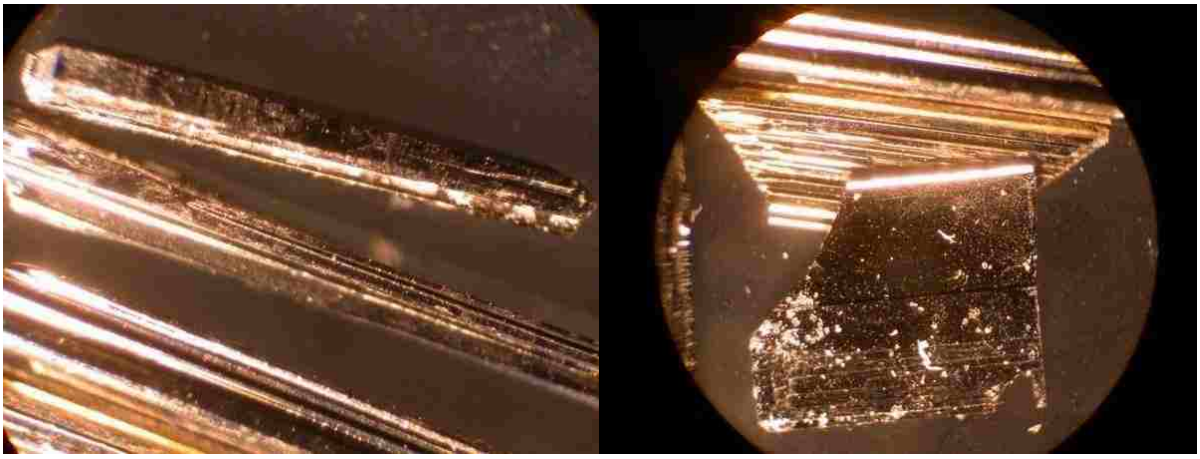

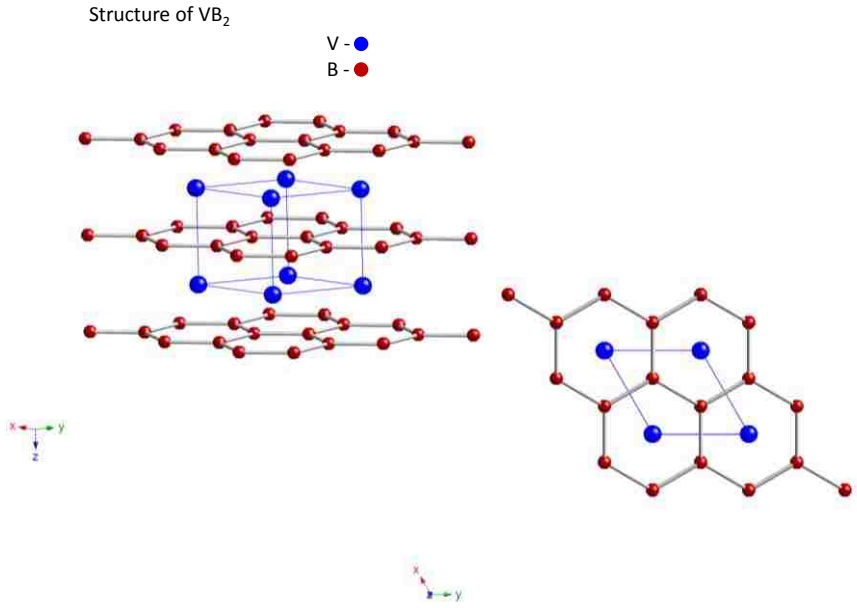

Fig: 5.1 Single crystals of VB_2 (Top) and Fig: 5.2 AlB_2 type- crystal structure of VB_2 (bottom).

The dc magnetic susceptibility was measured using the PPMS between 1.8 K and 10 K in a 20 Oe applied field to check for superconductivity. Then, to investigate the change in the magnetic ordering temperature, the dc magnetic susceptibility was measured between 2 K and 300K in 1000 Oe. We placed a bunch of single crystals in the ACMS sample holder, while an arc-melted sample was cut into a parallelepiped shape with dimensions: length = 3 mm, width = 1.5 mm and thickness = 0.3 mm. It was taped in a plastic straw for magnetization.

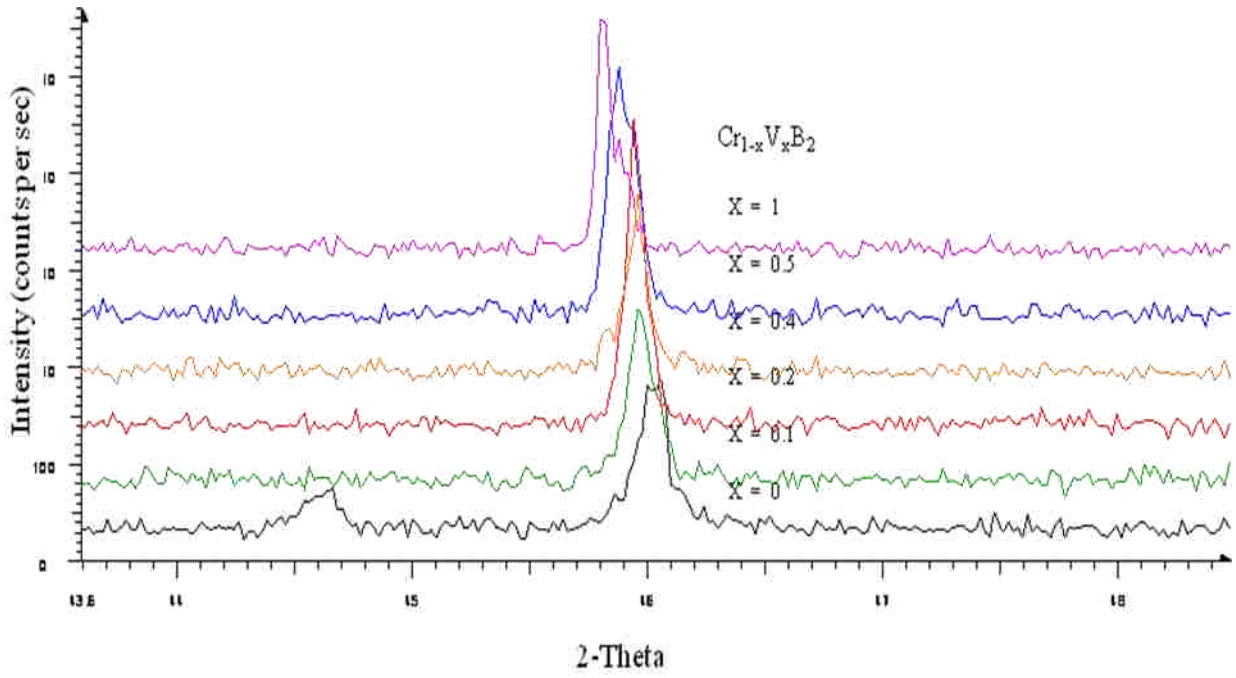

Fig: 5.3 Peak shift in powder X-ray pattern of polycrystalline $Cr_{1-x}V_xB_2$ samples due to doping.

Electrical resistivity and magneto-resistivity were measured using a standard 4-probe technique. 0.002-inch size platinum wires were attached to the sample using a conductive epoxy (Epotek H20E) for the current and voltage leads. Data were collected from 1.8 to 290 K and in magnetic fields up to 9 T using the PPMS system. The resistivity and magnetoresistivity were measured along the c-axis and b-axis of the single crystal of VB_2 applying the magnetic field in the direction perpendicular to the axis. The magnetoresistance was measured at 3 K, 100 K and

290 K from 0 to 9 T. Resistivity of a single crystal of VB_2 was also measured at 9 T in tilted field from 0˚ to 90˚ with respect to c-axis using a rotating sample puck .

dHvA measurements for single crystals of VB_2 were performed at the National High Magnetic Field Laboratory, Los Alamos, New Mexico. Measurements were taken using pulsed magnetic fields extending to 55 T in the temperature range from 450 mK to 6 K using a plastic [3] He refrigerator.

5.2.4 Results and Discussions

Room temperature X-ray diffraction (XRD) patterns for the $Cr_{1-x}V_xB_2$ with x = 0, 0.1, 0.2, 0.4, 0.5, and 1 are shown in Figure 5.3. All the samples crystallize in simple hexagonal AlB_2-type structure with space group P_6/mmm. With successive substitution of V at the Cr site in $Cr_{1-x}V_xB_2$, the structure and space group remain the same, although all XRD peak positions are shifted towards lower angle side, indicating a increase in lattice parameters.

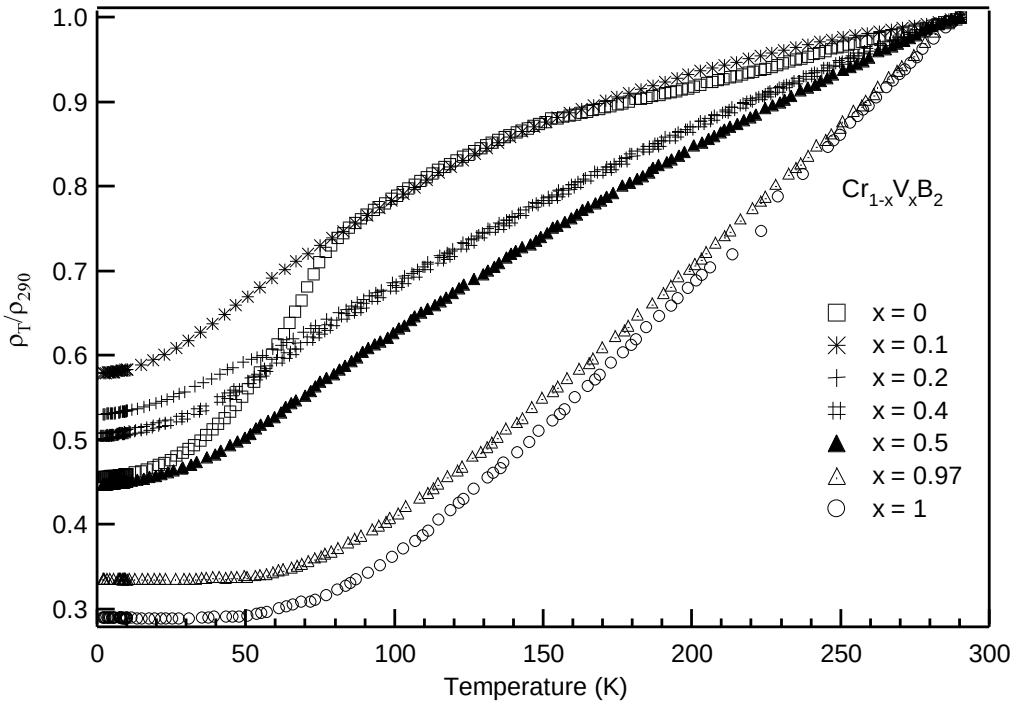

Fig: 5.4 Temperature dependence of normalized resistivity of arcmelted $Cr_{1-x}V_xB_2$ samples.

The lattice parameters of single crystal of VB_2, measured at the temperatures 298 K and 90 K are shown in table 2.

The resistivity versus temperature plots of the $Cr_{1-x}V_xB_2$ with x = 0, 0.1, 0.2, 0.4, 0.5, 0.97, and 1 are shown in Figure 5.4. All samples show metallic behavior over the entire temperature range. As reported in [14], magnetic susceptibility and resistivity measurement data show that CrB_2 has an antiferromagnetic transition around 85 K, and VB_2 is paramagnetic over the entire range of temperature. The *Neel* temperature (T_N) decreases with V concentration in $Cr_{1-x}V_xB_2$, and antiferromagnetic ordering completely disappears with x higher than 0.23. Samples with x higher than 0.23 are found paramagnetic, and no superconducting transition is observed above 1.9 K.

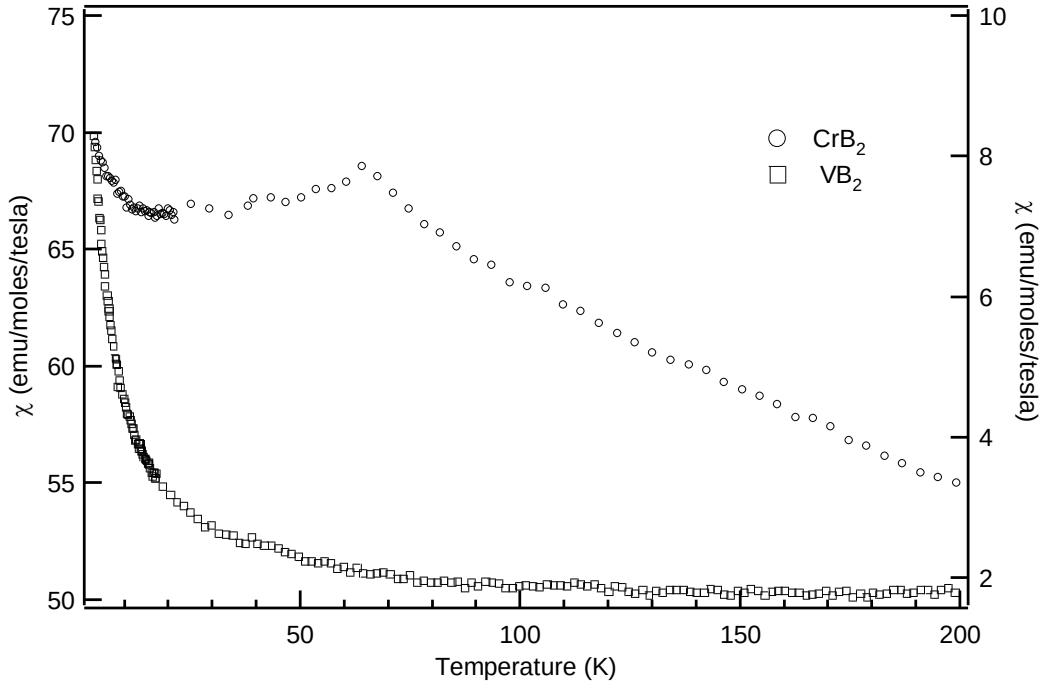

Fig: 5.5 Magnetic susceptibilities of CrB_2 (left axis) and VB_2 (right axis).

The electrical resistivity data of the VB_2 single crystals and polycrystalline samples measured from 290 K down to 1.9 K are shown in Figure 5.6. The samples are metallic, and no superconductivity was observed.

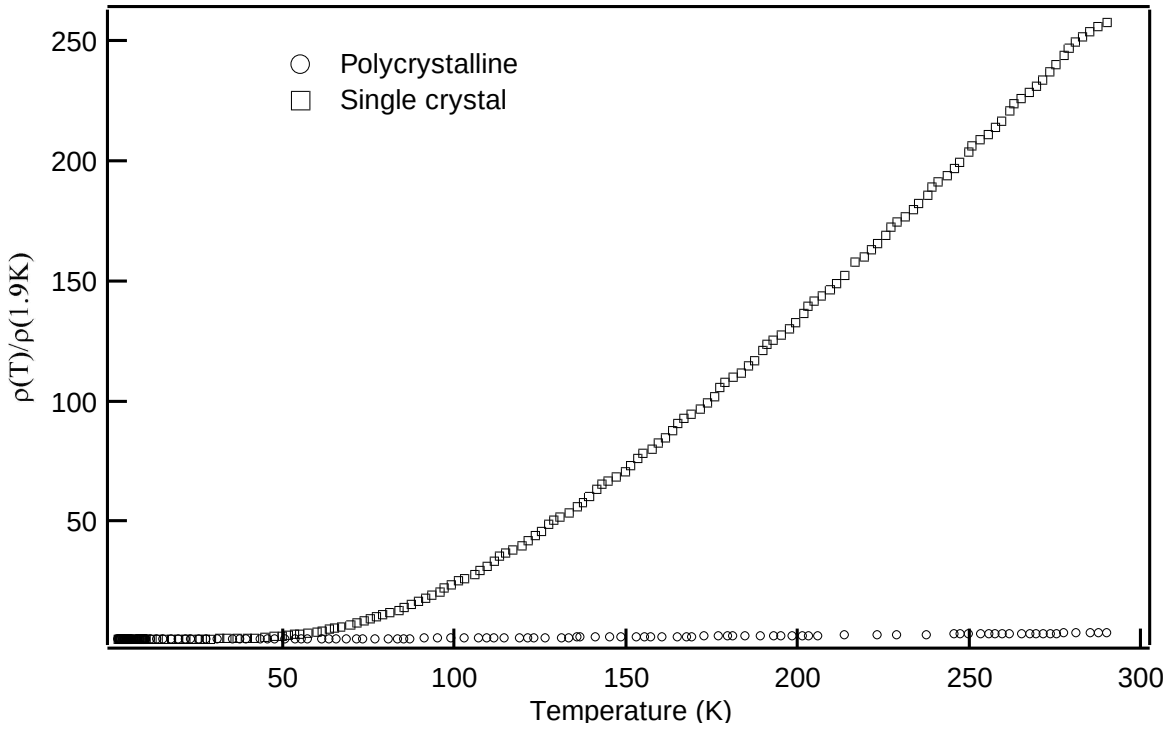

Fig: 5.6 Resistivity Ratios of a single crystal and an arc-melted sample of VB_2.

The residual resistivity ratio (RRR), which is defined as *RRR = ρ (290 K)/ρ (1.8K)* varied from crystal to crystal, with typical values falling in the range of 100 –150. Samples with RRR values as high as 258 were measured, and indicate excellent sample quality. The RRR for polycrystalline sample is just 3.8.

Typical fast Fourier transforms (FFTs) of the dHvA data for B // [001] and *B* // [010] giving the frequencies reported here are shown in Figure 5.7. The frequencies of the dHvA oscillations are proportional to extremal areas of the Fermi surface perpendicular to the applied field direction. From the temperature dependence of the amplitudes of the FFT peaks, the effective masses were obtained. Table 1 gives a summary of the measured frequencies and effective masses for each field orientation. From the band structure of VB_2 calculated using the WIEN2K full potential LAPW band package, [11] using the GGA exchange correlation potential [15] it is observed that the density of states at the Fermi level are derived almost entirely from

the d-bands of vanadium, in contrast to the case in MgB_2, where the high energy part of the valence band is made up predominantly of boron 2p states [13, 17].

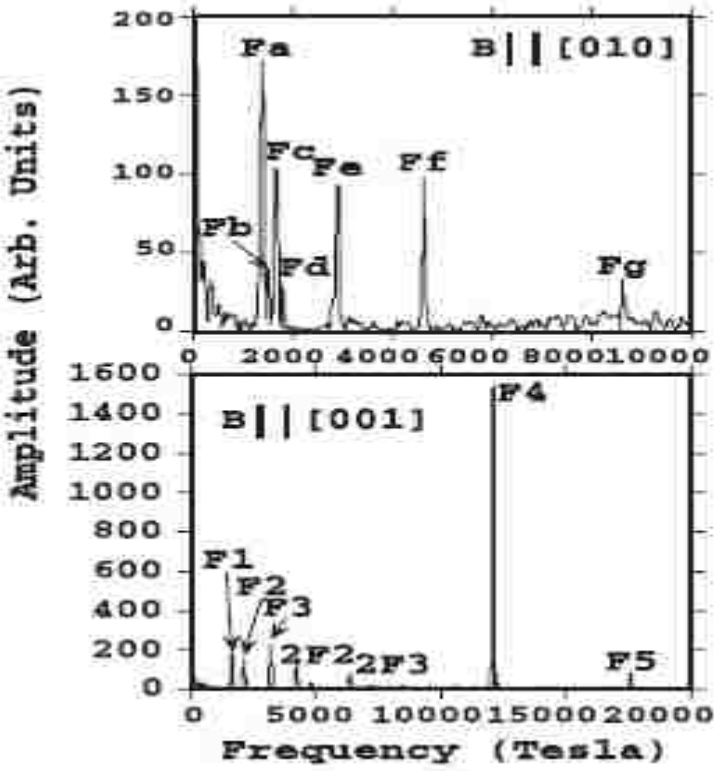

Fig: 5.7 FFTs of the dHvA data for B∥[010] and B∥[001]. The symbols are the names assigned to each fundamental frequency and some harmonics.

Table 5.1 Measured dHvA frequencies and effective masses for single crystalline VB_2. The left side of the table corresponds to B∥[001], and the right side corresponds to B∥[010].

$B \parallel [001]$			$B \parallel [010]$		
	Freq. (T)	$m^* = m/m_0$		Freq. (T)	$m^* = m/m_0$
F1	1668	0.58 ± 0.01	Fa	1404	0.53 ± 0.02
F2	2127	0.380 ± 0.008	Fb	1510	0.33 ± 0.04
F3	3200	0.491 ± 0.007	Fc	1662	0.36 ± 0.02
F4	12105	1.10 ± 0.04	Fd	1819	0.44 ± 0.05
F5	17613	1.7 ± 0.3	Fe	2898	0.74 ± 0.05
			Ff	4639	1.00 ± 0.14
			Fg	8625	1.05 ± 0.10

Calculations were performed using both the room temperature lattice constants and also the lattice constants measured at 90 K [16]. The results of these calculations are presented in Figure 5.8 for the bands and Figure 5.9 for the density of states.

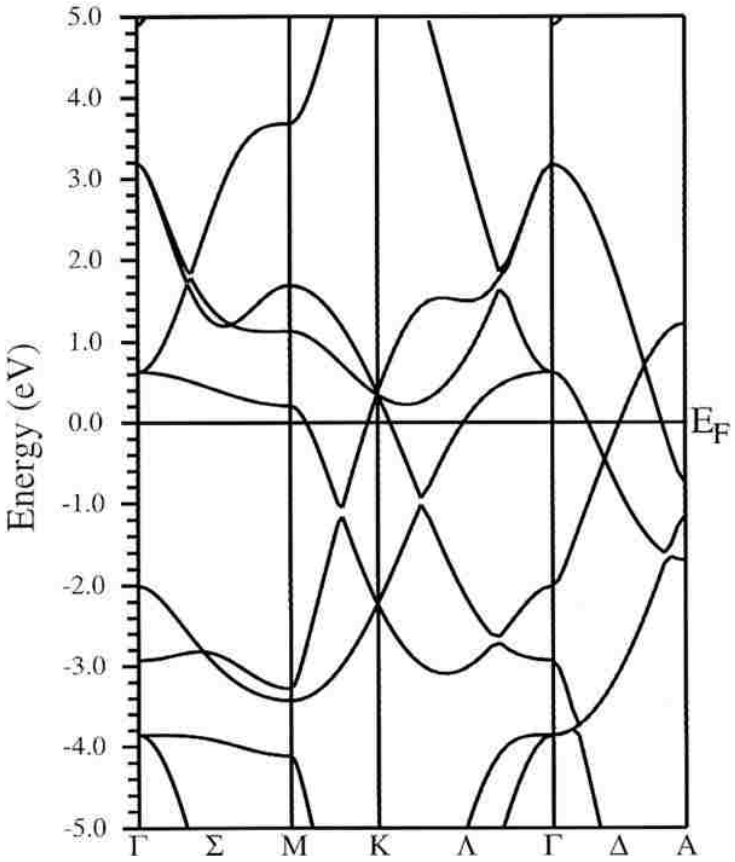

Fig: 5.8 The calculated electronic band structure of VB_2 in the vicinity of the Fermi level. Designations on the horizontal axis represent high symmetry directions in the hexagonal Brillouin zone [13].

It is observed that because of the relatively flat bands near the Fermi level, some of the Fermi surface areas change substantially (15%) as the lattice constants are changed by less than 1%. For example, the empty band just above the Fermi level from Gamma to M reaches the M-point just above the Fermi level, resulting in a small hole pocket there. Changes in the lattice constants by less than 1% can result in this pocket of holes vanishing.

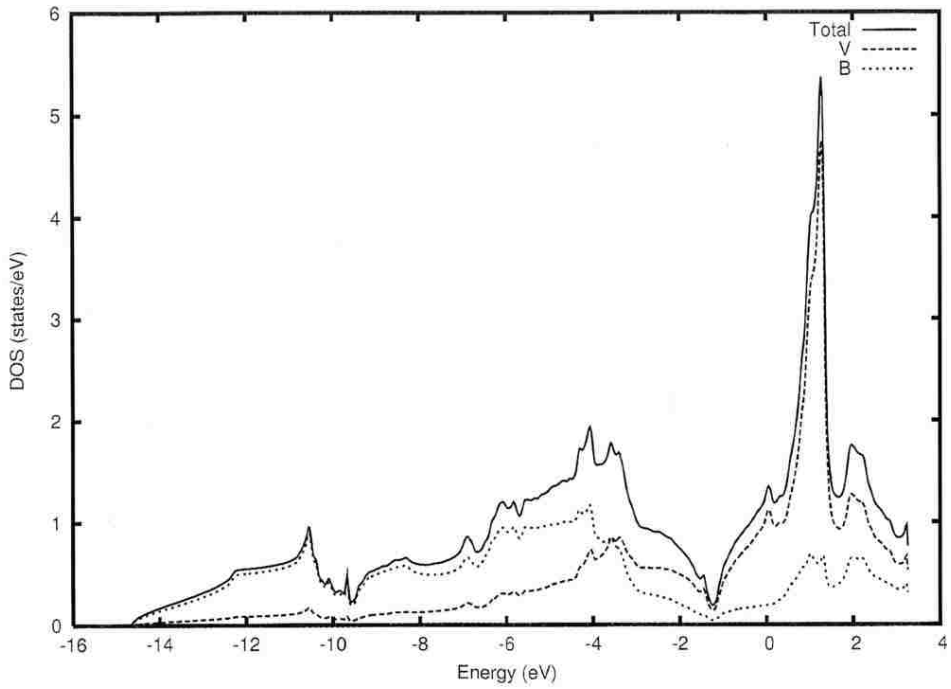

Fig: 5.9 The calculated total (solid line) and partial density of states for VB_2. The large peak in the density of states near the Fermi level is almost entirely composed of V d-orbitals [13].

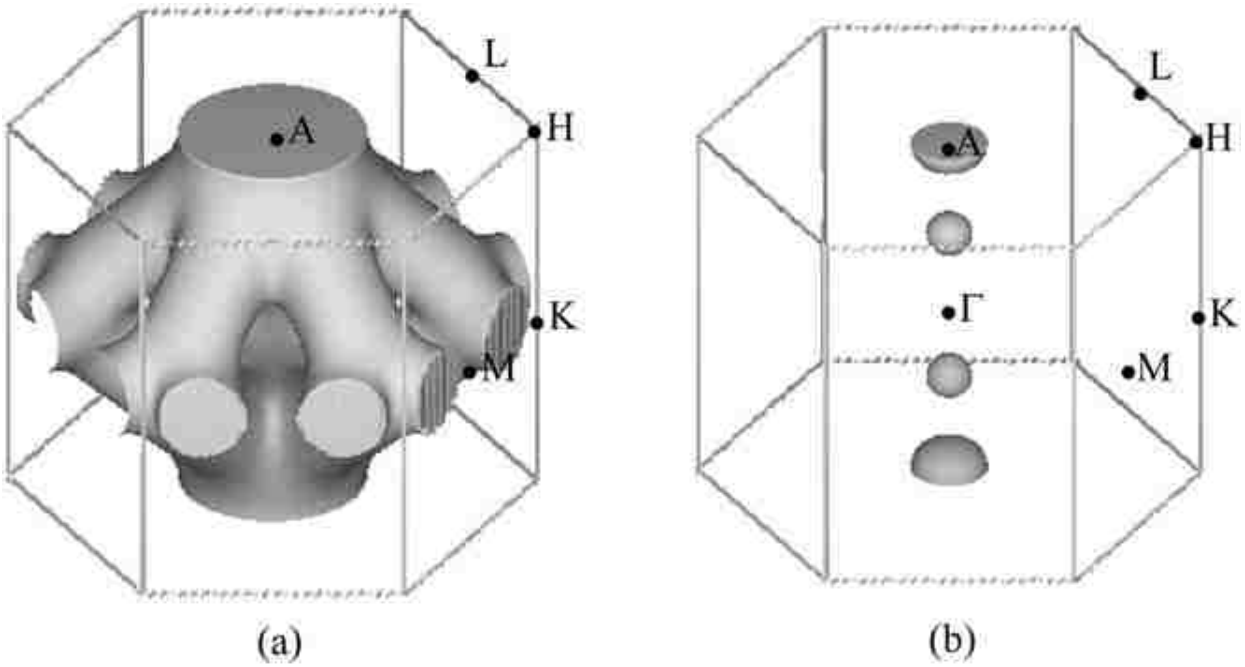

Fig: 5.10 Fermi surface of VB_2. a) The main section of the Fermi surface using the lattice constants measured at 90 K which resembles a six-sided tree trunk. b) The other sections are nearly spherical pockets of electron states where one pair is located at $q_z = \pm 0.16\pi/c$, and the other two are located on the upper face of the Brillouin zone at $q_z = \pi/c$[13].

Thus, while most of the overall topology of the Fermi surface agrees among the four calculations, the theoretical predictions of the Fermi surface shape are not in excellent agreement with the measured values [13]. The sensitivity of Fermi surface to lattice constant was not considered by other authors in their calculations done on VB_2 using other basis sets [12, 18, 19].

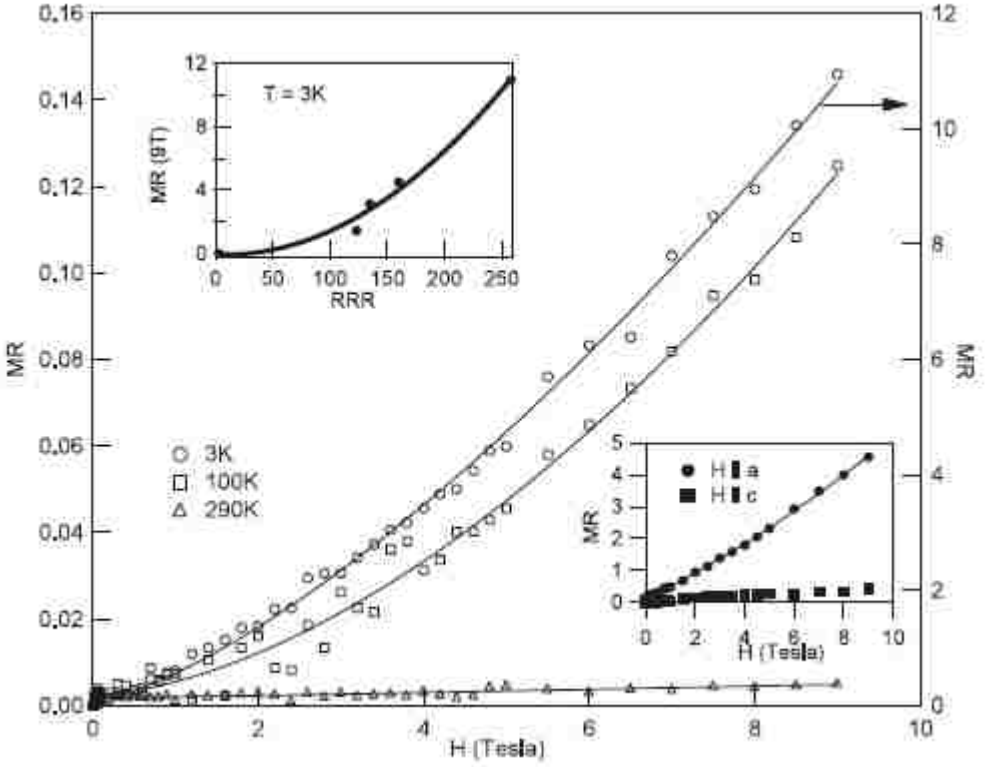

Fig: 5.11 Dependence of isothermal magnetoresistance (MR) of VB_2 on magnetic field at different temperature with H//a and I//c. The solid lines in the main panel and the two insets are fits proportional to H^2. Upper inset: shows the values of the MR measured at 3 K and 9 T versus the RRR value of several different single crystals and polycrystalline samples of VB_2. Lower inset: shows the large anisotropy in the magnetorsistance of a single crystal of VB_2 at 3 K for the field applied along the a-and c-axis [13].

The magnetotransport properties of VB_2 are shown in Figure 5.11. All the transport properties measurements were made with the current parallel to the *c*-axis. The magnetoresistance (*MR*), which is defined as $MR = [(\rho(H) - \rho(0))/\rho(0)]$, plotted versus applied magnetic field is shown at different temperatures for a single crystal of VB_2 with a RRR value of 258. At all temperatures, the magnetoresistance increases with applied field and decreases with

increasing temperature. At 3 K (right axis, Figure 5.11) the magnetoresistance at 9 T is unusually large (~1100%) and shows no tendency toward saturation. In general, classical theory predicts that the high field transverse magnetoresistance of a normal metal depends on the Fermi surface topology [20]. The magnetoresistance should saturate at high fields for closed orbits, or continue to increase as H^2 for open orbits. The solid lines in the main panel of Figure 5.11 are quadratic fits to the data, showing that the MR does indeed increase as H^2 up to a field of 9 T, suggesting open orbits for the field applied along the *a*-axis. The lower inset in Figure 5.11 demonstrates the large anisotropy in the magnetotransport for a single crystal of VB_2 at 3 K. The quadratic field dependence observed in the MR for $H \parallel a$ is not observed for $H \parallel c$, but a much weaker field dependence occurs. This is also consistent with the calculated Fermi surface. The calculation indicates that for a field in the [100] direction, an open orbit exists that runs along the trunk of the Fermi surface shown in Figure 5.10. For the [110], or *b* direction, this open orbit is absent. Any disorder in the sample that resulted in 30˚ twins would produce a mixture of open and closed orbits for electrons moving along the trunk. This may well explain the large, unsaturated magnetoresistance observed in these samples. There are six closed orbits for the magnetic fields aligned along the (001) direction. One small hole orbit and another larger electron orbit are found in the $q_z = 0$ plane, surrounding the K-point. This larger one gives rise to the high frequency dHvA signal seen in the experiment. In addition to these orbits, there is an electron orbit at $q_z = \pm 0.16\pi/c$, a hole orbit derived from the same band that gives rise to the trunk like piece of the Fermi surface at $q_z = \pi/c$, and an electron orbit at $q_z = \pi/c$ (Figure 5.10(b)). The areas and frequencies found for these surfaces for each of the four calculations are listed in table 2.

From Figure 5.10(a) it is also apparent that the tubular structure on each side of the main part of the Fermi surface will give a dHvA signal at a field about 30◦ above and below the *ab* plane and that the frequency dependence will vary as $1/\cos\theta$, where θ is the angle measured form the tube

direction. This would confirm the general features of the Fermi surface that we are seeing. The upper inset of Figure 5.11 demonstrates the sensitivity of the MR to the quality of the samples. Generally, a larger RRR value indicates higher crystal quality. Here, the value of the MR measured at 3 K and 9 T is plotted versus the RRR value for several different single crystals of VB_2. The size of the MR increases dramatically with the RRR value. The solid line in the inset represents the following fit to the data: MR = α (RRR) [4], where $\alpha = 1.65 \times 10^{-4}$.

Table 5.2 Calculated frequencies with magnetic field in different directions for experimentally determined lattice constants of VB_2 (columns 1,2, and 4) and for the theoretically determined equilibrium lattice constants (column 3).

	90K lattice constants	Room temperature lattice constants	Theoretical equilibrium	Lonmburg
a (Å)	2.998	3.000	3.006	2.998
c (Å)	3.044	3.062	2.997	3.055
Field along 001				
Large orbit at K (T)	15 900	16 400	14 100	16 500
Small orbit at K (T)	207	225	290	111
Large orbit on trunk at π/c (T)	10 400	10 400	9300	11 470
Larger ellipsoid at π/c (T)	1980	1970	1820	2270
Smaller ellipsoid at π/c (T)	1510	1520	1400	1710
Sphere at $q_z = 0.45\pi/c$ (T)	1100	1250	790	1590
Field along 100/210				
Larger ellipsoid at π/c (T)	1640	1670	1440	1920
Smaller ellipsoid at π/c (T)	1340	1360	1190	1550
Sphere at $q_z = 0.45\pi/c$ (T)	920	1150	700	1460
Interior below trunk (100 only) (T)	5000	4750	5540	4100
'Roots' on face (100 only) (T)	2400	2550	2100	2890
Around outside of trunk (210 only) (T)	20 500	21 500	18 000	24 300

In many metals the MR behavior is known to follow Kohler's rule i.e. $\Delta\rho/\rho(0) = f(H/\rho(0))$ [21]. Attempts to show that Kohler's rule is obeyed were inconclusive due to the scatter in the data at low fields. However, the correlation that exists between the MR and the RRR values suggest this to be the case. Based on Kohler's rule, the isothermal magnetoresistance should obey the following: $\Delta\rho/\rho 0 \sim (H/\rho_0)^2$. For metals, $\rho(0) \sim (1/l)$, where l is the mean free path. Thus, the magnetoresistance should follow: $\Delta\rho/\rho_0 \sim (Hl)^2$. The RRR value is proportional

to the mean free path (l) at low temperatures, so that $\Delta\rho/\rho_0 \sim (\mathrm{RRR})^2$, which is the behavior we observe (Figure 5.11 inset).

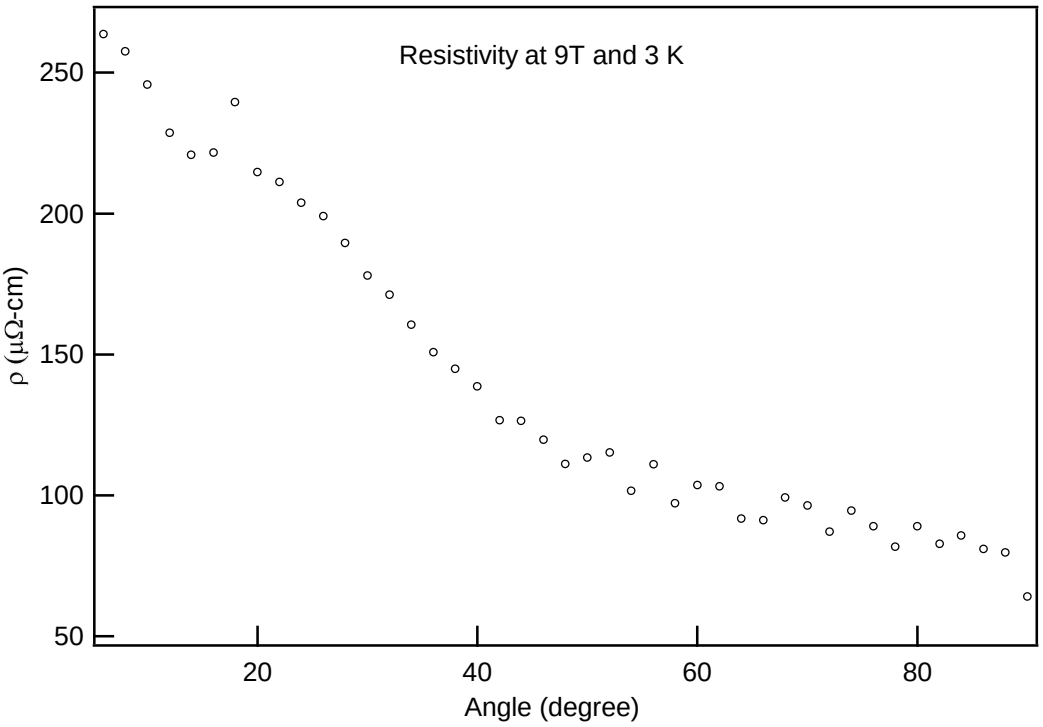

Fig: 5.12 Dependence of magnetoresistance (MR) of VB_2 on the direction of the applied magnetic field 9 T.

As shown in Figure 5.12, anisotropy in the single crystal of VB_2 is evident by the variation of the magnetoresistivity of the crystal with direction of the applied magnetic field with respect to c-axis measured at 9 T.

5.3 Other Transition Metal Diborides

Contradictory theoretical and experimental reports on superconductivity of some transition metal diborides persuaded me to continue the investigation of the superconductivity on those compounds and doped systems. Polycrystalline samples of $Ti_xZr_{1-x}B_2$, $TiB_{2-x}C_x$ and $VB_{2-x}C_x$ were arc-melted and their transport properties were measured. Very nice single crystals of $V_{1-x}Nb_xB_2$ were grown by Al flux following the same procedure used to grow VB_2. Structure and

phase purity of the samples were verified by powder X-ray diffraction. A systematic peak shift in the XRD pattern and the systematic change in electrical resistivity of each series with respect to x confirm the effective substitution. No superconductivity is observed in any of the compounds. However, magnetoresistances of the $Ti_xZr_{1-x}B_2$ system are found to be very interesting. Magnetoresistances of $Ti_xZr_{1-x}B_2$ for x = 0, 0.01, 0.03, 0.05, 0.07and 0.1 are shown in Figure 5.13. For the 5 % Zr doped sample the MR is around 30 % at 290 K, which is higher than that of a normal metal at room temperature, so it will be interesting to further investigate the magnetoresistance of this material.

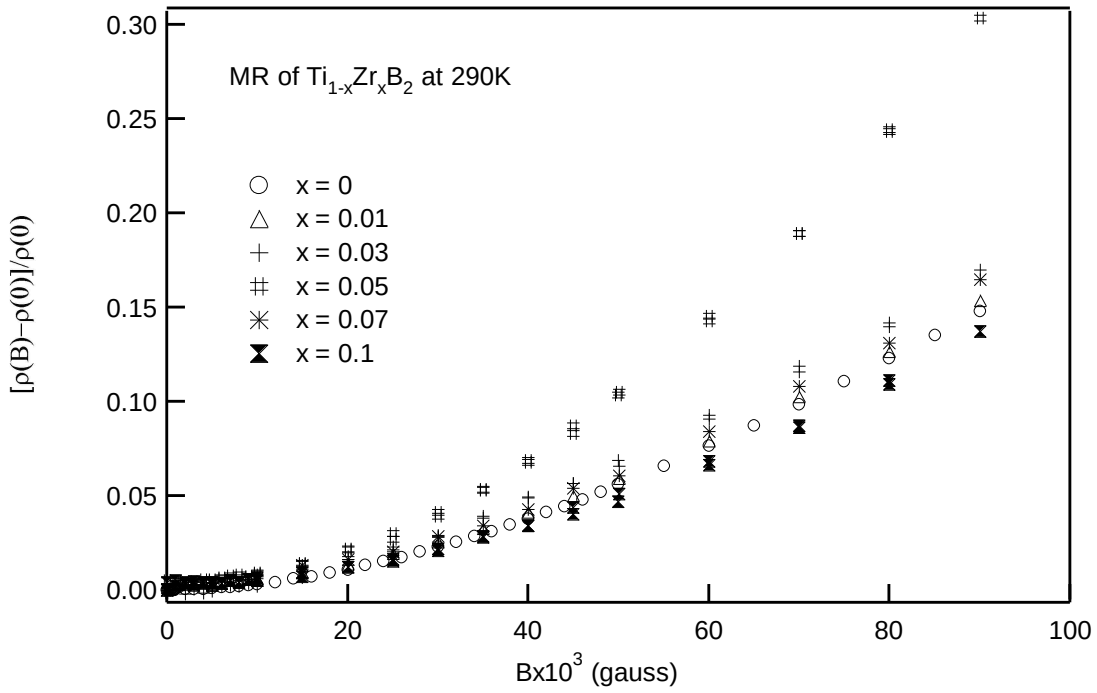

Fig: 5.13 Field dependence of magnetoresistance (MR) of $Ti_{1-x}Zr_xB_2$ samples at 290K.

5.4 Conclusions

The measurements of XRD, magnetization and resistivity of $Cr_{1-x}VB_2$ x = 0, 0.1, 0.2, 0.4, 0.5, 0.97, and 1 are presented. The Neel temperature of CrB_2 was tuned to zero by doping V but no superconductivity was observed above 1.9 K. I have succeeded in growing very high quality

single crystals of VB_2 and experimentally determined the Fermi surface via dHvA measurements. Some of the crystals had a RRR value in excess of 250. Electronic structure calculations confirm that the density of states near the Fermi surface is dominated by vanadium d-orbitals, unlike the case of MgB_2. Magnetotransport measurements show a very large magnetoresistance at low temperatures which scales quadratically with the residual resistivity ratio. Given the large sensitivity of the Fermi surface topology to the lattice constants, I am motivated in future work to investigate the magnetotransport properties of VB_2 under pressure.

The literature and the experience in synthesis and characterization of a lot of transition metal diborides show that the physical properties of the compounds depend clearly on the purity of samples. Single crystals of some transition metal diborides can be grown by RF-heated floating-zone method in our lab.

5.5 References

[1] Vasilos T and Rhodes W H 1973 *Am. Ceram. Soc. Bull.* **52** 643

[2] Nakano K, Matsubara H and Imura T 1976 *J. Less-Common Met.* **47** 259–64

[3] Lisy F, Abada A and Vedula K 1987 *J. Met.* **39** A61

[4] Nagamatsu J, Nakagawa N, Muranaka T, Zenitani Y and Akimitsu J 2001 *Nature* **410** 63–4

[5] Buzea C and Yamashita T 2001 *Supercond. Sci. Technol.* **14** R115

[6] Gasparov V A, Sidorov N S, Zver'kova II, Kulakov M P 2001 *JETP Letters* **73** (10): 532-535

[7] Young D P, Goodrich R G, Adams P W, Chan J Y, Fronczek F R, Drymiotis F, Henry L L 2002 *Physical Review B* **65** (18): Art. No. 180518

[8] Singh P P 2004 *Physical Review B* **69**, 094519

[9] Mudgel M, Awana V P S, Lal K, Kishan H, Sharth Chandra L S, Ganesan V, Narlikar A V 2008 *cond-mat/ arXiv:0801.2629*

[10] Ohira-Kawamura S, Shishido H, Yoshida A, Okazaki R, Kawano-Furukawa H, Shibauchi T, Harima H, Matsuda Y 2007 *Phyical Review B* **76**, 132507

[11] Blaha P, Schwarz K, Madsen G K H, Kvasnicka D and Luitz J 2001 *WIEN2K, An Augmented-Plane-Wave + Local Orbitals Program for Calculating Crystal Properties* Karlheinz Schwarz, Techn.Wien, Austria (ISBN 2-9501031-1-2)

[12] Mahmud S T, Islam A and Islam F N 2004 *J. Phys.: Condens Matter* **16** 2335–44

[13] Karki A B, Gautreaux D P, Chan J Y, Harrison N, Browne D A, Goodrich R G, Young D P 2008 *Journal of Physics : Condensed Matter* **20** 000000 (5pp)

[14] Casting J, Costa P, Hertier M, Lederer P 1972 *J.Phys.Chem.Solids* **33** 533-547[11] See, for example Shoenberg D 1984 *Magnetic Oscillations in Metals* (Cambridge: Cambridge University Press)

[15] Perdew J P, Burke K and ErnzerhofM 1966 *Phys. Rev. Lett.* **77** 3865

[16] Lonnberg B 1988 *J. Less-Common Met.* **141** 145

[17] Medvedeva N I, Ivanovskii A L, Medvedeva J E and Freeman A J 2001 *Phys. Rev.* B **64** 020502(R)

[18] Vajeeston P, Ravindran P, Ravi C and Asokamani R 2001 *Phys. Rev.* B **63** 045115–26

[19] Shein IR and Ivanovskii AL 2002 *Phys. Solid. State* **44** 1833–9

[20] See, for example Abrikosov A A 1988 *Fundamentals of the Theory of Metals* (Amsterdam: North-Holland)

[21] Lifshits I M and Peschanskii V G 1959 *Sov. Phys.—JETP* **8** 875

CHAPTER 6

FUTURE WORK

The substantial enhancement of the superconducting transition temperature, T_c, and the upper critical field, H_{c2}, of Mo_3Sb_7 in the form of wires, thin films and coatings in microfibers was observed. Experimental results that spin fluctuations is reduced in the low dimensional forms with higher T_c. I speculate that the origin of T_c enhancement is the reduced spin fluctuations due to the stress [1,2,3,4,5]. Further experiments will be necessary to strengthen these speculations. On the other hand, the 60-nm thick film of Mo_3Sb_7 shows 61% MR and a non-uniform field-dependent Hall voltage at low temperature. It will be interesting to investigate the behavior of the MR and Hall voltage (also the carrier density) with the variation of thickness of the film. This may provide additional base to understand the origin of high T_c in this system.

To have samples which are free from artificial effects due to strain or impurities, we need single crystals to study the anisotropic, or directionally dependent properties of the system. The synthesis of polycrystalline $MgCNi_3$ requires an excess of both Mg and C to compensate for Mg evaporation and to ensure carbon incorporation. Therefore, controlled doping at both the Mg site and the C site has been found difficult. Due to the high volatility of Mg, the growth of single crystals of $MgCNi_3$ and the doped systems is difficult. Recentlty, Hyun-Sook Lee *et al.* have reported the synthesis of $MgCNi_3$ single crystals under high-pressure 4.25 GPa and 1200 ^oC[6]. The crystals are in few hundred micrometers in size [6].

I have been exploring and designing an experimental set up to grow single crystals by a self flux technique in the vertical tube furnace in our lab. As explained in chapter 4 the starting materials Mg, C and Ni in stoichiometric ratio are put in a 10-mL alumina crucible with a lid. Ni metal itself is used here as flux. The crucible is sealed in a Ta crucible of a larger size in an Ar atmosphere in a glove box. The sealed crucible is placed inside the vertical tube furnace and

heated under flowing Ar. The heat treatment is as follows. The first set point temperature 1400 ^{o}C is reached at 5h and then heated in this temperature for 25 h. The sample is then cooled down to 650 ^{o}C at the rate 50 ^{o}C per hour and the furnace is shut down. The single crystals are then extracted out dissolving the flux in a mixture of weak HNO_3 and HCl. The profiles tested thus far have failed to produce crystals.

The discovery of superconductivity in MgB_2, $MgCNi_3$ and $Mg_{10}Ir_{19}B_{16}$ motivated a search for new superconducting materials containing light elements such as magnesium, boron, and carbon [7,8,9]. All three of these Mg intermetallic superconductors contain refractory elements like boron and carbon with different crystal structures. This reflects the future of the research of these systems. As I explained in chapter 1, I synthesized a few of existing intermetallic compounds of magnesium and checked for the superconductivity by low temperature susceptibility at the magnetic field of 20 Oe. Additionally, the exploration of new compounds of magnesium is also in progress. Since a few of them have shown some signature of superconductivity, these materials will be worthy of exploration.

Conventional electronics utilize semiconductor devices, such as silicon-based integrated circuits, that rely on the manipulation of the charge on the conduction electrons. Information storage technology, on the other hand, is achieved by magnetic recording using the spins of the electrons in ferromagnetic metals. More recently, the emerging field of "spintronics" [10] is attempting to use both attributes of the electron – the charge and spin. A successful fusion of these technologies would enhance device performance and allow the capability of mass data storage and information processing simultaneously.

One class of boride compounds that shows promise as a potential spintronic material is the system MB_6, where M is an alkaline earth metal. These compounds form in a simple cubic *CsCl*-type structure, where the metal atom sits at each corner of the cube, and a boron octahedron

occupies the center. Until recently, however, much less has been known about the divalent alkaline earth hexaborides (CaB_6, SrB_6, BaB_6). One would naively expect these compounds to be insulators based on simple electron counting, however, electronic structure calculations have predicted both insulating and semimetallic behavior for these materials [11-12]. Therefore, experimentally, we might expect vacancies and foreign-atom additions to alter significantly the transport properties of the divalent hexaborides even for very small doping levels.

Young et al [13] pointed out that the largest moments were found for the same critical concentration x_c in trivalent La-, Ce- and Sm- doped CaB_6 and SrB_6, where each dopant ion introduces a single electron. A spontaneous magnetization develops whose ferromagnetic ordering temperature is incredibly high (~600 - 1000 K) [13,14]. The saturation moment is small and sensitive to the La concentration, peaking at ~0.1 μ_B/mol-La for the 0.5% doping level. This is remarkable when one considers that none of the constituent elements in these materials is associated with a local magnetic moment, i.e. no partially filled *d*- or *f*-orbitals. Thus, one is led to believe that the ferromagnetism is due to, at least a partial, polarization at low carrier density of the Fermi surface, i.e. the itinerant charge carriers. The discovery of the high-T_c weak ferromagnetism has fueled theoretical interest, with several descriptions emerging. In spite of much theoretical and experimental effort, the origin of the exotic magnetic properties is still under much debate. The suggestion that the high-T_c weak ferromagnetism is of an extrinsic origin, resulting from iron impurities incorporated into the samples during synthesis [15] contradicts with experimental evidence. More recently it has been suggested that the ferromagnetism is driven by intrinsic defects [16-17], either defects on the Ca site or in the boron sublattice.

Irrespective of the origin of the ferromagnetism in AB_6, one now has a carrier-induced ferromagnetic metal with an extremely high ordering temperature. As pointed out by Tromp

[12] *et al*, it should be possible to inject a spin-polarized current from the doped material ($A_{1-x}La_xB_6$) into the undoped material and study the temperature-dependent spin dynamics. The incompatibility of crystal structures [18] in a junction would not be a problem in case of pure and doped hexaborides, given that the materials are isostructural and have nearly identical lattice constants. Furthermore, if a p-type hexaboride were also found to be ferromagnetic (for example, $A_{1-x}K_xB_6$), then it would be possible to make the spin-analogues of bipolar devices [12]. The exploration of the materials aspect of this problem, starting initially with the synthesis of bulk single crystals in the future is interesting. p-type doping in AB_6 with potassium has to be fully explored, as will the correlation between the doping level and the saturation moment. All of the hexaboride single crystals could be grown from molten aluminum flux after a borothermal reduction of the high-purity metal oxides.

In addition to the alkaline earth hexaborides mentioned above, the alkali earth hexaboride KB_6, the new cubic carbaborides of potassium (KB_5C), and their doped variants also have the potential to be useful in applications. These systems are isostructural to the alkaline earth hexaborides, and KB_5C is isoelectronic to CaB_6 [19]. Preliminary electrical resistivity measurements on pressed powder samples of KB_5C indicate that this material is a small band gap semiconductor (E_g = 0.19 eV) [19]. This result supports the Longuet-Higgins and Roberts [20] band structure rule, which states that the boron octahedron in the hexaboride crystal structure requires 20 electrons for a closed-shell configuration. The structural characterization and limited physical properties measurements on these alkali metal borides have been investigated only on powder samples [19,21]. As part of future research, I will attempt to synthesize single crystals of these materials and carefully explore their magnetic and transport properties, especially chemically doped samples to see if ferromagnetism can be induced. Given their similar

structural and electronic characteristics to the hexaborides, we feel these materials are good candidates for high-T_c ferromagnetism.

6.1 References

[1] Berk N F, Schriefler J R 1966 *Physical Review letter* **17** 433

[2] Rietschel H, Winter H 1979 *Physical Review Letter* **43** 1256

[3] Candolfi C, Lenoir B, Dauscher A, Bellouard C, Hejtmanek J, Santava E, Tobola *J Phys. Rev. Lett.* **99** 037006

[4] Trainor R J, Brodsky M B, Culbert H V 1975 *Physical Review Letter* **34** 1019

[5] Beal-Monod M T, Ma S K, Fredkin D R 1968 *Physical Review Letter* **20** 929

[6] Lee H S, Jang D J, Lee H G, Lee S I, Choi S M, In C J K 2007 *Advanced Materials* **19** 1807 – 1809

[7] Nagamatsu J, Nakagawa N, Muranaka T, Zenaitani Y and Akimitsu J 2001 *Nature* 410 63

[8] He T *et al* 2001 *Nature* 411 54

[9] Klimczuk T, Xu3 Q, Morosan E, Zandbergen H W, Cava R J*Cond-mat/papers/0608/0608576*

[10] Prinz G A 1998 *Science* **282** 1660

[11] Massidda S, Continenza A, de Pascale T M, Monnier R 1997 *Z. Phys. B* **102** 83-89

[12] Tromp H J, van Gelderen P, Kelly P J, Brocks G, Bobbert P A 2001 *Phys. Rev. Lett.* **87** 016401

[13] Young D P *et al* 1999 *Nature* 397 412

[14] Ott H R, Gavilano J L, Ambrosini B, Vonlanthen P, Felder E, Degiorgi L, Young D P, Fisk Z, Zysler R 2000 *Physica B* **281-282** 423-427

[15] Matsubayashi K, Maki M, Tsuzuki T, Nishioka T, Sato N K 2002 *Nature* **420** 143

[16] Fisk Z, Ott H R, Barzykin V, Gor'kov L P 2003 *Physica B* **312-313** 808

[17] Lofland S E, Seaman B, Ramanujachary K V, Hur N, Cheong 2003 *Phys. Rev. B* **67** 020410(R)

[18] Ohno H 1998 *Science* **281** 951

[19] Albert B, Schmitt K 1999 *Chem. Mater*. **11** 3406-3409

[20] Longuet-Higgins H C, deV. Roberts M 1954 *Proc. R. Soc. Lond. A* **224** 336-347

[21] Naslain R, Etourneau J 1966 *Serie C:Sciences Chimiques* **263C** 484-487

CHAPTER 7

CONCLUSIONS

Mo_3Sb_7 and MoN were successfully synthesized in the form of wires, thin films and microfibers by exposing them to either Sb or N at various temperatures for different periods to optimize and explore the superconducting and other physical properties. Similarly, a series of $MgCNi_3$ with the substitution of Be and Li for Mg and N for C were prepared by solid state reaction to understand the role of Mg and C in the superconductivity in the system. More than half a dozen of AlB_2-type transition metal diborides and doped samples were prepared by various methods. Some of them grew as nice single crystals and their high quality allowed us to measure the properties which have rarely been reported. Most of them were arc-melted which also offers the opportunity to investigate their physical properties quickly. The synthesized materials were extensively characterized using different techniques such as XRD, SEM, electrical and magnetic transport and magnetic susceptibility measurements. The aforementioned techniques clearly elucidated the single phase and excellent quality with the new results.

The research presented in this thesis is classified within superconductivity and magnetism in condensed matter physics. Nowadays, in the field of superconductivity, intermetallic superconductors are the focus of condensed matter physics because of their stability and practical applications. In this race, superconducting wires and fibers are a head of all in terms of applications. For examples NbTi, Nb_3Sn and MgB_2 wires are being used in high magnetic field applications like MRI. Actually, the success in fabrication and characterization of Mo_3Sb_7-and MoN-coated C microfibers has provided me the opportunity to understand the importance of the sample geometry in the study of superconductivity.

I found the strong dependence of the synthesis route adopted on to prepare a material on its chemical properties. Arc melting is suitable for the materials with high melting point but low

vapor pressure. This technique offers the opportunity for the quick preparation of the sample. Solid state methods are adopted for the compounds made of the elements with high vapor pressure and the elements with high melting point. $MgCNi_3$ can be taken as the best example. Single crystal growth is the best way of producing a high purity sample. Metallic flux and vapor transport are two novel synthetic routes available in our labs for large and high quality single crystal growth. We explored and applied the efficient methods to synthesize Mo based compounds in the form of thin wires, films and coatings in microfibers. The experimental details regarding the structural, electrical and magnetic characterizations of the synthesized single crystals, powders, wires, thin films and coatings in fibers using X-ray Diffraction (XRD), Scanning Electron Microscopy (SEM), electrical and magneto transport measurements and magnetic susceptibility measurements are also elaborated in chapter 2.

XRD confirmed the single phase of the cubic Ir_3Ge_7-type Mo_3Sb_7 and hexagonal δ-MoN. SEM of the Mo_3Sb_7 samples clearly revealed the expansion due to the reaction of Mo with Sb. Mo_3Sb_7 thin wire (13 μm in diameter) and microfiber obtained by the heat treatment at 900 ^oC for 1 h and 20 minutes exhibit the highest T_c ~ 8 K which is substantially higher than the 2.2 K that is reported for the single crystal and powder of Mo_3Sb_7. 60-nm thick Mo_3Sb_7 films produced by the heat treatment at 900 ^oC for 30 minutes also has a T_c close to 8 K. The H_{c2} = 11.2 T for the Mo_3Sb_7 thin wire is the highest among all the Mo_3Sb_7 samples. The suppression of the spin fluctuations in Mo_3Sb_7 is evident by the absence of a parabolic dependence of magnetic susceptibility at 1 T. MoN wires, thin films and coated microfibers obtained by heat treatment at 900 ^oC for 2 h have T_c ~13 K which is consistent with the values reported in literature. To the best my knowledge, this is the first report on the magnetotransport and critical current measurements for MoN and Mo_3Sb_7 in these forms. We show that though the scaling behavior near the transition temperature, T_c, is well described by a Ginzburg-Landau form (3) in both

systems, the overall critical current densities in the Mo_3Sb_7 fibers is an order of magnitude lower than would be expected from its transition temperature. We speculate that this may be a ramification of anomalously large spin fluctuation amplitude. As for the critical temperatures, it is known for a long time that spin fluctuations decrease T_c considerably in some superconductors. The increase in Tc could also be due to a strain effect because SEM clearly shows the expansion of the Mo_3Sb_7 wire by a factor of four. Long coherence lengths in these kinds of wires and fibers eliminates the problems with weak links, which are instead typically present in 'high T_c' materials, and suggests the possibility of achieving a remarkably high critical current density if proper technological treatments are adopted.

All of the Be- and Li-doped samples were obtained in the form of hard pellets without heating for an additional 2-3 h, unlike reported in the literature. The XRD results confirmed the single cubic phases (a~3.805 ± 0.005 Å) of the Be- and Li-substituted samples. The systematic peak shift on 2θ indicates the effect of the substitution for Mg. The encouraging result is the absence of oxides in Li-doped samples too. The sharp superconducting transitions in both the magnetic susceptibility and the resistivity data for x = 0 sample indicate the good quality of the samples. The T_c ~ 7.2 K and $H_{c2}(0)$ ~ 11.2 T are consistent with the values reported for pristine $MgCNi_3$. The Be substitution for Mg in $MgCNi_3$ has not shown any influential effect on the superconducting properties such T_c and H_{c2}. No substantial change in T_c for $Mg_{1-x}Li_xCNi_3$ is observed. The upper critical field of $Mg_{1-x}Li_xCNi_3$ for x > 0.1 is higher than that of pure $MgCNi_3$. The enhancement of the H_{c2} for Li-doped samples could be due to reduction of the mean free path which can be realized from the increase in resistivity with increase in x. To this point, electronic structure calculation of Be- and Li- substitution for Mg in $MgCNi_3$ may help to analyze effects of the substitution. In conclusion, the results suggest a small role of Mg in the superconductivity in this system. The reappearance of the superconductivity in the carbon

deficient samples $MgC_xN_yNi_3$ obtained by the heat treatment of MgC_xNi_3 in the stream of N at 900 ^oC for 2 h is an indication of the contribution of N to the superconductivity in $MgC_xN_yNi_3$. This is verified by the results of the characterization such as XRD and magnetic susceptibility measurements of the samples before and after the reaction.

We can conclude that high quality single crystals of VB_2 and $V_{1-x}T_xB_2$, where T stands for transition metals, were successfully grown by molten Al flux. Polycrystalline samples of $Cr_{1-x}V_xB_2$ for x = 0 to 1 were arc-melted. The single phase and the incorporation of the doped elements in the samples were confirmed by the result of XRD. CrB_2 shows the antiferromagnetic transition around 86 K, while VB_2 is paramagnetic above 1.9 K. The results are consistent with the previous reports. The *Neel* temperature could be tuned to zero by increasing the value of x but no superconductivity is observed. We were successful in measuring the dHvA frequencies to determine the Fermi surface and effective masses for the single crystals of VB_2 with *RRR* values as high as 258. The experimentally determined Fermi surfaces are in good qualitative agreement with the theoretical calculations. In the highest quality crystals, an unusually large magnetoresistance *MR* ~ 1100 % is observed at low temperature. The behavior of $MR \propto H^2$ indicates open orbits, which is consistent with the calculated Fermi surface for H//c. The parabolic increase in *MR* with increasing *RRR* reflects the importance of the quality of samples. The process we adopted here to grow single crystals could be used for the growth of single crystals of the other transition metal diborides.

This thesis has laid a strong foundation for the development of a novel synthesis route and guidelines in the search of new superconductors as well as in understanding the origin and nature of existing superconductors. There are many compounds which have the potential to be high T_c superconductors, and the effort for the development/upgrading of the synthesis techniques to produce them are in progress.

APPENDIX

LETTER OF PERMISSION

4/29/2008

To whom it may concern

I am preparing my dissertation entitled

"Investigation of superconductivity and physical properties of the intermetallic compounds MoN, Mo_3Sb_7, $MgCNi_3$ and Transition Metal Diborides"

to be submitted to the Graduate faculty of the Louisiana State University and Agricultural and Mechanical College in a partial fulfillment of the requirement for the degree of Doctor of Philosophy in the department of Physics and Astronomy.
I would appreciate permission to reproduce the following item(s) in both print and electronic editions of the dissertation. Unless you indicate otherwise, I will use the complete reference given above as the credit line. In case you do not control these rights, I would appreciate it if you could let me know to whom I should apply for permissions.

Figures : 1, 2, 3, 4 and 5
Tables : 1 and 2

Title : Magnetotransport properties and the Fermi surface of single crystal VB_2

Authors : A B Karki[1], D P Gautreaux[2], J Y Chan[2], N Harrison[3], D A Browne[1], R G Goodrich[1], D P Young[1,4]
Affiliations :
[1] Department of Physics and Astronomy, Louisiana State University, Baton Rouge, LA 70803, USA
[2] Department of Chemistry, Louisiana State University, Baton Rouge, LA 70803, USA
[3] National High Magnetic Field Laboratory, Los Alamos National Laboratory, Los Alamos, NM 87545, USA
[4] Author to whom any correspondence should be addressed
Email : dyoung@rouge.phys.lsu.edu

Journal : Journal of Physics: Condensed Matter
Issue : Volume 20, Number 3
Year : 2008
Citation : A B Karki, et al
2008 *J. Phys.: Condens. Matter* **20** 035209 **doi:** 10.1088/0953-8984/20/03/035209

For your convenience a copy of this letter may serve as a release form: the duplicate copy may be retained for your files.
Thank you for your prompt attention to this request. Permission is being requested of the authors and the publisher separately.
Yours sincerely,

Amar Bahadur Karki

Department of Physics and Astronomy,
Louisiana State University,
Baton Rouge, LA 70803, USA

I/We grant permission for the use of the work as set out above.
Signed:
Date:
On behalf of Publisher:

PERMISSION TO REPRODUCE AS REQUESTED
IS GIVEN PROVIDED THAT

~~(a) the consent of the author(s) is obtained~~
(b) the source of the material including author/editor, title, date and publisher is acknowledged. (*)

IOP Publishing Limited
Dirac House
Temple Back
BRISTOL
BS1 6BE

30/4/05
Date

Rights & Permission

(*) Please include mention of the journal's homepage at: www.iop.org/journals/jpcm and provide a link back to the article's abstract on our website from the electronic version of your thesis (if applicable).

Thank you!

VITA

Amar Karki was born in Nepal in October, 1970. After the completion of high school in 1986, he enrolled in intermediate level in science (I.Sc.) in Tribhuvan University, Patan Multiple Campus, Kathmandu, Nepal. He completed I.Sc. in 1988. He received a bachelor of science degree from Tribhuvan University, Patan Multiple Campus, in 1991. In 1995 he pursued a two-year master's program in physics with advanced solid state physics option from Tribhuvan University (TU), Central Department of Physics, Kathmandu, Nepal. He taught engineering physics course to undergraduate level in Nepal Engineering College until August 2002. In 2003, he received a master's degree in physics from Southern University and A&M College, Baton Rouge, Louisiana, USA. Then he enrolled in a doctoral program in condensed matter physics at Louisiana State University and A&M College, Baton Rouge, Louisiana, USA. He expects to graduate in summer 2008.